POLITECNICO
MILANO 1863

Mathematical and Numerical Modeling of Cardiac Fiber Generation and Electromechanical Function: Towards a Realistic Simulation of the Whole Heart

Advisor:
Prof. Alfio Quarteroni

Coadvisors:
Prof. Luca Dede'

Prof. Christian Vergara

Chair of the Doctoral Program:
Prof. Irene Sabadini

Doctoral dissertation of:
Roberto Piersanti

Politecnico di Milano
MOX – Dipartimento di Matematica
Mathematical Models and Methods in Engineering – XXXIV cycle

Abstract

Cardiovascular diseases are the primary cause of mortality worldwide, affecting millions of people every year. Although advancements in medical practice are continuously improving the diagnosis and treatment techniques, computer-based simulations of the cardiac function are gradually becoming a powerful tool to better understand the heart function and to support clinical decision-making.

Even though some area of heart modeling reached a certain level of maturity, whole heart models are a far-reaching endeavour and are still in their infancy. This thesis provides a detailed fully coupled multiscale mathematical and numerical model of cardiac electromechanics (EM) of the whole human heart.

Two crucial factors for accurate numerical simulations of cardiac EM, which are also essential to reproduce the synchronous activity of the heart, are: i) reconstructing the muscular fiber architecture that drives the electrophysiology signal and the myocardium contraction; ii) accounting for the interaction between the heart and the circulatory system, that determines pressures and volumes loads in the heart chambers. With the aim of facing the challenges formerly described, the main contributions in this thesis move along two strands: i) on the one hand, develop a unified mathematical framework, based on Laplace-Dirichlet-Rule-Based-Methods (LDRBMs), to prescribe myocardial fibers orientation in computational full heart geometries; ii) on the other hand, provide a biophysically detailed 3D EM model coupled with a 0D closed-loop lumped parameters model for the haemodynamics of the whole circulatory system.

This thesis gives a deeper account of existing biventricular LDRBMs, introducing also some modeling improvements, and presents a new biatrial LDRBM, which is able to quantitatively reproduce the atrial fiber architecture and can be easily applied to any arbitrary geometries. Systematic comparison of LDRBMs were performed in terms of meaningful electrophysiological and mechanical biomarkers computed as output of numerical EM simulations in physiological conditions. The validity of the proposed models were demonstrated through simulations on a realistic full heart geometry, showing that the obtained results match the experimental data available in literature.

In conclusion, the whole heart EM model of this thesis includes a detailed myocardial fibers architecture, simulates the electrophysiology, the mechanical activation and the mechanics of ventricles and atria, and is strongly coupled with a 0D closed-loop model of the whole cardiovascular system.

Keywords: *Cardiac electromechanics, Cardiac fiber architecture, Electromechanical simulations, Laplace-Dirichlet-Rule-Based-Methods, Whole heart modeling.*

Acknowledgements

This thesis project has received funding from the European Research Council (ERC) under the European Union's Horizon 2020 research and innovation programme (grant agreement No 740132, iHEART - An Integrated Heart Model for the simulation of the cardiac function, P.I. Prof. A. Quarteroni). We acknowledge the CINECA award under the class C ISCRA project HP10C3Z520 for the availability of high performance computing resources.

Sommario

Le malattie cardiovascolari sono la principale causa di mortalità nel mondo, affliggendo milioni di persone ogni anno. Sebbene i progressi nella pratica medica migliorino continuamente le tecniche di diagnosi e trattamento, le simulazioni computerizzate della funzione cardiaca stanno gradualmente diventando un potente strumento per comprendere meglio la funzione cardiaca e per supportare le decisioni cliniche.

Anche se alcune aree della modellazione cardiaca hanno raggiunto un certo livello di maturità, i modelli di cuore integrato, a causa della loro enorme complessità matematica e numerica, sono ancora nella loro infanzia. Questa tesi fornisce un modello matematico e numerico, completamente accoppiato, dell'elettromeccanica (EM) cardiaca dell'intero cuore umano.

Due fattori cruciali per poter ottenere delle simulazioni numeriche accurate di EM cardiaca, essenziali anche per riprodurre l'attività sincrona del cuore, sono: i) ricostruire l'architettura delle fibre muscolari che guida sia il segnale elettrofisiologico che la contrazione del miocardio; ii) tener conto in modo appropriato dell'interazione tra il cuore e il sistema cardiocircolatorio, che determina pressioni e carichi di volume nelle camere cardiache. Con l'obiettivo di affrontare le sfide precedentemente descritte, i principali contributi di questa tesi si muovono lungo due filoni: i) da un lato, sviluppare un quadro matematico unificato, basato sui Laplace-Dirichlet-Rule-Based-Methods (LDRBM), per prescrivere l'orientamento delle fibre miocardiche nelle geometrie computazionali di cuore totale; ii) d'altra parte, fornire un modello dettagliato di EM 3D accoppiato con un modello 0D a ciclo chiuso per l'emodinamica dell'intero sistema cardiocircolatorio.

Questa tesi fornisce un resoconto più approfondito dei LDRBM ventricolari esistenti, introducendo anche alcuni miglioramenti modellistici, e presenta un nuovo LDRBM atriale, che è in grado di riprodurre quantitativamente l'architettura delle fibre atriali e può essere facilmente applicato a qualsiasi geometria. Il confronto sistematico dei LDRBM è stato eseguito in termini di indicatori elettrofisiologici e meccanici significativi, calcolati come risultato di simulazioni numeriche di EM in condizioni fisiologiche. La validità dei modelli proposti è stata dimostrata attraverso simulazioni su una geometria realistica di cuore totale, dimostrando che i risultati ottenuti sono compatibili con i dati sperimentali disponibili in letteratura.

In conclusione, il modello di EM di cuore totale, presentato in questa tesi, include un'architettura dettagliata delle fibre miocardiche, simula l'elettrofisiologia, l'attivazione meccanica attiva e passiva di ventricoli e atri ed è fortemente accoppiato con un modello 0D a ciclo chiuso dell'intero sistema cardiovascolare.

Parole chiave: *Elettromeccanica cardiaca, Architettura delle fibre cardiache, Simulazioni di elettromeccanica, Laplace-Dirichlet-Rule-Based-Methods, Modellazione a cuore intero.*

Ringraziamenti

Questo progetto di tesi ha ricevuto finanziamenti dallo European Research Council (ERC) nell'ambito del programma di ricerca e innovazione Horizon 2020 dell'Unione Europea (convenzione di sovvenzione n. 740132, iHEART - Un modello di cuore integrato per la simulazione della funzione cardiaca, P.I. Prof. A. Quarteroni). Ringraziamo il premio CINECA nell'ambito del progetto ISCRA di classe C HP10C3Z520 per la disponibilità di risorse di calcolo ad alte prestazioni.

Contents

List of Figures

List of Tables

List of Abbreviations

Anatomical terms

LA	Left Atrium
LV	Left Ventricle
RA	Right Atrium
RV	Right Ventricle
MV	Mitral Valve
TV	Tricuspid Valve
AV	Aortic Valve
PV	Pulmonary Valve
LPV	Left Pulmonary Veins
RPV	Right Pulmonary Veins
SCV	Superior Caval Vein
ICV	Inferior Caval Vein
SAN	Sinoatrial Node
AVN	Atrioventricular Node
CCS	Cardiac Conduction System
OT	Outflow Tracks
IC	Inter-atrial connection
PM	Pectinate Muscles
CT	Crista Terminalis
CS	Coronary Sinus
CSM	Coronary Sinus Musculature
BB	Bachmann's Bundle
FO	Fossa Ovalis
RAS	Right Atrial Septum
LAS	Left Atrial Septum
RAW	Right Atrial lateral Wall
LAW	Left Atrial lateral Wall
RAA	Right Atrial Appendage
LAA	Left Atrial Appendage
LAR	Left Atrial Roof
IB	Inter-caval Bundle
IST	Isthmus

Models and Methods

EP	Electrophysiology
MA	Mechanical Activation
TM	Tissue Mechanics
EM	Electromechnics
EFM	Electrofluidmechnics
ODEs	Ordinary Differential Equations
PDEs	Partial Differential Equations
RBMs	Rule-Based-Methods
LDRBMs	Laplace-Dirichlet-Rule-Based-Methods
R-RBM	Rossi et al. [204] RBM
B-RBM	Bayer et al. [26] RBM
D-RBM	Doste et al. [58] RBM
CRN98	Courtemanche-Ramirez-Nattel
TTP06	ten-Tusscher-Panfilov
ICI	Ionic Current Interpolation
RDQ18	Regazzoni-Dedè-Quarteroni
ANN	Artificial Neural Network
SIS	Segragated-Intergrid-Staggered
IMEX	Implicit-Explicit
FE	Finite Element
FEM	Finite Element Method
FD	Finite Difference
BDF	Backward Difference Formulae
RLC	Resistance-inductance-capacitance

Others abbreviations

DOF	Degrees Of Freedom
HPC	High Performance Computing
DTI	Diffusion Tensor Imaging
MRI	Magnetic Resonance Imaging
DT-MRI	Diffusion Tensor Magnetic Resonance Imaging
CT-scan	Computed Tomography scan
CAD	Computer Aided Design
AVD	Atrioventricular plane Displacement
PV-loop	Pressure-Volume-loop
LFS	Longitudinal Fractional Shortening
WT	Fractional wall thickening
EDV	End Diastolic Volume
ESV	End Systolic Volume
EF	Ejection Fraction
SV	Stroke Volume

Chapter 1

Introduction

Cardiovascular diseases (CVD) represent the primary cause of morbidity and mortality worldwide, affecting millions of people every year [241, 257]. These are estimated as 31% of all deaths[1]. The 85% of all CVD deaths are due to heart failure[2]. One of the indirected reason behind such grim statistics is our limited understanding of the mechanisms driving these pathologies [148].

Although experimental research and advancements in medical practice are continuously improving the diagnosis and treatment techniques, computational modeling of the cardiac function [92, 20, 18, 124, 159, 234, 78] are gradually becoming a cornerstone in precision-medicine [172]. Computer-based numerical simulations provide a powerful tool to better understand the heart function in both physiological and pathological scenarios to improve and support clinical decision-making in cardiac diseases [172, 223, 227].

The mathematical modeling of the beating heart and its pumping action is an highly complex task involving several difficulties related to the complexity of its function. A single heartbeat involve multiphysics and multiscale processes. The corresponding mathematical models describing each physical sub-mechanism, involved in the heart function, require therefore multiphysics and multiscale numerical approaches, making the numerical modeling of the whole cardiac activity very challenging [188].

Even though heart modeling reached a certain level of maturity, whole heart models are a far-reaching endeavour and a field of current investigation. Four chambers cardiac models are still in their infancy: until today, the most comprehensive simulation of the entire cardiac function, including multiscale process in the tissue, blood haemodynamics in the heart chambers and valve dynamics, is the *UT heart simulator* developed by the research team of Tokio University [237].

This thesis is dedicated to develop a detailed fully-coupled multiscale mathematical and numerical model of the electrical and mechanical activity of the whole human heart. Our model includes state of the art models, based on human physiology, for both the cardiac electrophysiology and muscle mechanics, and also takes into account the presence of the whole circulatory system. A topic to which we devote particular attention is the detailed reconstruction, by means of a mathematical model, of all

---

[1] `https://www.world-heart-federation.org`

[2] `https://www.who.int/cardiovascular_diseases/en/`

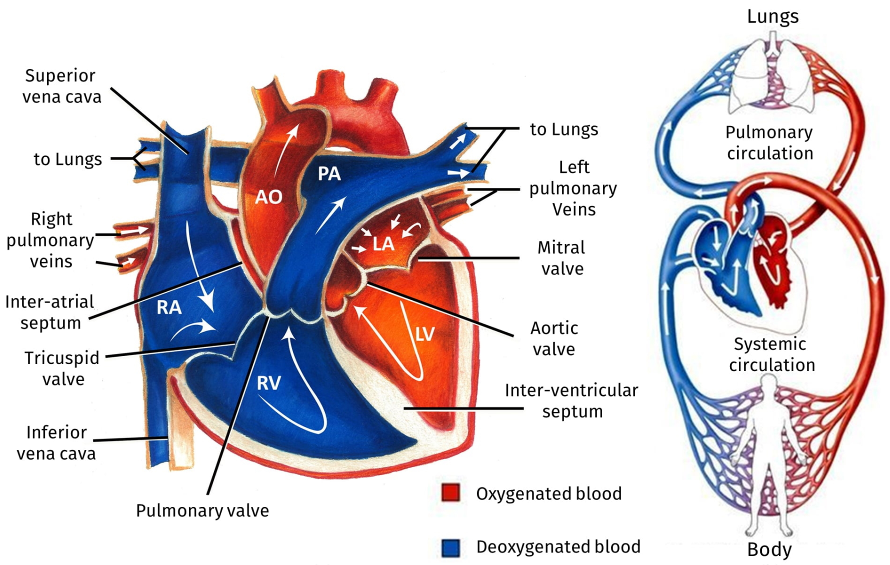

(a) (b)

Figure 1.1: (a) Blood flow through the heart; (b) The heart inside the whole circulatory system. Images taken from `www.pediatricheartspecialists.com` (a) and `www.pinterest.it` (b).

the main characteristic features of the cardiac muscular architecture, which is the main driver of the heart contraction-relaxation. We demonstrate the validity of the proposed model through simulations on realistic whole heart geometry.

In this introductory chapter, we provide a brief overview on the anatomy and the physiology of the heart function (Section 1.1), then we focus on the mathematical modeling, with particular attention on the cardiac muscular architecture and the heart electromechanical activity (Section 1.2). In the end, we detail the main objectives and the original contributions of this thesis (Section 1.3).

1.1 Overview of heart anatomy and physiology

The heart is a four chambers muscular organ whose function is to pump the blood throughout the whole circulatory system. It is divided into the *left atrium* (LA) and *left ventricle* (LV), forming the *left heart*, and the *right atrium* (RA) and *right ventricle* (RV), defining the *right heart*. Both sides act in a synchronized fashion: the left side pumps the oxygenated blood through the systemic arteries into the organs (*systemic circulation*), meanwhile the right one recycles the deoxygenated blood through the systemic veins into the lungs (*pulmonary circulation*) [188, 187]. The left and right hearts are separated by the *inter-atrial* and *inter-ventricular septa*, which prevent the mixing of oxygenated and deoxygenated blood, whereas the atria and the ventricles are connected by the *atrioventricular valves* (*mitral valve*, MV, and *tricuspid valve*, TV) that regulate the blood transfer from the upper to lower cavities. The four chambers are connected to the circulatory system: the ventricles with the *aorta* through the *aortic valve* (AV) and with the *pulmonary artery* via the *pulmonary valve* (PV); LA with the *left* and *right pulmonary veins* (LPV, RPV), whereas RA with *superior* and *inferior caval veins* (SCV, ICV), see Figure 1.1.

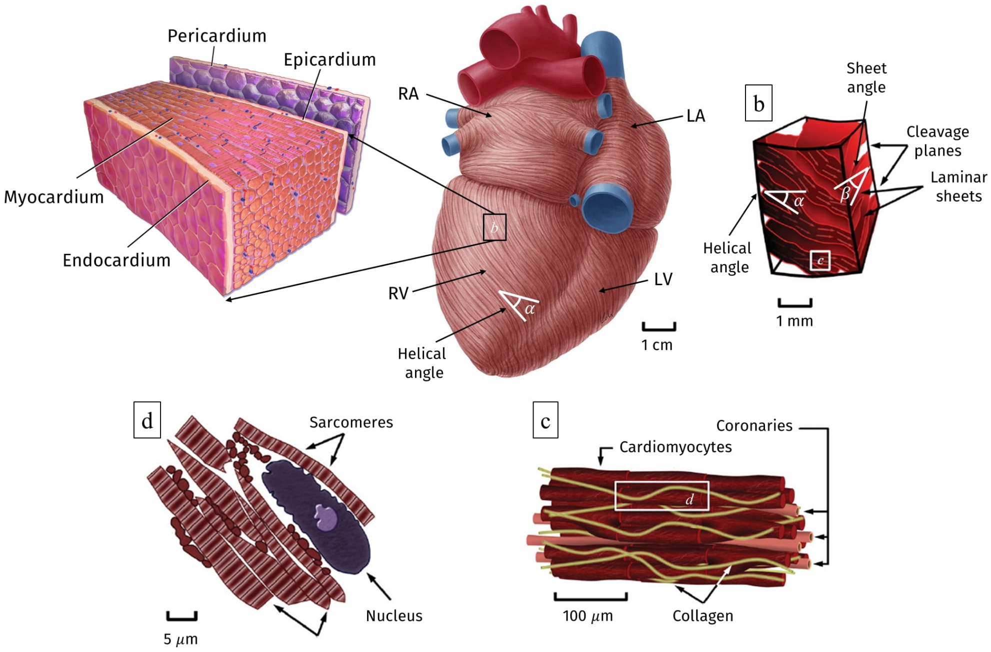

Figure 1.2: Representation of the multiscale cardiac muscle. Images taken from [41], `www.kenhub.com` and `www.biologyonline.com`.

1.1.1 The cardiac muscular architecture

The heart wall is made up of three layers: the internal thin *endocardium*, the external thin *epicardium*, that is surrounded by the *pericardium* (a membrane that isolates the heart from other organs), and the thick muscular cardiac tissue, the *myocardium*. Most of the myocardium is occupied by *cardiomyocytes*, striated excitable muscle cells specialized in the cardiac function, that are joined together in linear arrays. Each cell contains several *myofibrils*, which are stretched chains of *sarcomeres*, the basic contractile units of cardiac muscle. The result of cluster cardiomyocytes, locally organized as composite laminar sheet (or cleavage) planes, defines the muscular *fiber* (also called *myofibers*) orientations. Aggregations of myofibers give rise to the fiber-reinforced heart structure defining the cardiac muscular architecture [134, 232, 86, 128]. A schematic representation of the multiscale myocardial fiber-structure is shown in Figure 1.2. Ventricular muscular fibers are well-organized as two intertwined spirals wrapping around the heart, clockwise on the sub-epicardium and counter-clockwise on the sub-endocardium, defining the characteristic myocardial helical structure [134, 232]. Local orientation of myofibers are identified by their angle on the tangent plane and on the normal plane of the heart, called the *helical* and the *sheet* angles, respectively [232, 243], see Figure 1.2. The transition inside the myocardial wall is characterized by a continuous change in helical angle from about 60^o to 90^o at the epicardial surface to nearly 0^o in the mid-wall region to -20^o to -60^o at the endocardium [134, 232, 242], with circumferential and longitudinal fiber orientations predominant in RV with respect to LV [214, 154, 9, 211], see Figures 1.3(a-b).

Atrial fibers architecture is very different from that of the ventricles, where myofibers are aligned in a regular pattern [232]. Indeed, fibers in the atria are arranged

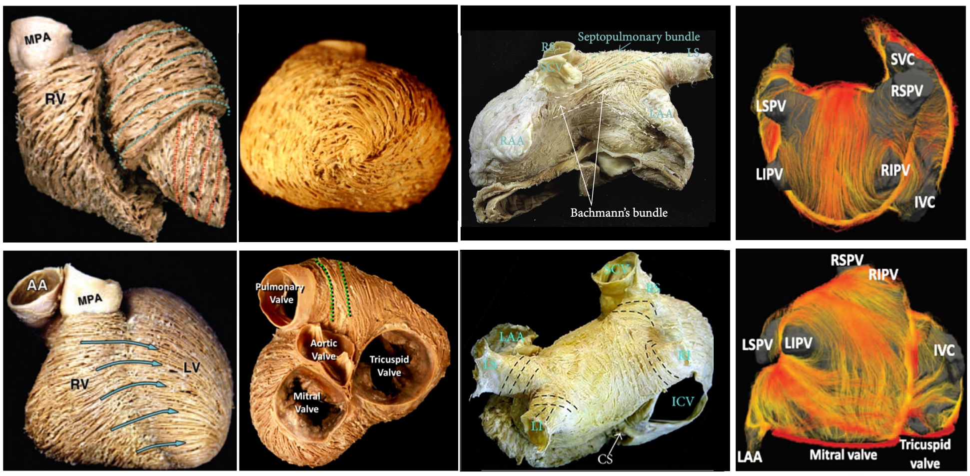

(a) (b) (c) (d)

Figure 1.3: Anatomical dissection of myocardial fibers in ventricles (a-b) and atria (c). Atrial fibers revealed by sub-millimiter *Diffusion Tensor Magnetic Resonance Imaging*, DT-MRI (d). Images taken from [214, 212, 167].

in individual bundles running along different directions throughout the wall chambers. Preferred orientation of myofibers in the human atria is characterized by multiple overlapping structures, which promote the formation of separate attached bundles [57], Figure 1.2 also 1.3(c-d).

The complex cardiac muscular architecture is the backbone of a proper pumping function and has a strong influence in the contraction of the heart [200, 185, 62, 163].

1.1.2 The heart electromechanical activity

The heart contraction, which is responsible for the blood pumping, is triggered by a series of electrochemical reactions occurring in the myocardium. Each heartbeat is initiated by an electrical signal, spontaneously generated in the *sinoatrial node* (SAN, the heart natural pacemaker located in the upper part of RA) consisting of self-excitable cells [36]. This impulse produces an electrical wave that propagates from RA to LA across all the cardiomyocytes, causing a rapid variation of their potential difference across the cell membrane, the so-called *transmembrane potential* [72]. The cell membrane depolarizes and the transmembrane potential increases from a negative resting value to a positive value (*deporalization*), remains nearly constant (*plateau*) and then returns to the resting value (*polarization*). This event is known as *action potential* and induces a release of calcium ions concentration by a complex biochemical reactions inside the cells [72]. The above intracellular mechanism produces the kinetic activation of the sarcomeres causing the shortening of the cardiac myofibers [112]. The highly organized structure of the fibers translates in the macroscopic muscle deformation enabling the atrial contraction. The transmembrane potential drives faster along the myofibers [200, 185] allowing the electric signal to reach the *atrioventricular node* (AVN, located between RA and the ventricles). AVN acts as a filter to ensure that the atria contract before the signal enters into the ventricular fast *cardiac conduction system*, CCS (mainly composed by the so-called *Purkinje network*, a sub-endocardial

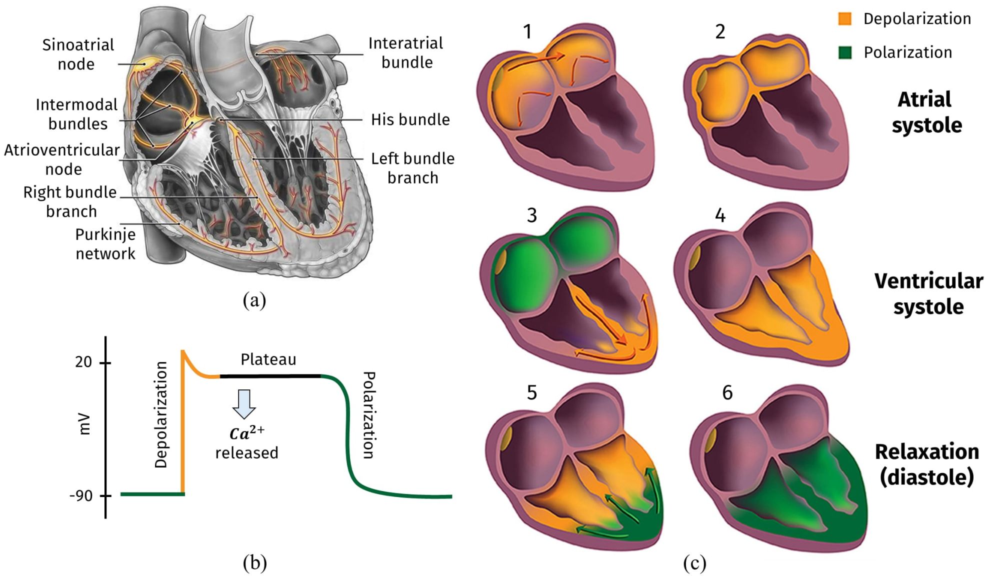

Figure 1.4: (a) CCS anatomy; (b) Characteristic action potential of cardiomyocytes; (c) Graphical representation of the electromechanical activity of the heart. Images taken from `www.alamy.com` and [225].

highly conductive system). CCS is responsible for the coordinated propagation of the electric signal in the ventricles [239]. Then, similarly to what happens in the atria, the signal travels from cell to cell throughout the myocardial muscle, allowing the ventricular twisting. Finally, this synchronized heart contraction governs the blood pressure inside the cardiac chambers, determining a ruled opening of the heart valves and ensuring, at each heartbeat, the physiological blood flow throughout the heart chambers and into the circulatory system [187, 112]. A schematic representation of the electromechanical activity of the heart is outlined in Figure 1.4. Each *cardiac cycle* can be summarized into the following three phases (see also Figure 1.4):

- **Atrial systole**: SAN generates an action potential yielding the contraction of both atria, forcing the blood flow from the atria to the ventricles. At this stage, TV and MV are opened, while AV and PV are closed.

- **Ventricular systole**: The activation front reaches AVN allowing, after a timed delay, the signal propagation into the ventricles, causing their contraction and the closing of MV and TV. The ventricular pressure raises until it overcome the pressures of the aorta and of the pulmonary artery, triggering AV and PV to open and the consequent ejection of the blood from the ventricle.

- **Relaxation**: AV and PV close and when the pressure of ventricles reaches that of atria, MV and TV open again. At the end of this phase, a slow filling phase (from the atria to the ventricles) begins. In the cardiac cycle, the relaxation period of the heart muscle is named *diastole*.

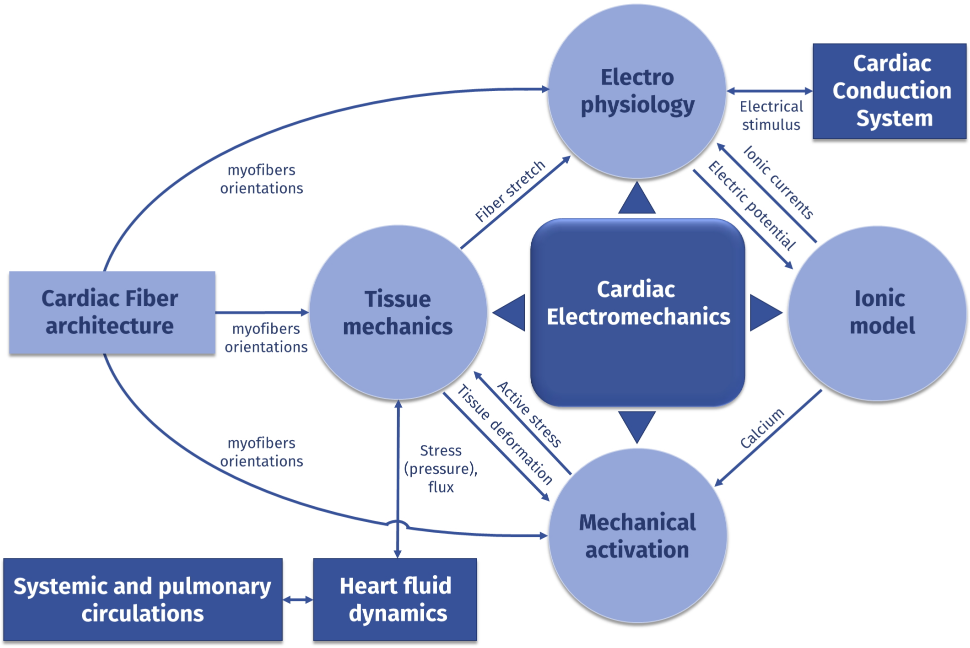

Figure 1.5: Sketch of the building blocks of a cardiac EM mathematical model. The references highlight the corresponding coupling quantities between each subsystem.

1.2 An overview of mathematical models for the cardiac electromechanics

The heart can be regarded as a complex system that involves different interacting physical phenomena at the molecular, cellular, tissue and organs levels: *electrophysiology*, EP (which drives the electrical potential propagation across the cardiomyocytes), *mechanical activation*, MA (governing the activation-contraction mechanism inside the sarcomeres), active and passive *tissue mechanics*, TM (of the fiber-muscle deformation), and *fluid haemodynamics* (of blood flow inside the heart chambers).

In mathematical modeling, these (single) physics are referred to as "*core models*", expressed by system of Ordinary Differential Equations (ODEs) and Partial Differential Equations (PDEs) and tightly coupled together [188]:

◇ The EP core model is set forth by a system of PDEs, such as the *bidomain*, the *monodomain* or the *eikonal* equations coupled with an *ionic model*, a system of ODEs characterizing the ionic fluxes dynamics across the cell membrane [72, 71, 246, 247, 47, 6, 145]. EP model needs to integrate the presence of CCS often providing a number of early activation points, that surrogate faster endocardial activation [43, 127, 59], or using physiologically-relevant methods that emulate the structure of CCS network [252, 251, 46, 218, 126, 82];

◇ The MA core model can be described by means of PDEs or Monte Carlo approximations of physics-based models [195, 261, 106]. However, due to the their huge computational costs, involved in their numerical solution, phenomenological models of system of ODEs, owing to represent the complex mechanisms behind the generation of active force at subcellular level, are typically preferred [125, 149, 196, 194, 204];

◇ The TM core model can be represented by the elastodynamics equation in the framework of non-linear elasticity by adopting, for the passive mechanics a suitable hyperelastic constitutive law [160, 102, 103, 89, 90, 12], and for the active parts, either an *active stress* [188, 7, 249, 248] or *active strain* paradigm [204, 23];

◇ The fluid core model can be described with either a 3D "full" model or a 0D "reduced" one. In the former, the blood haemodynamics is modeled employing the incompressible *Navier-Stokes* equations for a Newtonian fluid. In the latter, the fluid pressure, acting on the endocardia, is taken into account by means of ODE-based models [188, 187].

When the blood haemodynamics is modeled by means of a 3D fluid model, we generate a *Fluid-Structure Interaction* (FSI) problem also known as *electrofluidmechanics* (EFM) model [188, 237, 69, 213, 158]. Whereas, employing a 0D model, the fluid pressure, acting on the endocardia, is taken into account by means of ODE-based models, thus obtaining an *electromechanics* (EM) model of the heart [233, 78, 21, 19, 198].

In addition, the interaction mechanisms among the four chambers are also regulated by the systemic and pulmonary circulations. Therefore, an EM/EFM model needs to account for the coupling with the rest of the circulatory system (say, the complements of the four heart chambers), usually represented by simplified lumped-parameter *Windkessel* models [204, 53, 139, 80, 209, 130, 184] or, less common, closed-loop systems [19, 198, 113, 96]. A schematic representation of the building blocks constituting a mathematical model of cardiac EM is shown in Figure 1.5.

Finally, EM/EFM models should properly consider the strongly anisotropic nature of the cardiac fiber architecture by accurately prescribing their orientations, which is crucial in order to obtain physically meaningful results [30, 25]. Local fiber directions are mapped based on histological sectioning informations, taken from measurements on *ex-vivo* hearts [232, 253, 154, 93], or on digital processing (*structure tensor methods*) of high-resolution volumetric imaging techniques [95, 269, 268, 167, 179], sometimes using a statistical atlas heart [250, 161, 174]. In cases where neither histological nor imaging information is available, myofiber structures are typically incorporated by using *rule-based methods*, that estimate the fiber orientations associated to each element of the volumetric mesh from pre-established patterns derived from histo-anatomical findings [204, 176, 26, 260, 58]. Figure 1.6 shows a summary of the methods most commonly used to obtain the cardiac fiber architecture.

1.2.1 Cardiac fibers modeling overview

In computational models of cardiac EM/EFM, a major issue consists in modeling the complex arrangement of myocardial fibers that characterizes the cardiac tissue. Aggregations of myofibers determine how the electric potential propagates within the muscle [232, 200, 185, 176]. Indeed, the electrical propagation is three-four times faster along the fiber direction than along its orthogonal plane [110]. Moreover, also the muscle mechanical contraction, which is triggered by the propagation of the electric potential thorough the tissue, strongly depends on the fibers orientation [62, 163, 87, 164, 39, 81]. For instance, the essential ventricular twisting is attributed to the arrangement of the myocardial helical fibers [230]. However, while it is well recognized

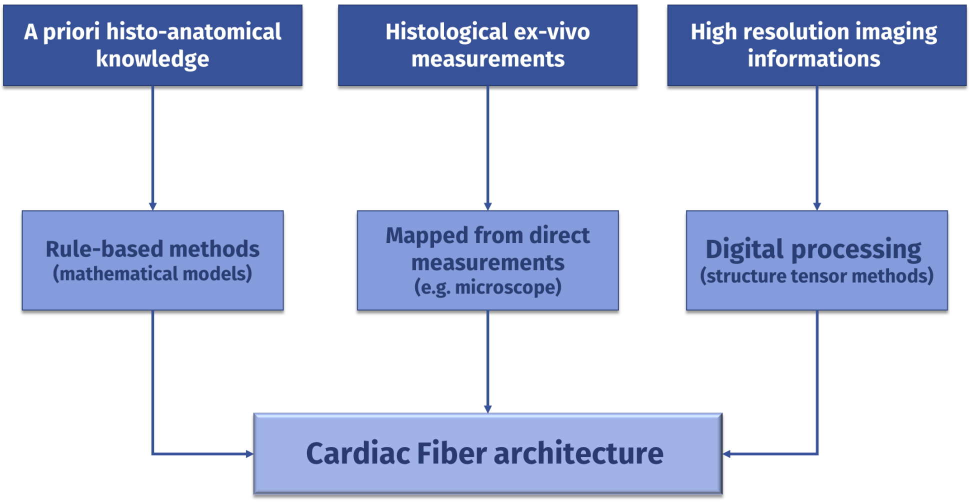

Figure 1.6: Diagram showing the main sources of information at muscular tissue level and the methods used to prescribe the cardiac fiber architecture in EM/EFM models.

that myofibers orientation is crucial for the construction of a realistic EM model, their architecture has been explored only in a few works and it is not fully understood [163, 87, 233, 21, 81, 182]. Recently, it has been shown that myofiber orientations are dispersed around a predominant direction [3, 228]. However, the modeling of contraction caused by dispersed myofibers was addressed in EM models only in [130, 63].

Over the years, myofibers orientation has been studied using mainly histological data, anatomical dissections and Diffusion Tensor Imaging (DTI) acquisitions [232, 9, 211, 8, 104, 95, 167, 97, 165, 240, 100, 98, 16, 51, 93], see Figure 1.3. DTI is a Magnetic Resonance Imaging (MRI) technique able to produce useful structural information about heart muscle fibers and largely applied to explanted *ex-vivo* hearts, coming from animal experiments [104, 95, 217, 267, 174] or from human corpses [134, 167]. However, acquired *in-vivo* DTI protocol lasts hours and generally produces a noisy low-resolution fibers reconstruction [243, 5, 143]. Furthermore, there is a paucity of imaging data on atrial fibers orientation with respect to the ventricles, mainly due to imaging difficulties in capturing the thin atrial walls [57]. Only recently, ex vivo atrial fibers have been analysed owing to submillimeter *Diffusion Tensor MRI* (DT-MRI) [167, 268, 269], see Figure 1.3(d). Moreover, since the atrial thickness is smaller than the DTI voxel size, it is not possible to obtain in-vivo myofibers in the atria [101]. All the above considerations make nowadays DTI techniques unusable to reconstruct accurate 3D myofibers field in the common clinical practice.

Because of the difficulties to acquire patient-specific data of fibers distribution, different methodologies have been proposed to provide a realistic surrogate of fiber orientation for in-vivo cardiac geometries [204, 134, 242, 26, 58, 101, 266, 120, 64]. Among these, atlas-based methods map and project a detailed fiber field, previously reconstructed on an atlas, on the geometry of interest, exploiting DT-MRI or histological data; see [134] for the ventricles and [101, 202] for the atria. However, these methods require complex registration algorithms and the results depends on the original atlas data upon which they have been built.

Alternative strategies for generating myofiber orientations are the so called *Rule-Based Methods* (RBMs) [30, 183, 154, 32]. RBMs describe fiber orientations with mathematically sound rules based on histological or DTI observations and require information only about the myocardial geometry [232]. These methods parametrize the transmural and apico-basal directions in the entire myocardium to assign orthotropic (longitudinal, transversal and normal) myofibers; see [204, 26, 58, 25, 266, 183] for the ventricles and [242, 120, 64, 67, 180] for the atria.

A particular class of RBMs, which relies on the solution of Laplace boundary-value problems, is known as *Laplace-Dirichlet-Rule-Based Methods* (LDRBMs), addressed in [204, 26, 58, 25, 266] for the ventricular case. LDRBMs define the transmural and apico-basal directions by taking the gradient of solutions corresponding to suitable Dirichlet boundary conditions. These directions are then properly rotated to match histological observations [86, 9, 211]. The above procedure ensures a smooth and continuous change in fibers directions throughout the whole myocardium.

Most of existing ventricular RBMs refer to LV only and usually introduce an artificial basal plane located well below the cardiac valves. Only recently, a LDRBM, that takes into account fiber directions in specific cardiac regions, such as RV, the inter-ventricular septum and the outflow tracks, has been developed [58]. This has provided a great improvement in RBMs since RV exhibits a different fiber orientation with respect to LV [134, 95, 217, 115]. The presence of a discontinuity in the inter-ventricular septal fibers is a crucial matter, still very debated [115, 34].

Regarding the atria, several RBMs have been developed. They either use semi-automatic rule-based approaches [242, 120, 64, 67, 180, 119, 123, 201] or prescribe manually the fiber orientations in specific atrial regions [94, 256, 108, 220]. Recently, atlas-based methods, in which fiber directions of a reference atrial geometry are warped on a target geometry, have been introduced [101, 202, 215, 141, 203]. All the former procedures require manual intervention introducing, for example, various distinct landmarks, seed-points and a network of auxiliaries lines [120, 64]. Furthermore, they are often designed for specific atrial morphologies [242, 120]. Moreover, no LDRBMs have been proposed so far for the atria. As a matter of fact, an extension of the ventricular LDRBMs is not straightforward, mainly because the atrial fibers architecture is characterized by the presence of multiple overlapping bundles running along different directions, differently from the ventricles one where myofibers are aligned along regular patterns. Hence, a processing procedure for generating atrial fibers field still remains a knotty procedure [64, 65].

1.2.2 Electromechanical modeling overview

Several of the past computational studies have focused their attention only on either the cardiac EP or TM, even if the electrical and mechanical functions of the heart are highly interconnected. The vast majority of EP modeling studies ignored any effects due to mechanical deformation and, vice versa, most TM modeling studies did not represent explicitly any feedback of deformation on EP [89, 13, 151, 244, 245, 207]. Indeed, in the cardiac modeling community, fully coupled EM models are still an exception rather than the common rule [188, 244]. Only in the last decade, great efforts have been spent to develop computational models of cardiac EM [92, 20, 18, 124, 159, 234, 78] with increasingly biophysical detail, by properly taking into account the interacting physical phenomena contributing to the heart EM [172, 223, 227, 41, 48]. However, most of the existing EM models refer to LV only [204, 198, 139, 80, 209, 130, 184] and neglect the important effects of the right ventricular deformation on the heart pumping function [163]. Only in the last decade, EM models have been purposely developed for biventricular geometries [19, 96, 224, 42, 83, 49, 4, 75] and, very recently, have been applied to four chambers hearts [233, 19, 78, 175, 124].

From a mathematical point of view, the effect of the electrochemical system on EP is represented by the so-called mechanoelectrical feedback, which influences the speed of propagation of the travelling wave: this is satisfactorily achieved by considering the monodomian/bidomain equations in a deforming medium, as well as accounting that some ionic channels opening is regulated by stretching [187, 130, 73]. At TM level, the direct coupling between the electrochemical model and tissue deformations is the prominent active contraction, which is typically expressed by considering an *active stress* formulation, where one-dimensional active tension, along the fiber, is imposed in the stress tensor [188, 7]. However, purely one-dimensional active stress cannot describe the macroscopic orthotropic behaviour of cardiac TM and more general orthotropic active stress formulations [249, 248] (or as an alternative the more complex orthotropic *active strain* formulations [204, 23]) were proposed. This orthotropic activation was able to better fit experimental data, but no clear explanation of the forces in the direction orthogonal to the fibers field was given. It has been argued that cross-fibre active contraction may be related to myofiber orientations that are dispersed around a predominant direction [3, 228]. Recently, based on experimental measures [132], cross-fibers active tension has been introduced in [87, 207, 77, 264, 88] to model the contraction caused by dispersed myofibers. However, this aspect has been addressed in EM models only in [130, 63].

From the numerical point of view, once the discretized core models are obtained, a central topic concerns the numerical strategy selected for the integrated coupled model: i.e. how the isolated problems are solved with respect to each other. Usually, electromechanical coupling has been achieved by either a *monolithic* approach, where the approximated equation are simultaneously solved in a single large system, or a *segregated* algorithm, where the approximated problems are solved sequentially (in a suitable order) [53, 80]. Monolithic solvers usually show better accuracy and stability properties with respect to segregated ones, but they are much more computationally demanding [96, 80]. Segregated solvers, that require less computational resources at the cost of a reduced accuracy and stability, are becoming popular for solving cardiac EM [20, 204, 78, 42, 83, 248, 22]. Recently, segregated solvers have been formulated so that different time step size, for the single core models, can be used, thus leading to the so called *segregated-staggered* algorithms [78, 53]. Moreover, segregated-staggered solvers have been extended allowing to adopt different resolution in space and time, thus leading to the *segregated-intergrid-staggered* (SIS) numerical schemes [209, 199, 177]. This is physically motivated by the fact that different space-time resolutions are required for the single core models: namely, EP requires a fine space-time discretization, to capture the fast transients and the steep depolarization wavefront [20, 181]; in contrast, TM can be solved with coarser resolutions, due to the smoother spatial and slower temporal scales governing the cardiac deformation [20, 89].

Two crucial aspects for an accurate numerical simulation of the cardiac EM, which are also essential to reproduce the synchronous activity of the heart, are:

i) properly imposing the mechanical boundary conditions able to replicate the realistic motion of the heart;

ii) accounting for the interaction between the heart and the whole circulation.

The motion of the heart underlies different constrains involving the interplay of ventricles, atria and the pericardium in which the heart is embedded. On the one hand, the pericardium has a direct impact on the cardiac motion, constraining the epicardium to slide on the parietal pericardium [263, 175]. On the other hand, the atrioventricular plane displacement (AVD) is considered to be the major contributor to the ventricular pumping function [38]. The pericardium effect is properly taken into account using contact mechanics [74] or applying normal Robin boundary conditions on the epicardium [175, 235]. However, the majority of ventricular EM models have limitations in reproducing the longitudinal systolic shortening, as excluding the atria from the geometry requires to fix the basal plane or restrict its radial motion [260, 75, 68, 50, 153]. This is in contrast with physiological contraction where the AVD moves significantly downwards in the apico-basal direction [38].

The coupling between the circulatory system haemodynamics and the cardiac TM determines pressures and volumes in the heart chambers [80, 19, 113, 54, 87, 260]. From a physical point of view, this coupling is most accurately described by an FSI problem [158, 111, 262]. This is relevant for investigating blood flow patterns or wall shear stresses, but often not needed for simulating cardiac EM. Typically, EM models are coupled with Windkessel-type preload/afterload models for the circulatory system comprising 2-, 3-, 4-elements [60, 133, 221, 231, 258, 265]. In these models, the different phases of the pressure-volume loop (PV-loop) are managed by solving different sets of differential equations, one for each phase [80, 53, 62, 248]. Still, more meaningful and physiologically sound interface conditions can be obtained by coupling the 3D EM model with a 0D closed-loop model of the complete circulatory system for the whole cardiac cycle. [198, 33, 15, 144, 162]. A further advantage of the latter approach is that closed-loop circulation models do not require to be adapted through the different phases of the cardiac cycle [159, 19, 54, 199]. However, solving efficiently the coupling between the EM model and the closed-loop model for the whole cardiovascular system is a challenging task [19]. This coupled problem has been so far addressed only in a few works, namely [198, 96, 19, 113, 233].

1.2.3 Whole heart electromechanical modeling overview

In the last decades, several cardiac computational models were developed to study pathological conditions affecting either the electrical or mechanical response in individual heart chambers. The origin of heart diseases is often local: e.g., fibrillation and myocardial infarction are typical electrical and mechanical dysfunctions. However, heart diseases almost always progress to affect the entire organ, impacting on the electrical and mechanical function of all four chambers [131]. In the quest for a more quantitative understanding of the heart functioning both in health and diseased scenarios, it became fundamental to model and simulate the entire heart as an whole organ [244]. Only recently, the scientific community moved to model and simulate the electro-mechanical response of the whole heart [22, 74, 20, 213, 124, 175, 235, 233, 234, 78, 117].

The step zero of any computational whole heart EM simulation consists in the so-called *preprocessing procedure*, which includes the generation of a computational heart mesh, the embedding of the cardiac fiber architecture and the recovering of the so-called stress-free *reference configuration*. This procedure is particularly important if we aim at realistic patient-specific simulations, since obtaining in-vivo data (with non invasive measurements) is a very complex task not routinely performed in current clinical procedures [140].

The discretization of a whole heart geometry can be obtained starting from segmented medical images, acquired from imaging techniques such as MRI or *Computed*

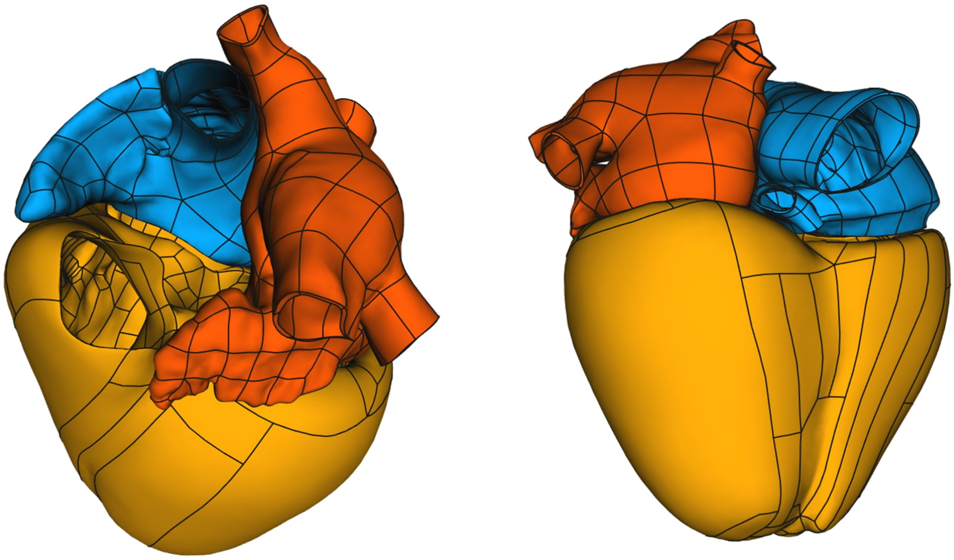

Figure 1.7: The Zygote heart CAD model [107] reconstructed from high-resolution CT-scan, representing an average healthy heart. Image taken from [37].

Tomography (CT) scan, or using detailed *Computer Aided Design* (CAD) models (see Figure 1.7). Given the geometry, the creation of a whole heart mesh is a challenging procedure mainly because the atrial wall is about an order of magnitude thinner than the ventricular wall. In addition, atria are typically entangled and their geometry can be quite involved, further complicating the heart meshing [22]. Furthermore, generating a whole heart mesh, starting from medical images data or CAD models, requires several meshing tools to move from a surface to a volumetric mesh and labelling of surfaces and volumes in order to impose specific electrical or mechanical tissue properties and boundary conditions. Along this side, promising results have been shown in [66, 146], where several meshing tools specific for cardiac modeling have been presented. One of the first high-resolution four chamber three-dimensional unstructured mesh, including the atria and a portion of the major vessels, was presented in [20]. Recently, a publicly available virtual cohort of about twenty linear tetrahedral four chamber meshes was reported in [234].

Prescribing the myofibers architecture is significantly more challenging in full heart geometries. Many of the existing four chambers heart models embed only the ventricular fibers [234, 20], include simplified architecture for the atria [124] or adopt different methodologies for considering the atrial fibers [233, 78, 175], either by using different RBMs for the ventricle and the atria [175, 78, 74] or by mapping the atrial fibers from ex-vivo DT-MRI dataset, using the so-called universal coordinate system [233, 203]. To the best of our knowledge, none of whole heart computational studies makes use of a unified methodology to directly embed reliable and detailed cardiac myofiber architecture that takes into account different fiber orientations specific of the four chambers [176].

Cardiac geometries, acquired from medical images (typically during the diastolic phase), are not in principle stress free, due to the blood pressure acting on the endocardia. Therefore, given the whole heart mesh embedded with the fiber architecture, the computation of the reference configuration consists in the estimation of the unloaded (i.e. stress-free) heart shape, which will revert back to the original reconstructed geometry when inflated with the measured end diastolic pressure. Several methods exist for estimating the reference configuration [85, 76]. The simplest one is the backward displacement method [222, 35, 118, 158]. Nevertheless, this inverse problem has been shown to produce non-unique solutions, especially when buckling may occur, due the thin RV wall or the intricate atrial geometry [85]. Recently, novel methodologies, based on relaxation techniques [191], have been successfully proposed and applied to recover the reference configuration in LV [140, 199] and biventricular geometries [177].

Attempting to build human whole organ EM models requires to integrate all the mathematical, numerical and computational issues previously highlighted in Section 1.2.2. Among them, the use of high resolution meshes becomes particularly challenging due to the larger size of a human heart and the overall increase in *degrees of freedoms* (DOFs) needed for discretizing both the ventricles and the atria [20]. This automatically translates in high computational costs for modeling the heart EP: bidomain/monodomain equations are usually coupled with simplified ionic models [22, 117], although recently advanced cellular models are being included in heart simulations with the help of *High Performance Computing* (HPC) resources [78, 37, 176]; as an alternative, reaction-eikonal models are preferred due to the significant computational savings in the space-time resolutions [145, 233].

Recently, four chamber studies focused their attention on ventricular contraction, investigating the importance of modeling the pericardium in order to reproduce physiological AVD [235, 233, 175, 74]. Only few whole heart EM models consider the atrial contraction, which is usually described by means of phenomenological MA atrial models [124, 233, 78, 74, 175].

Furthermore, only in the last few years, whole heart EM models begin to incorporate the presence of the whole cardiovascular system, strongly coupling the 3D EM model with a 0D closed-loop model [233, 78]. Currently, the modeling of whole heart EM remains an open problem.

1.3 Objectives of the thesis

With the aim of facing the computational challenges formerly described in Section 1.2, the main objectives of this thesis move along three strands:

1. **Fibers architecture:** develop a novel unified mathematical framework, based on LDRBMs, to prescribe myocardial fibers orientation in computational biventricular and biatrial geometries;

2. **Electromechanics:** provide a biophysically detailed biventricular 3D EM model coupled with a 0D closed-loop lumped parameters model for the haemodynamics of the whole circulatory system;

3. **Whole heart:** extend the unified LDRBMs mathematical framework and the biventricular 3D-0D model to the whole heart. Present a preprocessing procedure for the generation of a whole heart mesh. Perform full heart EP and EM simulations.

The ultimate goal of this thesis is to provide a fully-coupled multiscale mathematical and numerical model of the electrical and mechanical activity of the human heart. The main contribution to the whole heart EM model, presented in this thesis, is given by the generation a detailed whole heart myocardial fiber architecture, which is able to reproduce almost all the features of both the atria and the ventricles. Besides a very detailed muscular architecture, the whole heart EM includes state of the art models, based on human physiology, for the atrial and ventricular EP [72, 47, 247], and takes into account both MA and TM of the four chambers, which are strongly coupled with a closed-loop model of the whole cardiovascular system. The validity of the model is demonstrated through simulations on a realistic whole heart geometry [107].

1.3.1 Original contributions

The following major challenges are addressed in this thesis:

1. **Fiber architecture:**
    - Review existing ventricular LDRBMs, providing a communal mathematical description. Introduce also some modeling improvements with respect to the existing literature [26, 204, 58], extending the ventricular LDRBMs in order to include specific fiber directions for RV;
    - Propose for the first time an atrial LDRBM which is able to quantitatively reproduce all the important features, such as fiber bundles, needed to provide a realistic atrial musculature architecture. Unlike most of the existing RBMs, the new method, tested both on idealized and realistic atrial geometries, can be easily applied to any arbitrary geometries;
    - Compare the results of the new atrial LDRBM with the fiber orientations obtained by the RBM proposed in [242, 67], to histo-anatomical pictures [100, 51, 97, 212] and to DT-MRI fiber data [167];
    - Carry out a systematic comparison, on realistic and idealized cardiac geometries, of the effect produced by different LDRBMs on EP for relevant meaningful biomarkers (e.g. activation times) computed from numerical simulations. For the ventricles, study the importance of including different fiber orientations in RV and investigate the effect of the inter-ventricular septal fibers discontinuity. For the atria, analyse the strong effect of the complex bundles fiber architecture on the electric signal propagation.
2. **Electromechanics:**
    - Present a 3D biventricular EM model coupled with a 0D closed-loop model of the whole cardiovascular system, discussing in detail the coupling conditions that stand behind the 3D and the 0D models;
    - Introduce a boundary condition for the mechanical problem that accounts for the neglected part of the domain located on top of the biventricular basal plane and that is consistent with the principles of momentum and energy conservation;
    - Perform EM simulations in physiological conditions using the 3D-0D model, showing that our results match the experimental data of relevant mechanical biomarkers available in literature [137, 238, 138, 236, 31, 61, 219];
    - Study how different configurations in cross-fiber active contraction, that surrogate the myofibers dispersion, affect EM simulations;
    - Investigate the effect of several myofiber architectures on EM simulations.

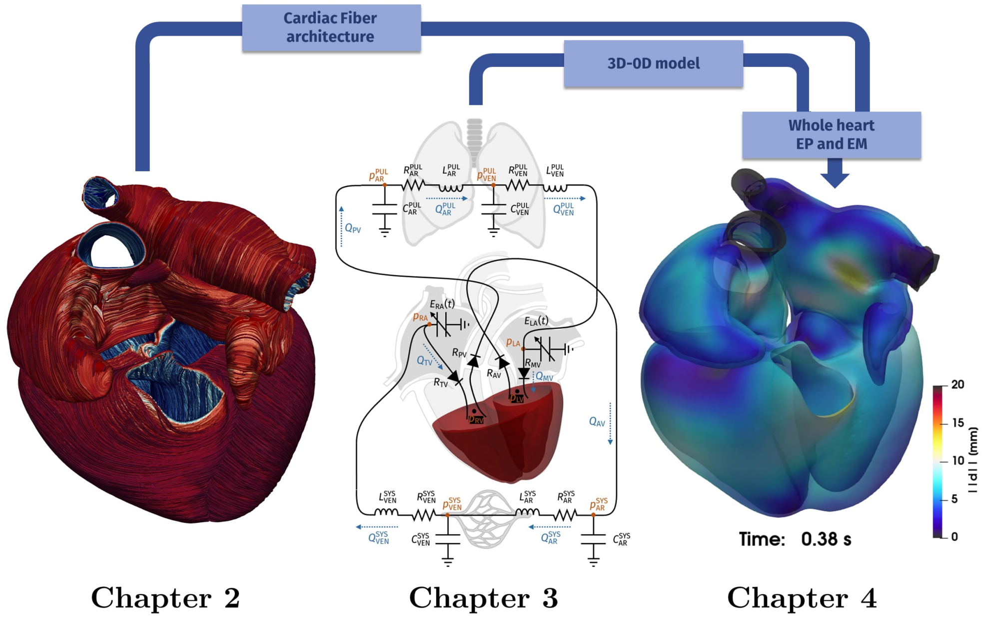

Figure 1.8: Graphical map of the thesis. Chapter 2 deals with myocardial fibers for biventricular and biatrial geometries. Chapter 3 presents the 3D-0D biventricular model. Chapter 4 provides the framework to perform full heart EP and EM simulations, extending the methodologies of Chapter 2 and 3 to the whole heart.

3. **Whole heart:**
   - Provide a detailed description of the process behind the generation of a whole heart mesh, starting from an acquired cardiac geometry;
   - Present a unified framework, based on LDRBMs, for generating myocardial fibers directly on the whole heart. The methodology is straightforward and can be easily applied to any four chambers heart geometry;
   - Extend the biventricular 3D-0D model to whole heart geometries. With this aim, present a 3D-0D model for the whole heart, composed by a 3D description of cardiac EM in all the four chambers and a 0D representation of the whole circulatory system, which includes the haemodynamics of all heart chambers;
   - Illustrate numerical results, including the full heart LDRBM, of EP and EM simulations, with physiological activation sites, in a realistic computational domain of the heart.

1.3.2 Structure of the thesis

This thesis is organized along the following chapters. A graphical map illustrating the main topic and the link of these chapter is shown in Figure 1.8.

Chapter 2: we review existing ventricular LDRBMs presented in a unified mathematical description. Then, we detail the new LDRBM for atrial fibers generation. We briefly explain the mathematical model and numerical methods used to perform EP simulations. Afterwards, we present numerical results where we show a comparison among different LDRBMs in terms of meaningful electrophysiological biomarker, computed as output of numerical simulations. Moreover, we compare the results of the atrial LDRBM with the fiber orientations obtained by another RBM and also to anatomical and DT-MRI data;

Chapter 3: we fully describe the biophysically detailed biventricular 3D-0D model. We present the new basal boundary condition for the mechanical problem. We detail the numerical approximation of the coupled 3D-0D model, carefully inspecting the coupling conditions of these heterogeneous models. We report the results of several electromechanical simulations in physiological conditions using the proposed 3D-0D model. We investigate the effect on EM of different myofiber architectures. Furthermore, we study at which extent different configurations in cross-fibers active contraction affect EM simulations;

Chapter 4: we present a preprocessing procedure for whole heart EM simulation which includes: the generation of a whole heart mesh, the prescription of the myocardial fibers and the computation of the reference configuration. We detail how to extend to whole heart geometries the biventricular 3D-0D model. Then, we illustrate numerical results of the whole heart EP and EM simulations;

Finally, we draw our conclusion and outline several possible future developments.

All the mathematical and numerical methods described in this thesis have been implemented within `life`$^{\texttt{x}}$, a new in-house high-performance `C++` Finite Elements (FE) library mainly focused on cardiac applications based on `deal.II` FE core [14] (`https://www.dealii.org`). A first public binary release of `life`$^{\texttt{x}}$ (including the fiber generation package) is freely available online (`https://lifex.gitlab.io/`), under an open-source license (`https://doi.org/10.5281/zenodo.5810269`) [2].

All the numerical simulations were executed using either the `iHeart` cluster (Lenovo SR950 192-Core Intel Xeon Platinum 8160, 2100 MHz and 1.7TB RAM) at MOX, Dipartimento di Matematica, Politecnico di Milano or the `GALILEO` supercomputer at Cineca (8 nodes endowed with 36 Intel Xeon E5-2697 v4 2.30 GHz). To analyse the results we used `ParaView` (`https://www.paraview.org`) an open-source, multi-platform data analysis and visualization application.

This thesis contains results which have already been published or accepted for publication in [176, 177].

Chapter 2

Modeling the cardiac muscular architecture

In this chapter, we provide a review, based on a unified mathematical description, for existing Laplace-Dirichlet-Rule-Based Methods (LDRBMs) in the ventricles [26, 204, 58], introducing also some modeling improvements (Section 2.1). In particular, we extend ventricular LDRBMs in order to include specific fiber directions for RV. We also propose a novel LDRBM for atrial fibers generation (Section 2.2). Afterwards, we introduce the mathematical and numerical model used to perform cardiac electrophysiology (EP) simulations (Section 2.3). Then, after a brief description related to the setting of numerical simulations (Section 2.4), we carry out a systematic comparison of the effect produced by different ventricular LDRBMs on EP, in terms of meaningful biomarkers (e.g. activation times), computed from numerical simulations (Section 2.5). Moreover, we test the new method for atrial fibers generation, both on idealized and realistic geometries, investigating the strong effect of the complex atrial fiber architecture on the electric signal propagation (Section 2.6). Finally, we compare the results of the novel atrial LDRBM with the fiber orientations obtained by another Rule-Based Method (RBM) [67] and also to anatomical [100, 51, 97, 212] and DT-MRI data [167] (Section 2.7). Part of the results presented in this chapter have been published in [176].

Contents

2.1 Ventricular Laplace-Dirichlet Rule-Based Methods

LDRBM is a particular class of RBMs for generating the myocardial fibers architecture, strictly related to the solution of Laplace boundary-value problems [204, 26, 58, 25, 266]. The keystone of any LDRBM is to properly define several inter and intra ventricular/atrial directions by taking the gradient of solutions of Laplace problems with suitable Dirichlet boundary conditions. These directions define the "flat" myofibers, that are then properly rotated in order to match histological and DT-MRI observations [86, 9, 211]. The above procedure ensures a smooth and continuous change in myofiber directions throughout the whole myocardial muscle.

2.1.1 Original ventricular LDRBMs

We start by giving a review of three popular LDRBMs introduced so far in the literature for the ventricles: specifically, we consider three LDRBMs proposed by Rossi et al. [204], by Bayer et al. [26] and by Doste et al. [58]. For each LDRBM, we first provide details on the original algorithm and then we propose a unified mathematical framework of such methods, highlighting similarities and differences, together with some improvements for the biventricular case.

Rule-Based Method by Rossi et al.

The ventricular LDRBM by Rossi et al. [204, 188] (in what follows R-RBM) is a modified version of the algorithm studied in [266] for generating fibers in left ventricular geometries [204], then extended to the biventricular ones in [188]. R-RBM is based on the definition of the transmural direction. In particular, the idea is to compute the sheetlet directions assuming that the orientation of collagen sheets is radial in the transmural direction of the ventricles (i.e. from epicardium to endocardium).

Considering a biventricular computational domain, Ω_{biv}, the first step of R-RBM consists in defining the boundary $\partial\Omega_{biv}$ as

$$\partial\Omega_{biv} = \Gamma_{vepi} \cup \Gamma_{base} \cup \Gamma_{\ell v} \cup \Gamma_{rs} \cup \Gamma_{rv-s}$$

where Γ_{vepi} is the ventricular epicardium, Γ_{base} the ventricular basal plane, $\Gamma_{\ell v}$ the left ventricular endocardium, Γ_{rs} the right ventricular septum and Γ_{rv-s} the right ventricular endocardium excluding the septum. Specifically, the right septum Γ_{rs} is identified exploiting the distance between LV and RV endocardia, see Figure 2.1(a).

The second step of R-RBM defines a normalized transmural distance, ϕ, by solving a Laplace problem with proper boundary conditions (see Figure 2.1(b))

$$\begin{cases} -\Delta\phi = 0 & \text{in } \Omega_{biv}, \\ \phi = 0 & \text{on } \Gamma_{vepi} \cup \Gamma_{rs}, \\ \phi = 1 & \text{on } \Gamma_{\ell v} \cup \Gamma_{rv-s}, \\ \nabla\phi \cdot \mathbf{n} = 0 & \text{on } \Gamma_{base}. \end{cases}$$

After solving the Laplace problem for ϕ, a local reference frame is build in each element

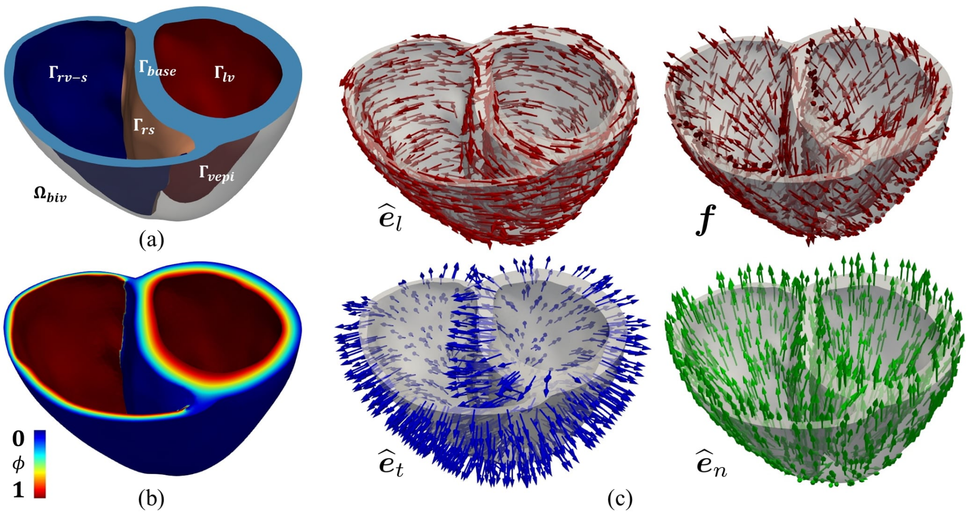

Figure 2.1: Procedure to generate myofibers with the original R-RBM.

of the biventricular mesh

$$\begin{aligned}\widehat{\boldsymbol{e}}_t &= \frac{\nabla\phi}{\|\nabla\phi\|},\\ \widehat{\boldsymbol{e}}_n &= \frac{\mathbf{n}_{base} - (\mathbf{n}_{base}\cdot\widehat{\boldsymbol{e}}_t)\widehat{\boldsymbol{e}}_t}{\|\mathbf{n}_{base} - (\mathbf{n}_{base}\cdot\widehat{\boldsymbol{e}}_t)\widehat{\boldsymbol{e}}_t\|},\\ \widehat{\boldsymbol{e}}_l &= \widehat{\boldsymbol{e}}_n \times \widehat{\boldsymbol{e}}_t,\end{aligned}$$

where $\nabla\phi$ is the gradient of the potential ϕ and $\mathbf{n}_{base}$ is the vector normal to the ventricular base and pointing apex-to-base (so that the term $\mathbf{n}_{base} - (\mathbf{n}_{base}\cdot\widehat{\boldsymbol{e}}_t)\widehat{\boldsymbol{e}}_t$ represents the projection of $\mathbf{n}_{base}$ on the plane orthogonal to $\widehat{\boldsymbol{e}}_t$). The vector $\widehat{\boldsymbol{e}}_t$ is the transmural direction , $\widehat{\boldsymbol{e}}_n$ is the apico-basal (normal) direction, and $\widehat{\boldsymbol{e}}_l$ is the "flat" fiber (longitudinal) direction, see Figure 2.1(c). Finally, the fiber field $\boldsymbol{f}$ is obtained by rotating $\widehat{\boldsymbol{e}}_l$ around the $\widehat{\boldsymbol{e}}_t$ axis by the helical angle α

$$\boldsymbol{f} = R'_{\widehat{\mathbf{e}}_t}(\alpha)\widehat{\boldsymbol{e}}_l,$$

where the rotation matrix $R'_{\widehat{\mathbf{e}}_t}(\alpha)$ is given by the Rodrigues' formula

$$R'_{\widehat{\mathbf{e}}_t}(\alpha) = \mathbf{I} + \sin(\alpha)[\widehat{\boldsymbol{e}}_t]_x + 2\sin^2(\alpha/2)[\widehat{\boldsymbol{e}}_t\otimes\widehat{\boldsymbol{e}}_t - \mathbf{I}],$$

with the matrix $[\widehat{\boldsymbol{e}}_t]_x$ defined as

$$[\widehat{\boldsymbol{e}}_t]_x = \begin{bmatrix} 0 & -[\widehat{\boldsymbol{e}}_t]_z & [\widehat{\boldsymbol{e}}_t]_y \\ [\widehat{\boldsymbol{e}}_t]_z & 0 & -[\widehat{\boldsymbol{e}}_t]_x \\ -[\widehat{\boldsymbol{e}}_t]_y & [\widehat{\boldsymbol{e}}_t]_x & 0 \end{bmatrix}.$$

The rotation helical angle $\alpha = \alpha(\phi)$ is given by the following linear relationship between ϕ and α

$$\alpha = \alpha_{epi}(1-\phi) + \alpha_{endo}\phi,$$

where α_{epi} and α_{endo} are fixed angle rotation on the epicardium and endocardium, respectively. For further details about the original R-RBM see [204, 188]. The procedure to generate myofibers with R-RBM is outlined in Figure 2.1.

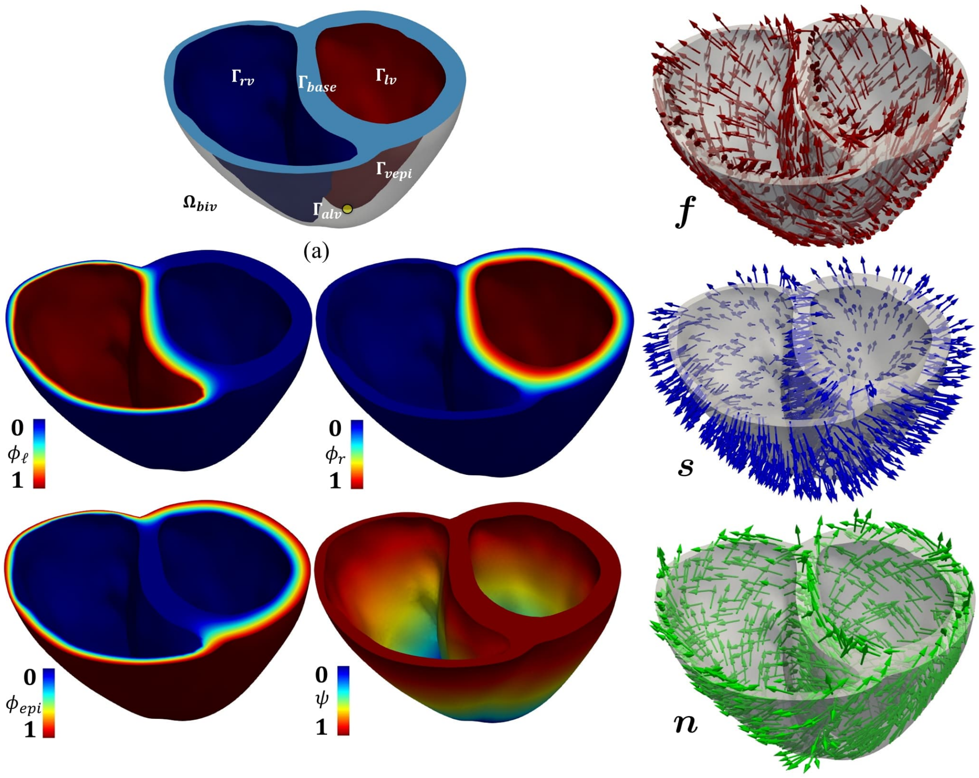

(a)

(b)

(c)

Figure 2.2: Procedure to generate myofibers with the original B-RBM.

Rule-Based Method by Bayer et al.

Bayer et al. [26] developed another LDRBM (in what follows B-RBM), for assigning ventricular fiber orientations, introducing two major novelties. The former is the use of Laplace-Dirichlet solutions to define both the transmural and apico-basal directions in the whole myocardium [25]. The latter consists in using the bi-direction spherical interpolation (`bislerp`) [226, 121] to manage the fiber orientations in order to guarantee a smooth and continuous change in the fiber field, particularly in the proximity of the septum and around the inter-ventricular junctions [26].

Considering a biventricular computational domain, Ω_{biv}, the first step of B-RBM consists in defining the boundary $\partial\Omega_{biv}$ as

$$\partial\Omega_{biv} = \Gamma_{vepi} \cup \Gamma_{base} \cup \Gamma_{\ell v} \cup \Gamma_{rv} \cup \Gamma_{a\ell v},$$

where Γ_{vepi} is the ventricular epicardium, Γ_{base} the ventricular basal plane, $\Gamma_{\ell v}$ the left ventricular endocardium, Γ_{rv} the right ventricular endocardium and $\Gamma_{a\ell v}$ the ventricular apex, selected as the LV epicardial point furthest from the ventricular base [26]; see Figure 2.2(a).

The second step of B-RBM requires to solve the Laplace equations in the domain Ω_{biv} with proper boundary conditions, in order to compute three different transmural distances ϕ_ℓ, ϕ_r and ϕ_{epi} and an apico-basal (normal) distance ψ (see Figure 2.2(b)):

$$\begin{cases} -\Delta\phi_\ell = 0 & \text{in } \Omega_{biv} \\ \phi_\ell = 1 & \text{on } \Gamma_{\ell v} \\ \phi_\ell = 0 & \text{on } \Gamma_{vepi} \cup \Gamma_{rv} \\ \nabla\phi_\ell \cdot \mathbf{n} = 0 & \text{on } \Gamma_{base} \end{cases}, \quad \begin{cases} -\Delta\phi_r = 0 & \text{in } \Omega_{biv} \\ \phi_r = 1 & \text{on } \Gamma_{rv} \\ \phi_r = 0 & \text{on } \Gamma_{vepi} \cup \Gamma_{\ell v} \\ \nabla\phi_r \cdot \mathbf{n} = 0 & \text{on } \Gamma_{base} \end{cases},$$

$$\begin{cases} -\Delta\phi_{epi} = 0 & \text{in } \Omega_{biv} \\ \phi_{epi} = 1 & \text{on } \Gamma_{vepi} \\ \phi_{epi} = 0 & \text{on } \Gamma_{\ell v} \cup \Gamma_{rv} \\ \nabla\phi_{epi} \cdot \mathbf{n} = 0 & \text{on } \Gamma_{base} \end{cases}, \quad \begin{cases} -\Delta\psi = 0 & \text{in } \Omega_{biv} \\ \psi = 1 & \text{on } \Gamma_{base} \\ \psi = 0 & \text{on } \Gamma_{a\ell v} \\ \nabla\psi \cdot \mathbf{n} = 0 & \text{on } \Gamma_{vepi} \end{cases}.$$

Gradients of the above Laplace solutions are used to define the apico-basal direction, $\nabla\psi$, and the transmural directions, $\nabla\phi_\ell$, $\nabla\phi_r$ or $\nabla\phi_{epi}$. Then, to construct a unique right-handed axis system in each point of the computational domain Ω_{biv}, B-RBM exploits three functions `axis`, `bislerp`, `orient`. The function `axis`

$$P_i = [\widehat{\boldsymbol{e}}_l, \widehat{\boldsymbol{e}}_n, \widehat{\boldsymbol{e}}_t] = \texttt{axis}(\nabla\psi, \nabla\phi_i) = \begin{cases} \widehat{\boldsymbol{e}}_t & = \frac{\nabla\phi_i}{\|\nabla\phi_i\|} \\ \widehat{\boldsymbol{e}}_n & = \frac{\nabla\psi - (\nabla\psi\cdot\widehat{\mathbf{e}}_t)\widehat{\mathbf{e}}_t}{\|\nabla\psi - (\nabla\psi\cdot\widehat{\mathbf{e}}_t)\widehat{\mathbf{e}}_t\|} \\ \widehat{\boldsymbol{e}}_l & = \widehat{\boldsymbol{e}}_n \times \widehat{\boldsymbol{e}}_t \end{cases} \qquad i = \ell, r, epi,$$

takes as inputs two vector, $\nabla\psi$ and either $\nabla\phi_r$, $\nabla\phi_\ell$ or $\nabla\phi_{epi}$, then returns an orthogonal matrix, $P_i = [\widehat{\boldsymbol{e}}_l, \widehat{\boldsymbol{e}}_n, \widehat{\boldsymbol{e}}_t]$ (with $i = \ell, r, epi,$), where $\widehat{\boldsymbol{e}}_l$, $\widehat{\boldsymbol{e}}_n$, $\widehat{\boldsymbol{e}}_t$ are the longitudinal, normal and transmural directions, respectively. The function `bislerp`

$$P_{ab} = \texttt{bislerp}(P_a, P_b, \eta),$$

where $\eta \in [0, 1]$ is an interpolation factor, is used to interpolate two orthonormal axis system (P_a, P_b) continuously within the whole myocardium, obtaining an interpolated axis system P_{ab}. When $\eta \to 0$ implies that $P_{ab} \to P_a$, while $\eta \to 1$ entails $P_{ab} \to P_b$. Specifically, `bislerp` is used first on P_ℓ and P_r, defining $P_{\ell r} = \texttt{bislerp}(P_\ell, P_r, \eta)$, and then to obtain the unique axis system $Q = \texttt{bislerp}(P_{\ell r}, P_{epi}, \eta)$. The function `orient`

$$[\boldsymbol{f}, \boldsymbol{n}, \boldsymbol{s}] = \texttt{orient}(Q, \alpha, \beta) = Q R_{\widehat{\mathbf{e}}_t}(\alpha) R_{\widehat{\mathbf{e}}_l}(\beta),$$

with

$$R_{\widehat{\mathbf{e}}_t}(\alpha) = \begin{bmatrix} \cos(\alpha) & -\sin(\alpha) & 0 \\ \sin(\alpha) & \cos(\alpha) & 0 \\ 0 & 0 & 1 \end{bmatrix}, \quad R_{\widehat{\mathbf{e}}_l}(\beta) = \begin{bmatrix} 1 & 0 & 0 \\ 0 & \cos(\beta) & \sin(\beta) \\ 0 & -\sin(\beta) & \cos(\beta) \end{bmatrix}, \tag{2.1}$$

takes as inputs Q, the coordinate system, α, and β, the fiber and sheet orientation angles, respectively, and gives as output, $[\boldsymbol{f}, \boldsymbol{n}, \boldsymbol{s}]$, an orthonormal axis system, where $\boldsymbol{f}$ is the fiber, $\boldsymbol{n}$ the sheet-normal, and $\boldsymbol{s}$ the sheet directions, see Figure 2.2(c).

Finally, to assign fiber orientations throughout the whole myocardium B-RBM exploits four functions representing the desired α and β angle rotations within the septum (s) and the ventricular walls (w):

$$\begin{aligned} \alpha_s(d) &= \alpha_{endo}(1 - 2d), \\ \alpha_w(d) &= \alpha_{endo} d + \alpha_{epi}(1 - d), \\ \beta_s(d) &= \beta_{endo}(1 - 2d), \\ \beta_w(d) &= \beta_{endo} d + \beta_{epi}(1 - d), \end{aligned}$$

where $d \in [0,1]$ is the transmural normalized distance, and α_{endo}, α_{epi}, β_{endo} and β_{epi} are fixed angle rotation on the epicardium and endocardium. For further details about the original B-RBM see [26]. The procedure to generate myofibers field with R-RBM is outlined in Figure 2.2.

Rule-Based Method by Doste et al.

Both R-RBM and B-RBM have the common issue of being mainly focused on based-biventricular computational models (meaning that they include an artificial basal plane well below the cardiac valves). To overcome this limitation, Doste el al. [58] proposed a LDRBM (hereafter named D-RBM) for generating cardiac muscle fibers in a full biventricular geometry, without the need to cut it with a basal plane. In addition, D-RBM prescribes the fiber orientations separately in each ventricle and includes specific fiber architecture in the inter-ventricular septum and outflow tracks[1] (OT), following observation from histological studies [58].

Considering a biventricular computational domain, Ω_{biv}, the first step of D-RBM consists in defining the boundary $\partial\Omega_{biv}$ as

$$\partial\Omega_{biv} = \Gamma_{vepi} \cup \Gamma_{\ell v} \cup \Gamma_{rv} \cup \Gamma_{a\ell v} \cup \Gamma_{arv} \cup \Gamma_{mv} \cup \Gamma_{av} \cup \Gamma_{tv} \cup \Gamma_{pv},$$

where Γ_{vepi} is the ventricular epicardium, $\Gamma_{\ell v}$ the left ventricular endocardium, Γ_{rv} the right ventricular endocardium, $\Gamma_{a\ell v}$ the left apex, Γ_{arv} the right apex (selected as the RV epicardial point furthest from the septal surface [216]) and $\Gamma_{rings} = \Gamma_{mv} \cup \Gamma_{av} \cup \Gamma_{tv} \cup \Gamma_{pv}$ the four valve rings, with Γ_{mv}, Γ_{av}, Γ_{tv} and Γ_{pv} the rings of MV, AV, TV and PV, respectively (see Figure 2.3(a)).

Laplace problems are solved in the domain Ω_{biv} with different boundary conditions, to compute the transmural distance ϕ, the left and right apico-basal and apico-OT distances $\psi_{ab,\ell}$, $\psi_{ab,r}$ and $\psi_{ot,\ell}$, $\psi_{ot,r}$, respectively (see Figure 2.3(b)):

$$\begin{cases} -\Delta\phi = 0 & \text{in } \Omega_{biv} \\ \phi = 2 & \text{on } \Gamma_{\ell v} \\ \phi = -1 & \text{on } \Gamma_{rv} \\ \phi = 0 & \text{on } \Gamma_{vepi} \\ \nabla\phi \cdot \mathbf{n} = 0 & \text{on } \Gamma_{rings} \end{cases},$$

$$\begin{cases} -\Delta\psi_{ab,\ell} = 0 & \text{in } \Omega_{biv} \\ \psi_{ab,\ell} = 0 & \text{on } \Gamma_{a\ell v} \\ \psi_{ab,\ell} = 1 & \text{on } \Gamma_{mv} \\ \nabla\psi_{ab,\ell} \cdot \mathbf{n} = 0 & \text{on } \partial\Omega_{biv}/(\Gamma_{a\ell v} \cup \Gamma_{mv}) \end{cases}, \begin{cases} -\Delta\psi_{ab,r} = 0 & \text{in } \Omega_{biv} \\ \psi_{ab,r} = 0 & \text{on } \Gamma_{arv} \\ \psi_{ab,r} = 1 & \text{on } \Gamma_{tv} \\ \nabla\psi_{ab,r} \cdot \mathbf{n} = 0 & \text{on } \partial\Omega_{biv}/(\Gamma_{arv} \cup \Gamma_{tv}) \end{cases},$$

$$\begin{cases} -\Delta\psi_{ot,\ell} = 0 & \text{in } \Omega_{biv} \\ \psi_{ot,\ell} = 0 & \text{on } \Gamma_{a\ell v} \\ \psi_{ot,\ell} = 1 & \text{on } \Gamma_{av} \\ \nabla\psi_{ot,\ell} \cdot \mathbf{n} = 0 & \text{on } \partial\Omega_{biv}/(\Gamma_{a\ell v} \cup \Gamma_{av}) \end{cases}, \begin{cases} -\Delta\psi_{ot,r} = 0 & \text{in } \Omega_{biv} \\ \psi_{ot,r} = 0 & \text{on } \Gamma_{arv} \\ \psi_{ot,r} = 1 & \text{on } \Gamma_{pv} \\ \nabla\psi_{ot,r} \cdot \mathbf{n} = 0 & \text{on } \partial\Omega_{biv}/(\Gamma_{arv} \cup \Gamma_{pv}) \end{cases}.$$

---

[1] LV and RV outflow tracks are the AV and PV annular rings, respectively.

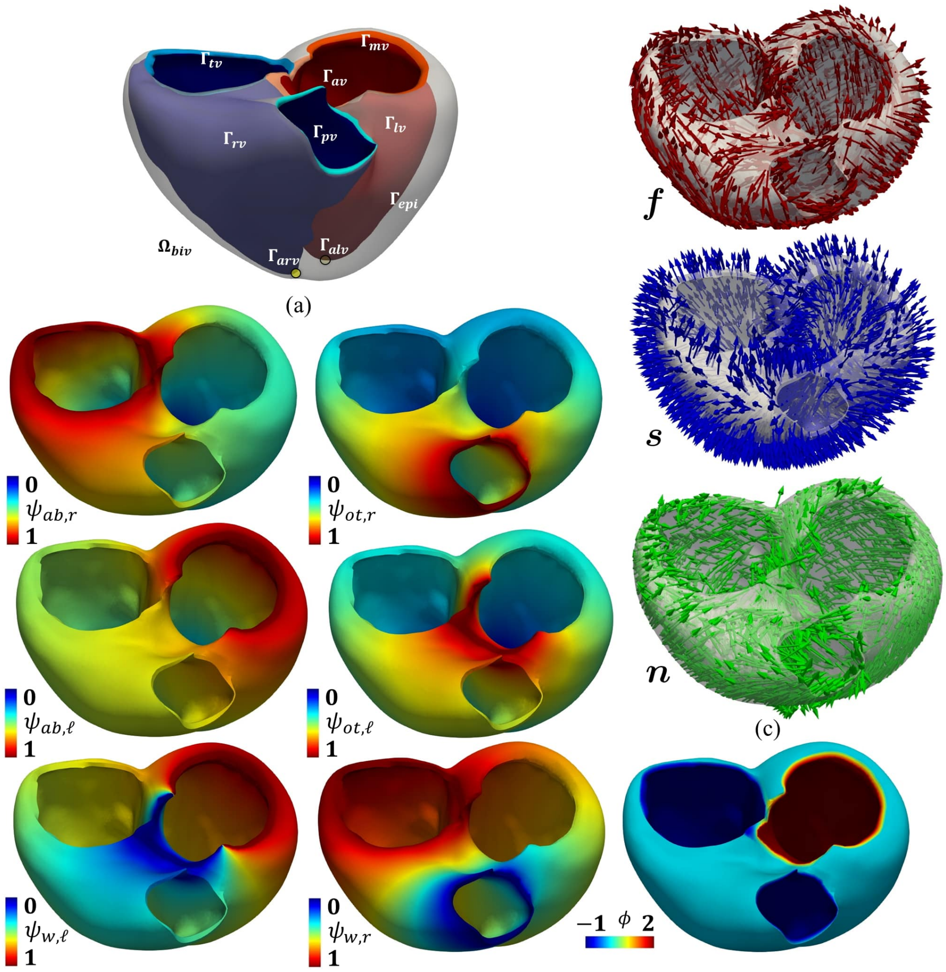

(a)

(c)

(b)

Figure 2.3: Procedure to generate myofibers with the original D-RBM.

Moreover also the following inter-ventricular distances $\psi_{w,\ell}$, and $\psi_{w,r}$ are computed:

$$\begin{cases} -\Delta\psi_{w,\ell} = 0 & \text{in } \Omega_{biv} \\ \psi_{w,\ell} = 1 & \text{on } \Gamma_{a\ell v} \cup \Gamma_{mv} \\ \psi_{w,\ell} = 0 & \text{on } \Gamma_{av} \\ \nabla\psi_{w,\ell} \cdot \mathbf{n} = 0 & \\ \qquad \text{on } \partial\Omega_{biv}/(\Gamma_{a\ell v} \cup \Gamma_{mv} \cup \Gamma_{av}) & \end{cases}, \quad \begin{cases} -\Delta\psi_{w,r} = 0 & \text{in } \Omega_{biv} \\ \psi_{w,r} = 1 & \text{on } \Gamma_{arv} \cup \Gamma_{tv} \\ \psi_{w,r} = 0 & \text{on } \Gamma_{pv} \\ \nabla\psi_{w,r} \cdot \mathbf{n} = 0 & \\ \qquad \text{on } \partial\Omega_{biv}/(\Gamma_{arv} \cup \Gamma_{tv} \cup \Gamma_{pv}) & \end{cases}.$$

The boundary conditions for ϕ are assigned in order to discriminate the two ventricles (positive and negative values for LV and RV, respectively), and also to take into account that two-third of the septum belong to LV and one-third to RV [58].

The next step of D-RBM consists in building the orthonormal coordinate system, needed to define the myofiber orientations, using gradients of the Laplace solutions previously computed. The transmural direction ($\widehat{\boldsymbol{e}}_t$) is obtained by taking the normalized gradients of $\nabla\phi$. The longitudinal direction ($\widehat{\boldsymbol{e}}_n$), defined separately in each ventricle, is a weighted sum of apico-basal ($\nabla\psi_{ab,i}$) and apico-OT ($\nabla\psi_{ot,i}$) directions, exploiting the inter-ventricular distances $\psi_{w,i}$ (with $i = \ell, r$):

$$\nabla\psi_i = \psi_{w,i}\nabla\psi_{ab,i} + (1 - \psi_{w,i})\nabla\psi_{ot,i} \qquad i = \ell, r.$$

Thus, $\widehat{\boldsymbol{e}}_n$ is retrieved by projecting the gradients of $\nabla\psi_l$ and $\nabla\psi_r$ for LV and RV, respectively, on the plane orthogonal to $\widehat{\boldsymbol{e}}_t$. Then, the longitudinal direction ($\widehat{\boldsymbol{e}}_l$) is the cross-product of the previously computed directions. Finally, the local coordinate system, $[\widehat{\boldsymbol{e}}_l, \widehat{\boldsymbol{e}}_n, \widehat{\boldsymbol{e}}_t]$, is set up in each nodal point of the mesh:

$$\begin{cases} \widehat{\boldsymbol{e}}_t &= \frac{\nabla\phi}{\|\nabla\phi\|} \\ \widehat{\boldsymbol{e}}_n &= \frac{\nabla\psi_i - (\nabla\psi_i \cdot \widehat{\boldsymbol{e}}_t)\widehat{\boldsymbol{e}}_t}{\|\nabla\psi_i - (\nabla\psi_i \cdot \widehat{\boldsymbol{e}}_t)\widehat{\boldsymbol{e}}_t\|} \\ \widehat{\boldsymbol{e}}_l &= \widehat{\boldsymbol{e}}_n \times \widehat{\boldsymbol{e}}_t \end{cases} \qquad i = \ell, r.$$

The last step of D-RBM provides rotations of the fiber, α_i, and sheet, β_i, angles for LV ($i = \ell$) and RV ($i = r$). The vector $\widehat{\boldsymbol{e}}_l$ is rotated around $\widehat{\boldsymbol{e}}_t$ by an angle α_i and then $\widehat{\boldsymbol{e}}_t$ is rotated around $\widehat{\boldsymbol{e}}_l$ by an angle β_i

$$[\boldsymbol{f}, \boldsymbol{n}, \boldsymbol{s}] = [\widehat{\boldsymbol{e}}_l, \widehat{\boldsymbol{e}}_n, \widehat{\boldsymbol{e}}_t] R_{\widehat{\boldsymbol{e}}_t}(\alpha_i) R_{\widehat{\boldsymbol{e}}_l}(\beta_i),$$

where $R_{\widehat{\boldsymbol{e}}_t}$, and $R_{\widehat{\boldsymbol{e}}_c}$ are the matrices previously defined in (2.1), and $\boldsymbol{f}$, $\boldsymbol{n}$, and $\boldsymbol{s}$ represent the fiber, sheet-normal and sheet directions, respectively (see Figure 2.3(c)). The expressions for α_i and β_i angles are the following

$$\alpha_i(d) = \alpha_{endo,i} d + \alpha_{epi,i}(1 - d) \qquad \beta_i(d) = \beta_{endo,i} d + \beta_{epi,i}(1 - d) \qquad i = \ell, r,$$

where $d \in [0, 1]$ is the transmural normalized distance. Moreover, OT regions are identified by $\psi_{w,\ell} = 0$, and $\psi_{w,r} = 0$. Thus, the angle values in OT regions can be fixed by selecting the mesh points where $\psi_{w,i} = 0$ ($i = \ell, r$). An optional feature of D-RBM is the possibility of setting septal discontinuity between the two ventricles by exploiting the intersection zone of both ventricles and using the solution ϕ that discriminate LV from RV (see [58] for further details). The procedure to generate myofibers with D-RBM is outlined in Figure 2.3.

2.1.2 A unified description for ventricular LDRBMs

The three ventricular LDRBMs under review (R-RBM, B-RBM and D-RBM) can be embedded in a unified mathematical description (presented in [176]), characterized by the following shared steps which are hereby reported:

1. **Labelled mesh:** Provide a labelled mesh of the ventricular domain Ω_{biv} to define specific partitions of the boundary $\partial\Omega_{biv}$, see Figure 2.4;

2. **Transmural distance:** A *transmural distance* is defined to compute the distance of the epicardium from endocardial surfaces;

3. **Transmural direction:** The transmural distance gradient is used to build the unit *transmural direction* $\widehat{\boldsymbol{e}}_t$ of the ventricles, see Figure 2.4;

4. **Normal direction:** An apico-basal direction (directed from the apex towards the ventricular base) is introduced and it is used to build the unit *normal direction* $\widehat{\boldsymbol{e}}_n$, orthogonal to the transmural one, see Figure 2.4;

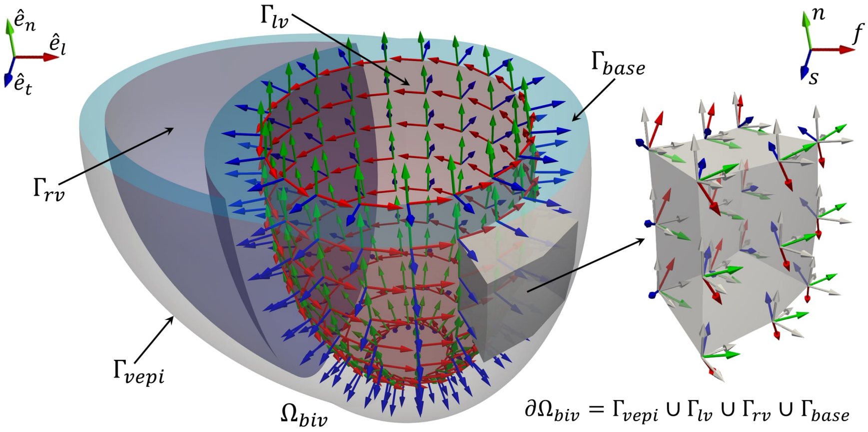

Figure 2.4: Left: Representation of the three directions employed by a LDRBM for an idealized biventricular domain Ω_{biv} whose border $\partial\Omega_{biv}$ is partitioned in the ventricular epicardium Γ_{vepi}, left $\Gamma_{\ell v}$ and right Γ_{rv} ventricular endocardium and the ventricular base Γ_{base}, $\partial\Omega_{biv} = \Gamma_{vepi} \cup \Gamma_{\ell v} \cup \Gamma_{rv} \cup \Gamma_{base}$. For visualization purpose, only directions on the left ventricular endocardium $\Gamma_{\ell v}$ are represented. In blue: unit transmural direction, $\widehat{\boldsymbol{e}}_t$; In green: unit normal direction, $\widehat{\boldsymbol{e}}_n$; In red: unit longitudinal direction, $\widehat{\boldsymbol{e}}_l$. Right: zoom on a slab of the left ventricular myocardium Ω_{biv} showing the three final myofibers orientations $\boldsymbol{f}$, $\boldsymbol{s}$, $\boldsymbol{n}$.

5. **Local coordinate system:** Build for each point of the ventricular domain an orthonormal local coordinate axial system composed by $\widehat{\boldsymbol{e}}_t$, $\widehat{\boldsymbol{e}}_n$ and the unit *longitudinal direction* $\widehat{\boldsymbol{e}}_l$ (orthogonal to the previous ones), see Figure 2.4;

6. **Rotate axis:** Finally, properly rotate the reference frame with the purpose of defining the myofiber orientations: $\boldsymbol{f}$ the *fiber direction*, $\boldsymbol{n}$ the *cross-fiber direction* and $\boldsymbol{s}$ the *sheet direction*, see Figure 2.4(Right). Rotations are chosen in order to match histology and DTI observations.

To characterize the ventricular distances computed by the three LDRBMs, it is useful to introduce the following generalized Laplace-Dirichlet problem

$$\begin{cases} -\Delta\chi = 0 & \text{in } \Omega_{biv}, \\ \chi = \chi_a & \text{on } \Gamma_a, \\ \chi = \chi_b & \text{on } \Gamma_b, \\ \nabla\chi \cdot \mathbf{n} = 0 & \text{on } \Gamma_n, \end{cases} \tag{2.2}$$

for a generic unknown χ and suitable boundary data χ_a, $\chi_b \in \mathbb{R}$ set on generic partitions of the ventricular boundary Γ_a, Γ_b, Γ_n, with $\Gamma_a \cup \Gamma_b \cup \Gamma_n = \partial\Omega_{biv}$. The variable χ will assume different meanings depending on the step and LDRBM considered. Moreover, the values χ_a, χ_b are fixed in order to evaluate specific ventricular distances between boundary partitions Γ_a, Γ_b.

We detail in what follows the six points aforementioned. We refer to Figures 2.5, 2.6 and 2.7, showing a schematic representations of the unified mathematical description for R-RBM, B-RBM, and D-RBM, respectively, on a biventricular domain Ω_{biv}.

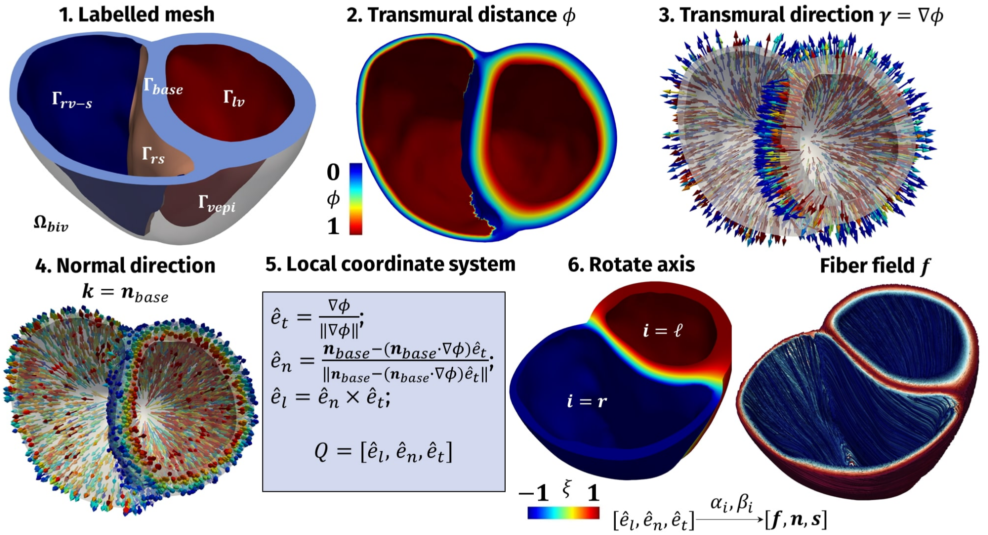

Figure 2.5: Schematic procedure of R-RBM for a biventricular geometry with an artificial basal plane.

1. Labelled mesh: prescribing the ventricular boundary $\partial\Omega_{biv}$. R-RBM, B-RBM, and D-RBM define the following boundaries:

Γ_{vepi} : the ventricular epicardium,
Γ_{base} : the ventricular base,
$\Gamma_{\ell v}$: the left ventricular endocardium,
Γ_{rv} : the right ventricular endocardium.

Moreover, R-RBM subdivides the right ventricular endocardium Γ_{rv} into the right septum Γ_{rs} and the remaining part Γ_{rv-s} such that $\Gamma_{rv} = \Gamma_{rs} \cup \Gamma_{rv-s}$, see step 1 in Figure 2.5. This subdivision is usually performed manually by the user, thus introducing some arbitrariness during the septum selection. For B-RBM and D-RBM the left ventricular apex $\Gamma_{a\ell v}$ is also introduced, whereas the right ventricular apex Γ_{arv} for D-RBM solely (see step 1 in Figures 2.6 and 2.7). Furthermore, D-RBM requires boundary labels for the four valve rings: Γ_{mv} (MV), Γ_{av} (AV), Γ_{tv} (TV) and Γ_{pv} (PV), see step 1 in Figure 2.7. It is also useful to define $\Gamma_{rings} = \Gamma_{lring} \cup \Gamma_{rring}$, with $\Gamma_{lring} = \Gamma_{mv} \cup \Gamma_{av}$ and $\Gamma_{rring} = \Gamma_{tv} \cup \Gamma_{pv}$. Notice that in B-RBM we considered the union of the four valve rings as the ventricular base $\Gamma_{base} = \Gamma_{rings}$. This allows the use of B-RBM also in the case of a full biventricular geometry, see step 1 in Figure 2.6. In summary, the three methods define the boundary $\partial\Omega_{biv}$ as follows:

$$\begin{aligned}
&\text{R-RBM} : \partial\Omega_{biv} = \Gamma_{vepi} \cup \Gamma_{\ell v} \cup \Gamma_{rs} \cup \Gamma_{rv-s} \cup \Gamma_{base},\\
&\text{B-RBM} : \partial\Omega_{biv} = \Gamma_{vepi} \cup \Gamma_{\ell v} \cup \Gamma_{rv} \cup \Gamma_{rings} \cup \Gamma_{a\ell v},\\
&\text{D-RBM} : \partial\Omega_{biv} = \Gamma_{vepi} \cup \Gamma_{\ell v} \cup \Gamma_{rv} \cup \Gamma_{mv} \cup \Gamma_{av} \cup \Gamma_{tv} \cup \Gamma_{pv} \cup \Gamma_{a\ell v} \cup \Gamma_{arv}.
\end{aligned}$$

2. Transmural distance: definition of transmural distances (generally indicated with the letter ϕ) obtained by solving Laplace-Dirichlet problems of the form (2.2). In particular, for R-RBM, the transmural distance ϕ is found by solving (2.2) with $\chi_a = 1$ on $\Gamma_{\ell v} \cup \Gamma_{rv-s}$, $\chi_b = 0$ on $\Gamma_{vepi} \cup \Gamma_{rs}$, and $\Gamma_n = \Gamma_{base}$. For D-RBM, ϕ is found by solving (2.2) with $\chi_a = 2$ on $\Gamma_{\ell v}$, $\chi_a = -1$ on Γ_{rv}, $\chi_b = 0$ on Γ_{vepi},

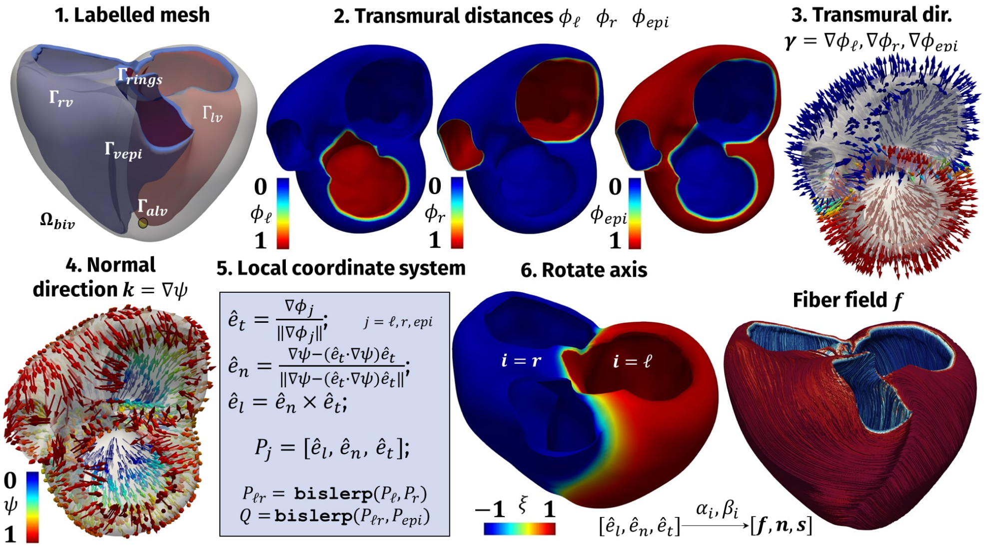

Figure 2.6: Schematic procedure of B-RBM for a full biventricular geometry.

LDRBM type	Transmural distances	χ_a	Γ_a	χ_b	Γ_b	Γ_n
R-RBM	ϕ	1	$\Gamma_{\ell v} \cup \Gamma_{rv-s}$	0	$\Gamma_{vepi} \cup \Gamma_{rs}$	Γ_{base}
B-RBM	ϕ_ℓ	1	$\Gamma_{\ell v}$	0	$\Gamma_{vepi} \cup \Gamma_{rv}$	Γ_{rings}
	ϕ_r	1	Γ_{rv}	0	$\Gamma_{vepi} \cup \Gamma_{\ell v}$	Γ_{rings}
	ϕ_{epi}	1	Γ_{vepi}	0	$\Gamma_{\ell v} \cup \Gamma_{rv}$	Γ_{rings}
D-RBM	ϕ	2 -1	$\Gamma_{\ell v}$ Γ_{rv}	0	Γ_{vepi}	Γ_{rings}

Table 2.1: Transmural distance boundary conditions for R-RBM, B-RBM and D-RBM used in step 2.

and $\Gamma_n = \Gamma_{rings}$. B-RBM requires to solve three Laplace problems (2.2) in order to compute three different transmural distances ϕ_ℓ, ϕ_r and ϕ_{epi}. We refer the reader to Table 2.1 for the specific choices in problem (2.2) made by the three methods. Notice that in D-RBM the boundary conditions χ_a are assigned in order to identify the two ventricles (positive and negative values for LV and RV, respectively) and to associate roughly two-thirds of the septum to LV and one-third to RV [58] (see step 2 in Figures 2.5, 2.6 and 2.7).

3. Transmural direction: after solving the Laplace problems for finding the transmural distances ϕ, ϕ_l, ϕ_r, ϕ_{epi}, their gradients define the transmural directions $\boldsymbol{\gamma}$ (see step 3 in Figures 2.5, 2.6 and 2.7). In particular, we have:

$$\begin{aligned} &\text{R-RBM} : \boldsymbol{\gamma} = \nabla\phi, \\ &\text{B-RBM} : \boldsymbol{\gamma} = \nabla\phi_i, \quad i = \ell, r, epi, \\ &\text{D-RBM} : \boldsymbol{\gamma} = \nabla\phi. \end{aligned}$$

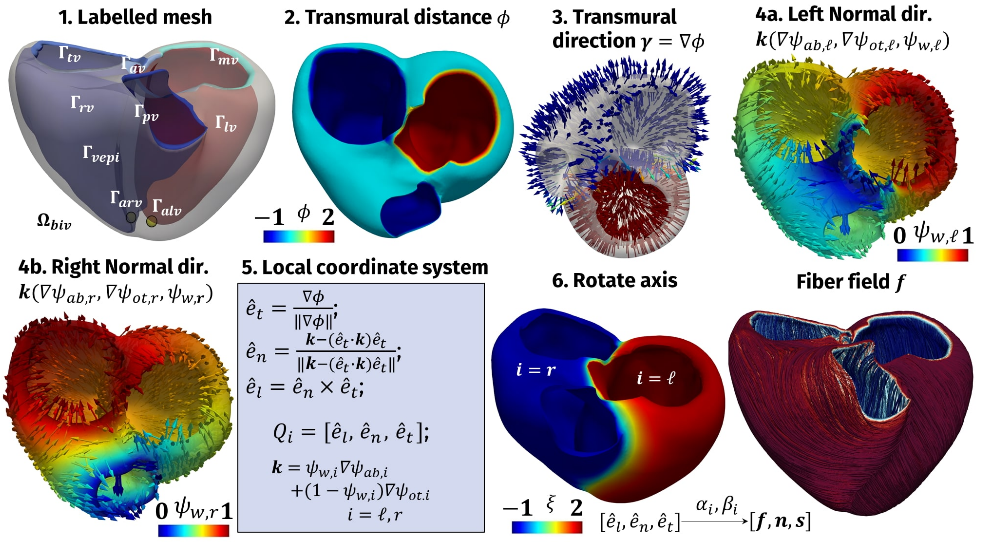

Figure 2.7: Schematic procedure of D-RBM for a full biventricular geometry.

4. Normal direction: definition of the normal direction $\boldsymbol{k}$. In R-RBM, this is done using the vector $\mathbf{n}_{base}$, i.e. the outward normal to the ventricular base, that is $\boldsymbol{k} = \mathbf{n}_{base}$ (see step 4 in Figure 2.5). For the other two LDRBMs, further variables (identified by the letter ψ) are introduced: they are found by solving the Laplace problem in the form (2.2) with suitable boundary conditions. Specifically, for B-RBM the vector $\boldsymbol{k}$ is the gradient of the solution ψ ($\boldsymbol{k} = \nabla\psi$) obtained with $\chi_a = 1$ on Γ_{rings}, $\chi_b = 0$ on $\Gamma_{a\ell v}$, and $\Gamma_n = \Gamma_{vepi} \cup \Gamma_{\ell v} \cup \Gamma_{rv}$, see step 4 in Figure 2.6. In D-RBM, instead, two normal directions are introduced, one for each ventricle:

$$\boldsymbol{k} = \psi_{w,i}\nabla\psi_{ab,i} + (1-\psi_{w,i})\nabla\psi_{ot,i}, \qquad i = \ell, r, \tag{2.3}$$

where $i = \ell, r$ refer to LV and RV, respectively, so that the normal direction is a weighted sum of apico-basal ($\nabla\psi_{ab,i}$) and apico-outflow-tract ($\nabla\psi_{ot,i}$) directions, obtained using an inter-ventricular interpolation function $\psi_{w,i}$ [58]; the latter are given again by solutions of problems like (2.2) (see step 4a and 4b in Figure 2.7). In particular, $\psi_{ab,\ell}$, $\psi_{ab,r}$, $\psi_{ot,\ell}$, $\psi_{ot,r}$, $\psi_{w,\ell}$, $\psi_{w,r}$ are found by solving (2.2) with $\chi_a = 1$ on Γ_a and $\chi_b = 0$ on Γ_b, where Γ_a and Γ_b are boundary subsets listed in Table 2.2. Summing up, the different methods compute the normal direction $\boldsymbol{k}$ as follows (see step 4 in Figures 2.5, 2.6 and 2.7):

$$\begin{aligned}
&\text{R-RBM}: \boldsymbol{k} = \mathbf{n}_{base},\\
&\text{B-RBM}: \boldsymbol{k} = \nabla\psi,\\
&\text{D-RBM}: \boldsymbol{k} = \psi_{w,i}\nabla\psi_{ab,i} + (1-\psi_{w,i})\nabla\psi_{ot,i}, \qquad i = \ell, r.
\end{aligned}$$

5. Local coordinate system: building an orthonormal local coordinate system (defined by letter Q) at each point of the domain Ω_{biv}. All the three methods make

Scalar potentials	Γ_a	Γ_b	Γ_n
$\psi_{ab,\ell}$	Γ_{mv}	$\Gamma_{a\ell v}$	$\Gamma_{vepi} \cup \Gamma_{\ell v} \cup \Gamma_{rv} \cup \Gamma_{av} \cup \Gamma_{rring}$
$\psi_{ab,r}$	Γ_{tv}	Γ_{arv}	$\Gamma_{vepi} \cup \Gamma_{\ell v} \cup \Gamma_{rv} \cup \Gamma_{pv} \cup \Gamma_{lring}$
$\psi_{ot,\ell}$	Γ_{av}	$\Gamma_{a\ell v}$	$\Gamma_{vepi} \cup \Gamma_{\ell v} \cup \Gamma_{rv} \cup \Gamma_{mv} \cup \Gamma_{rring}$
$\psi_{ot,r}$	Γ_{pv}	Γ_{arv}	$\Gamma_{vepi} \cup \Gamma_{\ell v} \cup \Gamma_{rv} \cup \Gamma_{tv} \cup \Gamma_{lring}$
$\psi_{w,\ell}$	$\Gamma_{mv} \cup \Gamma_{a\ell v}$	Γ_{av}	$\Gamma_{vepi} \cup \Gamma_{\ell v} \cup \Gamma_{rv} \cup \Gamma_{rring}$
$\psi_{w,r}$	$\Gamma_{tv} \cup \Gamma_{arv}$	Γ_{pv}	$\Gamma_{vepi} \cup \Gamma_{\ell v} \cup \Gamma_{rv} \cup \Gamma_{lring}$

Table 2.2: Scalar potentials used in D-RBM to build the normal direction.

use of the following function `axis`:

$$P = [\widehat{\boldsymbol{e}}_l, \widehat{\boldsymbol{e}}_n, \widehat{\boldsymbol{e}}_t] = \texttt{axis}(\boldsymbol{k}, \boldsymbol{\gamma}) = \begin{cases} \widehat{\boldsymbol{e}}_t & = \frac{\boldsymbol{\gamma}}{\|\boldsymbol{\gamma}\|}, \\ \widehat{\boldsymbol{e}}_n & = \frac{\boldsymbol{k} - (\boldsymbol{k} \cdot \widehat{\boldsymbol{e}}_t)\widehat{\boldsymbol{e}}_t}{\|\boldsymbol{k} - (\boldsymbol{k} \cdot \widehat{\boldsymbol{e}}_t)\widehat{\boldsymbol{e}}_t\|}, \\ \widehat{\boldsymbol{e}}_l & = \widehat{\boldsymbol{e}}_n \times \widehat{\boldsymbol{e}}_t, \end{cases} \tag{2.4}$$

which takes as input a normal direction $\boldsymbol{k}$ and a transmural direction $\boldsymbol{\gamma}$ and returns the orthonormal system P whose columns are the three orthonormal directions $\widehat{\boldsymbol{e}}_l$, $\widehat{\boldsymbol{e}}_n$, $\widehat{\boldsymbol{e}}_t$ which represent the longitudinal, the normal and the transmural unit directions, respectively. For R-RBM we have $Q = \texttt{axis}(\boldsymbol{k}, \nabla\phi)$. For B-RBM three orthonormal coordinate systems are introduced, that is $P_\ell = \texttt{axis}(\boldsymbol{k}, \nabla\phi_\ell)$, $P_r = \texttt{axis}(\boldsymbol{k}, \nabla\phi_r)$ and $P_{epi} = \texttt{axis}(\boldsymbol{k}, \nabla\phi_{epi})$, which are then interpolated through the function `bislerp` to obtain a continuous orthonormal coordinate system within the whole myocardium. Hence, B-RBM performs the following steps to obtain the final orthonormal coordinate system Q (see step 5 in Figure 2.6):

$$\begin{aligned} P_{\ell r} &= \texttt{bislerp}(P_\ell, P_r, \eta), \\ Q &= \texttt{bislerp}(P_{\ell r}, P_{epi}, \eta). \end{aligned}$$

D-RBM, instead, defines two different coordinate systems for LV and RV as a consequence of the normal directions defined in (2.3) (see step 5 in Figure 2.7):

$$Q_i = \texttt{axis}(\psi_{w,i}\nabla\psi_{ab,i} + (1 - \psi_{w,i})\nabla\psi_{ot,i}, \nabla\phi), \quad i = \ell, r.$$

6. Rotate axis: the orthonormal coordinate system, defined for each point of the myocardium at the previous step, should be aligned in order to match histological knowledge about fiber and sheet orientations. To this aim, the three LDRBMs introduce a rotation of $\widehat{\boldsymbol{e}}_l$, $\widehat{\boldsymbol{e}}_n$, $\widehat{\boldsymbol{e}}_t$ by means of suitable angles: the longitudinal direction $\widehat{\boldsymbol{e}}_l$ rotates counter-clockwise around $\widehat{\boldsymbol{e}}_t$ by an angle α_i, whereas the transmural direction $\widehat{\boldsymbol{e}}_t$ is rotated counter-clockwise around $\widehat{\boldsymbol{e}}_l$ by an angle β_i, where $i = \ell, r$ depend on LV or RV the point belongs to. Indeed, it is known that in LV and RV the fiber orientations feature a change in direction at the inter-ventricular septum [115]. In order to obtain a local orthonormal coordinate system, direction $\widehat{\boldsymbol{e}}_n$ is rotated accordingly.

These rotations produce a map $[\widehat{\boldsymbol{e}}_l, \widehat{\boldsymbol{e}}_n, \widehat{\boldsymbol{e}}_t] \xrightarrow{\alpha_i, \beta_i} [\boldsymbol{f}, \boldsymbol{n}, \boldsymbol{s}]$ from the original coordinate system $[\widehat{\boldsymbol{e}}_l, \widehat{\boldsymbol{e}}_n, \widehat{\boldsymbol{e}}_t]$ to a new coordinate system $[\boldsymbol{f}, \boldsymbol{n}, \boldsymbol{s}]$, by means of the function `orient`:

$$[\boldsymbol{f}, \boldsymbol{n}, \boldsymbol{s}] = \texttt{orient}(Q, \alpha_i, \beta_i) = [\widehat{\boldsymbol{e}}_l, \widehat{\boldsymbol{e}}_n, \widehat{\boldsymbol{e}}_t] R_{\widehat{\boldsymbol{e}}_t}(\alpha_i) R_{\widehat{\boldsymbol{e}}_l}(\beta_i), \quad i = \ell,\, r,$$

where $\boldsymbol{f}$ is the fiber direction, $\boldsymbol{n}$ is the sheet-normal direction and $\boldsymbol{s}$ is the sheet direction.

For all the three methods the rotation angles $\alpha_i = \alpha_i(d_i)$ and $\beta_i = \beta_i(d_i)$ are functions of the position within the myocardium, in particular of the *transmural normalized distance* $d_i \in [0,1]$, $i = \ell, r$, defined as:

$$\begin{aligned}
&\text{R-RBM} : d_\ell = d_r = \phi, \\
&\text{B-RBM} : d_\ell = \phi_\ell \quad d_r = \phi_r, \\
&\text{D-RBM} : d_\ell = \phi/2 \quad d_r = |\phi|.
\end{aligned}$$

Accordingly, the rotation angles are written by means of the following linear relationships:

$$\alpha_i(d_i) = \alpha_{epi,i}(1-d_i) + \alpha_{endo,i} d_i, \quad \beta_i(d_i) = \beta_{epi,i}(1-d_i) + \beta_{endo,i} d_i, \quad i = \ell, r, \tag{2.5}$$

where $\alpha_{endo,\ell}$, $\alpha_{epi,\ell}$, $\alpha_{endo,r}$, $\alpha_{epi,r}$, $\beta_{endo,\ell}$, $\beta_{epi,\ell}$, $\beta_{endo,r}$ and $\beta_{epi,r}$ are suitable rotation angles on the epicardium and endocardium chosen in order to match histological observations. For instance, classical values for the helical angles found in the literature are $\alpha_{epi,\ell} = +60^o$, $\alpha_{endo,\ell} = -60^o$, $\alpha_{epi,r} = -25^o$, $\alpha_{endo,r} = +90^o$ [134, 86, 9, 99, 210].

In order to differentiate between LV and RV and to apply the correct angles, we propose here to use the solution of an additional Laplace problem (2.2) in the unknown $\chi = \xi$ with $\chi_a = 1$ on $\Gamma_{\ell v}$, $\chi_b = -1$ on Γ_{rv}, and $\Gamma_n = \Gamma_{base} \cup \Gamma_{vepi}$[2]. In particular, positive values of ξ identify LV, whereas negative ones RV [24]. This new feature enables to perform different rotations for LV and RV (see steps 6 in Figures 2.5, 2.6 and 2.7) that is crucial in order to generate realistic fiber fields. An alternative method has been proposed in [58] but only for D-RBM. It is worth mentioning that the original R-RBM [204, 188] introduces a rotation, by means of the Rodrigues' formula, to obtain the fiber field $\boldsymbol{f}$ only. Here we propose an extension in order to define also $\boldsymbol{n}$ and $\boldsymbol{s}$.

Further, B-RBM exploits two other functions representing the rotation angles within the septum:

$$\alpha_s(d_i) = \alpha_{endo,i}(1-2d_i), \qquad \beta_s(d_i) = \beta_{endo,i}(1-2d_i), \qquad i = \ell, r,$$

whereas with similar expressions, D-RBM introduces also the possibility to set specific fiber and sheet angles rotation in the OT regions (see [26] and [58] for further details).

We conclude pointing out that B-RBM and D-RBM can be applied to the full biventricular geometry and to the based biventricular one (that is obtained with an artificial basal plane well below the cardiac valves). Indeed, in the based biventricular geometry the whole procedure for B-RBM and D-RBM remains the same as long as the ring labels are replaced by the base label, $\Gamma_{rings} = \Gamma_{base}$. On the contrary, R-RBM is less suitable for a full biventricular geometry because it is not able to strictly identify the normal direction $\boldsymbol{k}$ as the outward normal to the ventricular rings. Besides, the right septum Γ_{rs} can be very arbitrary to define for a full biventricular geometry.

---

[2] Let us observe that, for B-RBM $\Gamma_{base} = \Gamma_{rings}$ in the case of a full biventricular geometry. Moreover, for D-RBM solely $\chi_a = 2$ in order to be compliant with the transmural distance.

Type	χ	χ_a	Γ_a	χ_b	Γ_b	Γ_n
BIA	ξ	1	$\Gamma_{\ell a}$	-1	Γ_{ra}	$\partial\Omega_{bia}/(\Gamma_{\ell a} \cup \Gamma_{ra})$
	ϕ	1 -1	$\Gamma_{\ell a}$ Γ_{ra}	0	$\Gamma_{aepi} \cup \Gamma_{top,\ell} \cup \Gamma_{top,r}$	$\partial\Omega_{bia}/(\Gamma_{\ell a} \cup \Gamma_{ra} \cup \Gamma_{aepi} \cup \Gamma_{top,\ell} \cup \Gamma_{top,r})$
LA	ψ_{ab}	2 0	Γ_{rpv} Γ_{lpv}	1 -1	Γ_{mv} Γ_{lap}	$\partial\Omega_{bia}/(\Gamma_{rpv} \cup \Gamma_{lpv} \cup \Gamma_{mv} \cup \Gamma_{lap})$
	ψ_r	1	Γ_{mv}	0	$\Gamma_{lpv} \cup \Gamma_{rpv}$	$\partial\Omega_{bia}/(\Gamma_{mv} \cup \Gamma_{lpv} \cup \Gamma_{rpv})$
	ψ_v	1	Γ_{rpv}	0	Γ_{lpv}	$\partial\Omega_{bia}/(\Gamma_{rpv} \cup \Gamma_{lpv})$
	ψ_{sw}	1	Γ_{mv}	0	$\Gamma_{lpv} \cup \Gamma_{top,\ell} \cup \Gamma_{lap}$	$\Omega_{bia}/(\Gamma_{mv} \cup \Gamma_{lpv} \cup \Gamma_{top,\ell})$
	ψ_w	1 -1	Γ_{mv-s} Γ_{mv-f}	0	$\Gamma_{top,\ell}$	$\partial\Omega_{bia}/(\Gamma_{mv-s} \cup \Gamma_{mv-f} \cup \Gamma_{top,\ell})$
RA	ψ_{ab}	2 0	Γ_{icv} Γ_{scv}	1 -1 -2	Γ_{tv} Γ_{rap} Γ_{cs}	$\partial\Omega_{bia}/(\Gamma_{icv} \cup \Gamma_{scv} \cup \Gamma_{tv} \cup \Gamma_{rap} \cup \Gamma_{cs})$
	ψ_r	1	Γ_{tv}	0	$\Gamma_{top,r}$	$\partial\Omega_{bia}/(\Gamma_{tv} \cup \Gamma_{top,r})$
	ψ_v	1 0	Γ_{icv} Γ_{scv}	-1	Γ_{rap}	$\partial\Omega_{bia}/(\Gamma_{icv} \cup \Gamma_{scv} \cup \Gamma_{rap})$
	ψ_w	1 -1	Γ_{tv-s} Γ_{tv-f}	0	$\Gamma_{top,r}$	$\partial\Omega_{bia}/(\Gamma_{tv-s} \cup \Gamma_{tv-f} \cup \Gamma_{top,r})$

Table 2.3: Boundary data chosen in the Laplace problem (2.2) for the inter-atrial distances (BIA) ξ, ϕ and the intra-atrial distances ψ_i $(i = ab, r, v, sw, w)$ in LA and RA.

2.2 Atrial Laplace-Dirichlet Rule-Based Method

In this section, we present a novel LDRBM for the generation of atrial myofibers, which is able to qualitatively reproduce all the important features, such as the fiber bundles, needed to provide a realistic atrial musculature architecture. Our newly developed method has been proposed in [176], and in this thesis we present its extension to the biatrial geometries.

The atrial LDRBM is inspired by [203] where Laplace problems are introduced to map variables between two geometries and by LDRBMs, purposely built for the ventricles, presented in Section 2.1 [26, 204, 58]. The extension of the latter is not straightforward due to the nature of the atrial bundles which run in different directions. For this reason, the atrial LDRBM combines the gradient of several harmonic functions to represent the fiber bundles.

In what follows we detail the four steps of the atrial LDRBM. We refer to Figure 2.8 for a schematic representation of the method in a realistic biatrial geometry.

1. Labelled mesh: label the mesh of the biatrial computational domain Ω_{bia} to define the boundary partitions $\partial\Omega_{bia}$ (see step 1 in Figure 2.8):

$$\begin{aligned}\partial\Omega_{bia} =& \Gamma_{aepi} \cup \Gamma_{top,\ell} \cup \Gamma_{top,r} \cup \Gamma_{\ell a} \cup \Gamma_{ra} \cup \Gamma_{\ell ap} \cup \Gamma_{rap} \cup \\ & \Gamma_{lpv} \cup \Gamma_{rpv} \cup \Gamma_{icv} \cup \Gamma_{scv} \cup \Gamma_{mv} \cup \Gamma_{tv} \cup \Gamma_{cs}\end{aligned}$$

where Γ_{aepi} is the atrial epicardium, $\Gamma_{\ell a}$, Γ_{ra} the left and right atrial endocardium, $\Gamma_{\ell ap}$, Γ_{rap} the left and right atrial appendage, Γ_{lpv}, Γ_{rpv} LPV and RPV rings, Γ_{icv}, Γ_{scv} ICV and SCV rings, Γ_{mv}, Γ_{tv} MV and TV rings and Γ_{cs} the coronary sinus appendage. In particular, Γ_{mv} and Γ_{tv} are further subdivided in a part facing the atrial septum Γ_{mv-s}, Γ_{tv-s} and the other related to the free wall Γ_{mv-f}, Γ_{tv-f}, such that $\Gamma_{mv} = \Gamma_{mv-s} \cup \Gamma_{mv-f}$ and $\Gamma_{tv} = \Gamma_{tv-s} \cup \Gamma_{tv-f}$ (see step 1 in Figure 2.8). Furthermore, $\Gamma_{top,\ell}$ and $\Gamma_{top,r}$ are the boundary labels connecting the top upper region of the anterior LPV to anterior RPV rings and ICV to SCV rings, respectively (see step 1 in Figure 2.8).

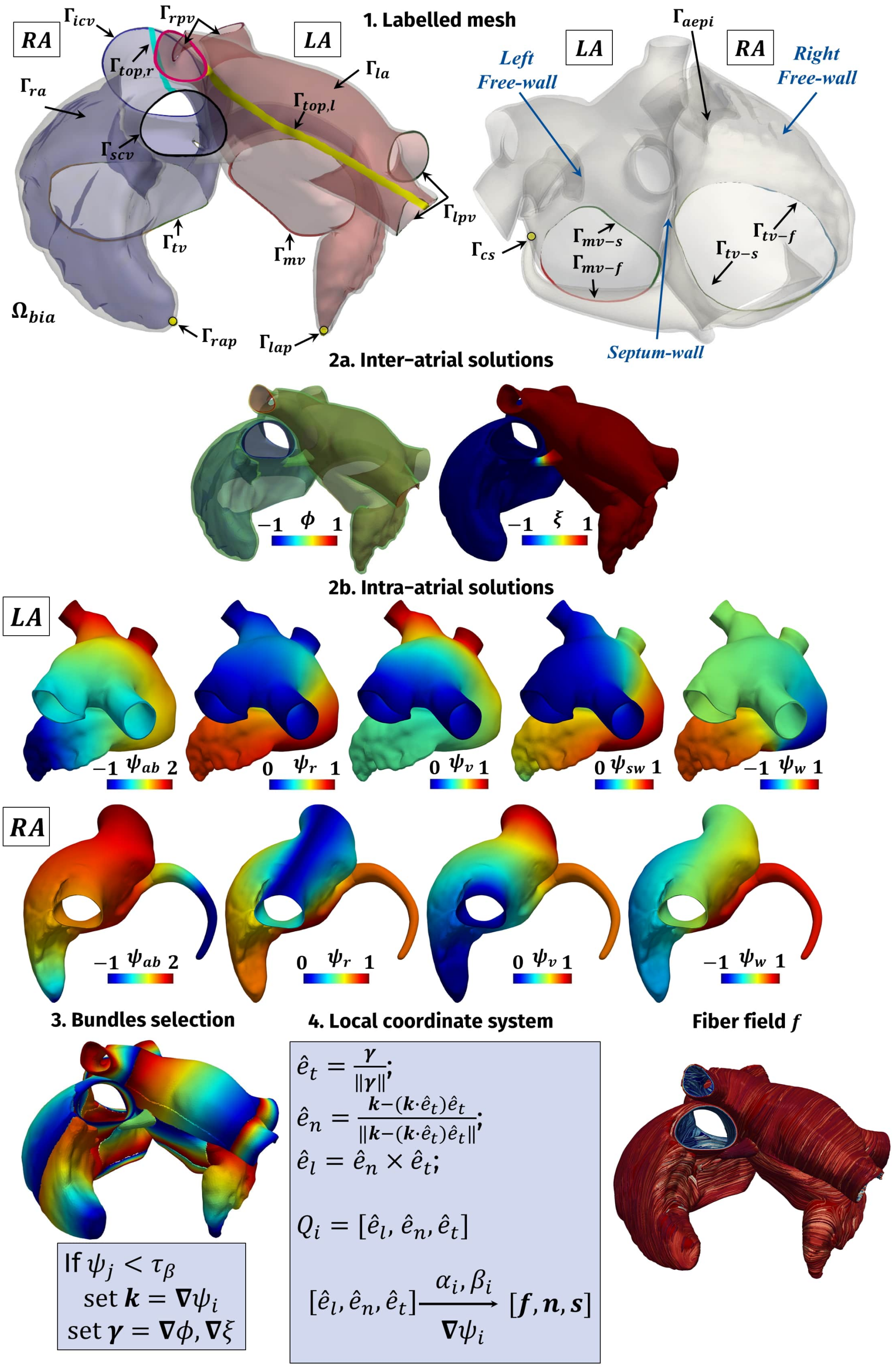

Figure 2.8: Schematic procedure of the atrial LDRBM in a realistic biatrial geometry.

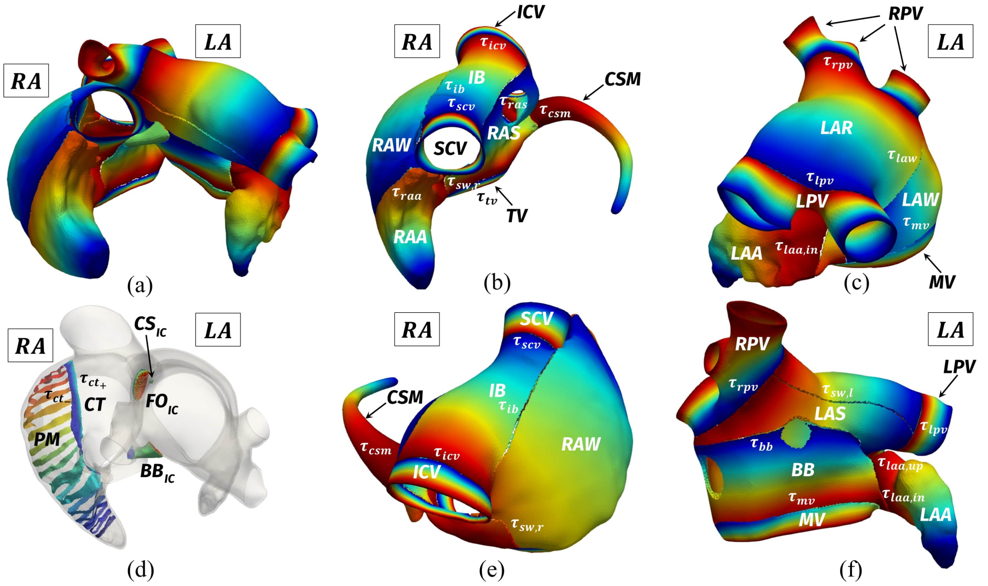

Figure 2.9: Definition of the bundles and their dimension throughout the biatrial domain following the rules reported in Algorithms 1, 2, 3 and 4; (a) Complete bundles selection in LA and RA; (b,e): bundles selection in RA following Algorithm 2; (c,f): bundles selection in LA following Algorithm 4. (d) Selection of the inter-atrial connection (IC), crista terminalis (CT), pectinate muscles (PM) bundles following Algorithms 1 and 3, respectively. τ_i (for the i-th bundle) is the parameter related to the bundle dimension.

2. Laplace problems: definition of biatrial distances, obtained by solving Laplace problems in the form of (2.2) with proper Dirichlet boundary conditions on the atrial boundaries, see step 2 in Figure 2.8. Specifically, the transmural ϕ and the inter-atrial ξ distances are introduced, see step 2a in Figure 2.8. Moreover, several intra-atrial distances ψ_i are computed, see step 2b in Figure 2.8. Refer to Table 2.3 for the specific choices in problem (2.2) made by the atrial LDRBM. In particular, ψ_{ab} is the solution of a Laplace problem (2.2) with different boundary data prescribed on the right atrial appendage Γ_{rap}, the rings of the caval veins $(\Gamma_{icv}, \Gamma_{scv})$, TV ring Γ_{tv} and the coronary sinus appendage Γ_{cs} for RA, and the left atrial appendage $\Gamma_{\ell ap}$, the pulmonary vein rings $(\Gamma_{lpv}, \Gamma_{rpv})$ and MV ring Γ_{mv} for LA; ψ_r stands for the distance between TV ring Γ_{tv} and $\Gamma_{top,r}$ (RA) and between MV ring Γ_{mv} and the union of the pulmonary veins rings $\Gamma_{lpv} \cup \Gamma_{rpv}$ (LA); ψ_v represents the distance between the caval veins for the RA and among the pulmonary veins for LA; ψ_w is the distance between the MV/TV ring of the free $(\Gamma_{mv-f}/\Gamma_{tv-f})$ and the septum $(\Gamma_{mv-s}/\Gamma_{tv-s})$ walls for LA/RA . Finally, ψ_{sw} is computed for LA solely prescribing suitable boundary conditions for LPV rings Γ_{lpv}, MV ring Γ_{mv} and the the boundary labels connecting LPV to RPV rings $\Gamma_{top,\ell}$, see step 2b in Figure 2.8.

Algorithm 1 . **compute$_{\mathbf{BIA}}$**: *bundles selection for biatrial geometry*

```
Let $\tau_{BBicr}$, $\tau_{BBicl}$, $\tau_{BBic}$, $\tau_{FOicr}$, $\tau_{FOicl}$, $\tau_{FOic}$, $\tau_{CSicr}$, $\tau_{CSicl}$ and $\tau_{CSic}$ the parameters
referring to IC bundles.
  if ($\xi \in [\tau_{BBicr}, \tau_{BBicl}]$ and $\psi_v^{\mathrm{RA}} \leq \tau_{BBic}$)
      set $\boldsymbol{k} = \nabla\phi$, $\boldsymbol{\gamma} = \nabla\xi \longrightarrow \mathrm{BB_{IC}}$
      flip($\widehat{\boldsymbol{e}}_l$,$\widehat{\boldsymbol{e}}_t$)
  else if ($\xi \in [\tau_{FOicr}, \tau_{FOicl}]$ and $\psi_{ab}^{\mathrm{LA}} \geq \tau_{FOic}$ and $\psi_v^{\mathrm{RA}} > \tau_{BBic}$)
      set $\boldsymbol{k} = \nabla\phi$, $\boldsymbol{\gamma} = \nabla\xi \longrightarrow \mathrm{FO_{IC}}$
  else if ($\xi \in [\tau_{CSicr}, \tau_{CSicl}]$ and $\psi_v^{\mathrm{RA}} > \tau_{BBic}$ and $\psi_{ab}^{\mathrm{RA}} \leq \tau_{CSic}$ )
      set $\boldsymbol{k} = \nabla\phi$, $\boldsymbol{\gamma} = \nabla\xi \longrightarrow \mathrm{CS_{IC}}$
      flip($\widehat{\boldsymbol{e}}_l$,$\widehat{\boldsymbol{e}}_t$)
  else
      set $\boldsymbol{\gamma} = \nabla\phi$
    if $\xi \geq 0$  compute$_{\mathbf{LA}}$
    else compute$_{\mathbf{RA}}$
  Note: we use $\psi_i^{\mathrm{RA}}$ and $\psi_i^{\mathrm{LA}}$ to distinguish LA and RA distances. Moreover, the
  function flip($\widehat{\boldsymbol{e}}_l$,$\widehat{\boldsymbol{e}}_t$) flips the longitudinal $\widehat{\boldsymbol{e}}_l$ and the transmural $\widehat{\boldsymbol{e}}_t$ directions.
```

3. Bundles selection: definition of the atrial bundles and their dimensions throughout the domain Ω_{bia}, in order to match histology and DTI observations. With this aim, the atrial LDRBM first selects LA, RA and the inter-atrial connection (IC) regions, following the rules reported in Algorithm 1 (**compute$_{\mathbf{BIA}}$**) and then compute LA and RA bundles, exploiting the rules reported in of Algorithms 2 (**compute$_{\mathbf{RA}}$**), 3 (**compute$_{\mathbf{PM}}$**) and 4 (**compute$_{\mathbf{LA}}$**). During this bundles selection procedure, a unique intra-atrial distance ψ_i, among those defined in step 2, is assigned for each point in Ω_{bia} (see step 3 in Figure 2.8 and also Figure 2.9). Moreover, at this step, the atrial LDRBM defines a unique transmural $\boldsymbol{\gamma}$ and normal $\boldsymbol{k}$ directions, by taking the gradient of a specified inter-atrial distance, $\boldsymbol{\gamma} = \nabla\phi, \nabla\xi$, and of a specific intra-atrial distance, $\boldsymbol{k} = \nabla\psi_i$, respectively. Following Algorithms 1-4, the principal anatomical atrial regions are introduced: for RA, superior (SCV) and inferior caval veins (ICV), tricuspid valve ring (TV), right appendage (RAA), right septum (RAS), inter-caval bundle (IB), crista terminalis (CT), coronary sinus musculature (CSM) and right atrial later wall (RAW), see Figure 2.9(b,e); for LA, left (LPV) and right pulmonary veins (RPV), mitral valve ring (MV), left appendage (LAA), left septum (LAS), bachmann's bundle (BB), left atrial lateral wall (LAW) and roof (LAR), see Figure 2.9(c,f); for IC, the bachmann's bundle ($\mathrm{BB_{IC}}$), the fossa ovalis ($\mathrm{FO_{IC}}$) and the coronary sinus ($\mathrm{CS_{IC}}$) connections, see Figure 2.9(c). Moreover, in order to specify the bundles dimension, the parameters τ_i are introduced: for RA τ_{tv}, τ_{icv}, τ_{scv}, τ_{raa}, τ_{csm}, $\tau_{sw,r}$, τ_{ct_+}, τ_{ct_-}, τ_{ib}, τ_{ras} refer to TV, ICV, SCV, RAA, CSM, RAW, upper and lower limit of CT, IB and RAS bundles, respectively; for LA τ_{mv}, τ_{rpv}, τ_{lpv}, $\tau_{sw,\ell}$, $\tau_{laa,in}$, $\tau_{laa,up}$, τ_{bb}, τ_{law}, refer to MV, RPV, LPV, LAS, LAA, BB, LAW bundles, respectively (see Figure 2.9); for IC, τ_{BBicr}, τ_{BBicl}, τ_{BBic}, τ_{FOicr}, τ_{FOicl}, τ_{FOic}, τ_{CSicr}, τ_{CSicl}, τ_{CSic} refer to $\mathrm{BB_{IC}}$, $\mathrm{FO_{IC}}$ and $\mathrm{CS_{IC}}$ connections. As an optional feature, the atrial LDRBM allows to embed the pectinate muscles bundles (PM) in RAW and RAA, exploiting the procedure outlined in Algorithm 3, which requires to specify the parameters pm_{thick}, pm_{range}, pm_{end} and the numbers N_{raa}, N_{raw} of PM in RAA and RAW, respectively. The complete bundles selection procedures for the atrial LDRBM are fully detailed in Algorithms 1-4 (see also step 3 in Figure 2.8 and Figure 2.9).

Algorithm 2 . compute$_{\mathbf{RA}}$: *bundles selection for RA*

Let toll $\ll 1$ and τ_{tv}, τ_{icv}, τ_{scv}, τ_{raa}, τ_{csm}, $\tau_{sw,r}$, τ_{ct_-}, τ_{ct_+}, τ_{ib}, τ_{ras}, N_{raw} and N_{raa} be the parameters referring to the related bundles.

```
if $\psi_r \geq \tau_{tv}$  set $\boldsymbol{k} = \nabla\psi_r \longrightarrow$ TV
else
    if $\psi_v \geq \tau_{icv}$  set $\boldsymbol{k} = \nabla\psi_v \longrightarrow$ ICV
    else if $\psi_v \leq \tau_{scv}$
        if $\psi_r \geq \tau_{raa}$
            if PM=true  compute$_{\mathbf{PM}}(0, N_{raa}) \longrightarrow$ PM
            else set $\boldsymbol{k} = \nabla\psi_{ab} \longrightarrow$ RAA
        else set $\boldsymbol{k} = \nabla\psi_v \longrightarrow$ SCV
    else
        if ($\psi_{ab} \leq \tau_{csm}$ and $\psi_v \geq 0.5$ and $\psi_{sw} \geq \tau_{sw,r}$)  set $\boldsymbol{k} = \nabla\psi_{ab} \longrightarrow$ CSM
        else
            if $\psi_r \leq \tau_{raw}$
                if ($\psi_w \geq \tau_{ct_-}$ and $\psi_w \leq \tau_{ct_+}$)
                    if $|\phi| \geq (1 - \text{toll})$  set $\boldsymbol{k} = \nabla\psi_w \longrightarrow$ CT
                    else set $\boldsymbol{k} = \nabla\psi_{ab} \longrightarrow$ RAW
                else if $\psi_w \geq \tau_{ct_+}$
                    if ($\psi_w \leq 0$ and $\psi_r \leq \tau_{ib}$)  set $\boldsymbol{k} = \nabla\psi_v \longrightarrow$ IB
                    else if ($\psi_w \leq 0$ and $\psi_r > \tau_{ib}$)  set $\boldsymbol{k} = \nabla\psi_{ab} \longrightarrow$ RAW
                    else
                        if $\psi_r \geq \tau_{ras}$  set $\boldsymbol{k} = \nabla\psi_r \longrightarrow$ RAS
                        else set $\boldsymbol{k} = \nabla\psi_v \longrightarrow$ IB
                else
                    if PM=true  compute$_{\mathbf{PM}}(\tau_{scv}, N_{raw}) \longrightarrow$ PM
                    else set $\boldsymbol{k} = \nabla\psi_{ab} \longrightarrow$ RAW
            else
                if $\psi_w \geq \tau_{sw,r}$  set $\boldsymbol{k} = \nabla\psi_r \longrightarrow$ RAS
                else
                    if PM=true  compute$_{\mathbf{PM}}(\tau_{scv}, N_{raw}) \longrightarrow$ PM
                    else set $\boldsymbol{k} = \nabla\psi_{ab} \longrightarrow$ RAW
```

Algorithm 3 . compute$_{\mathbf{PM}}$(ζ,N): *PM bundle selection in RA*

Let ζ and N the generic input parameters, toll $\ll 1$ and pm$_{thick}$, pm$_{range}$ and pm$_{end}$ the parameters referring to PM bundles.

```
for n=1:$N$
    $\mathrm{PM}_i = \zeta + (n-1)\,\mathrm{pm}_{thick} + (n-1)\,\mathrm{pm}_{range}$;
    $\mathrm{PM}_f = \zeta + n\,\mathrm{pm}_{thick} + (n-1)\,\mathrm{pm}_{range}$;
    $\mathrm{PM}_s = \zeta + n\,\mathrm{pm}_{thick} + n\,\mathrm{pm}_{range}$;
    if $|\phi| \geq (1 - \text{toll})$ and $\psi_v \leq \mathrm{pm}_{end}$ and $\psi_v \geq \mathrm{PM}_i$ and $\psi_v \leq \mathrm{PM}_f$
     set $\boldsymbol{k} = \nabla\psi_v \longrightarrow$ PM
    if ($|\phi| \geq (1 - \text{toll})$ and $\psi_v > \mathrm{PM}_f$ and $\psi_v < \mathrm{PM}_s$) or $\psi_v > \mathrm{pm}_{end}$ or $\psi_v < \zeta$
     set $\boldsymbol{k} = \nabla\psi_{ab} \longrightarrow$ RAW
    if $|\phi| \leq (1 - \text{toll})$  set $\boldsymbol{k} = \nabla\psi_{ab} \longrightarrow$ RAW
```

Algorithm 4 . compute$_{\mathbf{LA}}$:*bundles selection for LA*

```
Let $\tau_{mv}$, $\tau_{rpv}$, $\tau_{lpv}$, $\tau_{sw,\ell}$, $\tau_{laa,in}$, $\tau_{laa,up}$, $\tau_{bb}$, $\tau_{law}$ be the parameters referring to the related bundles.
  if $\psi_{sw} \geq \tau_{mv}$ set $\boldsymbol{k} = \nabla\psi_{sw} \longrightarrow$ MV
  else
      if $\psi_v \leq \tau_{rpv}$ set $\boldsymbol{k} = \nabla\psi_v \longrightarrow$ RPV
      else if $\psi_v \geq \tau_{lpv}$ set $\boldsymbol{k} = \nabla\psi_v \longrightarrow$ LPV
      else
          if $\psi_w \geq \tau_{sw,\ell}$
              if ( $\psi_{ab} \leq \tau_{laa,in}$ and $\psi_r \geq \tau_{laa,up}$) set $\boldsymbol{k} = \nabla\psi_{ab} \longrightarrow$ LAA
              else
                  if $\psi_r \geq \tau_{bb}$ set $\boldsymbol{k} = \nabla\psi_r \longrightarrow$ BB
                  else set $\boldsymbol{k} = \nabla\psi_{ab} \longrightarrow$ LAS
          else
              if $\psi_{sw} \geq \tau_{law}$ set $\boldsymbol{k} = \nabla\psi_v \longrightarrow$ LAW
              else set $\boldsymbol{k} = \nabla\psi_{ab} \longrightarrow$ LAR
```

4. Local coordinate system: definition of the myofiber orientations by rotating an orthonormal local coordinate system, $[\widehat{\boldsymbol{e}}_l, \widehat{\boldsymbol{e}}_n, \widehat{\boldsymbol{e}}_t]$ built at each point of the atrial domain. This step is performed in the same way as for the ventricles, by applying first the function `axis`, which takes as inputs the transmural direction $\boldsymbol{\gamma}$ together with the unique normal direction $\boldsymbol{k}$, and then exploiting the function `orient`

$$Q = [\widehat{\boldsymbol{e}}_l, \widehat{\boldsymbol{e}}_n, \widehat{\boldsymbol{e}}_t] = \texttt{axis}(\boldsymbol{k}, \boldsymbol{\gamma}), \qquad [\boldsymbol{f}, \boldsymbol{n}, \boldsymbol{s}] = \texttt{orient}(Q, \alpha, \beta). \tag{2.6}$$

A transmural fibers variation can be prescribed in each atrial bundle, in two combined ways:

1. by defining the unique normal direction $\boldsymbol{k}$, within the function `axis`, as a linear combination of the gradients of two intra-atrial distances

$$\boldsymbol{k} = (1 - |\phi|)\nabla\psi_j + |\phi|\nabla\psi_k \quad j, k = ab, r, v, sw, w$$

2. by setting a linear relationships for the angles $\alpha = \alpha_i(|\phi|)$ and $\beta = \beta_i(|\phi|)$ in the function `orient`

$$\alpha_i = \alpha_{epi_i}(1 - |\phi|) + \alpha_{endo_i}|\phi|, \qquad \beta_i = \beta_{epi_i}(1 - |\phi|) + \beta_{endo_i}|\phi|,$$

   where α_{epi_i}, α_{endo_i}, β_{epi_i} and β_{endo_i} are fixed rotation angles on the epicardium and endocardium of the i-th bundle, respectively.

The three unit directions correspond to the final fiber, sheet and sheet-normal directions $\boldsymbol{f}$, $\boldsymbol{n}$ and $\boldsymbol{s}$ (see step 4 in Figure 2.8).

2.2.1 Atrial LDRBM rules

The atrial LDRBM presented in Section 2.2, based on the procedure of Algorithms 1-4 and the definition of the local coordinate system (2.6), prescribes a fiber field $\boldsymbol{f}$ based on the following rules derived from histo-anatomical observations and DT-MRI fiber data [167, 212, 97, 100, 98, 51, 203], see Figures 2.9:

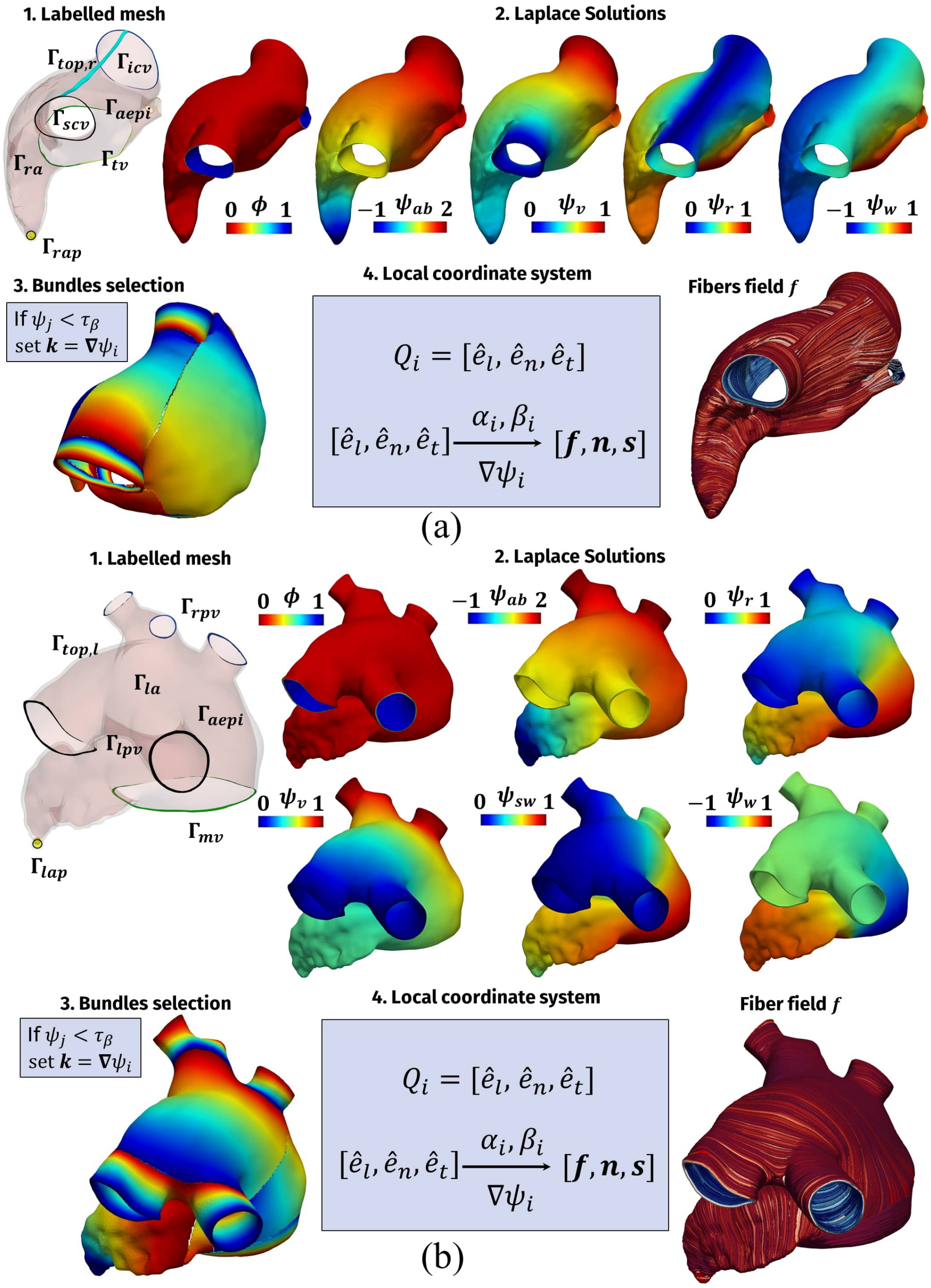

Figure 2.10: Schematic procedure of the atrial LDRBM in a realistic RA (a) and LA (b) geometries.

R1: Circular fiber arrangements are prescribed around LPV, RPV, SCV, ICV, CSM, TV, MV, and encircle both appendages (RAA and LAA) [167, 212, 203];

R2: Fibers direction of CT runs longitudinally from the base of SCV to ICV [210];

R3: PM fibers run on the endocardial surface, almost parallel to each other and perpendicular to CT fibers [67];

R4: RA structures like IB and RAW are vertically oriented, whereas those of RAS are parallel to CT [97, 100];

R5: BB fibers run longitudinally in the same direction of those of MV [51];

R6: LAS fibers are almost aligned (parallel) to the nearby RAS [67];

R7: Directions of LAR and LAW descend perpendicularly to MV, while fibers of LAS present a smooth transition going to LAS and LAA [67, 98, 203].

2.2.2 LDRBM for single atrial chamber

The atrial LDRBM, presented in Section 2.2 for the biatrial case, can also be applied to generate fibers architecture to single RA or LA chamber. The LA and RA version of the our novel atrial LDRBM has been proposed in [176].

In the single chamber atrial LDRBM, the inter-atrial solution ξ is no longer computed and the transmural distance ϕ is found by solving (2.2) with $\chi_a = 1$ on the atrial endocardium $\Gamma_{aendo} = \Gamma_{ra}, \Gamma_{\ell a}$ and $\chi_b = 0$ on the atrial epicardium Γ_{aepi} and $\Gamma_n = \partial\Omega_{bia}/(\Gamma_{aendo} \cup \Gamma_{aepi})$. The intra-atrial solutions ψ_i for RA or LA are computed as detailed in step 2 of the biatrial LDRBM, see Figure 2.10. Finally, the bundles selection procedure is performed starting directly from Algorithms 2 ($\mathbf{compute_{RA}}$) and 3 ($\mathbf{compute_{PM}}$) for RA, while from Algorithm 4 ($\mathbf{compute_{LA}}$) for LA. A schematic representation of the atrial LDRBM applied to single RA and LA chamber is sketched in Figure 2.10.

2.3 Modeling cardiac electrophysiology

In this section we briefly introduce the mathematical model for the description of the EP activity in the cardiac tissue, that is the monodomain equation endowed with suitable ionic models for human action potential [188, 57, 72, 255, 181, 245, 151]. For further details, we refer the reader to Section 3.1, where we fully present the mathematical models associated to the core physics.

Cardiac tissue is an orthotropic material, arising from the cellular organization of the myocardium in fibers, laminar sheets and sheet-normals, which is mathematically modelled by the conductivity tensor

$$\mathbf{D} = \sigma_f \boldsymbol{f} \otimes \boldsymbol{f} + \sigma_s \boldsymbol{s} \otimes \boldsymbol{s} + \sigma_n \boldsymbol{n} \otimes \boldsymbol{n}, \tag{2.7}$$

where σ_f, σ_s and σ_n are the conductivities along fiber ($\boldsymbol{f}$), sheet ($\boldsymbol{s}$), and sheet-normal ($\boldsymbol{n}$) directions, respectively. Given a computational domain Ω (with either $\Omega = \Omega_{biv}, \Omega_{bia}$) and a time interval $(0, T]$, the monodomain equations read:

Find, for each t, the transmembrane action potential $u : \Omega \times (0, T] \to \mathbb{R}$ and the ionic vector variable $\boldsymbol{w} : \Omega \times (0, T] \to \mathbb{R}^{n_{\boldsymbol{w}}}$, such that

$$\begin{cases} \chi_m \left[C_m \dfrac{\partial u}{\partial t} + \mathcal{I}_{ion}(u, \boldsymbol{w}) \right] - \nabla \cdot (\mathbf{D} \, \nabla u) = \mathcal{I}_{app}, & \text{in } \Omega \times (0, T], \quad (2.8a) \\ \dfrac{\partial \boldsymbol{w}}{\partial t} - \boldsymbol{H}(u, \boldsymbol{w}) = \mathbf{0} & \text{in } \Omega \times (0, T], \quad (2.8b) \\ \mathbf{D} \nabla u \cdot \mathbf{n} = 0 & \text{on } \partial\Omega \times (0, T], \quad (2.8c) \\ u = u_0, \quad \boldsymbol{w} = \boldsymbol{w}_0, & \text{in } \Omega \times \{0\}. \quad (2.8d) \end{cases}$$

where χ_m is the surface area-to-volume ratio of cardiomyocytes, C_m is the specific trans-membrane capacitance per unit area, $\mathcal{I}_{app}$ is an external applied current which serves to initiate the signal propagation, $\mathcal{I}_{ion}$ and $\boldsymbol{H} \in \mathbb{R}^{n_w}$ are the reaction terms, linking the macroscopic action potential propagation to the cellular dynamics. The unknown $\boldsymbol{w}$, encoding the gating-variables (representing the fraction of open channels per unit area across the cell membrane) and the concentration of specific ionic species, is a $n_{\boldsymbol{w}}$–th dimensional vector function fulfilling a system of differential algebraic equations. Specifically, we used the Courtemanche-Ramirez-Nattel (CRN98, $n_{\boldsymbol{w}} = 20$) in case of atrial action potential and the ten-Tusscher-Panfilov (TTP06, $n_{\boldsymbol{w}} = 18$) for the ventricular one (for further details see [47] for CRN98 and [247] for TTP06). Furthermore, system (2.8) is equipped with suitable initial conditions (2.8d) for u and $\boldsymbol{w}$ and homogeneous Neumann boundary conditions (2.8c) for u on the boundary $\partial\Omega$.

Regarding the numerical discretization of the monodomain system (2.8), we refer to Section 3.2, where we detail the numerical methods of the different core models. Here, we just mention that for the time discretization of system (2.8) we consider Finite Difference (FD) with *Backward Difference Formulae* approximation (BDF) employing an explicit treatment of the reaction term [189]. Moreover, the diffusion term is treated implicitly, whereas the ionic terms explicitly [72, 181, 254]. Regarding the space discretization, we use Finite Element Method (FEM) with continuous FE on hexahedral meshes. Moreover, the discretization of the ionic current term $\mathcal{I}_{ion}$ is performed following the Ionic Current Interpolation (ICI) approach [244, 188, 105, 109, 13, 116].

2.4 Setting of numerical simulations

In this section we describe the setting related to the numerical simulations, that will be presented in Sections 2.5 and 2.6. In Section 2.4.1, we first detail the procedure to build labelled FE meshes, used for prescribing the atrial and ventricular fibers by means of LDRBMs. In Section 2.4.2, we address the issue of estimating the parameters employed in EP simulations.

2.4.1 Labelling procedure for LDRBMs

In order to build FE meshes, a preprocessing procedure was applied to every ventricular and atrial geometries used for the generation of ventricular and atrial fibers by means of LDRBM, presented in Sections 2.1 and 2.2. For this preprocessing phase we rely on the novel semi-automatic meshing tool proposed in [66] which consists of multiple steps including labelling, geometry smoothing and hexahedral FE mesh

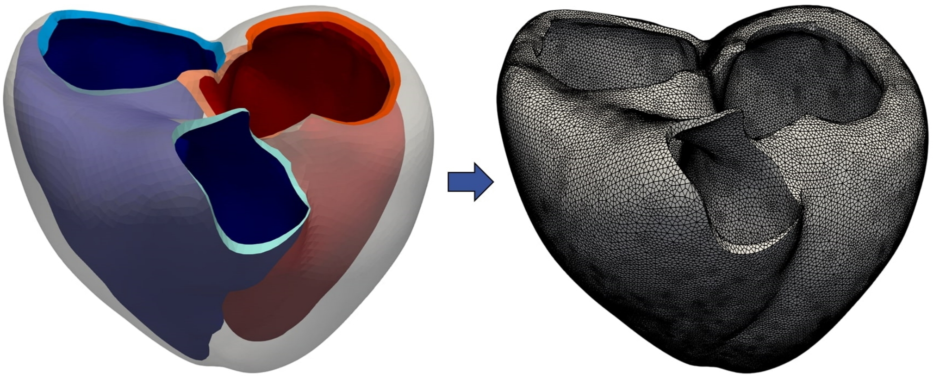

Figure 2.11: Preprocessing procedure applied to build a ventricles Finite Elements (FE) mesh [66]. Left: smoothing and labelling procedure; Right: FE mesh of hexahedral elements.

generation, see Figure 2.11. Specifically, the Vascular Modelling Toolkit `vmtk` software [11] (`http://www.vmtk.org`) together with a new meshing tool were used to perform such pre-processing phase.

The labelling procedures carried out in this work, for the ventricular and atrial LDRBMs, are detailed in what follows. We remark however that our labelling procedure is not crucial for the applicability of the ventricular and atrial LDRBMs. Indeed, they are perfectly compatible with other labelling processes presented in other works (see for example [58, 235]).

For the atria, the first labelling step consists in extracting the endocardium and the epicardium from the unlabelled surface model. Then, labels of the pulmonary and caval veins and the atrioventricular valves rings are selected by connecting the points laying on the border zone of the endocardium to the corresponding epicardial points, see Figure 2.12(b) (for further details about the connection procedure we refer to [66]). Furthermore, the label $\Gamma_{top,i}$ in RA ($i = r$) and LA ($i = \ell$) is carried out by manually producing a straightforward band connecting the top upper elements of SCV and ICV, for RA, and anterior LPV to anterior RPV, for LA, see Figure 2.12(a). Finally, TV and MV rings Γ_{tv}, Γ_{mv} in RA and LA, respectively, are subdivided in one part facing the atrial septum Γ_{tv-s}, Γ_{ms-s} and another one related to the free wall Γ_{tv-s}, Γ_{mv-f}, such that $\Gamma_{tv} = \Gamma_{tv-s} \cup \Gamma_{tv-f}$ and $\Gamma_{mv} = \Gamma_{mv-s} \cup \Gamma_{mv-f}$: this subdivision is produced by clipping the TV/MV ring with a plane passing through $\Gamma_{top,i}$ band, see Figure 2.12(a).

For the ventricles, the first labelling step consists in extracting the epicardium and the right and left endocardia from the unlabelled surface model. Moreover, for R-RBM, the right endocardium Γ_{rv} is subdivided into the right septum Γ_{rs} and the remaining part Γ_{rv-s} such that $\Gamma_{rv} = \Gamma_{rs} \cup \Gamma_{rv-s}$: this labelling subdivision is achieved by selecting a threshold in the distance between right and left endocardia, see step 1 in Figure 2.5. Furthermore, concerning a based biventricular geometry, the final labelling step consists in producing an upper basal plane between the ventricular endocardium and epicardium, see step 1 in Figure 2.5. Regarding a complete biventricular model, labels of the four valve rings (Γ_{mv} MV, Γ_{av} AV, Γ_{tv} TV and Γ_{pv} PV) are defined by selecting a threshold in the distance from the corresponding atrial rings for Γ_{mv} and Γ_{tv} and from the aortic and pulmonary OT roots for Γ_{av} and Γ_{pv}, respectively (see Figure 2.12(c)).

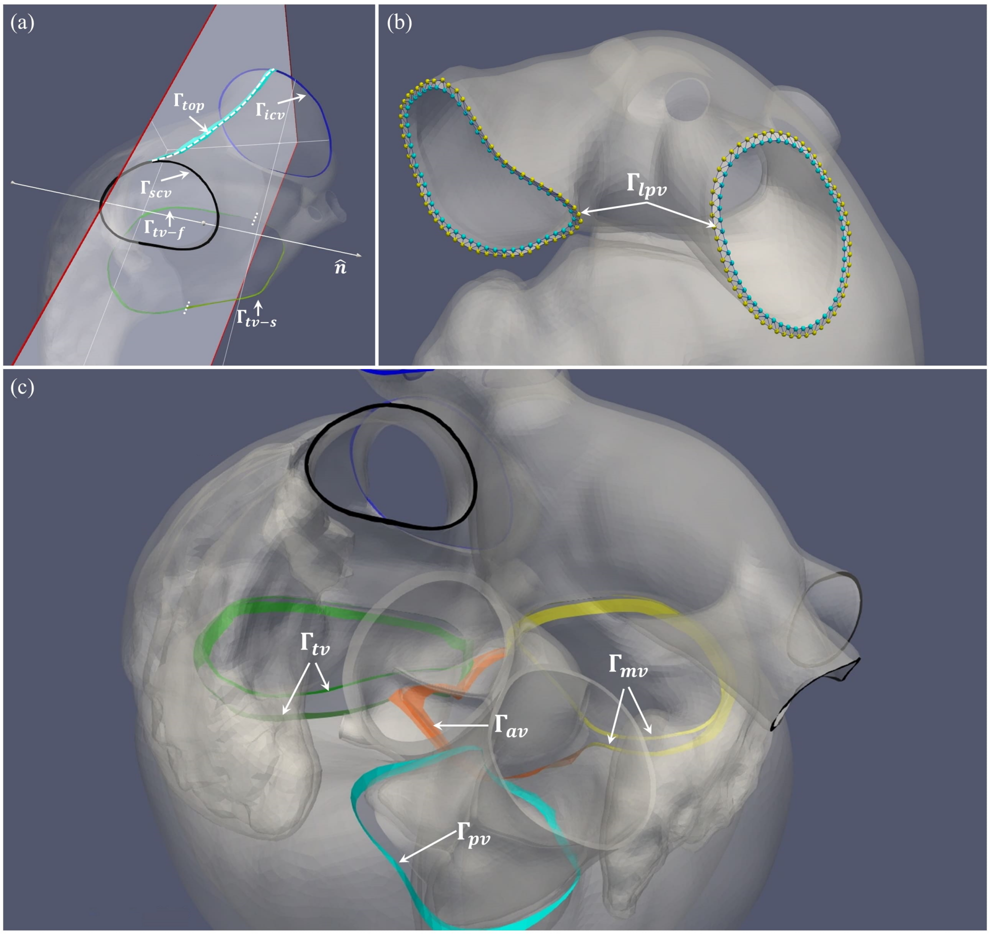

Figure 2.12: Labelling procedure performed to impose the boundary conditions for the ventricular and atrial LDRBMs (presented in Sections 2.1 and 2.2). (a) Labelling procedure for the top band $\Gamma_{top,r}$ and the tricuspid valve Γ_{tv} (such that $\Gamma_{tv} = \Gamma_{tv-s} \cup \Gamma_{tv-f}$) in RA: $\hat{n}$ is the normal of the plane passing trough $\Gamma_{top,r}$ while Γ_{scv} and Γ_{icv} are the rings of the caval veins; (b) labelling procedure for LPV rings Γ_{lpv} in LA: yellow and blue points lay on the epicardial and endocardial border zone, respectively; (c) result of the labelling procedure for the four valve rings (Γ_{mv} MV, Γ_{av} AV, Γ_{tv} TV and Γ_{pv} PV) in a complete biventricular geometry. For further details refer to [66].

Muscle type (ionic model)	σ_f[mS/cm]	σ_s[mS/cm]	σ_n[mS/cm]
Ventricles (TTP06)	1.07	0.49	0.16
Atria (CRN98)	7.00	0.77	0.77

Table 2.4: Conductivity values σ_f, σ_s and σ_n obtained after the fitting procedure, displayed in Figure 2.13, for the ventricles (using TTP06) and for the atria (using CRN98).

2.4.2 On the choice of physical parameters and numerical settings

The numerical approximation of the monodomain system (2.8) requires the following physical data: the transmembrane capacitance per unit area C_m, the membrane surface-to-volume ratio χ_m and the conductivities along the three direction of the myofibers σ_f, σ_s and σ_n appearing in the conductivity tensor $\mathbf{D}$. The values chosen for the first two quantities are $C_m = 1\ \mu\text{F/cm}^2$ and $\chi_m = 1400\ \text{cm}^{-1}$, which are within the physiological acceptable range of values reported in [183, 187, 205, 150].

The conductivity values σ_f, σ_s and σ_n were fitted by an iterative procedure described in [45] (see also [64, 20]) in order to match the following conduction velocity values [20, 64, 17, 55]:

$$\begin{aligned} \text{ventricles} : v_f &= 60\ \text{cm/s} \qquad v_s = 40\ \text{cm/s} \qquad v_n = 20\ \text{cm/s},\\ \text{atria} : v_f &= 120\ \text{cm/s} \qquad v_s = 40\ \text{cm/s} \qquad v_n = 40\ \text{cm/s}, \end{aligned}$$

where v_f, v_s and v_n are the conduction velocities in the fiber $\boldsymbol{f}$, sheet $\boldsymbol{s}$ and normal $\boldsymbol{n}$ directions. In Figures 2.13(a) and 2.13(b) we show the results of this fitting procedure. The estimated values for σ_f, σ_s and σ_n are reported in Table 2.4. Finally, to initiate the signal propagation in the cardiac muscle, the monodomain system (2.8) requires to specify the external applied current $\mathcal{I}_{app}(\mathbf{x}, t)$. In this work $\mathcal{I}_{app}(\mathbf{x}, t)$ was modeled as a series of spherical impulses (with radius 2.5 mm and duration 3 ms) applied in spherical subsets of the domain and prescribed alongside the ventricular and atrial endocardia. Its amplitude is 50000 $\mu\text{A/cm}^3$, for both atrial and ventricular domains, in agreement with [150]. We used this value for all the simulations, while the stimuli locations will be specified for each case reported in Sections 2.5 and 2.6. Regarding the mesh element size h and the time step Δt, related to the space and time discretizations of the system (2.8), accuracy constraints are imposed when biophysical models (as CRN98 [47] and TTP06 [247]) are used: $h = 100$–$500\ \mu$m and $\Delta t = 1$–$50\ \mu$s [181, 254, 150]. These strong restrictions are motivated mainly by the fast upstroke of cellular depolarization which produces a step-like wavefront over a small spatial extent [135]. For the space discretization, we used continuous bilinear FE ($\mathbb{Q}_1$) on hexahedral meshes with an average mesh size of $h = 350\ \mu$m, an acceptable value at least for linear finite element approximation and for physiological cases [244, 188, 105, 109, 13]. Concerning the time discretization, we used BDF of order $\sigma = 3$ with a time step of $\Delta t = 50\ \mu$s. Although, the most common time discretization used in literature for the monodomain system (2.8) is BDF1 (commonly known as the backward Euler method), which requires a time step at most of 10 μs [254], BDF3 allows us to use a larger value of Δt to obtain the same accuracy of BDF1. To confirm this, in Figures 2.13(c) and 2.13(d) we report a comparison between BDF3 with $\Delta t = 50\ \mu$s and BDF1 $\Delta t = 10\ \mu$s on a benchmark problem proposed in [150].

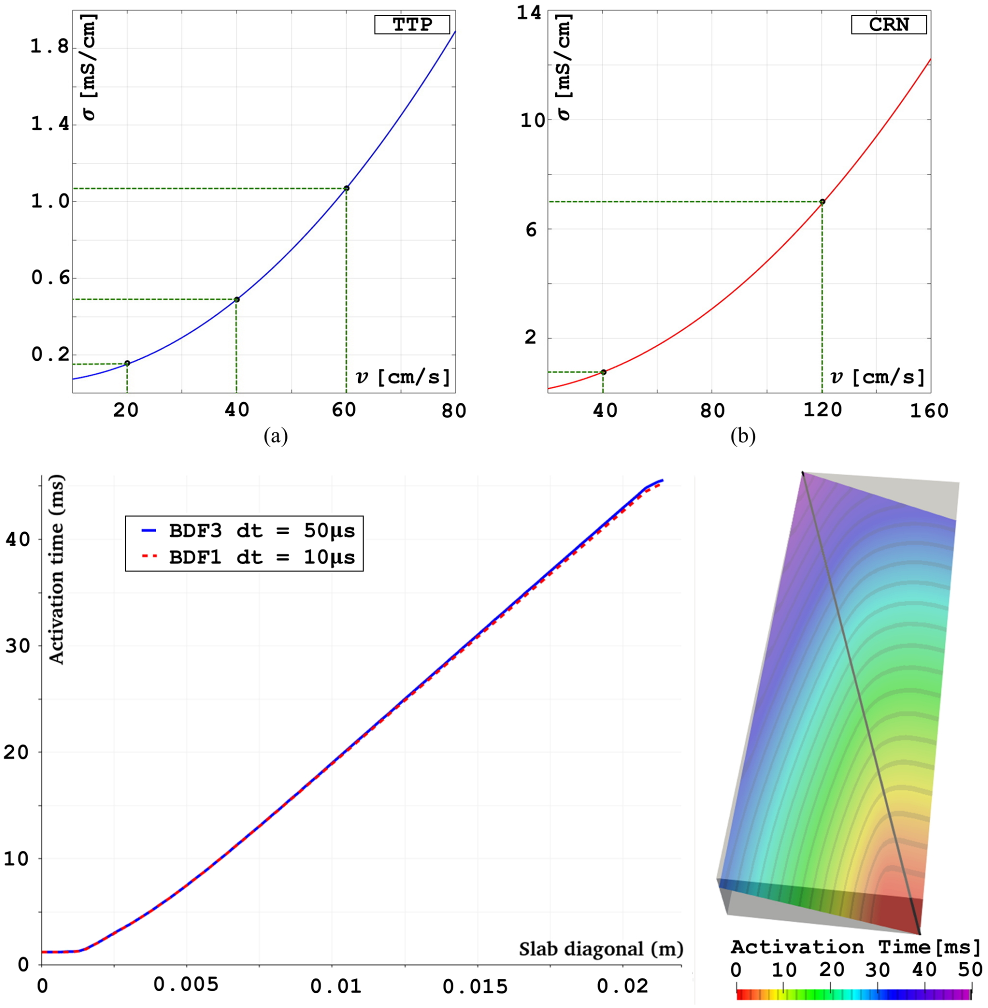

(a) (b)

(c) (d)

Figure 2.13: Top (a,b): Fitting procedure used to estimate the conductivity σ required to match specific conduction velocity v [45]; (a): using the TTP06 ionic model to obtain 60, 40 and 20 cm/s; (b): using the CRN98 ionic model to obtain 120 and 40 cm/s. The values for σ_f, σ_s and σ_n are reported in Table 2.4. Bottom (c,d): Comparison between BDF3 and BDF1 time discretization for the monodomain equation (2.8), endowed with the TTP06 ionic model, in the slab benchmark problem [150]; (c): plot of the activation time alongside the slab diagonal (displayed in black on the Right); Red: BDF1; Blue: BDF3. (d): activation time in a clipped slice of the slab for BDF3 time discretization.

2.5 Numerical results for cardiac fibers and electrophysiology in the ventricles

This section is dedicated to present numerical results related to both the fibers generation and EP simulations in the ventricles. These have been performed on either idealized and realistic human biventricular models: we built idealized geometry, adopting the prolate spheroid coordinate system [224, 192], while, as realistic geometry, we consider the 3D *Zygote* model [107], a complete heart geometry reconstructed from high-resolution CT-scans representing an average healthy heart.

We show various comparisons among the three LDRBMs for ventricular fiber generation, presented in Section 2.1. Specifically, we compare the fiber fields, generated by the three methods, and we investigate the influence of the different fibers orientation in terms of activation times, computed as output of numerical EP simulations. We first present the above analysis on the idealized biventricular geometry (Sections 2.5.1-2.5.2) and then on the Zygote biventricular model (Sections 2.5.3-2.5.4).

2.5.1 Idealized ventricular fibers

The first comparison among the three ventricular LDRBMs was performed on a well established idealized biventricular geometry that has been used in several computational studies [266, 224, 192, 84, 83, 4] and for ventricular volume estimation from 2D images [142]. The heart ventricles are approximated as two intersecting truncated ellipsoids.

We constructed the idealized biventricular geometry using the prolate spheroid coordinate systems in the built-in CAD engine of `gmsh`, an open source 3D finite element mesh generator (`http://gmsh.info`); see Figure 2.14. For details about the geometrical definition of the idealized biventricular model, we refer to [192, 4].

Fiber orientations obtained for the three LDRBMs (R-RBM, B-RBM and D-RBM) in the idealized biventricular model are shown in Figures 2.14(a-f). The input angles values $\alpha_{endo,\ell}$, $\alpha_{epi,\ell}$, $\alpha_{endo,r}$, $\alpha_{epi,r}$, $\beta_{endo,\ell}$, $\beta_{epi,\ell}$, $\beta_{endo,r}$ and $\beta_{epi,r}$ were chosen for all the three methods based on the observations of histological studies in the human heart [134, 86, 9, 99, 210, 136, 229] (see also [58]):

$$\begin{aligned} &\alpha_{epi,\ell} = -60^o, \quad \alpha_{endo,\ell} = +60^o, \quad \alpha_{epi,r} = -25^o, \quad \alpha_{endo,r} = +90^o; \\ &\beta_{epi,\ell} = +20^o, \quad \beta_{endo,\ell} = -20^o, \quad \beta_{epi,r} = +20^o, \quad \beta_{endo,r} = 0^o. \end{aligned} \tag{2.9}$$

We observe that all the LDRBMs represent the characteristic helical structure of LV and a compatible fiber orientations both in the right endocardium, not facing to the septum, and in the right epicardium, far enough from the inter-ventricular junctions. Most of the differences occur in the right ventricular endocardium facing the septum (see Figures 2.14(a-c)), in the inter-ventricular junctions between the two ventricles and in the right epicardial lower region (see Figures 2.14(d-f)).

We computed the difference $\text{diff}_{i,j}$ of the fiber field $\boldsymbol{f}$ among the three methods, defined as:

$$\text{diff}_{i,j}(\boldsymbol{x}) = 1 - |\boldsymbol{f}_i(\boldsymbol{x}) \cdot \boldsymbol{f}_j(\boldsymbol{x})| \qquad i,j = \mathrm{R}, \mathrm{B}, \mathrm{D} \quad (i \neq j), \tag{2.10}$$

where $\boldsymbol{f}_\mathrm{R}$, $\boldsymbol{f}_\mathrm{B}$ and $\boldsymbol{f}_\mathrm{D}$ are the vector fiber fields of R-RBM, B-RBM and D-RBM, respectively. If $\boldsymbol{f}_i$ and $\boldsymbol{f}_j$ are parallel, $\text{diff}_{i,j} = 0$, otherwise $\text{diff}_{i,j} = 1$ when orthogonal. The result of these comparisons is reported in Figures 2.14(g), 2.14(h) and 2.14(i). As expected, most of the discrepancies are found in the septum, in the inter-ventricular junctions and in the right epicardial lower region.

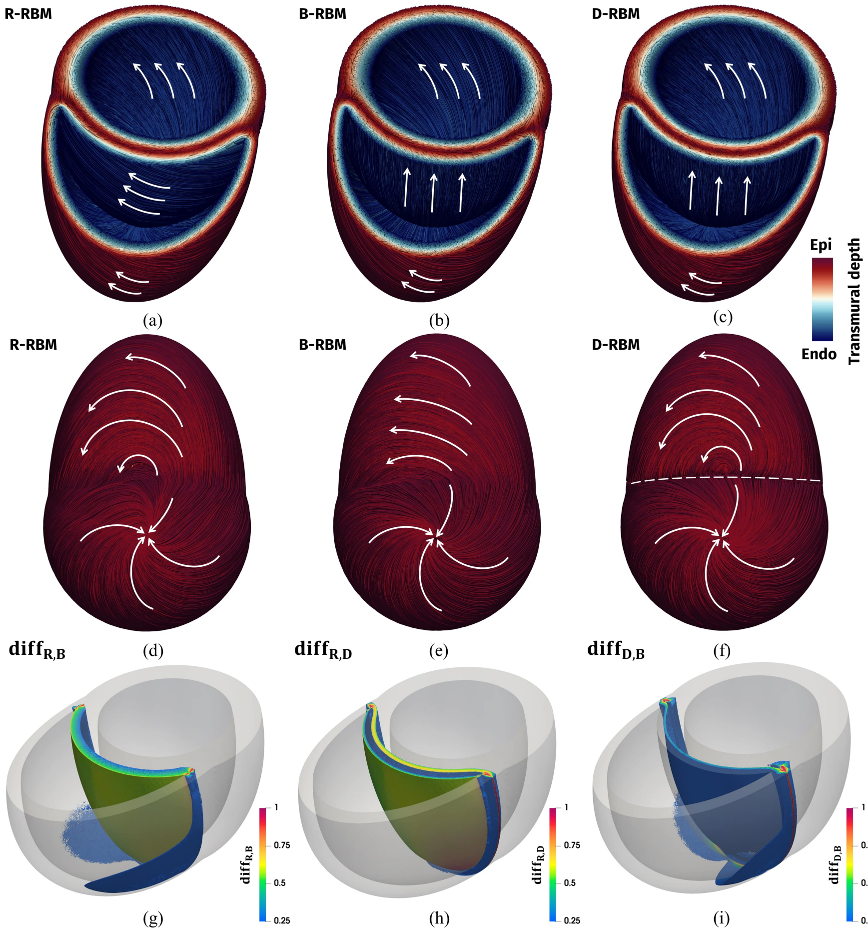

Figure 2.14: Comparison among LDRBMs in the idealized biventricular model. Streamlines of the vector $\boldsymbol{f}$ is depicted for R-RBM (a,d), B-RBM (b,e) and D-RBM (c,f). White arrows represent the main fibers direction in specific ventricular regions (displayed in red for the epicardium and in blue for the endocardium); the dashed line in Figure (f) highlights the inter-ventricular junctions discontinuity of D-RBM. Top: Frontal view; Centre: apex view; Bottom: Differences $\mathrm{diff}_{i,j}$ among the three LDRBMs, $\mathrm{diff}_{\mathrm{R,B}}$ (g), $\mathrm{diff}_{\mathrm{R,D}}$ (h) and $\mathrm{diff}_{\mathrm{D,B}}$ (i); only values $\mathrm{diff}_{i,j} \geq 0.25$ are displayed.

2.5.2 Electrophysiology in idealized ventricles

In order to evaluate the influence of the three LDRBMs fiber architectures in the electric signal propagation through the cardiac muscle, we performed three EP simulations (with the setting detailed in Section 2.4.2), one for each LDRBM. To initiate the action potential propagation we applied four endocardial stimuli: two for each ventricle, one in the mid-septal zone and one in the lateral endocardial wall. In Figures 2.15(a-c) we report the activation maps obtained with the three fibers configurations. The activation time of a given point in the cardiac muscle is computed as the time when the transmembrane potential derivative $\frac{du}{dt}$ reaches its maximal value. The activation

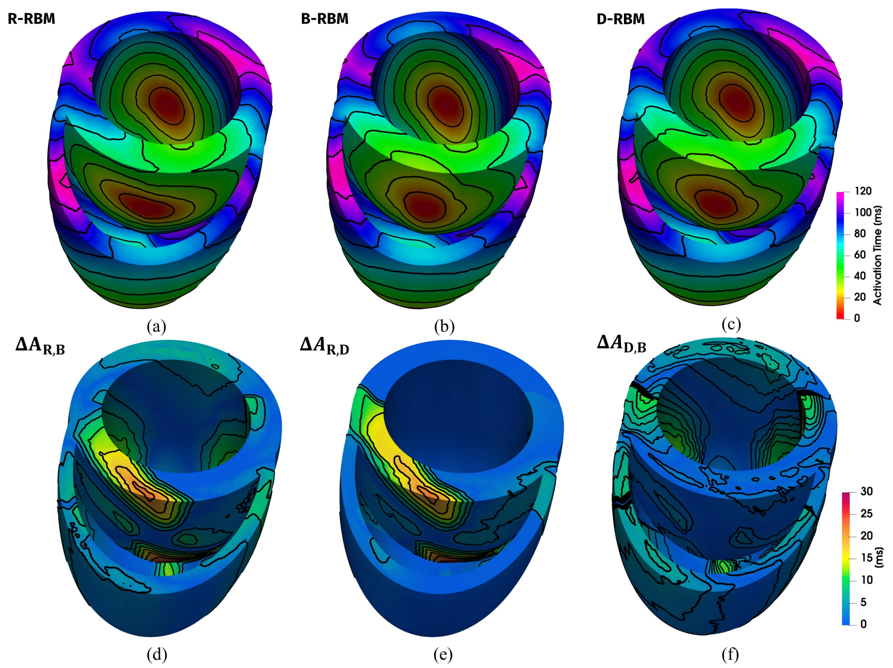

(a) (b) (c)

(d) (e) (f)

Figure 2.15: Top: Activation time for R-RBM (a), B-RBM (b) and D-RBM (c) in the idealized biventricular model. Bottom: Absolute difference among the activation maps, $\Delta A_{\mathrm{R,B}}$ (d), $\Delta A_{\mathrm{R,D}}$ (e) and $\Delta A_{\mathrm{D,B}}$ (f).

pattern for all the three methods are very similar in LV and RV, while most of the differences are visible in the septum, see Figures 2.15(a), 2.15(b) and 2.15(c). We computed also the absolute difference $\Delta A_{i,j}(\boldsymbol{x})$ in the activation pattern among the different methods as:

$$\Delta A_{i,j}(\boldsymbol{x}) = |A_i(\boldsymbol{x}) - A_j(\boldsymbol{x})| \qquad i, j = \mathrm{R}, \mathrm{B}, \mathrm{D} \quad (i \neq j), \tag{2.11}$$

where A_{R}, A_{B} and A_{D} are the activation times for R-RBM, B-RBM and D-RBM, respectively (see Figures 2.15(d), 2.15(e) and 2.15(f)).

The most remarkable differences in both $\Delta A_{\mathrm{R,B}}$ and $\Delta A_{\mathrm{R,D}}$ are exhibited in the septum, particularly in the part facing the right endocardium, while $\Delta A_{\mathrm{B,D}}$ does not exceeds 15 ms, see Figures 2.15(d), 2.15(e) and 2.15(f). Also in the activation maps, as expected, we retrieve differences in the septum zone caused by the different fiber orientations on that region made by the three methods, as seen in the fibers comparison, see Figure 2.14.

Finally, we evaluated the maximal discrepancies, $M_{i,j} = \max_{\boldsymbol{x} \in \Omega_{biv}} \Delta A_{i,j}(\boldsymbol{x})$, among the three methods, which are:

$$M_{\mathrm{R,B}} = 35\,\mathrm{ms}, \qquad M_{\mathrm{R,D}} = 33\,\mathrm{ms}, \qquad M_{\mathrm{B,D}} = 15\,\mathrm{ms}.$$

The location of both $M_{\mathrm{R,B}}$ and $M_{\mathrm{R,D}}$ is in the lower part of the right ventricular septum, while $M_{\mathrm{B,D}}$ is placed in the lower anterior region of LV, see Figures 2.15(d), 2.15(e) and 2.15(f). Considering a total activation time of about $A_{max} = 120$ ms for the all biventricular muscle, the maximum relative differences, $M_{i,j}^{\%} = M_{i,j}/A_{max}$, among the three ventricular LDRBMs are

$$M_{\mathrm{R,B}}^{\%} = 29\%, \qquad M_{\mathrm{R,D}}^{\%} = 28\%, \qquad M_{\mathrm{B,D}}^{\%} = 13\%.$$

The different orientations of the septal fibers produced a significant impact in terms of EP numerical results. A dissimilar activation pattern and timing were observed at the septum, especially in the right endocardial region, confirmed by the highest discrepancy between R-RBM and the other two methods reaching 28-29% of the total activation time (Figure 2.15). Conversely, D-RBM and B-RBM yield almost the same activation pattern, thanks to the extensions introduced in B-RBM (Figure 2.15). The above results confirmed the importance of including specific fiber orientations in RV with respect to those of LV.

2.5.3 Realistic ventricular fibers

The second comparison among the ventricular LDRBMs was performed on a realistic full biventricular geometry. For this purpose, we used the Zygote solid 3D heart model [107]. In order to obtain a smooth endocardium in both ventricles, we removed all the papillary muscles and the trabeculae carneae, using the CAD modeller `SolidWorks` (`https://www.solidworks.com`) in combination with the software `Meshmixer` (`http://www.meshmixer.com`); see Figure 2.16. Considering the characteristics of the electrical signal propagation, and the anatomical constituents of the valvular and sub-valvular apparatus, we expect our calculations should not be substantially influenced by the papillary muscles elimination. Furthermore, according to the motivations highlighted at the end of Section 2.1.2, we performed a comparison in the full biventricular model only between B-RBM and D-RBM.

Fiber orientation for B-RBM and D-RBM in the Zygote full biventricular model are displayed in Figures 2.16(a-b) and 2.16(d-e). We prescribed the same input angle values used for the ideal geometry, reported in Equation (2.9). Moreover, for D-RBM we also specified the angles in the OT regions as follows [58]:

$$\alpha_{epi,OT} = 0^o, \quad \alpha_{endo,OT} = +90^o, \quad \beta_{epi,OT} = 0^o, \quad \beta_{endo,OT} = 0^o. \tag{2.12}$$

The two LDRBMs well reproduce the helical structure of LV up to MV ring and exhibit a similar fiber orientation pattern in whole cardiac muscle, apart from the region among TV, PV and AV rings and far enough from the inter-ventricular junctions, see Figures 2.16(a-b) and 2.16(d-e). B-RBM presents a roll up in the fiber directions just after the AV ring, while D-RBM has a more longitudinal fiber orientations in that region, see Figure 2.16(a) and 2.16(d). As also observed in the idealized case, the B-RBM fiber field in the inter-ventricular junctions has a smooth change passing from LV to RV, whereas D-RBM produces a strong discontinuity in the transition across the two ventricles, see Figure 2.16(b) and 2.16(e).

We evaluated the mismatch of the fiber fields $\text{diff}_{\text{D,B}}$, defined in (2.10), between B-RBM and D-RBM. Indeed, $\text{diff}_{\text{D,B}}$ highlights the most relevant differences of the two methods in the septum, in the inter-ventricular junctions, in the regions of TV, PV and AV rings and around the right ventricular apex, see Figures 2.16(g) and 2.16(h).

2.5.4 Electrophysiology in realistic ventricles

We performed two EP simulations (with the setting detailed in Section 2.4.2), one with B-RBM and one with D-RBM. Two stimuli were here applied to each ventricle: one in the mid-septal zone and one in the lateral endocardial wall. Figures 2.16(c) and 2.16(f) depict the computed activation times, which result very similar in the whole myocardium. Figure 2.16(i) shows the absolute difference between the two activation maps, $\Delta A_{\text{D,B}}(\boldsymbol{x}) = |A_{\text{D}}(\boldsymbol{x}) - A_{\text{B}}(\boldsymbol{x})|$, where A_{B} and A_{D} are the activation

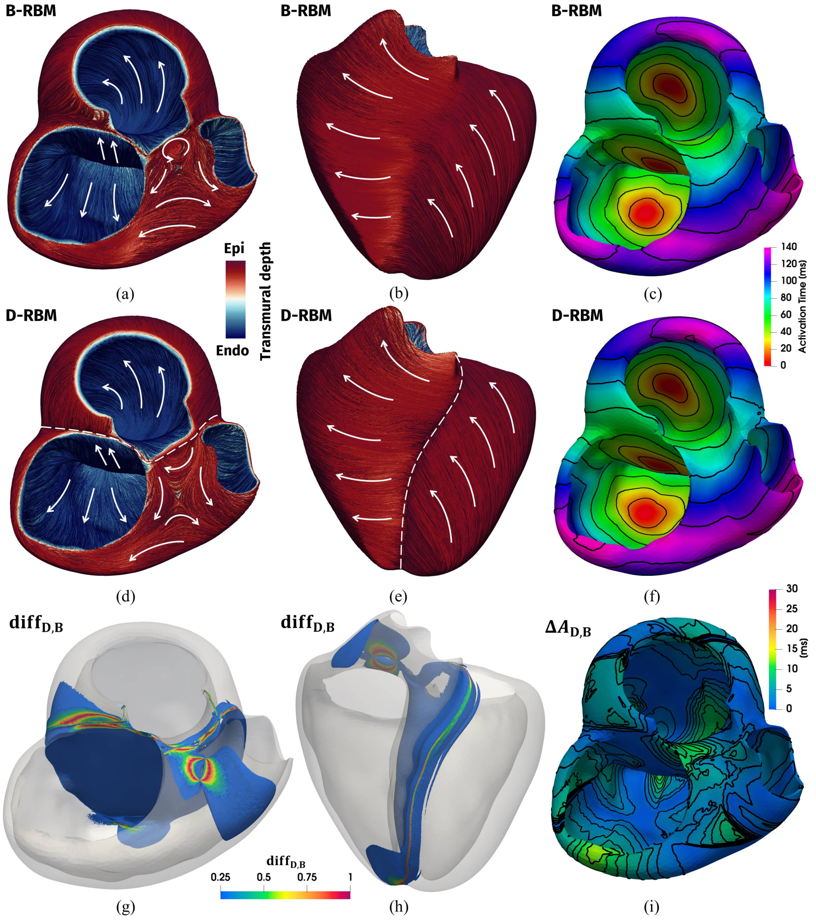

Figure 2.16: Comparison for B-RBM and D-RBM in a realistic full biventricular model. Top (a-c): B-RBM. Centre (d-f): D-RBM. Bottom (g-i): differences between B-RBM and D-RBM. Streamlines of the vector $\boldsymbol{f}$: top (a,d) and lateral views (b,e). White arrows represent the main fibers direction in specific ventricular regions (displayed in red for the epicardium and in blue for the endocardium); dashed line in Figures (d,e) highlights the inter-ventricular junctions discontinuity of D-RBM. Difference in the fiber orientations $\mathrm{diff}_{\mathrm{D,B}}$ (g,h), only the values $\mathrm{diff}_{i,j} \geq 0.25$ are displayed. Activation maps using B-RBM and D-RBM: B-RBM (c) and D-RBM (f). Absolute difference among B-RBM and D-RBM activation maps, $\Delta A_{\mathrm{D,B}}$ (i).

times for B-RBM and D-RBM, respectively. We observe some discrepancies in the activation pattern near TV, PV and AV rings, and also in the endocardium near the right ventricular apex, although $\Delta A_{\mathrm{D,B}}$ does not exceeds the value 14 ms, see Figure 2.16(i). The maximal relative discrepancy among the two methods is $M_{\mathrm{D,B}} = \max_{\boldsymbol{x}\in\Omega_{biv}} \Delta A_{\mathrm{D,B}}(\boldsymbol{x}) = 14$ ms, corresponding to

$$M^{\%}_{\mathrm{D,B}} = M_{\mathrm{D,B}}/A_{max} = 10\,\%,$$

with $A_{max} = 140$ ms the total activation time. The location of $M_{\mathrm{D,B}}$ is in the lower part of the endocardium just above the right ventricular apex, see Figure 2.16(i).

2.6 Numerical results for cardiac fibers and electrophysiology in the atria

This section is dedicated to present numerical results related to both the fibers generation and EP simulations in the atria. These have been performed on either idealized and realistic human atrial models. We construct idealized LA and RA geometries, starting form LA and RA NURBS surface representations presented in [171, 168]. As realistic geometries, we use the Zygote 3D heart [107] and the atrial model presented in [242, 67], in what follows referred to as *Riunet geometry* [3] (from the name of the data repository, which includes the geometry and the fiber orientations obtained by a RBM proposed in [67]). In particular, the 3D Zygote heart geometry, being a very detailed model of the human heart, demonstrates the applicability of the atrial LDRBM to arbitrary patient-specific scenarios.

We present the fiber generation results of the new atrial LDRBM (presented in Section 2.2) to reconstruct LA, RA and biatrial fiber architectures. We show LA and RA fiber bundles reconstruction applied to an idealized case (Section 2.6.1) and to realistic geometries (Section 2.6.2). Then, we illustrate the results of the new LDRBM applied to realistic biatrial models (Section 2.6.3). Finally, we investigate the influence of atrial fibers in EP simulations: we compare the fiber activation map with respect to a one obtained with an isotropic electrical propagation and then we studied how a change in size of a single bundle affects the total activation sequence (Section 2.6.4).

2.6.1 Idealized atrial fibers

We began applying the novel atrial LDRBM on idealized geometries. To construct them, we started by taking the surface representations of RA and LA, adopted in [171, 168], generated as separated NURBS patches. For each atrium, we created the corresponding triangular mesh using the constructive geometry module of `Netgen` (`https://ngsolve.org`). We considered this triangular mesh as the endocardium of our 3D model. To generate the atrial epicardium we extruded (using the `vmtk` software [11]) the endocardial surface by 2 mm, which correspond to an average thickness of the atrial wall [101, 27]. Finally, we produced 3D labelled hexahedral mesh following the preprocessing procedure described in Section 2.4.1, and then we applied our RA and LA LDRBM for single atrial chamber, see Figures 2.17(a-d) and 2.18(a). The input values of the parameters τ_i, which define the bundles dimension of the atrial LDRBM, are reported in Tables 2.5 and 2.6 for RA and LA, respectively. Moreover, $N_{raa} = N_{raw} = 0$ implying that we do not prescribe any PM in RA endocardium, see Figure 2.18(a).

2.6.2 Realistic atrial fibers

Afterwards, we treat the case of realistic RA and LA taken from the Zygote 3D heart model [107] and from the Riunet repository (`https://riunet.upv.es/handle/10251/55150`). In particular, concerning the Riunet geometry, we extracted both the endocardium and the epicardium (using `ParaView`), we removed all the interatrial connections (using `vmtk`) and then we created the corresponding 3D labelled hexahedral mesh (using the procedure described in Section 2.4.1). Fibers generated by our atrial LDRBM are shown in Figures 2.17(e-h) and 2.18(b) for the Zygote geometry and Figures 2.17(i-n) and 2.18(c) for the Riunet model.

---

[3] Freely available online at `https://riunet.upv.es/handle/10251/55150`.

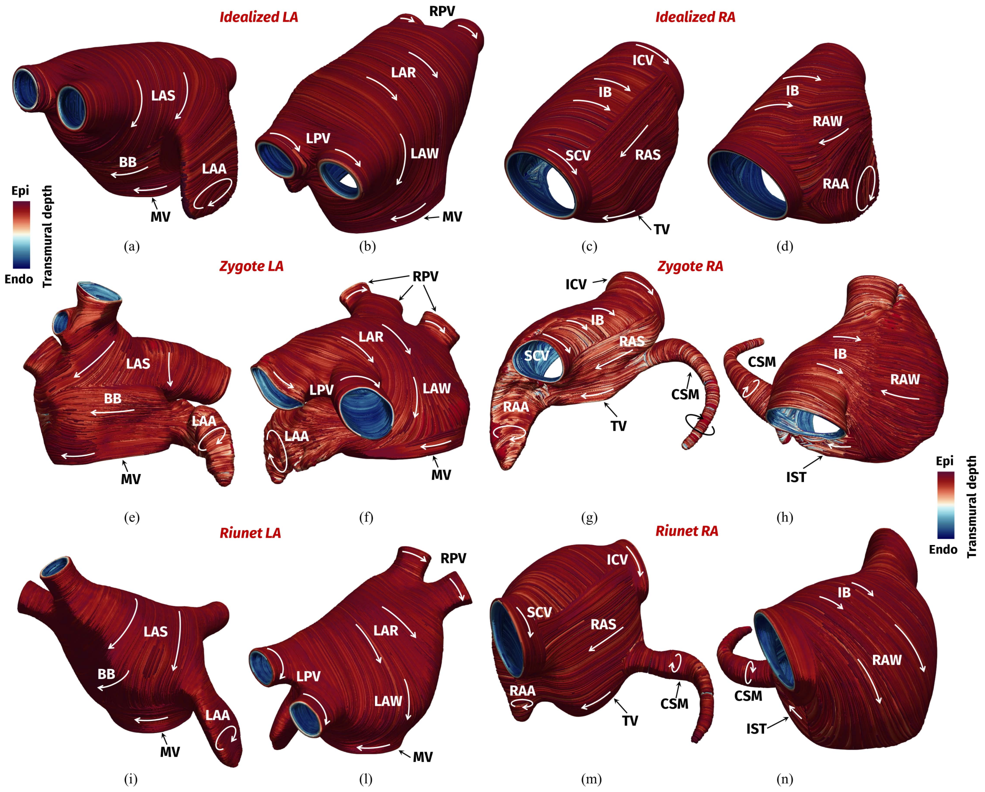

Figure 2.17: Atrial LDRBM fiber generation applied to idealized (a-d) and realistic (e-n) models (Zygote (e-h) and Riunet (i-n) geometries) of RA and LA. Frontal (a,c,e,g,i,m) and dorsal (b,d,f,h,l,n) views of the atria. SCV, ICV: superior and inferior caval veins; LPV, RPV: left and right pulmonary veins; TV, MV: tricuspid and mitral valve rings; RAA, LAA: right and left appendage; RAS, LAS: right and left septum; RAW, LAW: right and left atrial lateral wall; LAR: left atrial roof; IB: inter-caval bundle; IST: isthmus; BB: Bachmann's Bundle; CSM: Coronary Sinus Musculature.

RA	τ_{tv}	τ_{icv}	τ_{scv}	τ_{raa}	τ_{csm}	$\tau_{sw,r}$	τ_{raw}	τ_{ct_-}	τ_{ct_+}	τ_{ib}	τ_{ras}
Ideal	0.90	0.90	0.10	1.00	0.10	-0.15	0.50 (30^o-30^o)	-0.13	-0.10	0.12 (20^o-30^o)	0.20
Zygote	0.90	0.90	0.215	0.55	0.10	-0.15	0.75 (0^o-30^o)	-0.27	-0.22	0.44 (20^o-20^o)	0.28
Riunet	0.90	0.88	0.15	0.52	0.10	0.01	0.50 (0^o-30^o)	-0.095	-0.075	0.40 (20^o-20^o)	0.05

Table 2.5: Bundle parameters used for fibers generation in the idealized (Ideal) and realistic (Zygote and Riunet) RA. We use the convention $\tau_i(\alpha_{endo}$-$\alpha_{epi})$ to set a linear transmural angle variation for α inside the i-th bundle, while τ_i alone to imply $\alpha_{endo} = \alpha_{epi} = 0^o$.

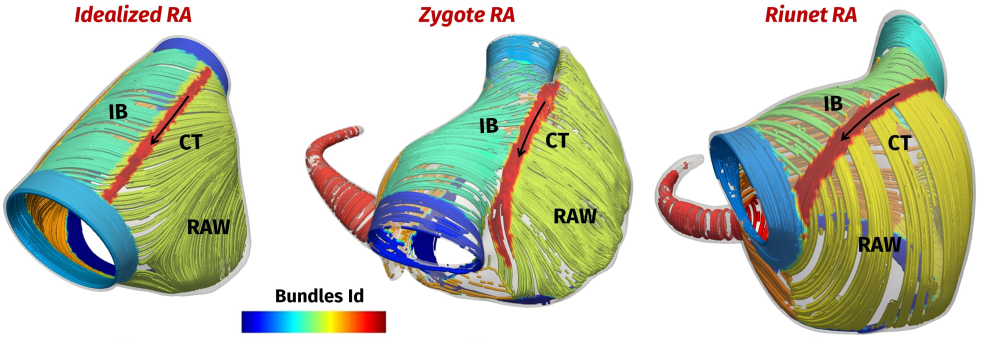

(a) (b) (c)

Figure 2.18: Endocardial RA fiber architecture in the atrial LDRBM for idealized (a) and realistic (b-c) models: Zygote (b) and Riunet (c). Dorsal view of the endocardial fibers in RA coloured by means of the bundles selection procedure (see step 3 in Section 2.2). RAW: right atrial lateral wall; IB: inter-caval bundle; CT: crista terminalis.

LA	τ_{mv}	τ_{rpv}	τ_{lpv}	$\tau_{sw,l}$	$\tau_{laa,in}$	$\tau_{laa,up}$	τ_{bb}	τ_{law}
Ideal	0.75	0.14	0.85	0.08	0.7	0.35	0.45	0.16
Zygote	0.90	0.15	0.835	0.04	0.45	0.60	0.45	0.65
Riunet	0.90	0.20	0.80	0.03	0.50	0.55	0.75	0.24

Table 2.6: Bundle parameters used for fibers generation in the idealized (Ideal) and realistic (Zygote and Riunet) LA and RA.

The input values of the parameters τ_i, which define the bundles dimension of the atrial LDRBM, are reported in Tables 2.5 and 2.6 for RA and LA, respectively. Moreover, $N_{raa} = N_{raw} = 0$ implying that we do not prescribe the any PM in RA endocardium, see Figure 2.18(b-c). We observe that the atrial LDRBM qualitatively capture the complex arrangement of fiber directions in almost all the principal anatomical atrial regions (see Figure 2.17):

RA: SCV, ICV, TV, RAA, RAS, IB, CT, isthmus (IST), CSM and RAW;

LA: LPV, RPV, MV, LAA, LAS, BB, LAW and LAR.

Following the atrial LDRBM rules defined at the end of Section 2.2, circular fiber arrangements are exhibited around LPV, RPV, SCV, ICV, TV, MV, and encircle CSM and both appendages (RAA and LAA), see Figures 2.17(a-d) and 2.17(e-g). Fibers direction of CT runs longitudinally on the endocardial surface from the base of the SCV to the ICV, see Figures 2.17(d) and 2.17(h). RA structures like the IB and RAW are vertically oriented, whereas those of RAS are almost parallel to the CT, see Figures 2.17(c-d) and 2.17(g-h). IST fibers have the same direction of those of the TV, see Figures 2.17(d) and 2.17(h). LAS fibers present a smooth transition going to LAA and the adjacent region of RAS (Figures 2.17(a,b) and 2.17(e,f)), while BB fibers run longitudinally in the same direction of those of MV (Figures 2.17(a,e,i)). Directions of LAR and LAW fibers descend perpendicularly to MV (Figures 2.17(b) and 2.17(f)).

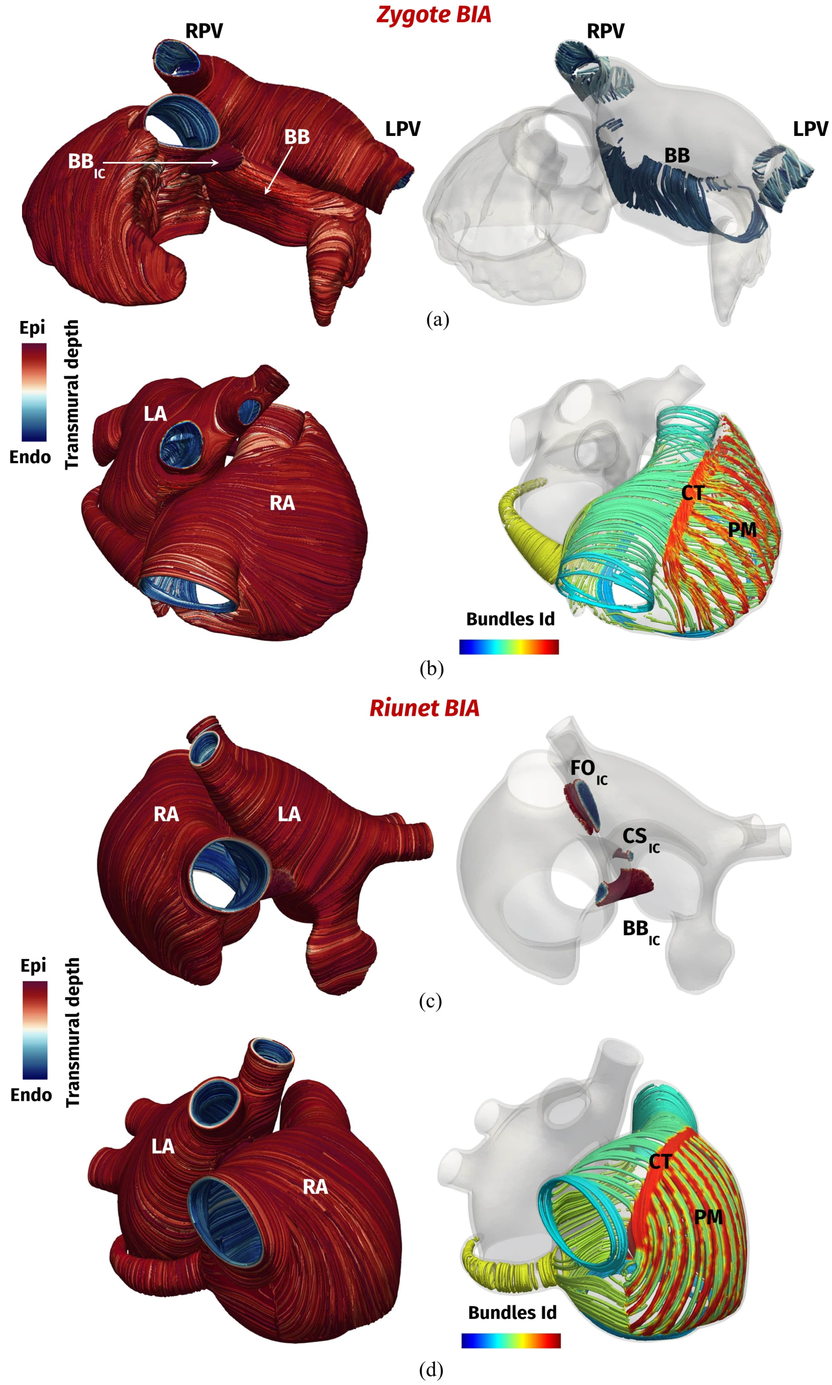

(a)

(b)

(c)

(d)

Figure 2.19: Atrial LDRBM fiber generation applied to realistic biatrial geometries: Zygote (a-b) and Riunet (c-d). (a) Transmural fibers architecture for BB, LPV and RPV in the Zygote geometry; BB$_{\text{IC}}$ connects RA to LA. (c) All the inter-atrial connections BB$_{\text{IC}}$, FO$_{\text{IC}}$, CS$_{\text{IC}}$ are displayed for the Riunet biatrial model. (b-d) Endocardial RA fiber architecture for the biatrial geometry of Zygote (b) and Riunet (c), revealing the presence of CT and PM.

BIA-IC	τ_{BBicr}	τ_{BBicl}	τ_{BBic}	τ_{FOicr}	τ_{FOicl}	τ_{FOic}	τ_{CSicr}	τ_{CSicl}	τ_{CSic}
Zygote	-0.99	0.99	0.45	-0.93	0.87	1.15	-0.80	0.60	0.60
Riunet	-0.97	0.98	0.45	-0.93	0.93	1.2	-0.92	0.92	0.20

Table 2.7: Bundle parameters used for IC fibers generation in realistic biatrial geometry (Zygote and Riunet).

BIA-RA	τ_{tv}	τ_{icv}	τ_{scv}	τ_{raa}	τ_{csm}	$\tau_{sw,r}$	τ_{raw}	τ_{ct_-}	τ_{ct_+}	τ_{ib}	τ_{ras}
Zygote	0.90	0.90	0.215	0.55(30^o-30^o)	0.10	-0.15	0.75 (30^o-30^o)	-0.27	-0.22	0.44 (20^o-20^o)	0.28
Riunet	0.90	0.90	0.18	0.52(30^o-30^o)	0.10	0.01	0.50 (30^o-30^o)	-0.095	-0.075	0.40 (20^o-20^o)	0.06

Table 2.8: Bundle parameters used for RA fibers generation in realistic biatrial geometry (Zygote and Riunet). We use the convention $\tau_i(\alpha_{endo}$-$\alpha_{epi})$ to set a linear transmural angle variation for α inside the i-th bundle, while τ_i alone to imply $\alpha_{endo} = \alpha_{epi} = 0^o$.

BIA-PM	N_{raw}	N_{raa}	pm_{thick}	pm_{range}	pm_{end}
Zygote	12	6	0.02	0.02	0.66
Riunet	13	3	0.025	0.025	0.88

Table 2.9: Bundle parameters used for PM fibers generation in realistic biatrial geometry (Zygote and Riunet).

BIA-LA	τ_{mv}	τ_{rpv}	τ_{lpv}	$\tau_{sw,l}$	$\tau_{laa,in}$	$\tau_{laa,up}$	τ_{bb}	τ_{law}
Zygote	0.90	0.15 (90^o-0^o)	0.835 (90^o-0^o)	0.04	0.43	0.60	0.45	0.65 (20^o-0^o)
Riunet	0.90	0.20	0.80	0.03	0.50	0.55	0.75	0.24

Table 2.10: Bundle parameters used for LA fibers generation in realistic biatrial geometry (Zygote and Riunet). We use the convention $\tau_i(\alpha_{endo}$-$\alpha_{epi})$ to set a linear transmural angle variation for α inside the i-th bundle, while τ_i alone to imply $\alpha_{endo} = \alpha_{epi} = 0^o$.

2.6.3 Biatrial fibers

Finally, we apply the atrial LDRBM to realistic biatrial models. With this aim the entire Riunet model, which includes IC, is considered. Meanwhile, in order to create a biatrial Zygote geometry, we physically connect RA to LA embedding IC coming from the Riunet model (using `vmtk`). Following the Algorithms 1-4 of LDRBM presented in Section 2.2, biatrial fiber architectures are generated for the Zygote geometry (see Figures 2.19(a-b)) and for the Riunet model (see Figures 2.17(c-d)).

The input values of the parameters τ_i, which define the bundle dimensions of the biatrial LDRBM, are reported in Tables 2.7, 2.8, 2.9 and 2.10 for IC, RA, PM and LA, respectively. Moreover, for the Zygote model we define a further transmural variation in BB (see Figure 2.19(a)) by defining the unique normal direction $\boldsymbol{k}$ as (see also point 1 in step 4 of Section 2.2)

$$\boldsymbol{k} = (1 - |\phi|)\nabla\psi_r + |\phi|\nabla\psi_{ab}.$$

We observe that the biatrial LDRBM captures the arrangement of fiber directions in all the principal anatomical atrial regions of RA, with the inclusion of PM (see Figures 2.19(b-d)), of LA, with the prescription of different transmural variations (e.g. in BB, LPV and RPV), see Figure 2.19(a). Moreover, it physically includes the principal IC connecting RA to LA: BB_{IC}, FO_{IC}, see Figure 2.19(c).

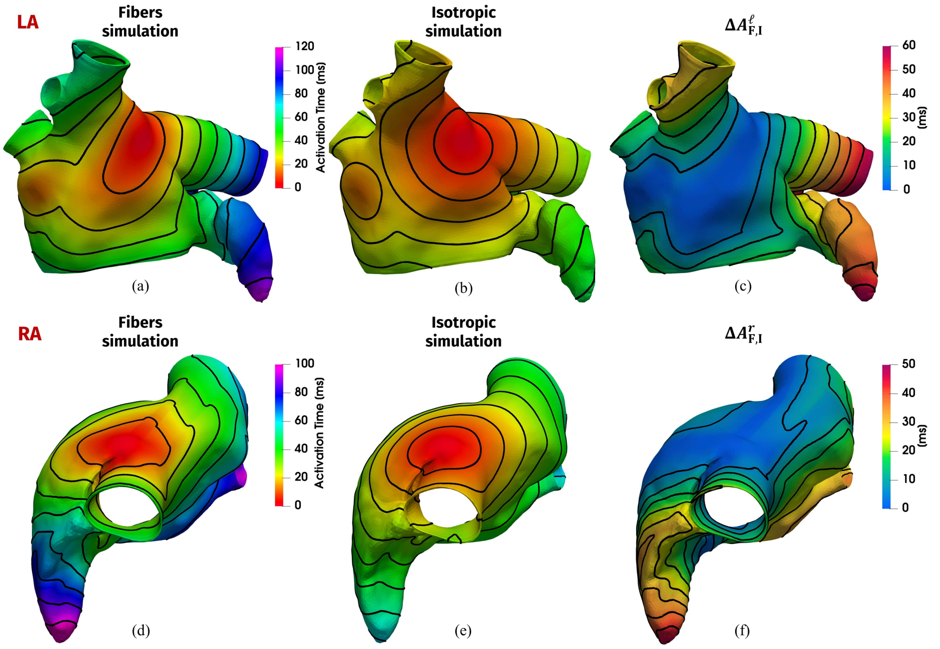

Figure 2.20: Comparison between the activation maps of EP simulations performed with the atrial LDRBM fiber generation and the isotropic model on the Zygote geometries. Left (a,d): Fibers simulation; Centre (b,e): Isotropic simulation. Right (c,f): absolute difference $\Delta A^{i}_{\mathrm{F,I}}$ in the activation times for LA ($i = \ell$) and RA ($i = r$). Top (a,b,c): LA; Bottom (d,e,f): RA.

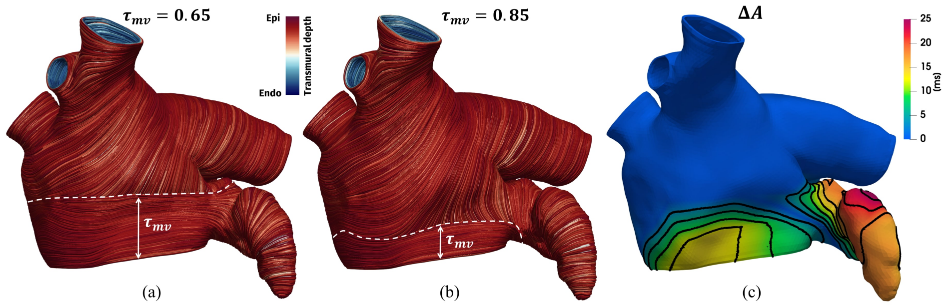

Figure 2.21: Comparison between EP simulations with different values of τ_{mv} in the atrial LDRBM fiber generation for the Zygote LA. Dashed lines in white represent the limit of the MV bundle. Left (a): $\tau_{mv} = 0.65$; Centre (b): $\tau_{mv} = 0.85$; Right (c): absolute difference ΔA in the activation times.

2.6.4 Atrial electrophysiology

In order to analyse the influence of atrial fiber bundles in the electric signal propagation we performed several EP simulations (with the setting specified in Section 2.4.2) on the realistic Zygote LA and RA geometries.

Firstly, we made a comparison with an isotropic model. For the atrial LDRBM fiber parameters, we considered those reported in Tables 2.5 and 2.6. The fiber EP simulations were carried out using the conductivity values of Table 2.4, while the isotropic EP simulations by setting in (2.7) $\sigma_f = \sigma_s = \sigma_n = 7.0$ mS/cm, that is a representative value chosen for the conductivity along the atrial fiber direction (see Table 2.4). To initiate the signal propagation in RA we applied a single stimulus in SAN which lies in the musculature of CT at the anterolateral junction with the SCV [100]. For LA we stimulated at the location of the main IC to surrogate the electric signal coming from RA: in the centre of BB (representing the $\mathrm{BB_{IC}}$); in the centre of LAS (standing for $\mathrm{FO_{IC}}$); in the limbs of CSM at the bottom of LAW (surrogating the $\mathrm{CS_{IC}}$) [208]. Activation of $\mathrm{FO_{IC}}$ and $\mathrm{CS_{IC}}$ were delayed, with respect to the $\mathrm{BB_{IC}}$ stimulus, by 14 ms and 52 ms, respectively.

Figure 2.20 displays the results of the comparison among simulations performed with the atrial LDRBM fibers and the isotropic model for both RA and LA. Both the activation pattern and activation time present significant differences. To provide a quantification, we computed the absolute difference $\Delta A^i_{\mathrm{F,I}}$ in the activation time:

$$\Delta A^i_{\mathrm{F,I}}(\boldsymbol{x}) = |A^i_{\mathrm{F}}(\boldsymbol{x}) - A^i_{\mathrm{I}}(\boldsymbol{x})| \qquad i = r, \ell, \tag{2.13}$$

where $i = r, \ell$ refer to LA ($i = \ell$) and RA ($i = r$) and A^i_{F} and A^i_{I} are the activation times obtained by the simulations with and without fibers, respectively. Most of the differences occur at LPV and LAA for LA, and at RAA and TV for RA. Finally, we computed the maximal discrepancy, $M^i_{F,I} = \max_{\boldsymbol{x}\in\Omega_{bia}} \Delta A^i_{F,I}(\boldsymbol{x})$, $i = \ell, r$:

$$M^{\ell}_{F,I} = 60\,\mathrm{ms}\,(52\,\%), \qquad M^{r}_{F,I} = 48\,\mathrm{ms}\,(44\,\%),$$

where in brackets we reported the relative values computed as $M^i_{F,I}/A^i_{max}$, with $A^{\ell}_{max} = 116$ ms and $A^{r}_{max} = 108$ ms the total activation times. For RA $M^r_{F,I}$ is placed in RAA, while for LA $M^{\ell}_{F,I}$ is located in LPV.

Then, we investigated how a local change in a single LA bundle (the MV one) affects the total activation pattern. We performed two EP simulations with the same fiber setting used for the comparison with an isotropic model, except for the value of τ_{mv}, which was set equal to 0.65 and 0.85, and excluding the presence of BB bundle. Figures 2.21(a-b) depict the corresponding generated fibers: notice that with $\tau_{mv} = 0.65$ the MV bundle is thicker with respect to the one obtained with $\tau_{mv} = 0.85$, see Figures 2.21(a-b). We also reported the absolute difference in the computed activation times for the two fiber architectures, see Figure 2.21(c). The maximal discrepancy, located in LAA, is of 28 ms which corresponds to 24% of the total activation time for LA (116 ms).

The atrial EP simulations revealed a strong influence of the complex atrial fiber architecture on the electric signal propagation. The activation pattern and timing, induced by the atrial LDRBM fibers, were consistently different from the isotropic model (Figure 2.20) in accordance with the previous findings [120, 64]. Furthermore, EP simulations, embedded with the atrial LDRBM fibers, provided a total activation time of 108 ms for RA and 116 ms for LA (Figure 2.20). These values are compatible with the timings predicted in [44] for RA (102 ms) and in [120] for LA (115 ms).

2.7 Towards the validation of atrial fibers

In order to verify the reliability of the atrial LDRBM, we compare the results of the novel atrial LDRBM with anatomical pictures [100, 51, 97, 212] (Section 2.7.1), with

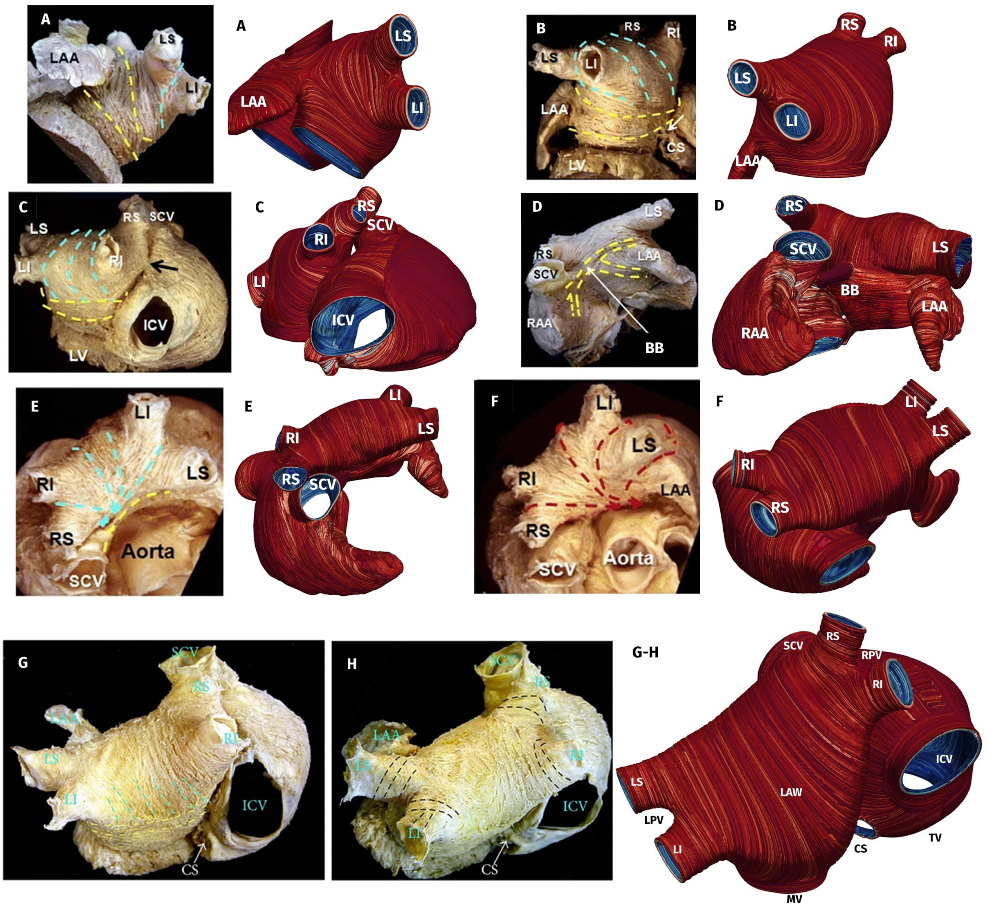

Figure 2.22: Comparison between anatomical atrial dissections in a normal human atria and fibers obtained by the atrial LDRBM in the Riunet and Zygote geometries. Fiber orientations, displayed with dashed lines in anatomical pictures, are compared with fiber generated by the atrial LDRBM rules (R1-R7). ICV, SCV: inferior and superior caval veins; CT: crista terminalis; CS: coronary sinus; LV: left ventricle; TV, MV: tricuspid and mitral valve rings; LPV: left pulmonary superior (LS) and inferior (LI) veins; RPV: right pulmonary superior (RS) and inferior (RI) veins; BB: Bachmann's Bundle. Anatomical pictures are readapted from [100, 51, 97, 212].

the fiber orientations obtained by another RBM [67] (Section 2.7.2) and with DT-MRI fiber data [167] (Section 2.7.3).

2.7.1 Comparison with anatomical data

We provide a graphical comparison of the results obtained in the Riunet and Zygote geometries, by means of the LDRBM, with anatomical pictures of atrial dissections in a normal human heart taken from [100, 51, 97, 212], see Figure 2.22. The fiber directions predicted by the atrial LDRBM rules showed an excellent agreement with the anatomical studies, sustaining the validity of rules R1-R7 (Section 2.2).

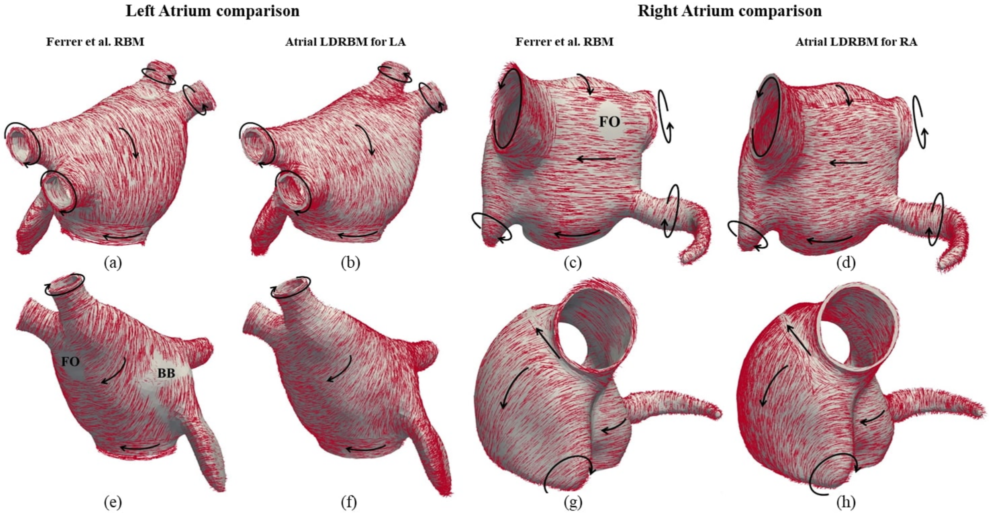

Figure 2.23: Fiber orientations (rendered in red glyphs) comparison in the Riunet geometry between the atrial LDRBM and RBM in [67] for RA and LA. First column (a,e): RBM in [67] for LA; Second column (b,f): atrial LDRBM for LA; Third column (c,g): RBM in [67] for RA; Fourth column (d,h): atrial LDRBM for RA; Black arrows represent the main fibers direction in specific atrial regions; FO: Fossa Ovalis; BB: Bachmann's Bundle.

BIA-RA	τ_{tv}	τ_{icv}	τ_{scv}	τ_{raa}	τ_{csm}	$\tau_{sw,r}$
JHU-geo	0.90	0.90 (90^o-0^o)	0.10 (90^o-0^o)	0.50	0.60 (90^o-90^o)	-0.30
BIA-RA	τ_{raw}	τ_{ct_-}	τ_{ct_+}	τ_{ib}	τ_{ras}	
JHU-geo	0.75 (0^o--20^o)	-0.22	-0.22	0.40	0.40 (90^o-90^o)	

Table 2.11: Bundle parameters used for RA fibers generation in the reconstructed real biatrial geometry. We use the convention $\tau_i(\alpha_{endo}$-$\alpha_{epi})$ to set a linear transmural angle variation for α inside the i-th bundle, while τ_i alone to imply $\alpha_{endo} = \alpha_{epi} = 0^o$.

2.7.2 Comparison with another Rule-Based Method

The results obtained by our novel fiber generation strategy in the Riunet geometry were compared with those previously reported in [67][4], prescribed by means of a RBM incorporating a detailed regional description of fiber directions provided by anatomical observations [242, 67]. Specifically, RBM in [67] was built by a manual subdivision of the atrial geometry in several regions to embed a detailed fibers description [67]. This model includes also IC bundles, i.e. the Bachmann's Bundle (BB), the limb of Fossa Ovalis (FO) and the connections of the Coronary Sinus Musculature (CSM). We removed IC from the Riunet model, in order to separately apply the atrial LDRBM for RA and LA. The fibers field generated by our LDRBM (Figure 2.23), owing to a suitable choice of the input parameters τ_i (Tables 2.5 and 2.6), is in excellent agreement with the finding of RBM previously proposed [67], reproducing almost the same fiber orientations among the different atrial bundles.

---

[4] Freely available online at `https://riunet.upv.es/handle/10251/55150`

BIA-LA	τ_{mv}	τ_{rpv}	τ_{lpv}	$\tau_{sw,l}$	$\tau_{laa,in}$	$\tau_{laa,up}$	τ_{bb}	τ_{law}
JHU-geo	0.85	0.15	0.85 (90^o-0^o)	0.05	0.60 (40^o-40^o)	0.80 (40^o-40^o)	0.40 (0^o-40^o)	0.50 (90^o-90^o)

Table 2.12: Bundle parameters used for LA fibers generation in the reconstructed real biatrial geometry. We use the convention $\tau_i(\alpha_{endo}$-$\alpha_{epi})$ to set a linear transmural angle variation for α inside the i-th bundle, while τ_i alone to imply $\alpha_{endo} = \alpha_{epi} = 0^o$.

2.7.3 Comparison with DT-MRI fiber data

We compare the fiber generation results of LDRBM with DT-MRI fiber data in a reconstructed real biatrial geometry [167]. Moreover, we investigate the differences in using LDRBM and DT-MRI fibers in EP simulations.

DT-MRI fiber data and the segmented tetrahedral biatrial mesh are from the study of Pashakhanloo et al. [167] (in which ex-vivo human biatrial anatomies were obtained from high resolution sub-millimeters DT-MRI) and were procured by the *Trayanova Lab* (`http://www.trayanovalab.org/`) of Johns Hopkins University (JHU). Starting from the volumetric segmented mesh we extracted (using `vmtk` [11, 66] and `Meshmixer`[5] software) LA and RA endocardia and the biatrial epicardium. Then, we produced 3D labelled hexahedral mesh following the procedure described in Section 2.4.1. Finally, we projected DT-MRI fiber data, embedded in the segmented tetrahedral biatrial mesh, into the hexahedral mesh by means of a linear projection interpolation (using `vmtk`).

For the atrial LDRBM, we considered the parameters detailed in Tables 2.11 and 2.12. In addition, we fix $N_{raa} = N_{raw} = 0$, and we prescribe further transmural angle variations in LAS, by setting a linear relationship for the angle α at endocardium ($\alpha_{endo} = 0^o$) and epicardium ($\alpha_{endo} = -40^o$), and in BB, by defining the unique normal direction $\boldsymbol{k}$ as a linear combination of ψ_r and ψ_{ab} (see also points 1-2 in step 4 of Section 2.2). Finally, since no IC were prescribed for this case, LA and RA fibers are computed using the function $\mathbf{compute_{LA}}$ and $\mathbf{compute_{RA}}$, for positive and negative values of ξ, respectively (see Algorithm 1, 2, 4 of Section 2.2).

Figure 2.24 displays the comparison between the fibers generated by LDRBM (see Figures 2.24(a,d)) and those coming from DT-MRI data (see Figures 2.24(b,e)). The two architectures reproduce globally the same fiber orientations among the different atrial bundles, with visible major differences only in a restricted zone of LAA, at the top of RAA, in the region embracing SCV (see Figures 2.24(a,b)) and in the inter-atrial septal junction (see Figure 2.24(d,e)).

To quantitative compare the atrial LDRBM and DT-MRI fibers, we compute the difference between the two architecture, defined as:

$$\mathrm{diff}(\boldsymbol{x}) = 1 - |\boldsymbol{f}_{\mathrm{DTMRI}}(\boldsymbol{x}) \cdot \boldsymbol{f}_{\mathrm{LDRBM}}(\boldsymbol{x})|, \tag{2.14}$$

where $\boldsymbol{f}_{\mathrm{DTMRI}}$, $\boldsymbol{f}_{\mathrm{LDRBM}}$ are the vector fiber fields associated to DT-MRI data and LDRBM, respectively. The two fiber architectures match quite well with most of the discrepancies arising only in LAA, RAA, SCV and inter-atrial septal junctions, with value diff > 0.3 (see Figure 2.24(c,f)).

In order to evaluate the influence of using LDRBM and DT-MRI fiber architectures in the electric signal propagation, we performed three different EP simulations: one with DT-MRI fiber data, another with LDRBM fibers and the last one with an isotropic model. We considered the conductivity parameters detailed

---

[5] `http://www.meshmixer.com`

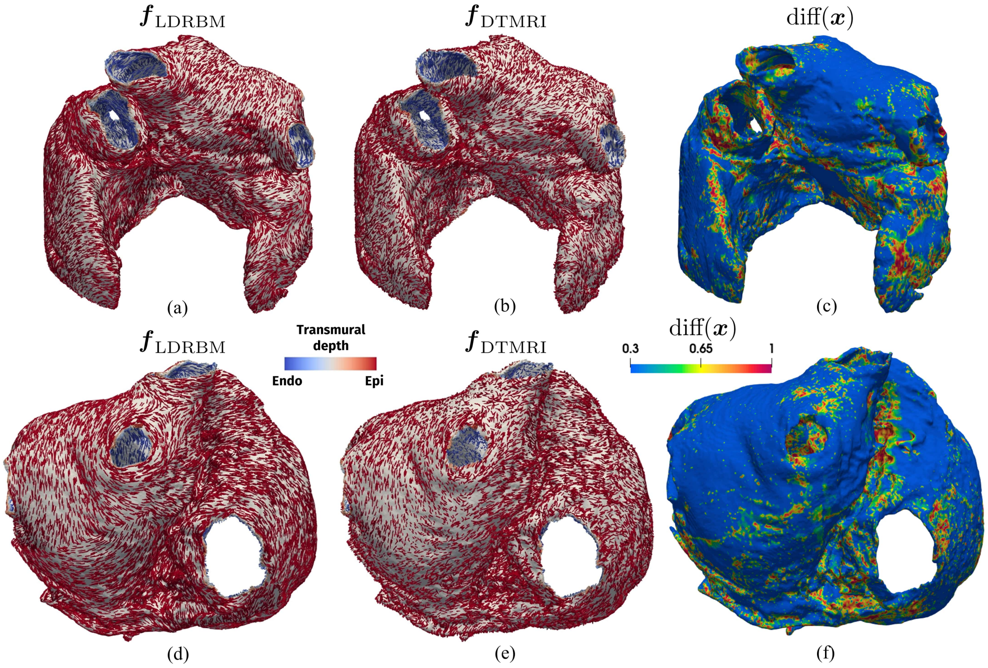

Figure 2.24: Comparison between the atrial LDRBM fibers and the DT-MRI fiber data, in a reconstructed biatrial real geometry. Left: Fiber vector fields $\boldsymbol{f}$ are rendered in Glyphs for LDRBM (a-d) and DT-MRI data (b-e) in the anterior (a-b) and posterior view (d-e). Right: differences between LDRBM and DT-MRI fibers, computed as $\mathrm{diff}(\boldsymbol{x}) = 1 - |\boldsymbol{f}_{\mathrm{DTMRI}}(\boldsymbol{x}) \cdot \boldsymbol{f}_{\mathrm{LDRBM}}(\boldsymbol{x})|$. Colour-bar saturated for values diff ≥ 0.3. Top: frontal view; Bottom: anterior view.

in Table 2.4 for both the simulations with LDRBM and DT-MRI fibers. Whereas, the isotropic simulation is carried out by setting in the conductivity tensor (2.7), $\sigma_f = \sigma_s = \sigma_n = 7.0$ mS/cm. To initiate the action potential propagation we applied a single stimuli in SAN region (located near SCV in RA).

In Figure 2.25, we report the comparison of the activation maps obtained with the three configurations. The total activation time is around 130 ms, for both the simulations with LDRBM and DT-MRI fibers, while the isotropic model produces a remarkably different value of 92 ms, see Figures 2.25(a-c). Moreover, the activation patters, coming from DT-MRI and LDRBM fibers, are compatible with only marginal discrepancies in LAA and RAA appendages, and near TV and MV regions, see Figures 2.25(a-b).

Finally, we compute the absolute difference $\Delta A_{\mathrm{DTMRI},i}(\boldsymbol{x})$ in the activation pattern among the different configurations as

$$\Delta A_{\mathrm{DTMRI},i}(\boldsymbol{x}) = |A_{\mathrm{DTMRI}}(\boldsymbol{x}) - A_i(\boldsymbol{x})| \qquad i = \mathrm{LDRBM}, \mathrm{Iso}, \tag{2.15}$$

where A_{DTMRI}, A_{LDRBM} and A_{Iso} are the activation times for DT-MRI, LDRBM and isotropic simulations, respectively (see Figures 2.25(d,e)). The discrepancies between the simulations with LDRBM and DT-MRI fibers exceed the 15 ms (i.e. 11% of the total activation time) only in restricted zones of TV, MV and LAA (Figure 2.25(d)), while it extend almost over the whole LA volume between the simulations with DT-MRI fibers and the isotropic model.

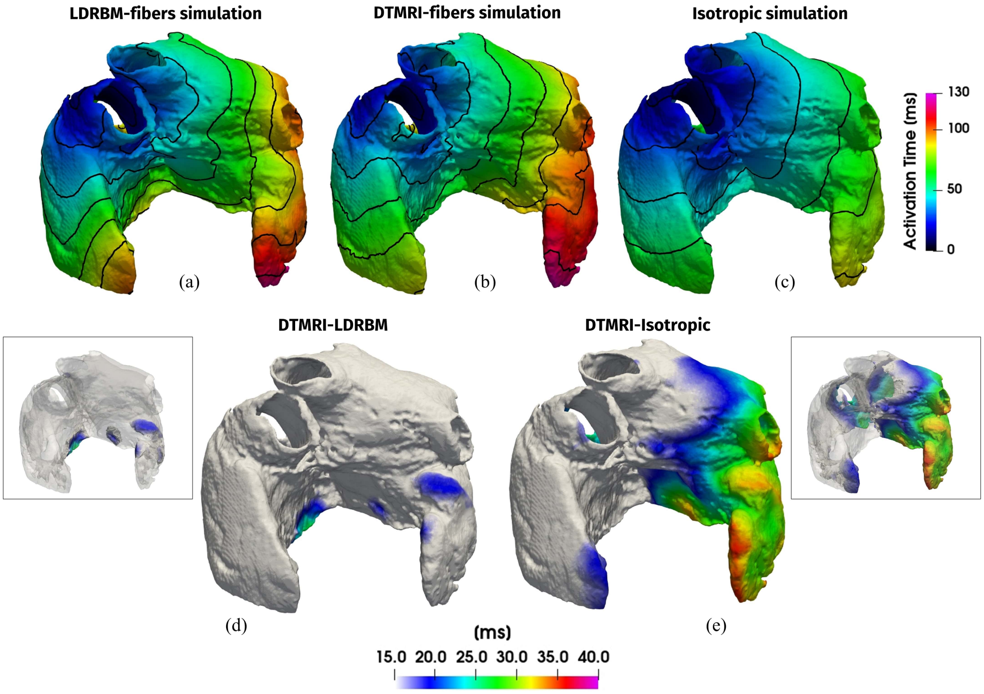

Figure 2.25: Comparison among the activation maps of EP simulations with LDRBM fibers, DT-MRI fiber data and the isotropic model, in a reconstructed biatrial real geometry. Top-Left (a): LDRBM fiber simulation; Top-Centre (b): DT-MRI fiber simulation; Top-Right (b): Isotropic simulation. Bottom: absolute difference ΔA_{i} in the activation times for i=DTMRI-LDRBM (d) and i=DTMRI-Iso (e); colour-bar saturated for values $\Delta A_{\text{i}} \geq 15$ ms; boxed figures show the volumetric differences.

Chapter 3

Modeling the biventricular cardiac electromechanics

In this chapter, we introduce the biventricular 3D-0D model, composed by a biophysically detailed 3D electromechanics (EM) model, which includes electrophysiology (EP), mechanical activation (MA) and tissue mechanics (TM), strongly coupled with a 0D closed-loop lumped parameters haemodynamics model of the whole circulatory system, including the heart blood flow. We begin by carefully detailing the mathematical formulation of the different core models, composing the 3D-0D model, plus the coupling condition between the 3D EM and the 0D fluid models (Section 3.1). Moreover, we provide an effective boundary condition for the mechanical problem that accounts for the neglected part of the domain located above the biventricular basal plane. Then, we illustrate the space and time numerical discretizations of the different core models, carefully addressing the coupling approach to solve, at the algebraic level, the 3D-0D coupled problem (Section 3.2). Afterwards, we present physiological EM simulations using the 3D-0D model (Section 3.3). Specifically, we show that our results match the experimental data of relevant mechanical biomarkers available in literature [137, 238, 138, 236, 31, 61, 219]. Furthermore, we study at which extent different configurations in cross-fibers active contraction, that surrogate the myofibers dispersion, affect EM simulations. Finally, we investigate the impact of using different myofiber architectures on EM simulations. The results presented in this chapter have been accepted for publication in [177].

Contents

3.1 3D-0D closed-loop model for cardiac electromechanics

In this section, we provide a detailed mathematical description of the multiphysics and multiscale 3D biventricular EM model coupled with a 0D closed-loop (lumped parameters) hemodynamical model of the whole cardiovascular system, including the heart blood flow. Our model features several extensions and novel additions with respect to the previous papers [198, 199], that are limited to LV.

The 3D-0D model includes a detailed myofiber architecture, characterizing the different fiber orientations of LV and RV, and it comprises four core models supplemented by suitable coupling conditions between the 3D EM and the 0D fluid models. The core models are related to the different interacting physical phenomena (at the molecular, cellular, tissue and organ levels) involved in the heart pumping function[1]: cardiomyocytes EP ($\mathscr{E}$) [130, 72, 73, 155], sarcomere MA ($\mathscr{A}$) [204, 153, 206, 125, 195, 196], myocardial TM ($\mathscr{M}$) [90, 89, 160, 103] and blood circulation ($\mathscr{C}$) [198, 96, 19, 113, 33, 15, 190]. The coupling conditions are established by the conservation constraints ($\mathscr{V}$) [198].

In the following sections, we first briefly recall the fiber generation methods used to reconstruct the cardiac muscular architecture in biventricular geometries (Section 3.1.1). Then, we detail the different core models ($\mathscr{E} - \mathscr{A} - \mathscr{M} - \mathscr{C}$) and the coupling conditions ($\mathscr{V}$) comprising the 3D-0D model (Sections 3.1.2−3.1.7). Finally, we show the strategy to reconstruct the unloaded (i.e. stress-free) configuration (Section 3.1.8).

3.1.1 Fibers generation

We denote by Ω^0_{biv} the computational domain occupied by the cardiac muscle tissue at rest (reference configuration), see Figure 3.1(a), representing the region occupied by LV and RV, whose boundary $\partial\Omega^0_{biv}$ is partitioned into the epicardium Γ^0_{vepi}, the left $\Gamma^0_{\ell v}$ and right Γ^0_{rv} endocardial surfaces and the biventricular base Γ^0_{base} (namely an artificial basal plane located well below the cardiac valves), so that we have

$$\partial\Omega^0_{biv} = \Gamma^0_{vepi} \ \cup \ \Gamma^0_{\ell v} \ \cup \ \Gamma^0_{rv} \ \cup \ \Gamma^0_{base}.$$

To prescribe the cardiac muscle fiber architecture in the biventricular computational domain Ω^0_{biv}, we use Laplace-Dirichlet-Rule-Based Methods (LDRBMs), see Section 2.1. Specifically, we consider three LDRBM types: R-RBM [188], B-RBM [26] and D-RBM [58]. For further details about LDRBMs, we refer the reader to Section 2.1. Here, we just recall that LDRBMs define the transmural ϕ, the apico-basal ψ and the inter-ventricular ξ distances as the solutions of suitable Laplace boundary-value problems of the type (2.2), see Figure 3.1(b). Then, for each point of the biventricular domain, the transmural and apico-basal distances are used to build an orthonormal local coordinate axial system $[\widehat{\boldsymbol{e}}_l, \widehat{\boldsymbol{e}}_n, \widehat{\boldsymbol{e}}_t]$ owing to

$$\widehat{\boldsymbol{e}}_t = \tfrac{\nabla\phi}{\|\nabla\phi\|}, \quad \widehat{\boldsymbol{e}}_n = \tfrac{\nabla\psi - (\nabla\psi\cdot\widehat{\boldsymbol{e}}_t)\widehat{\boldsymbol{e}}_t}{\|\nabla\psi - (\nabla\psi\cdot\widehat{\boldsymbol{e}}_t)\widehat{\boldsymbol{e}}_t\|}, \quad \widehat{\boldsymbol{e}}_l = \widehat{\boldsymbol{e}}_n \times \widehat{\boldsymbol{e}}_t,$$

defined as the unit transmural, longitudinal and normal directions, respectively. Finally, the reference frame $[\widehat{\boldsymbol{e}}_l, \widehat{\boldsymbol{e}}_n, \widehat{\boldsymbol{e}}_t]$ is properly rotated with the purpose of defining

---

[1] We indicate with a calligraphic letter the name we give to the mathematical core model.

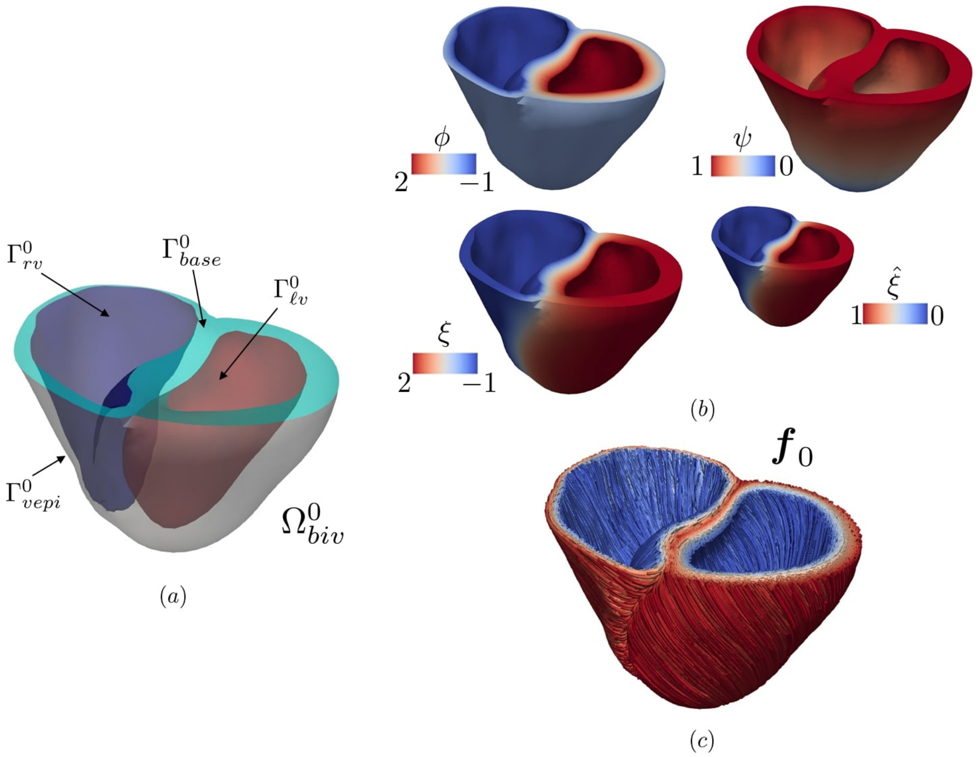

Figure 3.1: Left (a): representation of a biventricular reference domain Ω^0_{biv} whose border is partitioned in Γ^0_{vepi}, Γ^0_{base}, $\Gamma^0_{\ell v}$ and Γ^0_{rv}. Top Right (b): solutions of the Laplace problem (2.2) defining ϕ the transmural, ψ the apico-basal and ξ the inter-ventricular distances that are used to prescribe the myofiber orientations using LDRBM of type D-RBM. Bottom Right (c): fiber field $\boldsymbol{f}_0$ obtained using D-RBM.

the myofiber orientations:

$$[\widehat{\boldsymbol{e}}_l, \widehat{\boldsymbol{e}}_n, \widehat{\boldsymbol{e}}_t] \xrightarrow{\alpha_i,\beta_i} [\boldsymbol{f}_0, \boldsymbol{n}_0, \boldsymbol{s}_0], \quad i = \ell v, rv$$

where $\boldsymbol{f}_0$ is the fiber, $\boldsymbol{n}_0$ the sheet-normal and $\boldsymbol{s}_0$ the sheet directions in the reference configuration, respectively. Moreover, $i = \ell v, rv$ refers to LV or RV, and α_i and β_i are suitable helical and sheetlet angles following linear relationships

$$\theta_i(d_i) = \theta_{epi,i}(1 - d_i) + \theta_{endo,i} d_i, \qquad \text{with } \theta = \alpha, \beta \quad \text{and} \quad i = \ell v, rv,$$

in which $d_i \in [0, 1]$ is the transmural normalized distance and $\theta_{endo,i}$, $\theta_{epi,i}$ are suitable prescribed rotation angles on the endocardium and epicardium, see Figure 3.1(c). To embed different myofiber orientations for LV and RV, we employ the inter-ventricular distance ξ in which positive values of ξ identify the LV, whereas negative values refer to the RV [176]. Moreover, we define the normalized inter-ventricular distance $\hat{\xi} \in [0, 1]$ by rescaling ξ, see Figure 3.1(b).

An example of LDRBM boundary-value solutions for the fiber generation procedure (of D-RBM type) is sketched in Figure 3.1(b). For further details about ventricular LDRBMs we refer the reader to Section 2.1.

3.1.2 Electrophysiology Core Model ($\mathscr{E}$)

The mathematical description of electric activity in the cardiac tissue is expressed by EP core model, comprising two building blocks: a system of ODE, describing the activity at cellular-level, and a PDE related to the transmembrane potential propagation through the cardiac muscle [71, 72]. In this thesis, we consider the monodomain equation endowed with a suitable ionic model for the human action potential [246, 247, 47].

Given the computational domain Ω^0_{biv} and the time interval $t \in (0, T]$, the monodomain system ($\mathscr{E}$), written in Lagrangian coordinates, reads as follows

Electrophysiology ($\mathscr{E}$) :

Find, for each t, the transmembrane action potential $u\colon \Omega^0_{biv} \times (0, T] \to \mathbb{R}$, and the ionic variables vector $\boldsymbol{w}\colon \Omega^0_{biv} \times (0, T] \to \mathbb{R}^{n_{\boldsymbol{w}}}$ such that

$$\begin{cases} J\chi_m \left[C_m \dfrac{\partial u}{\partial t} + \mathcal{I}_{ion}(u, \boldsymbol{w}) \right] - \nabla \cdot \left(J\mathbf{F}^{-1}\mathbf{D}\,\mathbf{F}^{-T}\nabla u \right) = J\chi_m \mathcal{I}_{app} & \\ \qquad\qquad\qquad\qquad\qquad\qquad\qquad\qquad\qquad \text{in } \Omega^0_{biv} \times (0, T], & (3.1a) \\ \dfrac{\partial \boldsymbol{w}}{\partial t} - \boldsymbol{H}(u, \boldsymbol{w}) = \mathbf{0} \qquad \text{in } \Omega^0_{biv} \times (0, T], & (3.1b) \\ \left(J\mathbf{F}^{-1}\mathbf{D}\,\mathbf{F}^{-T}\nabla u \right) \cdot \mathbf{N} = 0 \qquad \text{on } \partial\Omega^0_{biv} \times (0, T], & (3.1c) \\ u = u_0, \quad \boldsymbol{w} = \boldsymbol{w}_0 \qquad \text{in } \Omega^0_{biv} \times \{0\}. & (3.1d) \end{cases}$$

Specifically, $\boldsymbol{w} = \{w_k\}_{k=1}^{n_{\boldsymbol{w}}}$ encodes the gating-variables (representing the fraction of open channels per unit area across the cell membrane) and the concentration of specific ionic species. Among them, one ionic variables (let say w_1) represents the intracellular calcium ions concentration $[\mathrm{Ca}^{2+}]_\mathrm{i}$, indicated in what follows with w_{Ca}. The constant χ_m represents the surface area-to-volume ratio of cardiomyocytes, while C_m stands for the trans-membrane capacitance per unit area. The reaction terms $\mathcal{I}_{ion}$ and $\boldsymbol{H}$ (specified by the ionic model at hand) couple together the action potential propagation and the cellular dynamics. Specifically, we use the human ventricular ten Tusscher-Panfilov ionic model (TTP06, $n_{\boldsymbol{w}} = 18$ of which 12 gating variables and 6 ionic concentrations), which is able to accurately describe ions dynamics across the cell membrane, at least in physiological conditions; see [247] for details on the specific definition of $\boldsymbol{w}$, $\boldsymbol{H}$ and $\mathcal{I}_{ion}$ related to TTP06.

The action potential propagation is driven by the diffusion term $\nabla\cdot(J\mathbf{F}^{-1}\mathbf{D}\mathbf{F}^{-T}\nabla u)$, appearing in (3.1a), where we introduced the deformation gradient tensor $\mathbf{F} = \mathbf{I} + \nabla\mathbf{d}$ with $J = \det(\mathbf{F}) > 0$. In the former expression for $\mathbf{F}$, $\mathbf{d}$ is the cardiac tissue displacement, which is given by the solution of TM core model ($\mathscr{M}$), that will be provided later in Section 3.1.4. The diffusion tensor reads:

$$\mathbf{D} = \sigma_f(\phi_{fast}) \frac{\mathbf{F}\boldsymbol{f}_0 \otimes \mathbf{F}\boldsymbol{f}_0}{|\mathbf{F}\boldsymbol{f}_0|^2} + \sigma_s(\phi_{fast}) \frac{\mathbf{F}\boldsymbol{s}_0 \otimes \mathbf{F}\boldsymbol{s}_0}{|\mathbf{F}\boldsymbol{s}_0|^2} + \sigma_n(\phi_{fast}) \frac{\mathbf{F}\boldsymbol{n}_0 \otimes \mathbf{F}\boldsymbol{n}_0}{|\mathbf{F}\boldsymbol{n}_0|^2},$$

where $\sigma_f(\phi_{fast}), \sigma_s(\phi_{fast}), \sigma_n(\phi_{fast})$ are the fiber, sheet and sheet-normal conductivities, respectively, defined as

$$\sigma_k(\phi_{fast}) = \begin{cases} \sigma_{k,fast} & \text{if } \phi_{fast} \le \epsilon, \quad k = f, s, n, \\ \sigma_{k,myo} & \text{if } \phi_{fast} > \epsilon, \quad k = f, s, n, \end{cases}$$

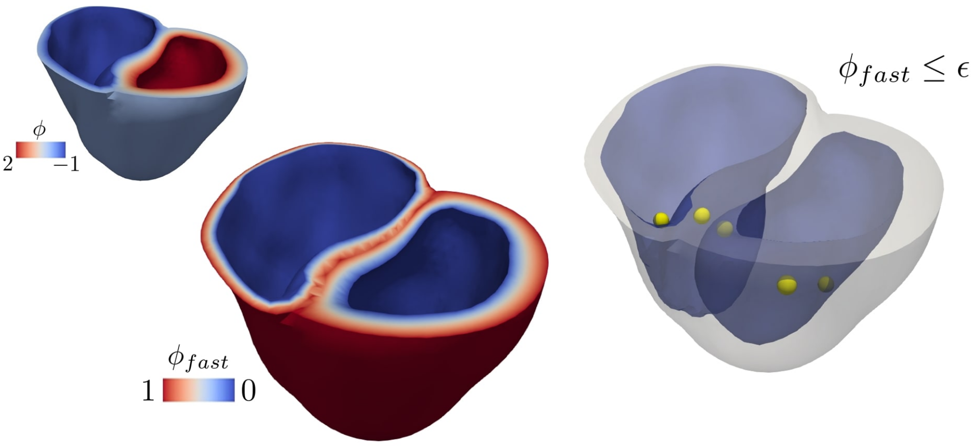

Figure 3.2: Left: solution ϕ_{fast} of the Laplace problem (2.2) built as a function of the transmural distance ϕ. Right: selection of the fast endocardial layer $\phi_{fast} \leq \epsilon$ [127] and the five spherical impulses in LV and RV endocardia: in the anterior para-septal wall, in the left surface of inter-ventricular septum and in the bottom of postero-basal area, for LV; in the septum and in the free endocardial wall, for RV.

where $\sigma_{k,fast}$ and $\sigma_{k,myo}$ (with $k = f, s, n$) are the prescribed conductivities inside and outside the fast endocardial layer, defined as $\phi_{fast}(\phi) \leq \epsilon$ (with $\epsilon \ll 1$) and built as a function of the transmural distance as (see Figure 3.2)

$$\phi_{fast}(\phi) = 1 - \left| \frac{2\,(\phi - \min(\phi))}{\max(\phi) - \min(\phi)} - 1 \right|. \tag{3.2}$$

The electric current $\mathcal{I}_{app}$, stimulating the heart tissue, originates from the Purkinje network [252, 46, 126]. In this thesis, we do not explicitly model the Purkinje network (as for instance done in [252, 46, 126]). Instead, to surrogates the effect of the Purkinje network (as done in [127]), we combined a series of spherical impulses, taken along LV and RV endocardia where an electrical stimulus is applied, with the fast endocardial conduction layer, see also Figure 3.2. To model the spherical stimuli, we set:

$$\mathcal{I}_{app} = \mathcal{I}_{app}(\boldsymbol{x}, t) = \begin{cases} \mathcal{I}^{max} \sum_{k=1}^{N_{app}} \mathbf{1}_{S(\boldsymbol{x}, \boldsymbol{x}_k)} & \text{if } \operatorname{mod}(t, T_{\text{HB}}) \in [t^0_{app,k}, t^0_{app,k} + t_{app}] \\ 0 & \text{otherwise} \end{cases}$$

where $\mathcal{I}^{max}$ is the electrical impulse amplitude and $S(\boldsymbol{x}, \boldsymbol{x}_k) = |\boldsymbol{x} - \boldsymbol{x}_k|^2 \leq \delta^2_{app}$, with $\{\boldsymbol{x}_k\}_{k=1}^{N_{app}}$, the spherical region wherein the k-th stimulus, with radius δ_{app}, initial time $t^0_{app,k}$ and duration t_{app}, is applied at every heartbeat with period T_{HB}[2].

Finally, problem $(\mathscr{E})$ is closed by the initial conditions (3.1d) and equipped with homogeneous Neumann boundary condition (3.1c), where $\mathbf{N}$ represents the generic outer vector normal, taken in the reference configuration, to the boundary surface.

Notice that, in the case of a fixed domain (i.e with $\mathbf{d} = \mathbf{0}$ which implies $\mathbf{F} = \mathbf{I}$ and $J = 1$) we retrieve the monodomain expression (2.8) presented in Section 2.3.

---

[2] For further details about the specific values chosen for δ_{app}, t_{app}, T_{HB} and $\mathcal{I}^{max}$ we refer to Table 3.1 (see also Section 2.4.2)

3.1.3 Activation Core Model ($\mathscr{A}$)

Among the ionic species involved in the ionic dynamics of cardiac EP, calcium ions enter inside the cell a few instants after the beginning of the cell excitation. In turn, the increase of calcium concentration, triggering the activation of the thin filaments inside the sarcomeres, play a key role in the active force generation mechanism.

In this thesis, we model MA of cardiac tissue by using a system of ODEs ($\mathscr{A}$), standing for an Artificial Neural Network (ANN) based model: the so called RDQ18-ANN (recently proposed in [196]), which surrogates the high-fidelity RDQ18 [195]. The RDQ18 model is based on a biophysically detailed description of the microscopic active force generation mechanisms taking place at the scale of sarcomeres [29, 195]. The RDQ18-ANN model has the great advantage of strikingly reducing the computational burden associated to the numerical solution of the RDQ18 model, yet reproducing its results with a very good accuracy, as shown in [196].

Given the computational domain Ω^0_{biv} and the time interval $t \in (0, T]$, the MA core model ($\mathscr{A}$) reads as follows

Activation ($\mathscr{A}$) :

Find, for each t, the two-variable state vector $\mathbf{s}\colon \Omega^0_{biv} \times (0, T] \to \mathbb{R}^2$, such that

$$\begin{cases} \dfrac{\partial \mathbf{s}}{\partial t} = \boldsymbol{K}(\mathbf{s}, w_{\text{Ca}}, SL) & \text{in } \Omega^0_{biv} \times (0, T], \qquad (3.3\text{a}) \\ \mathbf{s} = \mathbf{s}_0 & \text{in } \Omega^0_{biv} \times \{0\}, \qquad (3.3\text{b}) \end{cases}$$

where $\boldsymbol{K}$ represents a suitable function associated to ANN, previously trained from a collection of simulations obtained with the high-fidelity RDQ18 model [194, 196].

The model ($\mathscr{A}$) has two inputs: the first one is the scalar field w_{Ca}, denoting the intracellular calcium ions concentration $[\text{Ca}^{2+}]_{\text{i}}$ over the domain Ω^0_{biv}, provided by the TTP06 ionic model (3.1b), which gives a description of the intracellular calcium dynamics directly from one of the ionic variables $w_{\text{Ca}} \in \boldsymbol{w}$; the second one is the scalar field SL, denoting the elongation of the sarcomeres belonging to each region of the domain Ω^0_{biv}, defined as

$$SL = SL_0\sqrt{\mathcal{I}_{4f}(\mathbf{d})},$$

where SL_0 stands for the sarcomere length at rest and $\mathcal{I}_{4f} = \mathbf{F}\boldsymbol{f}_0 \cdot \mathbf{F}\boldsymbol{f}_0$ is a measure of the tissue stretch along the fibers direction. This creates a feedback between the mechanical model ($\mathscr{M}$) and the force generation model ($\mathscr{A}$) [198].

The RDQ18-ANN output is the permissivity $P \in [0, 1]$ which is obtained as a function of $\mathbf{s}$, $P = G(\mathbf{s})$, where G is a linear function defined in [196]. Since P is the fraction of the contractile units in the force-generation state, the active tension is given by $T_a = T_a^{max}\, P$, where T_a^{max} denotes the tension generated when all the contractile units are generating force (i.e. for $P = 1$), see [196] for further details.

To differentiate the active tension in LV and RV, we define a spatial heterogeneous active tension

$$T_a(\mathbf{s}, \boldsymbol{x}) = T_a^{max} G(\mathbf{s}) \left[\hat{\xi}(\boldsymbol{x}) + C_{\ell rv}(1 - \hat{\xi}(\boldsymbol{x}))\right],$$

where $\hat{\xi} \in [0, 1]$ is the normalized inter-ventricular distance, defined in Section 3.1.1, and $C_{\ell rv} \in (0, 1]$ represents the left-right ventricular contractility ratio, see Figure 3.1(b). Finally, problem ($\mathscr{A}$) is closed by the initial condition (3.3b).

3.1.4 Mechanics Core Model ($\mathscr{M}$)

The heart muscle can be described as an anisotropic hyperelastic viscous medium, whose architecture is characterized by the presence of the muscular fibers. Indeed, the heart passive mechanical response spreads into three mutually orthogonal preferential directions, namely the fiber $\boldsymbol{f}_0$, the sheet $\boldsymbol{s}_0$ and the sheet-normal $\boldsymbol{n}_0$ directions, which form a local orthogonal frame of reference spanning the whole cardiac domain Ω^0_{biv}, see Section 3.1.1. In this thesis we disregard the visco-elastic properties of the heart [91, 157] and we simply assume that the cardiac muscular tissue is represented by an hyperelastic material constitutive relation. Many transversely isotropic or orthotropic constitutive laws have been proposed in the literature so far (see e.g. [160, 102, 103, 89, 90, 12]), accounting for the different response along the myofiber directions $\boldsymbol{f}_0$, $\boldsymbol{s}_0$ and $\boldsymbol{n}_0$. Meanwhile, the tissue active contraction is typically expressed, either within an active stress [188, 7, 249, 248] or active strain formalism [204, 23].

In this thesis, the mechanical response of the cardiac tissue is described by the momentum conservation equation ($\mathscr{M}$) under the hyperelasticity assumption and by adopting an active stress approach [89, 160], employing the orthotropic Guccione constitutive law [90].

Given the computational domain Ω^0_{biv} and the time interval $t \in (0, T]$, the TM core model ($\mathscr{M}$) reads as follows

Mechanics ($\mathscr{M}$) :

Find, for each t, the displacement $\mathbf{d}\colon \Omega^0_{biv} \times (0,T] \to \mathbb{R}^3$, such that

$$\begin{cases} \rho_s \dfrac{\partial^2 \mathbf{d}}{\partial t^2} - \nabla \cdot \mathbf{P}(\mathbf{d}, T_a(\mathbf{s}, \boldsymbol{x})) = \mathbf{0} & \text{in } \Omega^0_{biv} \times (0,T], \quad (3.4a) \\ \mathbf{P}(\mathbf{d}, T_a(\mathbf{s}, \boldsymbol{x}))\mathbf{N} = \mathbf{K}^{vepi}\mathbf{d} + \mathbf{C}^{vepi} \dfrac{\partial \mathbf{d}}{\partial t} & \text{on } \Gamma^0_{vepi} \times (0,T], \quad (3.4b) \\ \mathbf{P}(\mathbf{d}, T_a(\mathbf{s}, \boldsymbol{x}))\mathbf{N} = -\pi_{\ell v}(t)\, J\mathbf{F}^{-T}\mathbf{N} & \text{on } \Gamma^0_{\ell v} \times (0,T], \quad (3.4c) \\ \mathbf{P}(\mathbf{d}, T_a(\mathbf{s}, \boldsymbol{x}))\mathbf{N} = -\pi_{rv}(t)\, J\mathbf{F}^{-T}\mathbf{N} & \text{on } \Gamma^0_{rv} \times (0,T], \quad (3.4d) \\ \mathbf{P}(\mathbf{d}, T_a(\mathbf{s}, \boldsymbol{x}))\mathbf{N} = |J\mathbf{F}^{-T}\mathbf{N}| \left[\pi_{\ell v}\mathbf{v}^{base}_{\ell v} + \pi_{rv}\mathbf{v}^{base}_{rv}\right] & \text{on } \Gamma^0_{base} \times (0,T], \quad (3.4e) \\ \mathbf{d} = \mathbf{d}_0, \quad \dfrac{\partial \mathbf{d}}{\partial t} = \dot{\mathbf{d}}_0 & \text{in } \Omega^0_{biv} \times \{0\}, \quad (3.4f) \end{cases}$$

where ρ_s is the density. Within the active stress formulation, the first Piola-Kirchhoff stress tensor $\mathbf{P} = \mathbf{P}(\mathbf{d}, T_a)$ is additively decomposed according to

$$\mathbf{P}(\mathbf{d}, T_a) = \frac{\partial \mathcal{W}^{(\mathrm{G})}(\mathbf{F})}{\partial \mathbf{F}} + T_a(\mathbf{s}, \boldsymbol{x}) \left[n_f \frac{\mathbf{F}\boldsymbol{f}_0 \otimes \boldsymbol{f}_0}{\sqrt{\mathcal{I}_{4f}}} + n_s \frac{\mathbf{F}\boldsymbol{s}_0 \otimes \boldsymbol{s}_0}{\sqrt{\mathcal{I}_{4s}}} + n_n \frac{\mathbf{F}\boldsymbol{n}_0 \otimes \boldsymbol{n}_0}{\sqrt{\mathcal{I}_{4n}}} \right], \quad (3.5)$$

where the first term represents the passive mechanics with $\mathcal{W}^{(\mathrm{G})}$ being the strain energy density function, whereas the second one stands for the orthotropic active stress, with $T_a(\mathbf{s}, \boldsymbol{x})$ the active tension provided by the activation model ($\mathscr{A}$). Moreover, $\mathcal{I}_{4s} = \mathbf{F}\boldsymbol{s}_0 \cdot \mathbf{F}\boldsymbol{s}_0$ and $\mathcal{I}_{4n} = \mathbf{F}\boldsymbol{n}_0 \cdot \mathbf{F}\boldsymbol{n}_0$ are the tissue stretches along the sheet and sheet-normal directions, respectively, and n_f, n_s and n_n the prescribed proportion of active tension along the fiber, sheet and sheet-normals directions, respectively. In this thesis we adopt the orthotropic active stress formulation (3.5), which surrogates the contraction caused by dispersed myofibers [87, 88, 77, 207, 79].

To model the passive behaviour of the cardiac tissue, we employ the orthotropic Guccione constitutive law [90], according to which the strain energy function is defined as

$$\mathcal{W}^{(\mathrm{G})} = \frac{a}{2}\left(e^{Q}-1\right) + \frac{\kappa^{(\mathrm{G})}}{2}\left(J-1\right)\log(J),$$

where the second term is the volumetric energy with the bulk modulus $\kappa^{(\mathrm{G})}$, which penalizes large variation of volume to enforce a weakly incompressible behaviour [173, 56], and the exponent Q reads

$$Q = b_{ff}E_{ff}^2 + b_{ss}E_{ss}^2 + b_{nn}E_{nn}^2 + b_{fs}\left(E_{fs}^2 + E_{sf}^2\right) + b_{fn}\left(E_{fn}^2 + E_{nf}^2\right) + b_{sn}\left(E_{sn}^2 + E_{ns}^2\right),$$

where a is the stiffness scaling parameter, $E_{ij} = \boldsymbol{E}\boldsymbol{i}_0 \cdot \boldsymbol{j}_0$, for $i,j \in \{f,s,n\}$ and $\boldsymbol{i}_0, \boldsymbol{j}_0 \in \{\boldsymbol{f}_0, \boldsymbol{s}_0, \boldsymbol{n}_0\}$, are the entries of $\mathbf{E} = \frac{1}{2}\left(\mathbf{C}-\mathbf{I}\right)$, i.e the Green-Lagrange strain tensor, being $\mathbf{C} = \mathbf{F}^T\mathbf{F}$ the right Cauchy-Green deformation tensor.

Finally, problem ($\mathscr{M}$) is closed by the initial conditions (3.4f) and equipped with proper boundary conditions (3.4b)−(3.4e) detailed in what follows. We remark that the boundary conditions (3.4b)−(3.4e) are one of the possible choices for the mechanical problem (3.4). However, for the sake of exposition, we decide to consider (3.4f) as the ($\mathscr{M}$) core model.

Epicardial boundary condition

The heart is surrounded by the pericardium membrane, that prevents the cardiac motion from large stretching and protects the heart from external shocks. The pericardial cavity is filled with a lubricating serous fluid to ensure minimal friction of the heart wall with nearby organs, when the myocardium contracts and relaxes [263, 175].

To model the mechanical constraint provided by the pericardium [80, 175, 235], we impose at the epicardial boundary Γ_{vepi}^0 a generalized Robin boundary condition (3.4b) by defining the tensors $\mathbf{K}^{vepi}$ and $\mathbf{C}^{vepi}$ as

$$\mathbf{K}^{vepi} = K_{\parallel}^{vepi}(\mathbf{N}\otimes\mathbf{N}-\mathbf{I}) - K_{\perp}^{vepi}(\mathbf{N}\otimes\mathbf{N}), \tag{3.6}$$

$$\mathbf{C}^{vepi} = C_{\parallel}^{vepi}(\mathbf{N}\otimes\mathbf{N}-\mathbf{I}) - C_{\perp}^{vepi}(\mathbf{N}\otimes\mathbf{N}), \tag{3.7}$$

where $K_{\perp}^{vepi}$, $K_{\parallel}^{vepi}$, $C_{\perp}^{vepi}$, $C_{\parallel}^{vepi} \in \mathbb{R}^+$ are the stiffness and viscosity parameters of the epicardial tissue in the normal and tangential directions, respectively. In this way, the epicardial tissues surrounding the heart wall are modeled as a system of springs and dashpots that mimic the elastic and viscous effects, respectively. Hence, the coefficient $K_{\perp}^{vepi}$ and $K_{\parallel}^{vepi}$ represent the spring stiffness per unit area, while $C_{\perp}^{vepi}$, $C_{\parallel}^{vepi}$ are the dashpot viscosities per unit area. For simplicity, we use a unique set of parameters for the epicardial region of LV and RV.

Endocardial boundary condition

The endocardial surfaces of LV and RV are in contact with the blood inside the cardiac chambers. To accurately model the coupling between the blood and the heart muscle, FSI models can be adopted. In this thesis, we neglect the shear stresses produced by the fluid on the endocardial wall, rather we consider only the effect of fluid pressure, that we assume to be constant in the whole endocardial cavities of LV and RV, respectively. Therefore, normal stress boundary conditions (3.4c)–(3.4d) were imposed at the endocardia $\Gamma_{\ell v}^0$ and Γ_{rv}^0 of both ventricles, where $\pi_{\ell v}(t)$ and $\pi_{rv}(t)$ represent the pressures exerted by the blood in LV and RV, respectively.

Notice that, in the 3D-0D model (that will be presented hereafter in Section 3.1.7), the fluid pressures $\pi_{\ell v}(t)$ and $\pi_{rv}(t)$, acting on LV and RV endocardia, are given by the coupling between the TM ($\mathscr{M}$) and the fluid circulation ($\mathscr{C}$) problems, thanks to the coupling conditions ($\mathscr{V}$). Both the circulation model ($\mathscr{C}$) and the coupling conditions ($\mathscr{V}$) are detailed later in Sections 3.1.5 and 3.1.6, respectively.

Basal boundary condition

The base Γ^0_{base} is an artificial boundary and, as such, it must be provided with suitable boundary conditions that account for the effect of the neglected part of the domain above the ventricular basal plane considered. In the TM core model ($\mathscr{M}$), we set on Γ^0_{base} the energy-consistent boundary condition (3.4e) in the weighted-stress-distribution form, where

$$\mathbf{v}^{base}_{\ell v}(t,\hat{\xi}) = \frac{\hat{\xi}\int_{\Gamma^0_{\ell v}} J\mathbf{F}^{-T}\mathbf{N} d\Gamma_0}{\int_{\Gamma^0_{base}} \hat{\xi}\,|J\mathbf{F}^{-T}\mathbf{N}| d\Gamma_0}, \quad \mathbf{v}^{base}_{rv}(t,\hat{\xi}) = \frac{(1-\hat{\xi})\int_{\Gamma^0_{rv}} J\mathbf{F}^{-T}\mathbf{N} d\Gamma_0}{\int_{\Gamma^0_{base}} (1-\hat{\xi})\,|J\mathbf{F}^{-T}\mathbf{N}| d\Gamma_0}, \tag{3.8}$$

with $\hat{\xi}$ the normalized inter-ventricular distance defined in Section 3.1.1. The boundary condition (3.4e) represents the extension to the biventricular geometries of the energy-consistent boundary condition originally proposed in [196] for LV. The complete derivation of the energy-consistent boundary conditions are hereafter detailed.

Energy-consistent boundary condition in biventricular geometries

The energy-consistent boundary condition (3.4e), accounting for the effect of the neglected part of the domain located above the biventricular base Γ^0_{base}, is consistently with the principles of momentum and energy conservation [196]. It represents a generalization, for biventricular geometries, of the boundary condition proposed in [196].

In what follows, we denote by $\Omega^t_{f,\ell v}$ (respectively $\Omega^t_{f,rv}$) the volume occupied at time t, within LV (respectively, RV), by the fluid located below the base. Moreover, we employ the tilde symbol ($\sim$) to refer to volumes and surfaces located on top of the ventricular base. Specifically, we denote by $\widetilde{\Omega}^t_{f,\ell v}$ and $\widetilde{\Omega}^t_{f,rv}$ the fluid volumes in LV and RV, located above the base. Similarly, we denote by $\widetilde{\Gamma}^t_{vepi}$, $\widetilde{\Gamma}^t_{\ell v}$ and $\widetilde{\Gamma}^t_{rv}$ the epicardial, and endocardial (left and right) surfaces located above the ventricular base. Finally, we denote by $\widetilde{\Gamma}^t_{base}$ the ventricular base surface itself, but endowed with outer normal vector directed towards the apex, differently than for Γ^t_{base}.

Following the derivation of [196] and by defining $\mathbf{T} = J^{-1}\mathbf{P}\mathbf{F}^T$ as the Cauchy stress tensor, the balance of momentum, with a quasi-static approximation, entails

$$\begin{aligned}\mathbf{0} &= \int_{\widetilde{\Omega}_t} \nabla\cdot\mathbf{T}\,d\mathbf{x} = \int_{\partial\widetilde{\Omega}_t} \mathbf{T}\mathbf{n}\,d\Gamma_t = \\ &= \int_{\widetilde{\Gamma}^t_{vepi}} \mathbf{T}\mathbf{n}\,d\Gamma_t + \int_{\widetilde{\Gamma}^t_{\ell v}} \mathbf{T}\mathbf{n}\,d\Gamma_t + \int_{\widetilde{\Gamma}^t_{rv}} \mathbf{T}\mathbf{n}\,d\Gamma_t + \int_{\widetilde{\Gamma}^t_{base}} \mathbf{T}\mathbf{n}\,d\Gamma_t.\end{aligned} \tag{3.9}$$

The normal stress on the endocardium is given by $\mathbf{T}\mathbf{n} = -\pi_{\ell v}\mathbf{n}$ and $\mathbf{T}\mathbf{n} = -\pi_{rv}\mathbf{n}$ (on $\widetilde{\Gamma}^t_{\ell v}$ and $\widetilde{\Gamma}^t_{rv}$, respectively), while we assume negligible the load on the epicardium (i.e. $\mathbf{T}\mathbf{n} = \mathbf{0}$ on $\widetilde{\Gamma}^t_{vepi}$). Thanks to the divergence (Gauss) theorem, it is possible to write the endocardial terms of Equation (3.9) as integrals over $\Gamma^t_{\ell v}$ and Γ^t_{rv}. Indeed, we have the identities:

$$\begin{aligned}\mathbf{0} &= \int_{\Omega^t_{f,\ell v}\cup\widetilde{\Omega}^t_{f,\ell v}} \nabla\pi_{\ell v}\, d\mathbf{x} = \int_{\Gamma^t_{\ell v}} \pi_{\ell v}\mathbf{n}\, d\Gamma_t + \int_{\widetilde{\Gamma}^t_{\ell v}} \pi_{\ell v}\mathbf{n}\, d\Gamma_t,\\ \mathbf{0} &= \int_{\Omega^t_{f,rv}\cup\widetilde{\Omega}^t_{f,rv}} \nabla\pi_{rv}\, d\mathbf{x} = \int_{\Gamma^t_{rv}} \pi_{rv}\mathbf{n}\, d\Gamma_t + \int_{\widetilde{\Gamma}^t_{rv}} \pi_{rv}\mathbf{n}\, d\Gamma_t,\end{aligned}$$

from which we have

$$\textstyle\int_{\widetilde{\Gamma}^t_{\ell v}} \pi_{\ell v}\mathbf{n}\, d\Gamma_t = -\int_{\Gamma^t_{\ell v}} \pi_{\ell v}\mathbf{n}\, d\Gamma_t, \qquad \int_{\widetilde{\Gamma}^t_{rv}} \pi_{rv}\mathbf{n}\, d\Gamma_t = -\int_{\Gamma^t_{rv}} \pi_{rv}\mathbf{n}\, d\Gamma_t.$$

Hence, for the Equation (3.9), we end up with

$$\begin{aligned}\int_{\Gamma^t_{base}} \mathbf{T}\mathbf{n}\, d\Gamma_t = -\int_{\widetilde{\Gamma}^t_{base}} \mathbf{T}\mathbf{n}\, d\Gamma_t = -\int_{\widetilde{\Gamma}^t_{\ell v}} \pi_{\ell v}\mathbf{n}\, d\Gamma_t - \int_{\widetilde{\Gamma}^t_{rv}} \pi_{rv}\mathbf{n}\, d\Gamma_t =\\ = \int_{\Gamma^t_{\ell v}} \pi_{\ell v}\mathbf{n}\, d\Gamma_t + \int_{\Gamma^t_{rv}} \pi_{rv}\mathbf{n}\, d\Gamma_t,\end{aligned}$$

which entails, by considering the pull-back, to the reference configuration

$$\int_{\Gamma^t_{base}} \mathbf{T}\mathbf{n}\, d\Gamma_t = \int_{\Gamma^0_{\ell v}} \pi_{\ell v}\, J\mathbf{F}^{-T}\mathbf{n}\, d\Gamma_0 + \int_{\Gamma^0_{rv}} \pi_v\, J\mathbf{F}^{-T}\mathbf{n}\, d\Gamma_0. \tag{3.10}$$

Equation (3.10) provides the overall stress acting on the ventricular base. However, we need some additional assumptions to define the point-wise distribution of stress, among the infinitely many satisfying Equation (3.10). In the original derivation of the energy-consistent boundary condition [196], at this stage, a uniform stress distribution assumption is made. However, while this assumption is reasonable in a single-ventricle geometry, it is unrealistic when the ventricular base surrounds both ventricles. Indeed, the blood pressures acting in LV are typically much larger than those in RV. For this reason, we propose to distribute stress over the basal surface not uniformly, but rather according to a weight function $\zeta\colon \Gamma^0_{base} \to [0,1]$, that indicates the fraction of stress attributable to the pressure acting on LV, relative RV, at each base point. Hence, we assume that, on Γ^0_{base}, we have:

$$\mathbf{T}\mathbf{n} = \zeta \frac{\int_{\Gamma^0_{\ell v}} \pi_{\ell v}\, J\mathbf{F}^{-T}\mathbf{n}\, d\Gamma_0}{\int_{\Gamma^t_{base}} \zeta\, d\Gamma} + (1-\zeta)\frac{\int_{\Gamma^0_{rv}} \pi_{rv}\, J\mathbf{F}^{-T}\mathbf{n}\, d\Gamma_0}{\int_{\Gamma^t_{base}} (1-\zeta)\, d\Gamma}, \tag{3.11}$$

which reads, in the reference configuration:

$$\mathbf{P}\mathbf{n} = |J\mathbf{F}^{-T}\mathbf{n}| \left[\frac{\zeta \int_{\Gamma^0_{\ell v}} \pi_{\ell v}\, J\mathbf{F}^{-T}\mathbf{n}\, d\Gamma_0}{\int_{\Gamma^0_{base}} |J\mathbf{F}^{-T}\mathbf{n}|\, \zeta\, d\Gamma_0} + \frac{(1-\zeta) \int_{\Gamma^0_{rv}} \pi_{rv}\, J\mathbf{F}^{-T}\mathbf{n}\, d\Gamma_0}{\int_{\Gamma^0_{base}} |J\mathbf{F}^{-T}\mathbf{n}|\, (1-\zeta)\, d\Gamma_0} \right]. \tag{3.12}$$

In what follows we consider three different choices for the weight function ζ, corresponding to as many boundary condition formulations (see also Figure 3.3):

- **Uniform stress distribution**. By setting $\zeta \equiv \frac{1}{2}$, we recover the case of stress uniformly distributed on the whole Γ^0_{base} boundary:

$$\mathbf{P}\mathbf{n} = \frac{|J\mathbf{F}^{-T}\mathbf{n}|}{\int_{\Gamma^0_{base}} |J\mathbf{F}^{-T}\mathbf{n}| d\Gamma_0} \left[\int_{\Gamma^0_{\ell v}} \pi_{\ell v}\, J\mathbf{F}^{-T}\mathbf{n}\, d\Gamma_0 + \int_{\Gamma^0_{rv}} \pi_{rv}\, J\mathbf{F}^{-T}\mathbf{n}\, d\Gamma_0 \right] \tag{3.13}$$

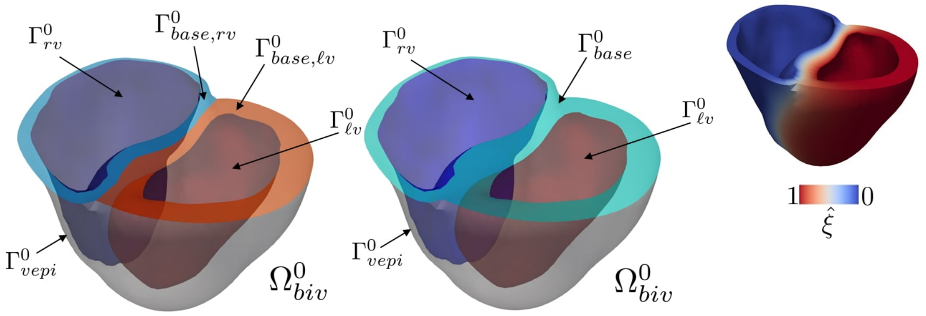

(a) (b)

Figure 3.3: Different choices of the basal boundary corresponding to the three type of formulations for the energy consistent biventricular boundary condition: (a) for the uniform stress distribution over each base $\Gamma^0_{base,\ell v}$ and $\Gamma^0_{base,rv}$; (b) for the uniform and weighted stress distributions, with the weight function $\zeta \equiv \frac{1}{2}$ and $\zeta \equiv \hat{\xi}$, respectively.

- **Uniform stress distribution over each base**. Let us suppose to split the base into two subsets $\Gamma^0_{base,\ell v}$ and $\Gamma^0_{base,rv}$, respectively denoting the portion of ventricular base surrounding LV and RV. Then, we define ζ as the indicator function of the set $\Gamma^0_{base,\ell v}$ (that is $\zeta = 1$ on $\Gamma^0_{base,\ell v}$, while $\zeta = 0$ on $\Gamma^0_{base,rv}$). In this case, we get:

$$\begin{cases} \mathbf{Pn} = \dfrac{|J\mathbf{F}^{-T}\mathbf{n}|}{\int_{\Gamma^0_{base,\ell v}} |J\mathbf{F}^{-T}\mathbf{n}| d\Gamma_0} \displaystyle\int_{\Gamma^0_{\ell v}} \pi_{\ell v}\, J\mathbf{F}^{-T}\mathbf{n}\, d\Gamma_0 & \text{on } \Gamma^0_{base,\ell v} \\ \mathbf{Pn} = \dfrac{|J\mathbf{F}^{-T}\mathbf{n}|}{\int_{\Gamma^0_{base,rv}} |J\mathbf{F}^{-T}\mathbf{n}| d\Gamma_0} \displaystyle\int_{\Gamma^0_{rv}} \pi_{rv}\, J\mathbf{F}^{-T}\mathbf{n}\, d\Gamma_0 & \text{on } \Gamma^0_{base,rv} \end{cases} \tag{3.14}$$

- **Weighted stress distribution**. Finally, we consider the case in which we set $\zeta = \hat{\xi}$ (as defined in Section 3.1.1). The function $\hat{\xi}$ is defined such that we have $\hat{\xi} \simeq 1$ on $\Gamma^0_{base,\ell v}$, $\hat{\xi} \simeq 0$ on $\Gamma^0_{base,rv}$ and we have a smooth transition on the septum. With this choice, the energy-consistent boundary condition of Equation (3.12) reads

$$\mathbf{Pn} = |J\mathbf{F}^{-T}\mathbf{N}| \left[\pi_{\ell v}(t)\mathbf{v}^{base}_{\ell v}(t,\hat{\xi}) + \pi_{rv}(t)\mathbf{v}^{base}_{rv}(t,\hat{\xi}) \right], \tag{3.15}$$

  having defined the vectors $\mathbf{v}^{base}_{\ell v}$ and $\mathbf{v}^{base}_{rv}$ as in Equation (3.8).

Based upon our experience, the uniform stress distribution approach usually does not provide meaningful results. Indeed, since the stress is redistributed on the whole base without accounting for the closeness to the two chambers, a net angular momentum results on the elastic body, making it rotate during systole. Conversely, both the uniform stress distribution approach over each base and the weighted stress distribution approach overcome this issue, thanks to a more realistic distribution of the stress. While the two strategies globally provide very similar results, the latter allows for a smoother solution close to the interface between the left and right bases. For this reason, in this thesis we adopt the weighted stress distribution approach.

3.1.5 Blood circulation Core Model ($\mathscr{C}$)

EM models need to account for the interaction with the circulatory system [190]. In this thesis, we describe the blood haemodynamics through the entire cardiovascular network, by means of a 0D closed-loop lamped-parameters model, inspired by [96, 33] and recently proposed in [198]. Specifically, systemic and pulmonary circulations are modeled with resistance-inductance-capacitance (RLC) circuits, one for the arterial part and the other one for the venous part. The heart chambers are described by time-varying elastance elements and non-ideal diodes stand for the heart valves [198]; see Figure 3.4.

Given the time interval $t \in (0, T]$, the 0D closed-loop circulation model is represented by a system of ODEs:

$$
\begin{cases}
\dfrac{dV_{\ell a}(t)}{dt} = Q_{ven}^{pul}(t) - Q_{mv}(t), & (3.16a)\\
\dfrac{dV_{\ell v}(t)}{dt} = Q_{mv}(t) - Q_{av}(t), & (3.16b)\\
\dfrac{dV_{ra}(t)}{dt} = Q_{ven}^{sys}(t) - Q_{tv}(t), & (3.16c)\\
\dfrac{dV_{rv}(t)}{dt} = Q_{tv}(t) - Q_{pv}(t), & (3.16d)\\
C_{ar}^{sys}\dfrac{dp_{ar}^{sys}(t)}{dt} = Q_{av}(t) - Q_{ar}^{sys}(t), & (3.16e)\\
C_{ven}^{sys}\dfrac{dp_{ven}^{sys}(t)}{dt} = Q_{ar}^{sys}(t) - Q_{ven}^{sys}(t), & (3.16f)\\
C_{ar}^{pul}\dfrac{dp_{ar}^{pul}(t)}{dt} = Q_{pv}(t) - Q_{ar}^{pul}(t), & (3.16g)\\
C_{ven}^{pul}\dfrac{dp_{ven}^{pul}(t)}{dt} = Q_{ar}^{pul}(t) - Q_{ven}^{pul}(t), & (3.16h)\\
\dfrac{L_{ar}^{sys}}{R_{ar}^{sys}}\dfrac{dQ_{ar}^{sys}(t)}{dt} = -Q_{ar}^{sys}(t) - \dfrac{p_{ven}^{sys}(t) - p_{ar}^{sys}(t)}{R_{ar}^{sys}}, & (3.16i)\\
\dfrac{L_{ven}^{sys}}{R_{ven}^{sys}}\dfrac{dQ_{ven}^{sys}(t)}{dt} = -Q_{ven}^{sys}(t) - \dfrac{p_{ra}(t) - p_{ven}^{sys}(t)}{R_{ven}^{sys}}, & (3.16j)\\
\dfrac{L_{ar}^{pul}}{R_{ar}^{pul}}\dfrac{dQ_{ar}^{pul}(t)}{dt} = -Q_{ar}^{pul}(t) - \dfrac{p_{ven}^{pul}(t) - p_{ar}^{pul}(t)}{R_{ar}^{pul}}, & (3.16k)\\
\dfrac{L_{ven}^{pul}}{R_{ven}^{pul}}\dfrac{dQ_{ven}^{pul}(t)}{dt} = -Q_{ven}^{pul}(t) - \dfrac{p_{\ell a}(t) - p_{ven}^{pul}(t)}{R_{ven}^{pul}}, & (3.16l)
\end{cases}
$$

where:

$$p_{\ell v}(t) = p_{ex}(t) + E_{\ell v}(t)\left(V_{\ell v}(t) - V_{0,\ell v}\right), \tag{3.17a}$$

$$p_{rv}(t) = p_{ex}(t) + E_{rv}(t)\left(V_{rv}(t) - V_{0,rv}\right), \tag{3.17b}$$

$$p_{\ell a}(t) = p_{ex}(t) + E_{la}(t)\left(V_{\ell a}(t) - V_{0,la}\right), \tag{3.17c}$$

$$p_{ra}(t) = p_{ex}(t) + E_{ra}(t)\left(V_{ra}(t) - V_{0,ra}\right), \tag{3.17d}$$

$$Q_{mv}(t) = \frac{p_{\ell a}(t) - p_{\ell v}(t)}{R_{mv}(p_{\ell a}(t), p_{\ell v}(t))}, \qquad Q_{av}(t) = \frac{p_{\ell v}(t) - p_{ar}^{sys}(t)}{R_{av}(p_{\ell v}(t), p_{ar}^{sys}(t))}, \tag{3.17e}$$

$$Q_{tv}(t) = \frac{p_{ra}(t) - p_{rv}(t)}{R_{tv}(p_{ra}(t), p_{rv}(t))}, \qquad Q_{pv}(t) = \frac{p_{rv}(t) - p_{ar}^{pul}(t)}{R_{pv}(p_{rv}(t), p_{ar}^{pul}(t))}. \tag{3.17f}$$

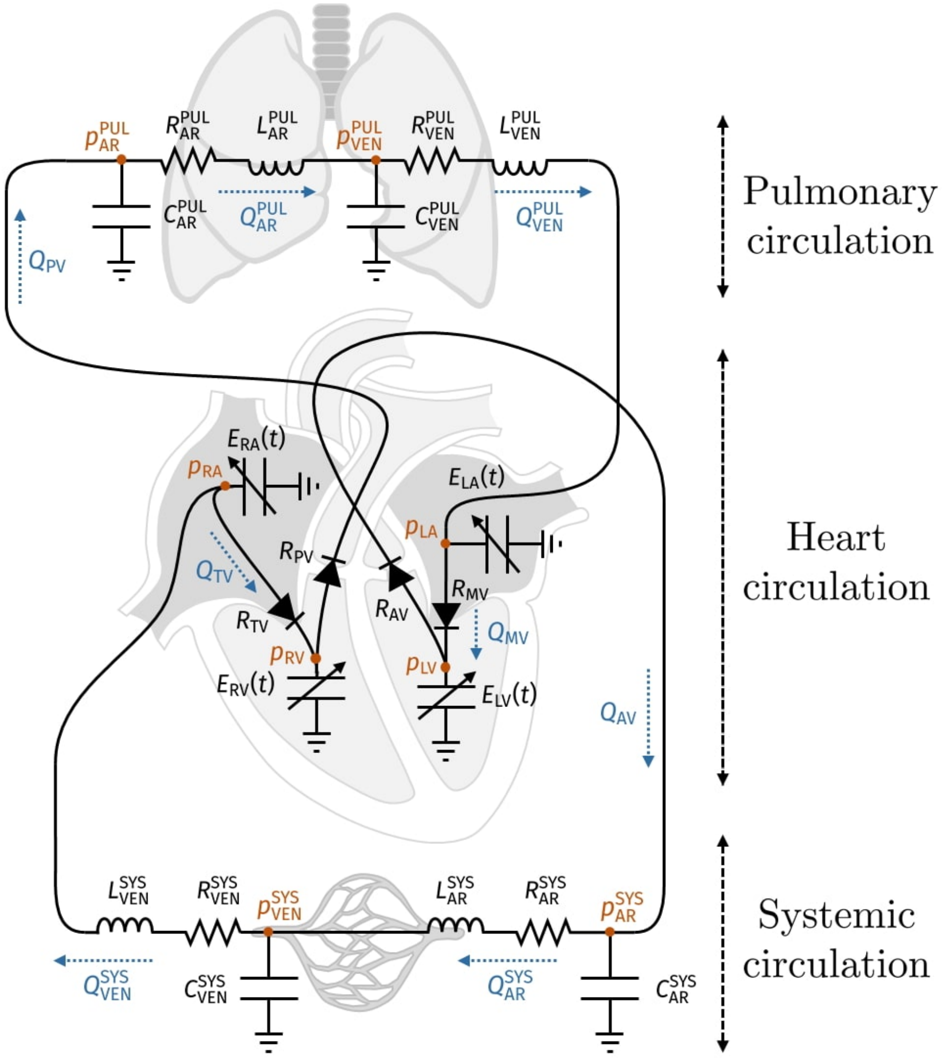

Figure 3.4: 0D closed-loop model for the circulatory system. The state variables corresponding to pressures and fluxes are depicted in orange and blue, respectively.

In this model, $p_{\ell a}(t)$, $p_{ra}(t)$, $p_{\ell v}(t)$, $p_{rv}(t)$, $V_{\ell a}(t)$, $V_{ra}(t)$, $V_{\ell v}(t)$ and $V_{rv}(t)$ refer to pressures and volumes in LA, RA, LV and RV, respectively. The variables $Q_{mv}(t)$, $Q_{av}(t)$, $Q_{tv}(t)$ and $Q_{pv}(t)$ indicate the flow rates through MV, AV, TV and PV, respectively. Furthermore, $p_{ar}^{sys}(t)$, $Q_{ar}^{sys}(t)$, $p_{ven}^{sys}(t)$ and $Q_{ven}^{sys}(t)$ are pressures and flow rates of the systemic circulation (arterial and venous). Similarly, $p_{ar}^{pul}(t)$, $Q_{ar}^{pul}(t)$, $p_{ven}^{pul}(t)$ and $Q_{ven}^{pul}(t)$ define pressures and flow rates of the pulmonary circulation (arterial and venous). Moreover, $p_{ex}(t)$ represents the exerted pressure by the respiration and the organs surrounding the heart. For the four cardiac chambers, time varying elastances $E_{la}(t)$, $E_{\ell v}(t)$, $E_{ra}(t)$ and $E_{rv}(t)$ are analytically prescribed by means of

$$\begin{aligned} E_{\ell v}(t) &= E_{\ell v}^{act,max} e_{\ell v} + E_{\ell v}^{A}, & E_{rv}(t) &= E_{rv}^{act,max} e_{rv} + E_{rv}^{A}, \\ E_{la}(t) &= E_{\ell a}^{act,max} e_{\ell a} + E_{\ell a}^{A}, & E_{ra}(t) &= E_{ra}^{act,max} e_{ra} + E_{ra}^{A}, \end{aligned}$$

with

$$e_{iv}(t) = \begin{cases} \frac{1}{2}\left[1 - \cos\left(\pi \frac{t}{T_{vc}^{(i)}}\right)\right] & 0 \le t \le T_{vc}^{(i)}, \\ \frac{1}{2}\left[1 + \cos\left(\pi \frac{(t - T_{vc}^{(i)})}{T_{vr}^{(i)}}\right)\right] & T_{vc}^{(i)} < t \le T_{vc}^{(i)} + T_{vr}^{(i)}, \\ 0 & T_{vc}^{(i)} + T_{vr}^{(i)} < t \le T_{\mathrm{HB}}, \end{cases} \quad \text{for} \quad i = \ell, r,$$

$$e_{ia}(t) = \begin{cases} \frac{1}{2}\left[1 + \cos\left(\pi \frac{(t + T_{\mathrm{HB}} - t_{ar}^{(i)})}{T_{ar}}\right)\right] & 0 \le t \le t_{ar}^{(i)} + T_{ar}^{(i)} - T_{\mathrm{HB}}, \\ 0 & t_{ar}^{(i)} + T_{ar}^{(i)} - T_{\mathrm{HB}} < t \le t_{ac}^{(i)}, \\ \frac{1}{2}\left[1 - \cos\left(\pi \frac{(t - t_{ac}^{(i)})}{T_{ac}^{(i)}}\right)\right] & t_{ac}^{(i)} < t \le t_{ac}^{(i)} + T_{ac}^{(i)}, \\ \frac{1}{2}\left[1 + \cos\left(\pi \frac{(t - t_{ar}^{(i)})}{T_{ar}^{(i)}}\right)\right] & t_{ac}^{(i)} + T_{ac}^{(i)} < t \le T_{\mathrm{HB}}, \end{cases} \quad \text{for} \quad i = \ell, r,$$

where $T_{vc}^{(i)}$, $T_{ac}^{(i)}$ are the duration of the (left $i = \ell$ and right $i = r$) ventricular and atrial contraction, $T_{vr}^{(i)}$, $T_{ar}^{(i)}$ are the duration of the (left $i = \ell$ and right $i = r$) ventricular and atrial relaxation, $t_{vc}^{(i)}$, $t_{ac}^{(i)}$ the time beginning of the (left $i = \ell$ and right $i = r$) ventricular and atrial contraction and T_{HB} is the heartbeat period. The above parameters are physiologically calibrated with values ranging from $E_{\ell a}^{A}$, $E_{\ell v}^{A}$, E_{ra}^{A}, E_{rv}^{A} – when the chambers are at rest – to $(E_{\ell a}^{A} + E_{\ell a}^{act,max})$, $(E_{\ell v}^{A} + E_{\ell v}^{act,max})$, $(E_{ra}^{A} + E_{ra}^{act,max})$, $(E_{rv}^{A} + E_{rv}^{act,max})$ – when the chambers are contracted. Finally, $R_{mv}(p_1, p_2)$, $R_{av}(p_1, p_2)$, $R_{tv}(p_1, p_2)$ and $R_{pv}(p_1, p_2)$ define the behaviour of valves as diodes, according to:

$$R_i(p_1, p_2) = \begin{cases} R_{min}, & p_1 < p_2 \\ R_{max}, & p_1 \ge p_2 \end{cases} \quad \text{for} \quad i \in \{mv, av, tv, pv\},$$

where p_1 and p_2 stand for the pressures ahead and behind the valve leaflets with respect to the flow direction, whereas R_{min} and R_{max} are the minimum and maximum resistance of the valves.

Introducing the vector $\boldsymbol{c}(t)$ defined as

$$\begin{aligned} \boldsymbol{c}(t) = (&V_{\ell a}(t), V_{\ell v}(t), V_{ra}(t), V_{rv}(t), p_{ar}^{sys}(t), p_{ven}^{sys}(t), p_{ar}^{pul}(t), p_{ven}^{pul}(t), \\ &Q_{ar}^{sys}(t), Q_{ven}^{sys}(t), Q_{ar}^{pul}(t), Q_{ven}^{pul}(t))^T, \end{aligned} \tag{3.18}$$

which includes pressures, volumes and fluxes of the different compartments composing the vascular network, Systems (3.16)–(3.17) can be expressed, as the core model ($\mathscr{C}$), in the following compact form

Circulation$(\mathscr{C})$:

Find, for each t, the unknown vector $\boldsymbol{c}(t)\colon (0,T] \to \mathbb{R}^{n_c}$, such that

$$\begin{cases} \dfrac{d\boldsymbol{c}(t)}{dt} = \boldsymbol{G}(t, \boldsymbol{c}(t)) & \text{for } t \in (0,T], \qquad (3.19a) \\ \boldsymbol{c}(0) = \boldsymbol{c}_0 & t = 0, \qquad (3.19b) \end{cases}$$

where $\boldsymbol{G}$ is a proper function that collects the whole right hand sides of Equations (3.16) and (3.17). Finally, Equation (3.19b) closes the system (3.19).

3.1.6 Coupling conditions $(\mathscr{V})$

In the 0D closed-loop haemodynamics model (3.19), cardiac chambers are surrogates by simplified 0D counterparts in the form of time-varying elastance elements. To couple the 0D circulation model (3.19) with the 3D EM biventricular model, given by $(\mathscr{E})$–$(\mathscr{A})$–$(\mathscr{M})$, we follow the strategy proposed in [198] and here extended to the biventricular case: we replace, in the circulation model, the time-varying elastance elements representing 0D LV and RV models with their corresponding 3D mechanical descriptions, obtaining the coupled 3D-0D closed-loop model depicted in Figure 3.5. Hence, the pressure-volume relationships between $p_{\ell v}$, p_{rv} and $V_{\ell v}$, V_{rv} are no longer prescribed by Equations (3.17a)-(3.17b), but by the 3D TM model resolution. More precisely, in place of Equations (3.17a)-(3.17b), we introduce the volume-consistency coupling conditions $(\mathscr{V})$

Volume constraints $(\mathscr{V})$:

$$\begin{cases} V_{\ell v}^{\mathrm{3D}}(\mathbf{d}(t)) = V_{\ell v}(\boldsymbol{c}(t)) & \text{for } t \in (0,T], \qquad (3.20a) \\ V_{rv}^{\mathrm{3D}}(\mathbf{d}(t)) = V_{rv}(\boldsymbol{c}(t)) & \text{for } t \in (0,T], \qquad (3.20b) \end{cases}$$

where $V_{\ell v}$ and V_{rv} are LV and RV volumes within the 0D circulation model, while $V_{\ell v}^{\mathrm{3D}}$ and V_{rv}^{3D} represent the 3D ventricular volume for LV and RV computed as:

$$V_i^{\mathrm{3D}}(\mathbf{d}(t)) = \int_{\Gamma_i^0} J(t)\,((\mathbf{h} \otimes \mathbf{h})\,(\mathbf{x} + \mathbf{d}(t) - \mathbf{b}_i)) \cdot \mathbf{F}^{-T}(t)\,\mathbf{N}\,d\Gamma_0 \qquad i = \ell v, rv,$$

wherein $\mathbf{h}$ is a vector orthogonal to LV/RV centreline (i.e. lying on the biventricular base) and $\mathbf{b}_i$ $(i = \ell v, rv)$ lays inside LV/RV [198]. Notice that, subtracting to the space coordinate $\mathbf{x} + \mathbf{d}(t)$ that of a point $\mathbf{b}_i$ improves the accuracy of the formula when the ventricular base changes its orientation [198].

Thanks to the coupling conditions (3.20), the 3D TM model $(\mathscr{M})$ must satisfy at each time $t \in (0,T]$ the volume-consistency coupling conditions $(\mathscr{V})$. Moreover, having introduced two additional scalar Equations (i.e (3.20a)-(3.20b)), two additional unknowns arise from the 3D TM model: the left $\pi_{\ell v}(t)$ and right $\pi_{rv}(t)$ ventricular pressures act as Lagrange multipliers associated to the constraint $(\mathscr{V})$. Hence, we introduce the 3D-0D $(\mathscr{M}) - (\mathscr{C})$ coupled problem as follows:

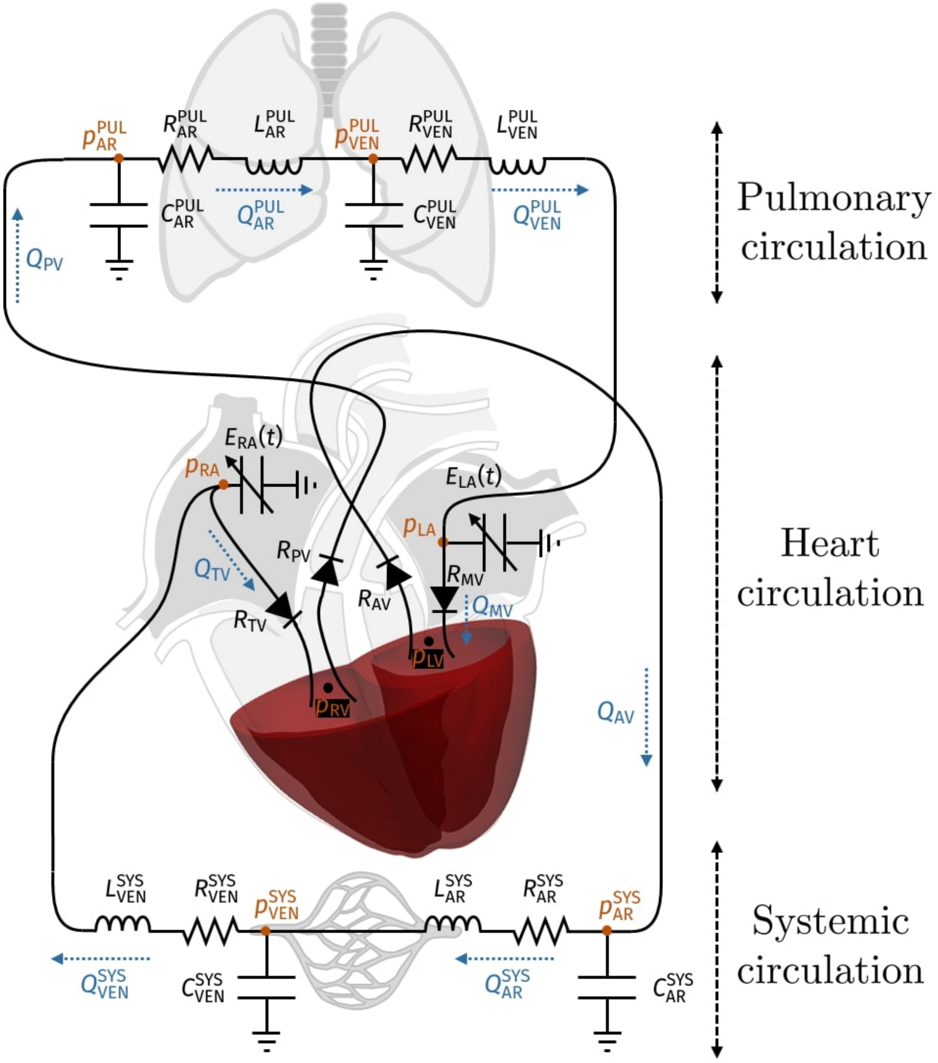

Figure 3.5: Biventricular 3D-0D closed-loop model for the circulatory system, coupling the biventricular 3D-EM model and the 0D-fluid model. The state variables corresponding to pressures and fluxes are depicted in orange and blue, respectively.

Find, for each t, the displacement $\mathbf{d}\colon \Omega^0_{biv} \times (0,T] \to \mathbb{R}^3$ and the pressures $\pi_{\ell v}, \pi_{rv}\colon (0,T] \to \mathbb{R}$ such that

$$\begin{cases}
\rho_s \dfrac{\partial^2 \mathbf{d}}{\partial t^2} - \nabla \cdot \mathbf{P}(\mathbf{d}, T_a(\mathbf{s}, \boldsymbol{x})) = \mathbf{0} & \text{in } \Omega^0_{biv} \times (0,T], \quad (3.21a)\\
\mathbf{P}(\mathbf{d}, T_a(\mathbf{s}, \boldsymbol{x}))\mathbf{N} = \mathbf{K}^{vepi}\mathbf{d} + \mathbf{C}^{vepi}\dfrac{\partial \mathbf{d}}{\partial t} & \text{on } \Gamma^0_{vepi} \times (0,T], \quad (3.21b)\\
\mathbf{P}(\mathbf{d}, T_a(\mathbf{s}, \boldsymbol{x}))\mathbf{N} = -\pi_{\ell v}(t)\, J\mathbf{F}^{-T}\mathbf{N} & \text{on } \Gamma^0_{\ell v} \times (0,T], \quad (3.21c)\\
\mathbf{P}(\mathbf{d}, T_a(\mathbf{s}, \boldsymbol{x}))\mathbf{N} = -\pi_{rv}(t)\, J\mathbf{F}^{-T}\mathbf{N} & \text{on } \Gamma^0_{rv} \times (0,T], \quad (3.21d)\\
\mathbf{P}(\mathbf{d}, T_a(\mathbf{s}, \boldsymbol{x}))\mathbf{N} = |J\mathbf{F}^{-T}\mathbf{N}| \left[\pi_{\ell v}(t)\mathbf{v}^{base}_{\ell v} + \pi_{rv}(t)\mathbf{v}^{base}_{rv}\right] & \text{on } \Gamma^0_{base} \times (0,T], \quad (3.21e)\\
V^{3\text{D}}_{\ell v}(\mathbf{d}(t)) = V_{\ell v}(\boldsymbol{c}(t)) & \text{for } t \in (0,T], \quad (3.21f)\\
V^{3\text{D}}_{rv}(\mathbf{d}(t)) = V_{rv}(\boldsymbol{c}(t)) & \text{for } t \in (0,T], \quad (3.21g)\\
\mathbf{d} = \mathbf{d}_0, \quad \dfrac{\partial \mathbf{d}}{\partial t} = \dot{\mathbf{d}}_0 & \text{in } \Omega^0_{biv} \times \{0\}, \quad (3.21h)\\
\pi_{\ell v} = \pi_{\ell v,0}, \quad \pi_{rv} = \pi_{rv,0} & t = 0. \quad (3.21i)
\end{cases}$$

Moreover, to ensure the continuity of the pressures between the 3D TM and the 0D circulation models, we introduce the following the pressure-consistency coupling conditions

Pressure constraints:

$$\begin{cases}
p_{\ell v}(t) = \pi_{\ell v}(t) & \text{for } t \in (0,T], \quad (3.22a)\\
p_{rv}(t) = \pi_{rv}(t) & \text{for } t \in (0,T]. \quad (3.22b)
\end{cases}$$

Therefore, we introduce the coupled 3D-0D version of the circulation model ($\mathscr{C}$) as: Find, for each t, the unknown vector $\boldsymbol{c}(t)\colon (0,T] \to \mathbb{R}^{n_c}$, such that

$$\begin{cases}
\dfrac{d\boldsymbol{c}(t)}{dt} = \boldsymbol{G}_{\text{B}}(t, \boldsymbol{c}(t), p_{\ell v}(t), p_{rv}(t)) & \text{for } t \in (0,T], \quad (3.23a)\\
p_{\ell v}(t) = \pi_{\ell v}(t) & \text{for } t \in (0,T], \quad (3.23b)\\
p_{rv}(t) = \pi_{rv}(t) & \text{for } t \in (0,T], \quad (3.23c)\\
\boldsymbol{c}(0) = \boldsymbol{c}_0, & t = 0. \quad (3.23d)
\end{cases}$$

where $\boldsymbol{G}_{\text{B}}$ is a proper function that collects the right hand sides of Equations (3.16) and (3.17), apart from those corresponding to the pressures of LV and RV (3.17a)-(3.17b).

We remark that the following coupling strategy for the 3D-0D model, where the pressures of both ventricles act as Lagrange multipliers associated to the volume-consistent constrains, has been proved to be complaint with the principles of conservation of mechanical energy, which is achieved in virtue of the energy consistent boundary conditions, that account for the interaction among the cardiac chambers within the computational domain. In particular, the power exerted by the cavity pressures in the 3D EM model balances that exchanged with the 0D circulation model at the coupling interface [198]. For the derivation of the balance of mechanical energy for the 3D-0D model, we refer the reader to [198].

3.1.7 The coupled electromechanical problem

Putting together the five building blocks $(\mathscr{E})$–$(\mathscr{A})$–$(\mathscr{M})$–$(\mathscr{C})$–$(\mathscr{V})$, just detailed, we get the 3D-EM-0D-fluid problem, a system of coupled PDEs and ODEs.

Given the computational domain Ω^0_{biv} and the time interval $t \in (0, T]$, our complete 3D-0D biventricular model reads:

3D-0D Biventricular model

$$
\begin{cases}
J\chi_m \left[C_m \dfrac{\partial u}{\partial t} + \mathcal{I}_{ion}(u, \boldsymbol{w}) \right] - \nabla \cdot (J\mathbf{F}^{-1}\mathbf{D}\,\mathbf{F}^{-T}\nabla u) = J\chi_m \mathcal{I}_{app} & \\
\qquad\qquad\qquad\qquad\qquad\qquad\qquad\qquad\qquad \text{in } \Omega^0_{biv} \times (0, T], & (3.24\text{a}) \\
\dfrac{\partial \boldsymbol{w}}{\partial t} - \boldsymbol{H}(u, \boldsymbol{w}) = \mathbf{0} \qquad\qquad\qquad\qquad \text{in } \Omega^0_{biv} \times (0, T], & (3.24\text{b}) \\
\left(J\mathbf{F}^{-1}\mathbf{D}\,\mathbf{F}^{-T}\nabla u\right) \cdot \mathbf{N} = 0 \qquad\qquad \text{on } \partial\Omega^0_{biv} \times (0, T], & (3.24\text{c}) \\
\dfrac{\partial \mathbf{s}}{\partial t} = \boldsymbol{K}(\mathbf{s}, [\mathrm{Ca}^{2+}]_{\mathrm{i}}, SL) \qquad\qquad \text{in } \Omega^0_{biv} \times (0, T], & (3.24\text{d}) \\
\rho_s \dfrac{\partial^2 \mathbf{d}}{\partial t^2} - \nabla \cdot \mathbf{P}(\mathbf{d}, T_a(\mathbf{s}, \boldsymbol{x})) = \mathbf{0} \qquad \text{in } \Omega^0_{biv} \times (0, T], & (3.24\text{e}) \\
\mathbf{P}(\mathbf{d}, T_a(\mathbf{s}, \boldsymbol{x}))\mathbf{N} = \mathbf{K}^{vepi}\mathbf{d} + \mathbf{C}^{vepi}\dfrac{\partial \mathbf{d}}{\partial t} \qquad \text{on } \Gamma^0_{vepi} \times (0, T], & (3.24\text{f}) \\
\mathbf{P}(\mathbf{d}, T_a(\mathbf{s}, \boldsymbol{x}))\mathbf{N} = -p_{\ell v}(t)\, J\mathbf{F}^{-T}\mathbf{N} \qquad \text{on } \Gamma^0_{\ell v} \times (0, T], & (3.24\text{g}) \\
\mathbf{P}(\mathbf{d}, T_a(\mathbf{s}, \boldsymbol{x}))\mathbf{N} = -p_{rv}(t)\, J\mathbf{F}^{-T}\mathbf{N} \qquad \text{on } \Gamma^0_{rv} \times (0, T], & (3.24\text{h}) \\
\mathbf{P}(\mathbf{d}, T_a(\mathbf{s}, \boldsymbol{x}))\mathbf{N} = |J\mathbf{F}^{-T}\mathbf{N}| \left[p_{\ell v}(t)\mathbf{v}^{base}_{\ell v} + p_{rv}(t)\mathbf{v}^{base}_{rv}\right] \text{ on } \Gamma^0_{base} \times (0, T], & (3.24\text{i}) \\
\dfrac{d\boldsymbol{c}(t)}{dt} = \boldsymbol{G}_{\mathrm{B}}(t, \boldsymbol{c}(t), p_{\ell v}(t), p_{rv}(t)) \qquad \text{for } t \in (0, T], & (3.24\text{j}) \\
V^{\mathrm{3D}}_{\ell v}(\mathbf{d}(t)) = V_{\ell v}(\boldsymbol{c}(t)) \qquad\qquad \text{for } t \in (0, T], & (3.24\text{k}) \\
V^{\mathrm{3D}}_{rv}(\mathbf{d}(t)) = V_{rv}(\boldsymbol{c}(t)) \qquad\qquad \text{for } t \in (0, T], & (3.24\text{l})
\end{cases}
$$

where the model unknowns are

$$
\begin{gathered}
u \colon \Omega^0_{biv} \times (0, T] \to \mathbb{R}, \;\; \boldsymbol{w} \colon \Omega^0_{biv} \times (0, T] \to \mathbb{R}^{n_{\boldsymbol{w}}}, \;\; \mathbf{s} \colon \Omega^0_{biv} \times (0, T] \to \mathbb{R}^{n_{\mathbf{s}}}, \\
\mathbf{d} \colon \Omega^0_{biv} \times (0, T] \to \mathbb{R}^3, \quad \boldsymbol{c} \colon (0, T] \to \mathbb{R}^{n_{\boldsymbol{c}}}, \quad p_{\ell v} \colon (0, T] \to \mathbb{R}, \;\; p_{rv} \colon (0, T] \to \mathbb{R},
\end{gathered}
$$

Finally, the model is closed by the initial conditions in $\Omega^0_{biv} \times \{0\}$:

$$
u = u_0, \;\; \boldsymbol{w} = \boldsymbol{w}_0, \;\; \mathbf{s} = \mathbf{s}_0, \;\; \mathbf{d} = \mathbf{d}_0, \;\; \frac{\partial \mathbf{d}}{\partial t} = \dot{\mathbf{d}}_0, \;\; \boldsymbol{c} = \boldsymbol{c}_0, \;\; p_{\ell v} = p_{\ell v,0}, \;\; p_{rv} = p_{rv,0}.
$$

Notice that, in the 3D-0D problem (3.24) the continuity of the pressures, expressed by the coupling condition (3.22), is implicitly recovered by the coupling approach for the 3D mechanical model $(\mathscr{M})$ and the 0D closed-loop hemodynamical model $(\mathscr{C})$ by means of the volume conservation constraints $(\mathscr{V})$, where the pressures of LV and RV act as Lagrange multipliers. Hence, Equation (3.22a) and (3.22b) are not formally included in the 3D-0D problem (3.24).

We remark that the number of equations, in the 3D-0D problem (3.24), balances with the number of unknowns: we have in total $1 + n_{\boldsymbol{w}} + n_{\mathbf{s}} + 3 + n_{\boldsymbol{c}} + 2$ unknowns and equations, respectively.

3.1.8 Reference configuration and initial displacement

Cardiac geometries are acquired from in vivo medical images through imaging techniques. In principle, these geometries are not stress free, due to the blood pressure

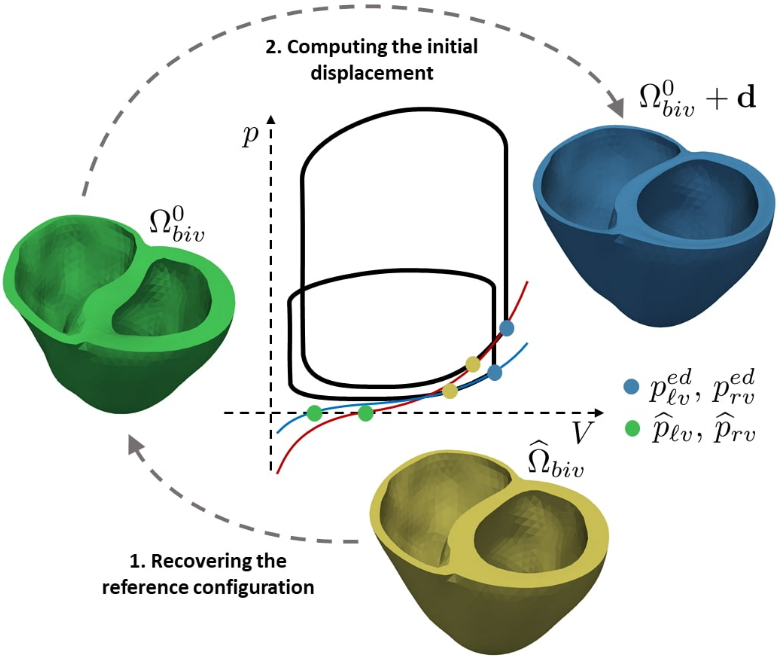

Figure 3.6: Schematic representation of the strategy used to recover the reference configuration and to set the mechanics initial condition. The red and blue lines represent the Klotz curves [114] (i.e. the pressure-volume relationship of the relaxed ventricles) for LV and RV. The black lines represent schematic pressure-volume loops.

acting on the endocardia. Therefore, we need to estimate the unloaded (i.e. stress-free) configuration (also named reference configuration) to which the 3D-0D model (3.24) refers. To recover the reference configuration Ω^0_{biv}, starting from a geometry $\widehat{\Omega}_{biv}$ (where a pressure $\widehat{p}_{\ell v} > 0$ and $\widehat{p}_{rv} > 0$ acts on LV and RV endocardia, respectively) acquired from medical images (typically during the diastolic phase), we extend to the biventricular geometries the procedure proposed for LV in [198]. We assume that the configuration $\widehat{\Omega}_{biv}$ is acquired during the diastole, when the biventricular geometry is loaded with pressures $\pi_{\ell v} = \widehat{p}_{\ell v}$, $\pi_{rv} = \widehat{p}_{rv}$ and a residual active tension $T_a = \widehat{T}_a$ is present. To recover the reference configuration Ω^0_{biv} we solve the following inverse problem:
Find the domain Ω^0_{biv} such that, if we inflate Ω^0_{biv} by $\mathbf{d}$, solution of the differential problem[3]

$$\begin{cases} \nabla \cdot \mathbf{P}(\mathbf{d}, T_a(\mathbf{s}, \boldsymbol{x})) = \mathbf{0} & \text{in } \Omega^0_{biv}, \\ \mathbf{P}(\mathbf{d}, T_a(\mathbf{s}, \boldsymbol{x}))\mathbf{N} + \mathbf{K}^{vepi}\mathbf{d} = \mathbf{0} & \text{on } \Gamma^0_{vepi}, \\ \mathbf{P}(\mathbf{d}, T_a(\mathbf{s}, \boldsymbol{x}))\mathbf{N} = -\pi_{\ell v}\, J\mathbf{F}^{-T}\mathbf{N} & \text{on } \Gamma^0_{\ell v}, \\ \mathbf{P}(\mathbf{d}, T_a(\mathbf{s}, \boldsymbol{x}))\mathbf{N} = -\pi_{rv}\, J\mathbf{F}^{-T}\mathbf{N} & \text{on } \Gamma^0_{rv}, \\ \mathbf{P}(\mathbf{d}, T_a(\mathbf{s}, \boldsymbol{x}))\mathbf{N} = |J\mathbf{F}^{-T}\mathbf{N}| \left[\pi_{\ell v}\mathbf{v}^{base}_{\ell v}(\hat{\xi}) + \pi_{rv}\mathbf{v}^{base}_{rv}(\hat{\xi})\right] & \text{on } \Gamma^0_{base}, \end{cases} \tag{3.25}$$

obtained for $\pi_{\ell v} = \widehat{p}_{\ell v}$, $\pi_{rv} = \widehat{p}_{rv}$ and $T_a = \widehat{T}_a$, we get the domain $\widehat{\Omega}_{biv}$.

---

[3] The problem (3.25) is derived from ($\mathscr{M}$) setting aside the time dependent terms.

After recovering Ω^0_{biv}, we inflate the biventricular reference configuration Ω^0_{biv} by solving again problem (3.25) (but now as a forward problem), where we set the pressures $\pi_{\ell v} = p^{ed}_{\ell v}$ and $\pi_{\ell v} = p^{ed}_{rv}$ with the superscript ed stands for the end-diastolic phase. In this way we obtain the end-diastolic configuration for the biventricular geometry. Hence, the solution $\mathbf{d}$ of the problem (3.25) and the pressures $p^{ed}_{\ell v}$ and p^{ed}_{rv} are set as initial conditions $\mathbf{d}_0$ (for $\mathbf{d}$), $p_{\ell v,0}$ (for $p_{\ell v}$) and $p_{rv,0}$ (for p_{rv}) in the 3D-0D problem (3.24). The above procedure is represented in Figure 3.6. For the numerical resolution of the above inverse problem we refer to [199], where several algorithms, based on fixed-point iteration schemes, are proposed.

3.2 Numerical approximation of the 3D-0D model

In this section, we illustrate the numerical discretization of the 3D-0D problem (3.24). Specifically, we follow the segregated-intergrid-staggered (SIS) approach proposed in [199, 209], which is extended here to the biventricular case. In the SIS numerical scheme, the core models $(\mathscr{E}) - (\mathscr{A}) - (\mathscr{M}) - (\mathscr{C})$ are solved sequentially in a segregated manner by using different resolutions in space and time, to properly handle the different space-time scales of the core models, contributing to both cardiac EM and blood circulation [159, 188, 187].

We begin by introducing, in Sections 3.2.1 and 3.2.2, the space and time discretizations of the 3D-0D problem (3.24), explaining how the core models $(\mathscr{E}) - (\mathscr{A}) - (\mathscr{M}) - (\mathscr{C})$ are reciprocally solved within the adopted SIS numerical scheme. Then, in Section 3.2.3, we detail how to solve, at the algebraic level, the 3D-0D coupled problem. In Section 3.2.4, we summarize the SIS numerical scheme. Finally, in Section 3.2.5, we explain the strategy that we adopt to reach a limit-cycle.

3.2.1 Space discretization

For the space discretization, we use continuous Finite Element Method (FEM) built on hexahedral meshes [186]. We consider two nested meshes Ω_{h_1} and Ω_{h_2} of the computational domain Ω^0_{biv}, where h_1 and h_2, with $h_1 < h_2$, represent the mesh sizes. The mesh Ω_{h_1} is built by uniformly refining Ω_{h_2} [1, 40]. We adopt the finer mesh Ω_{h_1} for $(\mathscr{E})$, where it is essential to accurately capture the dynamics of travelling waves, while the coarser one Ω_{h_2} is used for both $(\mathscr{A})$ and $(\mathscr{M})$, which feature larger spatial scale [20, 199, 73], see Figure 3.7.

We employ an efficient intergrid transfer operator between the two nested grids Ω_{h_1} and Ω_{h_2}, which allows to evaluate the feedback between $(\mathscr{E})$ and $(\mathscr{A}) - (\mathscr{M})$ [199]. The intergrid transfer operator can be generalized to the case of locally-refined non conforming nested grids. For more details about this strategy, we refer the reader to [209].

We denote by $\boldsymbol{a}_h(t) \approx \boldsymbol{a}(t)$, with either $h = h_1, h_2$, the semi-discretized FE approximation of the generic (scalar a_h, vectorial $\boldsymbol{a}_h$ or tensorial $\mathbf{A}_h$) variable $\boldsymbol{a}(t) \colon \Omega^0_{biv} \times (0, T] \to \mathbb{R}^d$, defined over the computational mesh Ω_{h_1} $(h = h_1)$ or Ω_{h_2} $(h = h_2)$. Meanwhile, we identify by $\underline{\boldsymbol{a}}_h(t)$ the vector collecting the DOFs associated with $\boldsymbol{a}_h(t)$, with either $h = h_1, h_2$.

We introduce the following finite dimensional space:

$$\mathcal{X}^r_h = \{v_h \in C^0(\overline{\Omega}^0_{biv}) : v_h|_{\mathrm{K}} \in \mathbb{Q}_r(K) \;\; \forall K \in \Omega_h\}, \qquad r \in \mathbb{N}^+, \;\; h = h_1, h_2,$$

where $\mathbb{Q}_r(K)$ is the space of polynomials of degree less than or equal to r (with $r \geq 1$), over a mesh element K of either Ω_{h_1} $(h = h_1)$ or Ω_{h_2} $(h = h_2)$.

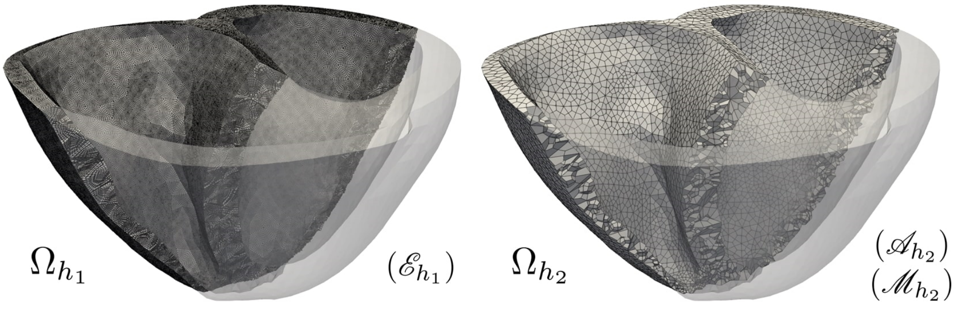

Figure 3.7: Nested meshes Ω_{h_1} (on the left) and Ω_{h_2} (on the right), with $h_1 < h_2$, used for space discretization of the 3D-0D model: the finer mesh Ω_{h_1} for $(\mathscr{E})$, while the coarser one (Ω_{h_2}) for both $(\mathscr{A})$ and $(\mathscr{M})$.

The FE approximation of the generic $\boldsymbol{a}_h$ and the corresponding vector $\underline{\boldsymbol{a}}_h$ collecting all the DOFs are then expressed respectively by

$$\boldsymbol{a}_h(t) = \sum_{i=1}^{N_a} a_i(t)\boldsymbol{\varphi}_i \qquad \text{and} \qquad \underline{\boldsymbol{a}}_h(t) = [a_i(t), \dots, a_{N_a}(t)]^T,$$

where $\{\boldsymbol{\varphi}_i\}_{i=1}^{N_a}$ is the set of basis functions for the FE space $[\mathcal{X}_{h_1}^r]^d$ with $N_a = \dim([\mathcal{X}_{h_1}^r]^d)$ and a_i $(i = 1, \dots, N_a)$ are the nodal values (DOFs) of the FE approximation variable, entering in the vector $\underline{\boldsymbol{a}}_h$.

Electrophysiology $(\mathscr{E}_{h_1})$

The semi-discretized in space formulation $(\mathscr{E}_{h_1})$ of the monodomain system (3.1) reads: Find $(u_{h_1}(t), \boldsymbol{w}_{h_1}(t)) \in \mathcal{X}_{h_1}^r \times [\mathcal{X}_{h_1}^r]^{n_{\boldsymbol{w}}}$ for all $t \in (0, T]$, given $u_{h_1}(0)$ and $\boldsymbol{w}_{h_1}(0)$, such that

$$\begin{cases} \chi_m C_m \displaystyle\int_{\Omega_{h_1}} J_{h_1} \dot{u}_{h_1}(t)\varphi_i \, d\Omega + \chi_m \int_{\Omega_{h_1}} J_{h_1} \mathcal{I}_{ion}(u_{h_1}(t), \boldsymbol{w}_{h_1}(t))\varphi_i \, d\Omega + \\ + \displaystyle\int_{\Omega_{h_1}} (J_{h_1} \mathbf{F}_{h_1}^{-1} \mathbf{D} \mathbf{F}_{h_1}^{-T} \nabla u_{h_1}(t)) \cdot \nabla \varphi_i \, d\Omega - \chi_m \int_{\Omega_{h_1}} J_{h_1} \mathcal{I}_{app}(t) \varphi_i \, d\Omega = 0, \\ \qquad \qquad \qquad \qquad \forall i = 1, \dots, N_u, \qquad (3.26a) \\ \displaystyle\int_{\Omega_{h_1}} \dot{\boldsymbol{w}}_{h_1}(t) \cdot \boldsymbol{\varphi}_i \, d\Omega - \int_{\Omega_{h_1}} \boldsymbol{H}(u_{h_1}(t), \boldsymbol{w}_{h_1}(t)) \cdot \boldsymbol{\varphi}_i \, d\Omega = 0, \\ \qquad \qquad \qquad \qquad \forall i = 1, \dots, N_{n_{\boldsymbol{w}}}, \qquad (3.26b) \end{cases}$$

where the over-dot notation is used for the time derivative and $\{\varphi_i\}_{i=1}^{N_u}$ and $\{\boldsymbol{\varphi_i}\}_{i=1}^{N_{n_{\boldsymbol{w}}}}$ are the sets of basis functions for the FE spaces $\mathcal{X}_{h_1}^r$ and $[\mathcal{X}_{h_1}^r]^{n_{\boldsymbol{w}}}$, with $N_u = \dim(\mathcal{X}_{h_1}^r)$ and $N_{n_{\boldsymbol{w}}} = \dim([\mathcal{X}_{h_1}^r]^{n_{\boldsymbol{w}}})$, respectively. Moreover, $\boldsymbol{w}_{h_1}(t)$ and $u_{h_1}(t)$ are the semi-discretized versions of the transmembrane potential and the ionic vector variable, respectively. The tensor $\mathbf{F}_{h_1}$, with $J_{h_1} = \det(\mathbf{F}_{h_1})$, is the interpolated deformation tensor, obtained through the following procedure [1, 209]:

- First $\nabla\mathbf{d}_{h_2}$ is recovered from Ω_{h_2}, thanks to an L^2 projection [209], from the approximated solution $\mathbf{d}_{h_2}$ of problem ($\mathscr{M}_{h_2}$) (that will be presented shortly in this section);

- Then $\nabla\mathbf{d}_{h_2}$ is interpolated on Ω_{h_1}, exploiting our intergrid transfer operator between nested meshes [209], obtaining $\nabla\mathbf{d}_{h_1}$;

- Finally, we build $\mathbf{F}_{h_1} = \mathbf{I}_{h_1} + \nabla\mathbf{d}_{h_1}$ directly on Ω_{h_1}.

Introducing the vectors $\underline{\boldsymbol{u}}_{h_1}(t)$ and $\underline{\boldsymbol{w}}_{h_1}(t)$ collecting the DOFs associated with $u_{h_1}(t)$ and $\boldsymbol{w}_{h_1}(t)$, respectively, Equation (3.26) can be written as a system of non-linear ODEs:

$$\begin{cases} \mathcal{M}^{(J)}\dot{\underline{\boldsymbol{u}}}_{h_1}(t) + \mathcal{K}(\underline{\mathbf{d}}_{h_1}(t))\underline{\boldsymbol{u}}_{h_1}(t) + \boldsymbol{I}_{ion}(\underline{\boldsymbol{u}}_{h_1}(t), \underline{\boldsymbol{w}}_{h_1}(t)) - \boldsymbol{I}_{app}(t) = \mathbf{0} & \forall t \in (0,T], \\ \mathcal{M}^{(1)}\dot{\underline{\boldsymbol{w}}}_{h_1}(t) - \overline{\boldsymbol{H}}(\underline{\boldsymbol{u}}_{h_1}(t), \underline{\boldsymbol{w}}_{h_1}(t)) = \mathbf{0} & \forall t \in (0,T], \\ \underline{\boldsymbol{u}}_{h_1}(0) = \underline{\boldsymbol{u}}_{0,h_1}, \quad \underline{\boldsymbol{w}}_{h_1}(0) = \underline{\boldsymbol{w}}_{0,h_1} & t = 0, \end{cases} \tag{3.27}$$

where the following matrices and vectors have been defined

$$\begin{aligned} \mathcal{M}_{ij}^{(J)} &= \chi_m C_m \int_{\Omega_{h_1}} J_{h_1}\varphi_j\varphi_i \, d\Omega, \\ \mathcal{M}_{ij}^{(1)} &= \int_{\Omega_{h_1}} \boldsymbol{\varphi_j} \cdot \boldsymbol{\varphi_i} \, d\Omega, \\ \mathcal{K}_{ij}(\underline{\mathbf{d}}_{h_1}(t)) &= \int_{\Omega_{h_1}} (J_{h_1}\mathbf{F}_{h_1}^{-1}\mathbf{D}\mathbf{F}_{h_1}^{-T}\nabla\varphi_j) \cdot \nabla\varphi_i \, d\Omega, \\ \left(\boldsymbol{I}_{ion}(\underline{\boldsymbol{u}}_{h_1}(t), \underline{\boldsymbol{w}}_{h_1}(t))\right)_i &= \chi_m \int_{\Omega_{h_1}} J_{h_1}\mathcal{I}_{ion}(u_{h_1}(t), \boldsymbol{w}_{h_1}(t))\varphi_i \, d\Omega, \\ \left(\boldsymbol{I}_{app}(t)\right)_i &= \chi_m \int_{\Omega_{h_1}} J_{h_1}\mathcal{I}_{app}(t)\varphi_i \, d\Omega, \\ \left(\overline{\boldsymbol{H}}(\underline{\boldsymbol{u}}_{h_1}(t), \underline{\boldsymbol{w}}_{h_1}(t))\right)_i &= \int_{\Omega_{h_1}} \boldsymbol{H}(u_{h_1}(t), \boldsymbol{w}_{h_1}(t)) \cdot \boldsymbol{\varphi_i} \, d\Omega. \end{aligned}$$

For the evaluation of the nonlinear term $\boldsymbol{I}_{ion}(\underline{\boldsymbol{u}}_{h_1}(t), \underline{\boldsymbol{w}}_{h_1}(t))$, three strategies are available (see [188, 116, 170, 169] for further details). Here, we use the so-called ionic current interpolation (ICI) approach [116], which yields a faster assembly of the ionic term [116]. Specifically, denoting by $\{\boldsymbol{x}_q^K\}_{q=1}^{N_q}$ and $\{\omega_q^K\}_{q=1}^{N_q}$ the quadrature nodes and weights of a generic mesh element $K \in \Omega_{h_1}$, the term $\boldsymbol{I}_{ion}(\underline{\boldsymbol{u}}_{h_1}(t), \underline{\boldsymbol{w}}_{h_1}(t))$ is firstly evaluated at the DOFs and then interpolated at the quadrature nodes, i.e.

$$\begin{aligned} &\int_{\Omega_{h_1}} \mathcal{I}_{ion}(u_{h_1}(t), \boldsymbol{w}_{h_1}(t))\varphi_i \, d\Omega \approx \\ &\qquad \approx \sum_{K \in \Omega_{h_1}} \left(\sum_{q=1}^{N_q} \sum_{j=1}^{N_u} \mathcal{I}_{ion}\left(u_j(t), \boldsymbol{w}_j(t)\right) \varphi_j(\boldsymbol{x}_q^K)\varphi_i(\boldsymbol{x}_q^K)\omega_q^K \right). \end{aligned} \tag{3.28}$$

Activation ($\mathscr{A}_{h_2}$)

The semi-discretized in space formulation ($\mathscr{A}_{h_2}$) of MA core model (3.3) reads:

Find $\mathbf{s}_{h_2}(t) \in [\mathcal{X}_{h_2}^r]^2$ for all $t \in (0, T]$, given $\mathbf{s}_{h_1}(0)$, such that

$$\int_{\Omega_{h_2}} \dot{\mathbf{s}}_{h_2}(t) \cdot \boldsymbol{\varphi_i}\, d\Omega - \int_{\Omega_{h_2}} \boldsymbol{K}(\mathbf{s}_{h_2}(t), w_{\mathrm{Ca},h_2}(t), SL_{h_2}(t)) \cdot \boldsymbol{\varphi_i}\, d\Omega = 0, \qquad \forall i = 1, \dots, N_{n_\mathbf{s}}, \tag{3.29}$$

where $\{\boldsymbol{\varphi_i}\}_{i=1}^{N_{n_\mathbf{s}}}$ is the set of basis functions for the FE space $[\mathcal{X}_{h_2}^r]^2$ with $N_{n_\mathbf{s}} = \dim([\mathcal{X}_{h_2}^r]^2)$. Furthermore, $\mathbf{s}_{h_2}(t)$ is the semi-discretized activation vector variable and $w_{\mathrm{Ca},h_2}(t)$ is obtained by interpolating the intracellular calcium concentration variable of TTP06 ionic model from Ω_{h_1} to Ω_{h_2}, using the intergrid transfer operator between nested meshes [209]. On the other hand, $SL_{h_2}(t)$ is directly obtained by $SL_{h_2} = SL_0\sqrt{\mathcal{I}_{4f}(\mathbf{d}_{h_2})}$, where $\mathcal{I}_{4f,h_2}(t) = \mathbf{F}_{h_2}(t)\boldsymbol{f}_0 \cdot \mathbf{F}_{h_2}(t)\boldsymbol{f}_0$. Finally, the output of $(\mathscr{A}_{h_2})$ is $T_{a,h_2}(t)$, which denotes the semi-discretized active tension, evaluated as

$$T_{a,h_2}(t) = T_a^{max} G(\mathbf{s}_{h_2}(t)) \left[\hat{\xi}_{h_2} + C_{\ell rv}(1 - \hat{\xi}_{h_2})\right].$$

Introducing the vector $\underline{\mathbf{s}}_{h_2}(t)$ collecting the DOFs associated with $\mathbf{s}_{h_2}(t)$, Equation (3.29) can be written as a system of ODEs:

$$\begin{cases} \mathcal{M}^{(2)}\dot{\underline{\mathbf{s}}}_{h_2}(t) - \overline{\boldsymbol{K}}(\underline{\mathbf{s}}_{h_2}(t), \underline{w_{\mathrm{Ca}}}_{h_2}(t), \underline{SL}_{h_2}(t)) = \mathbf{0} & \forall t \in (0, T], \\ \underline{\mathbf{s}}_{h_2}(0) = \underline{\mathbf{s}}_{0,h_2} & t = 0, \end{cases} \tag{3.30}$$

where the following matrices and vectors have been defined

$$\mathcal{M}_{ij}^{(2)} = \int_{\Omega_{h_2}} \boldsymbol{\varphi_j} \cdot \boldsymbol{\varphi_i}\, d\Omega,$$

$$\left(\overline{\boldsymbol{K}}(\underline{\mathbf{s}}_{h_2}(t), \underline{w_{\mathrm{Ca}}}_{h_2}(t), \underline{SL}_{h_2}(t))\right)_i = \int_{\Omega_{h_2}} \boldsymbol{K}(\mathbf{s}_{h_2}(t), w_{\mathrm{Ca},h_2}(t), SL_{h_2}(t)) \cdot \boldsymbol{\varphi_i}\, d\Omega.$$

Finally, the semi-discretized active tension, evaluated in the DOFs, reads:

$$\underline{T_a}_{h_2}(t) = T_a^{max} G(\underline{\mathbf{s}}_{h_2}(t)) \left[\underline{\hat{\xi}}_{h_2} + C_{\ell rv}(1 - \underline{\hat{\xi}}_{h_2})\right].$$

Mechanics $(\mathscr{M}_{h_2})$

The semi-discretized in space formulation $(\mathscr{M}_{h_2})$ of TM core model (3.4) reads: Find $\mathbf{d}_{h_2}(t) \in [\mathcal{X}_{h_2}^s]^3$ for all $t \in (0, T]$, given $\mathbf{d}_{h_2}(0)$ and $\dot{\mathbf{d}}_{h_2}(0)$, such that

$$\begin{aligned} &\int_{\Omega_{h_2}} \rho_s \ddot{\mathbf{d}}_{h_2}(t) \cdot \boldsymbol{\varphi}_i\, d\Omega + \int_{\Omega_{h_2}} \mathbf{P}(\mathbf{d}_{h_2}(t), T_{a,h_2}(t)) : \nabla \boldsymbol{\varphi}_i d\Omega + \\ &\quad - \int_{\Gamma_{h_2}^{vepi}} \Big[(\mathbf{N}_{h_2} \otimes \mathbf{N}_{h_2}) \left(K_\perp^{vepi} \mathbf{d}_{h_2}(t) + C_\perp^{vepi} \dot{\mathbf{d}}_{h_2}(t) \right) + \\ &\quad + (\mathbf{N}_{h_2} \otimes \mathbf{N}_{h_2} - \mathbf{I}) \left(K_\parallel^{vepi} \mathbf{d}_{h_2}(t) + C_\parallel^{vepi} \dot{\mathbf{d}}_{h_2}(t) \right) \Big] \cdot \boldsymbol{\varphi}_i\, d\Gamma + \\ &\quad + p_{\ell v}(t) \int_{\Gamma_{h_2}^{\ell v}} J_{h_2} \mathbf{F}_{h_2}^{-T} \mathbf{N}_{h_2} \cdot \boldsymbol{\varphi}_i\, d\Gamma - p_{\ell v}(t) \int_{\Gamma_{h_2}^{base}} |J_{h_2} \mathbf{F}_{h_2}^{-T} \mathbf{N}_{h_2}| \mathbf{v}_{\ell v,h_2}^{base} \cdot \boldsymbol{\varphi}_i\, d\Gamma + \\ &\quad + p_{rv}(t) \int_{\Gamma_{h_2}^{rv}} J_{h_2} \mathbf{F}_{h_2}^{-T} \mathbf{N}_{h_2} \cdot \boldsymbol{\varphi}_i\, d\Gamma - p_{rv}(t) \int_{\Gamma_{h_2}^{base}} |J_{h_2} \mathbf{F}_{h_2}^{-T} \mathbf{N}_{h_2}| \mathbf{v}_{rv,h_2}^{base} \cdot \boldsymbol{\varphi}_i\, d\Gamma = 0 \\ &\qquad \forall i = 1, \dots, N_\mathbf{d}, \end{aligned} \tag{3.31}$$

where[4] we denoted by $[\mathcal{X}^r_{h_2}]^3$ the finite dimensional subspace of vector valued functions and by $\{\boldsymbol{\varphi}_i\}_{i=1}^{N_\mathbf{d}}$ its basis, with $N_\mathbf{d} = \dim([\mathcal{X}^r_{h_2}]^3)$, and we introduced

$$
\begin{aligned}
\mathbf{v}^{base}_{\ell v,h_2} &= \hat{\xi}_{h_2} \frac{\int_{\Gamma^{\ell v}_{h_2}} J_{h_2} \mathbf{F}^{-T}_{h_2} \mathbf{N}_{h_2} \, d\Gamma}{\int_{\Gamma^{base}_{h_2}} \hat{\xi}_{h_2} |J_{h_2} \mathbf{F}^{-T}_{h_2} \mathbf{N}_{h_2}| \, d\Gamma}, \\
\mathbf{v}^{base}_{rv,h_2} &= (1-\hat{\xi}_{h_2}) \frac{\int_{\Gamma^{rv}_{h_2}} J_{h_2} \mathbf{F}^{-T}_{h_2} \mathbf{N}_{h_2} \, d\Gamma}{\int_{\Gamma^{base}_{h_2}} (1-\hat{\xi}_{h_2}) |J_{h_2} \mathbf{F}^{-T}_{h_2} \mathbf{N}_{h_2}| \, d\Gamma}.
\end{aligned}
$$

Moreover, $T_{a,h_2}(t)$ is given by the solution of problem $(\mathscr{A}_{h_2})$, previously described.

Denoting by $\underline{\mathbf{d}}_{h_2}(t)$ the vector collecting the DOFs associated with $\mathbf{d}_{h_2}(t)$, the corresponding algebraic formulation of Equation (3.31) reads:

$$
\begin{cases}
\rho_s \mathcal{M}^{(2)} \ddot{\underline{\mathbf{d}}}_{h_2}(t) + \mathcal{F} \dot{\underline{\mathbf{d}}}_{h_2}(t) + \mathcal{G} \underline{\mathbf{d}}_{h_2}(t) + \boldsymbol{S}(\underline{\mathbf{d}}_{h_2}(t), \underline{T_a}_{h_2}(t)) + & \\
\qquad - p_{\ell v}(t)\, \boldsymbol{B}_{\ell v}(\underline{\mathbf{d}}_{h_2}(t)) - p_{rv}(t)\, \boldsymbol{B}_{rv}(\underline{\mathbf{d}}_{h_2}(t)) + & \\
\qquad + p_{\ell v}(t)\, \boldsymbol{P}_{\ell v}(\underline{\mathbf{d}}_{h_2}(t)) + p_{rv}(t)\, \boldsymbol{P}_{rv}(\underline{\mathbf{d}}_{h_2}(t)) = \mathbf{0} & \forall t \in (0,T], \\
\underline{\mathbf{d}}_{h_2}(0) = \underline{\mathbf{d}}_{0,h_2}, \quad \dot{\underline{\mathbf{d}}}_{h_2}(0) = \dot{\underline{\mathbf{d}}}_{0,h_2} & t = 0,
\end{cases}
\tag{3.32}
$$

where the following matrices and vectors have been defined

$$
\begin{aligned}
\boldsymbol{S}_i(\underline{\mathbf{d}}_{h_2}(t), \underline{T_a}_{h_2}(t)) &= \int_{\Omega_{h_2}} \mathbf{P}(\mathbf{d}_{h_2}(t), T_{a,h_2}(t)) : \nabla \boldsymbol{\varphi}_i \, d\Omega, \\
\mathcal{F}_{ij} &= \int_{\Gamma^{vepi}_{h_2}} \left[C^{vepi}_{\parallel} (\mathbf{N}_{h_2} \otimes \mathbf{N}_{h_2} - \mathbf{I}_{h_2}) - C^{vepi}_{\perp} (\mathbf{N}_{h_2} \otimes \mathbf{N}_{h_2}) \right] \boldsymbol{\varphi}_j \cdot \boldsymbol{\varphi}_i \, d\Gamma, \\
\mathcal{G}_{ij} &= \int_{\Gamma^{vepi}_{h_2}} \left[K^{vepi}_{\parallel} (\mathbf{N}_{h_2} \otimes \mathbf{N}_{h_2} - \mathbf{I}_{h_2}) - K^{vepi}_{\perp} (\mathbf{N}_{h_2} \otimes \mathbf{N}_{h_2}) \right] \boldsymbol{\varphi}_j \cdot \boldsymbol{\varphi}_i \, d\Gamma, \\
(\boldsymbol{B}_k(\underline{\mathbf{d}}_{h_2}(t)))_i &= \int_{\Gamma^{base}_{h_2}} |J_{h_2} \mathbf{F}^{-T}_{h_2} \mathbf{N}_{h_2}| \mathbf{v}^{base}_{k,h_2} \cdot \boldsymbol{\varphi}_i \, d\Gamma, \quad k = \ell v, rv. \\
(\boldsymbol{P}_k(\underline{\mathbf{d}}_{h_2}(t)))_i &= \int_{\Gamma^{k}_{h_2}} J_{h_2} \mathbf{F}^{-T}_{h_2} \mathbf{N}_{h_2} \cdot \boldsymbol{\varphi}_i \, d\Gamma, \quad k = \ell v, rv.
\end{aligned}
$$

Equations (3.27), (3.30) and (3.32) provide the splitted semi-discretization in space of the entire 3D EM model.

3.2.2 Time discretization

For the time discretization, we employ Finite Difference (FD) schemes [189] in a staggered approach: different time step sizes are used for the core models $(\mathscr{E}) - (\mathscr{A}) - (\mathscr{M}) - (\mathscr{V}) - (\mathscr{C})$, allowing to separate and properly manage the temporal scales related to the cardiac 3D-0D problem (3.24).

We consider a coarse uniform subdivision $0 = t_0 < t_1 < \cdots < t_N = T$ of the time interval $[0,T]$ with a time step size Δt, and a finer one with $\tau = \Delta t / N_{sub}$, where $N_{sub} \in \mathbb{N}$, see Figure 3.8. We adopt the finer time-grid, with τ, to account for the faster dynamics of $(\mathscr{E})$, and the coarser one, with Δt, for $(\mathscr{A}) - (\mathscr{M}) - (\mathscr{V}) - (\mathscr{C})$,

---

[4] Notice that in the space discretization (3.31) of the TM core model (3.4), we set $\pi_{\ell v} = p_{\ell v}$ and $\pi_{rv} = p_{rv}$ in order to be complaint with the 3D-0D problem (3.24).

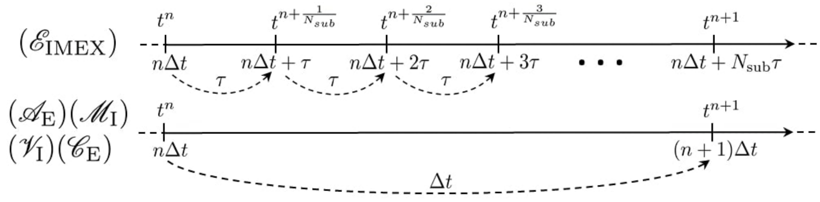

Figure 3.8: Graphical representation of the time advancement scheme.

which are characterized by a larger temporal scales [20, 199, 73]. In particular, the cardiac EP model is solved by means of the Backward Difference Formulae (BDF) discretization of order $\sigma \geq 2$ (BDFσ), adopting an implicit-explicit (IMEX) scheme, denoted by $(\mathscr{E}_{\mathrm{IMEX}})$ [193, 199, 152]. For the MA we employ an explicit BDF1 time scheme, marked as $(\mathscr{A}_{\mathrm{E}})$, whereas for TM we use a fully implicit scheme, indicated by $(\mathscr{M}_{\mathrm{I}}) - (\mathscr{V}_{\mathrm{I}})$ [199]. Finally, we utilize an explicit BDF1 for $(\mathscr{C}_{\mathrm{E}})$ [199], see Figure 3.8.

To denote a generic variable at the n-th time step, we use the n superscript, e.g. $\boldsymbol{a}^n \approx \boldsymbol{a}(t^n)$. Finally, we denote by $\underline{\boldsymbol{a}}_h^n \simeq \underline{\boldsymbol{a}}_h(t^n)$ (with either $h = h_1, h_2$) the vector collecting the DOFs associated to the fully discretized FEM problem, for the generic variable $\boldsymbol{a}(t)$ (scalar a, vectorial $\boldsymbol{a}$ or tensorial $\mathbf{A}$).

We begin our time advancing scheme, from t^n to t^{n+1}, with the problem $(\mathscr{E}_{\mathrm{IMEX}})$, which is the time discretization of the system (3.27). Once we set $t^{n+\frac{m}{N_{sub}}} = t^n + m\tau$, for $m = 1, \dots, N_{sub}$, $(\mathscr{E}_{\mathrm{IMEX}})$ reads as follows:

- We find $\underline{\boldsymbol{w}}_{h_1}^{n+\frac{m}{N_{sub}}}$ defined on Ω_{h_1} by solving:

  $$\frac{\alpha_{\mathrm{BDF}\sigma}}{\tau}\mathcal{M}^{(1)}\underline{\boldsymbol{w}}_{h_1}^{n+\frac{m}{N_{sub}}} = \frac{1}{\tau}\mathcal{M}^{(1)}\underline{\boldsymbol{w}}^{n}_{h_1,\mathrm{BDF}\sigma} + \overline{\boldsymbol{H}}\Big(\underline{\boldsymbol{u}}_{h_1,\mathrm{EXT}\sigma}^{n+\frac{m}{N_{sub}}}, \underline{\boldsymbol{w}}_{h_1,\mathrm{EXT}\sigma}^{n+\frac{m}{N_{sub}}}, \underline{\boldsymbol{w}}_{h_1}^{n+\frac{m}{N_{sub}}}\Big), \tag{3.33}$$

  where $\alpha_{\mathrm{BDF}\sigma}$ and $\underline{\boldsymbol{w}}^{n}_{h_1,\mathrm{BDF}\sigma}$ are the terms associated to the BDFσ discretization of the time derivative $\dot{\underline{\boldsymbol{w}}}_{h_1}$, while the subscript EXTσ denotes the extrapolation to time step $n + \frac{m}{N_{sub}}$, from previous time steps, given by the BDFσ at hand [70]. Specifically, for the ionic variables [5] we employ an explicit (extrapolation) treatment of the ionic concentration variables (indicated with $\underline{\boldsymbol{w}}_{h_1,\mathrm{EXT}\sigma}^{n+\frac{m}{N_{sub}}}$) to avoid the solution of a nonlinear system. This does not compromise the stability of the scheme, thanks to the non-stiff dynamics of concentrations. On the other hand, we use an implicit treatment of the gating variables (referred to $\underline{\boldsymbol{w}}_{h_1}^{n+\frac{m}{N_{sub}}}$), due to the severe CFL condition on the time step induced by an explicit scheme. Indeed, thanks to the linear dynamics of the gating variables, such implicit handling does not require the solution of a system of linear or nonlinear equations [193]. The following approach is an extension, to the BDFσ case, of the first order IMEX scheme proposed in [193].

---

[5] We recall that the ionic vector variable $\boldsymbol{w}$ is constituted by the ionic concentrations and gating variables. More precisely, the 18 ionic variables TTP06 model embeds 6 ionic concentrations (featuring a nonlinear but non-stiff dynamics) and 12 gating variables (linear but with an highly stiff dynamics) [193].

- We interpolate $\underline{\mathbf{d}}_{h_2}^n$ on the finer mesh Ω_{h_1} once per time step, at $t = t^n$, obtaining $\underline{\mathbf{d}}_{h_1}^n$. We use $\underline{\boldsymbol{w}}_{h_1}^{n+\frac{m}{N_{sub}}}$ from (3.33) and $\underline{\mathbf{d}}_{h_1}^n$ to find $\underline{\boldsymbol{u}}_{h_1}^{n+\frac{m}{N_{sub}}}$ over Ω_{h_1} by solving:

$$\begin{aligned}\Big(\frac{\alpha_{\mathrm{BDF}\sigma}}{\tau}\mathcal{M}^{(J)} + \mathcal{K}(\underline{\mathbf{d}}_{h_1}^n) + \boldsymbol{I}_u^{ion}\left(\underline{\boldsymbol{u}}_{h_1,\mathrm{EXT}\sigma}^{n+\frac{m}{N_{sub}}}, \underline{\boldsymbol{w}}_{h_1}^{n+\frac{m}{N_{sub}}}\right)\Big)\,\underline{\boldsymbol{u}}_{h_1}^{n+\frac{m}{N_{sub}}} = \\ \frac{1}{\tau}\mathcal{M}^{(J)}\underline{\boldsymbol{u}}_{h_1,\mathrm{BDF}\sigma}^{n} - \tilde{\boldsymbol{I}}^{ion}\left(\underline{\boldsymbol{u}}_{h_1,\mathrm{EXT}\sigma}^{n+\frac{m}{N_{sub}}}, \underline{\boldsymbol{w}}_{h_1}^{n+\frac{m}{N_{sub}}}\right) + \boldsymbol{I}_{app}\left(t^{n+\frac{m}{N_{sub}}}\right),\end{aligned} \tag{3.34}$$

  where $\boldsymbol{I}_u^{ion}$ is the derivative of the terms of $\boldsymbol{I}_{ion}$ that linearly depends on $\underline{\boldsymbol{u}}_{h_1}$, while $\tilde{\boldsymbol{I}}^{ion}$ collects all the other terms.

After having solved ($\mathscr{E}_{\mathrm{IMEX}}$), by means of Equations (3.33) and (3.34) for N_{sub} steps, we advance, from t^n to t^{n+1}, ($\mathscr{A}_{\mathrm{E}}$)–($\mathscr{M}_{\mathrm{I}}$)–($\mathscr{V}_{\mathrm{I}}$)–($\mathscr{C}_{\mathrm{E}}$) in the following way:

- We interpolate the calcium ionic variable $w_{\mathrm{Ca},h_1}^{n+1}$ from (3.33) on the coarser mesh Ω_{h_2}, obtaining $w_{\mathrm{Ca},h_2}^{n+1}$, and we find $\underline{\mathbf{s}}_{h_2}^{n+1}$ by solving ($\mathscr{A}_{\mathrm{E}}$) as follows:

$$\frac{1}{\Delta t}\mathcal{M}^{(2)}\underline{\mathbf{s}}_{h_2}^{n+1} = \frac{1}{\Delta t}\mathcal{M}^{(2)}\underline{\mathbf{s}}_{h_2}^{n} + \overline{\boldsymbol{K}}(\underline{\mathbf{s}}_{h_2}^{n}, \underline{w_{\mathrm{Ca}}}_{h_2}^{n+1}, \underline{SL}_{h_2}^{n}). \tag{3.35}$$

  where $\underline{SL}_{h_2}^n$ is obtained using $\underline{SL}_{h_2}^n = SL_0\sqrt{\mathcal{I}_{4f}(\underline{\mathbf{d}}_{h_2}^n)}$. Finally, we evaluate the fully discretized active tension, obtained as

$$\underline{T_a}_{h_2}^{(n+1)} = T_a^{max}G\left(\underline{\mathbf{s}}_{h_2}^{(n+1)}\right)\left[\underline{\hat{\xi}}_{h_2} + C_{\ell rv}(1 - \underline{\hat{\xi}}_{h_2})\right].$$

- We use $\underline{T_a}_{h_2}^{(n+1)}$, to update $\underline{\mathbf{d}}_{h_2}^{n+1}$, $p_{\ell v}^{n+1}$ and p_{rv}^{n+1} by solving the system ($\mathscr{M}_{\mathrm{I}}$)–($\mathscr{V}_{\mathrm{I}}$):

$$\begin{cases}\left(\rho_s\dfrac{1}{\Delta t^2}\mathcal{M}^{(2)} + \dfrac{1}{\Delta t}\mathcal{F} + \mathcal{G}\right)\underline{\mathbf{d}}_{h_2}^{n+1} + \boldsymbol{S}(\underline{\mathbf{d}}_{h_2}^{n+1}, \underline{T_a}_{h_2}^{(n+1)}) + \\ \qquad + p_{\ell v}^{n+1}\boldsymbol{P}_{\ell v}(\underline{\mathbf{d}}_{h_2}^{n+1}) + p_{rv}^{n+1}\boldsymbol{P}_{rv}(\underline{\mathbf{d}}_{h_2}^{n+1}) + \\ \qquad - p_{\ell v}^{n+1}\boldsymbol{B}_{\ell v}(\underline{\mathbf{d}}_{h_2}^{n}) - p_{rv}^{n+1}\boldsymbol{B}_{rv}(\underline{\mathbf{d}}_{h_2}^{n}) = \\ \qquad = \rho_s\dfrac{2}{\Delta t^2}\mathcal{M}^{(2)}\underline{\mathbf{d}}_{h_2}^{n} - \rho_s\dfrac{1}{\Delta t^2}\mathcal{M}^{(2)}\underline{\mathbf{d}}_{h_2}^{n-1} + \dfrac{1}{\Delta t}\mathcal{F}\underline{\mathbf{d}}_{h_2}^{n}, \\ V_{\ell v}^{\mathrm{3D}}(\underline{\mathbf{d}}_{h_2}^{n+1}) = V_{\ell v}(\boldsymbol{c}^n), \\ V_{rv}^{\mathrm{3D}}(\underline{\mathbf{d}}_{h_2}^{n+1}) = V_{rv}(\boldsymbol{c}^n).\end{cases} \tag{3.36}$$

- Finally, we update $\boldsymbol{c}^{n+1}$, using $p_{\ell v}^{n+1}$ and p_{rv}^{n+1}, by solving ($\mathscr{C}_{\mathrm{E}}$) with the forward Euler method (BDF1):

$$\boldsymbol{c}^{n+1} = \boldsymbol{c}^n + \Delta t\,\boldsymbol{G}_{\mathrm{B}}\left(t^n, \boldsymbol{c}^n, p_{\ell v}^{n+1}, p_{rv}^{n+1}\right). \tag{3.37}$$

In the next Section 3.2.3, we provide details about the numerical resolution, at the algebraic level, of the coupled problem (3.36). We refer the reader to Sections 3.1.6 and 3.2.1 for a detailed description of the terms involved in the problem (3.36).

3.2.3 Numerical solution of the 3D-0D coupled problem

Equation (3.36) is a non-linear saddle-point problem, which is numerically solved by means of a Newton strategy employing the Schur complement reduction [28].

The fully discretized version of $(\mathscr{M}_{\mathrm{I}}) - (\mathscr{V}_{\mathrm{I}})$, expressed by the system (3.36), can be compactly written as:

$$\begin{cases} \mathbf{r}_{\mathbf{d}}(\underline{\mathbf{d}}_h^{n+1}, p_{\ell v}^{n+1}, p_{rv}^{n+1}) & = \mathbf{0} \\ r_{p_{\ell v}}(\underline{\mathbf{d}}_h^{n+1}) & = 0 \\ r_{p_{rv}}(\underline{\mathbf{d}}_h^{n+1}) & = 0 \end{cases} \tag{3.38}$$

where we moved all the terms to the right hand side and $r_{p_{\ell v}}$, $r_{p_{rv}}$ and $\mathbf{r}_{\mathbf{d}}$ are suitable functions. Moreover, $h = h_2$ is understood.

We solve the non-linear saddle-point problem (3.38) by means of the following Newton algorithm (where the temporal index $n+1$ is understood) using, at the algebraic level, the Schur complement reduction [28]:

- We initialize, for $j = 0$, $\underline{\mathbf{d}}_h^{(0)} = \underline{\mathbf{d}}_h^n$, $p_{\ell v}^{(0)} = p_{\ell v}^n$ and $p_{rv}^{(0)} = p_{rv}^n$
- For $j = 1, 2, \ldots$, we solve the linear system
$$\begin{pmatrix} J_{\mathbf{d},\mathbf{d}}^{(j-1)} & J_{\mathbf{d},p_{\ell v}}^{(j-1)} & J_{\mathbf{d},p_{rv}}^{(j-1)} \\ J_{p_{\ell v},\mathbf{d}}^{(j-1)} & 0 & 0 \\ J_{p_{rv},\mathbf{d}}^{(j-1)} & 0 & 0 \end{pmatrix} \begin{pmatrix} \Delta\underline{\mathbf{d}}_h^{(j)} \\ \Delta p_{\ell v}^{(j)} \\ \Delta p_{rv}^{(j)} \end{pmatrix} = \begin{pmatrix} \mathbf{r}_{\mathbf{d}}^{(j-1)} \\ r_{p_{\ell v}}^{(j-1)} \\ r_{p_{rv}}^{(j-1)} \end{pmatrix}, \tag{3.39}$$
where
$J_{\mathbf{d},\mathbf{d}}^{(j-1)} = \frac{\partial}{\partial \underline{\mathbf{d}}}\mathbf{r}_{\mathbf{d}}(\underline{\mathbf{d}}_h^{(j-1)}, p_{\ell v}^{(j-1)}, p_{rv}^{(j-1)})$,
$J_{\mathbf{d},p_{\ell v}}^{(j-1)} = \frac{\partial}{\partial p_{\ell v}}\mathbf{r}_{\mathbf{d}}(\underline{\mathbf{d}}_h^{(j-1)}, p_{\ell v}^{(j-1)}, p_{rv}^{(j-1)})$, $J_{\mathbf{d},p_{rv}}^{(j-1)} = \frac{\partial}{\partial p_{rv}}\mathbf{r}_{\mathbf{d}}(\underline{\mathbf{d}}_h^{(j-1)}, p_{\ell v}^{(j-1)}, p_{rv}^{(j-1)})$,
$J_{p_{\ell v},\mathbf{d}}^{(j-1)} = \frac{\partial}{\partial \underline{\mathbf{d}}} r_{p_{\ell v}}(\underline{\mathbf{d}}_h^{(j-1)})$, $J_{p_{rv},\mathbf{d}}^{(j-1)} = \frac{\partial}{\partial \underline{\mathbf{d}}} r_{p_{rv}}(\underline{\mathbf{d}}_h^{(j-1)})$,
- We update
$\underline{\mathbf{d}}_h^{(j)} = \underline{\mathbf{d}}_h^{(j-1)} - \Delta\underline{\mathbf{d}}_h^{(j)}$, $p_{\ell v}^{(j)} = p_{\ell v}^{(j-1)} - \Delta p_{\ell v}^{(j)}$ and $p_{rv}^{(j)} = p_{rv}^{(j-1)} - \Delta p_{rv}^{(j)}$.
- When the convergence criterion (based on the increment) is satisfied, we set
$\underline{\mathbf{d}}_h^{n+1} = \underline{\mathbf{d}}_h^{(j)}$, $p_{\ell v}^{n+1} = p_{\ell v}^{(j)}$ and $p_{rv}^{n+1} = p_{rv}^{(j)}$.

We solve the saddle-point problem (3.39) via Schur complement reduction [28]. Specifically, system (3.38) can be written as

$$\begin{cases} J_{\mathbf{d},\mathbf{d}}\Delta\underline{\mathbf{d}}_h + J_{\mathbf{d},p_{\ell v}}\Delta p_{\ell v} + J_{\mathbf{d},p_{rv}}\Delta p_{rv} = \mathbf{r}_{\mathbf{d}} \\ J_{p_{\ell v},\mathbf{d}}\Delta\underline{\mathbf{d}}_h = r_{p_{\ell v}} \\ J_{p_{rv},\mathbf{d}}\Delta\underline{\mathbf{d}}_h = r_{p_{rv}} \end{cases}, \tag{3.40}$$

where for simplicity we omitted the superscript (j). Deriving $\Delta\underline{\mathbf{d}}_h$ form the first equation of (3.40) we have

$$\begin{cases} \Delta\underline{\mathbf{d}}_h = J_{\mathbf{d},\mathbf{d}}^{-1}(\mathbf{r}_{\mathbf{d}} - J_{\mathbf{d},p_{\ell v}}\Delta p_{\ell v} - J_{\mathbf{d},p_{rv}}\Delta p_{rv}) \\ J_{p_{\ell v},\mathbf{d}}J_{\mathbf{d},\mathbf{d}}^{-1}\mathbf{r}_{\mathbf{d}} - J_{p_{\ell v},\mathbf{d}}J_{\mathbf{d},\mathbf{d}}^{-1}J_{\mathbf{d},p_{\ell v}}\Delta p_{\ell v} - J_{p_{\ell v},\mathbf{d}}J_{\mathbf{d},\mathbf{d}}^{-1}J_{\mathbf{d},p_{rv}}\Delta p_{rv} = r_{p_{\ell v}} \\ J_{p_{rv},\mathbf{d}}J_{\mathbf{d},\mathbf{d}}^{-1}\mathbf{r}_{\mathbf{d}} - J_{p_{rv},\mathbf{d}}J_{\mathbf{d},\mathbf{d}}^{-1}J_{\mathbf{d},p_{\ell v}}\Delta p_{\ell v} - J_{p_{rv},\mathbf{d}}J_{\mathbf{d},\mathbf{d}}^{-1}J_{\mathbf{d},p_{rv}}\Delta p_{rv} = r_{p_{rv}} \end{cases}. \tag{3.41}$$

System (3.41) can be written as

$$\begin{cases} \Delta\underline{\mathbf{d}}_h = J_{\mathbf{d},\mathbf{d}}^{-1}(\mathbf{r}_{\mathbf{d}} - J_{\mathbf{d},p_{\ell v}}\Delta p_{\ell v} - J_{\mathbf{d},p_{rv}}\Delta p_{rv}) \\ J_{p_{\ell v},\mathbf{d}}J_{\mathbf{d},\mathbf{d}}^{-1}J_{\mathbf{d},p_{\ell v}}\Delta p_{\ell v} + J_{p_{\ell v},\mathbf{d}}J_{\mathbf{d},\mathbf{d}}^{-1}J_{\mathbf{d},p_{rv}}\Delta p_{rv} = J_{p_{\ell v},\mathbf{d}}J_{\mathbf{d},\mathbf{d}}^{-1}\mathbf{r}_{\mathbf{d}} - r_{p_{\ell v}} \\ J_{p_{rv},\mathbf{d}}J_{\mathbf{d},\mathbf{d}}^{-1}J_{\mathbf{d},p_{\ell v}}\Delta p_{\ell v} + J_{p_{rv},\mathbf{d}}J_{\mathbf{d},\mathbf{d}}^{-1}J_{\mathbf{d},p_{rv}}\Delta p_{rv} = J_{p_{rv},\mathbf{d}}J_{\mathbf{d},\mathbf{d}}^{-1}\mathbf{r}_{\mathbf{d}} - r_{p_{rv}} \end{cases}. \tag{3.42}$$

Introducing

$$\alpha_{\mathrm{LL}} = J_{p_{\ell v},\mathbf{d}}\mathbf{w}_{\mathrm{L}}, \qquad \alpha_{\mathrm{LR}} = J_{p_{\ell v},\mathbf{d}}\mathbf{w}_{\mathrm{R}}, \qquad \alpha_{\mathrm{RL}} = J_{p_{rv},\mathbf{d}}\mathbf{w}_{\mathrm{L}}, \qquad \alpha_{\mathrm{RR}} = J_{p_{rv},\mathbf{d}}\mathbf{w}_{\mathrm{R}},$$

$$b_{\mathrm{L}} = J_{p_{\ell v},\mathbf{d}}\mathbf{v} - r_{p_{\ell v}}, \qquad b_{\mathrm{R}} = J_{p_{rv},\mathbf{d}}\mathbf{v} - r_{p_{rv}},$$

with

$$\mathbf{w}_{\mathrm{L}} = J_{\mathbf{d},\mathbf{d}}^{-1}J_{\mathbf{d},p_{\ell v}} \qquad \mathbf{w}_{\mathrm{R}} = J_{\mathbf{d},\mathbf{d}}^{-1}J_{\mathbf{d},p_{rv}}, \qquad \mathbf{v} = J_{\mathbf{d},\mathbf{d}}^{-1}\mathbf{r}_{\mathbf{d}}. \tag{3.43}$$

System (3.42) reads:

$$\begin{cases} \Delta\underline{\mathbf{d}}_h = \mathbf{v} - \mathbf{w}_{\mathrm{L}}\Delta p_{\ell v} - \mathbf{w}_{\mathrm{R}}\Delta p_{rv} \\ \alpha_{\mathrm{LL}}\Delta p_{\ell v} + \alpha_{\mathrm{LR}}\Delta p_{rv} = b_{\mathrm{L}} \\ \alpha_{\mathrm{RL}}\Delta p_{\ell v} + \alpha_{\mathrm{RR}}\Delta p_{rv} = b_{\mathrm{R}} \end{cases}. \tag{3.44}$$

Solving Equation (3.44) we obtain

$$\Delta\underline{\mathbf{d}}_h = \mathbf{v} - \mathbf{w}_{\mathrm{L}}\Delta p_{\ell v} - \mathbf{w}_{\mathrm{R}}\Delta p_{rv},$$

$$\Delta p_{\ell v} = \frac{b_{\mathrm{L}}\alpha_{\mathrm{RR}} + b_{\mathrm{R}}\alpha_{\mathrm{LR}}}{\alpha_{\mathrm{LL}}\alpha_{\mathrm{RR}} - \alpha_{\mathrm{RL}}\alpha_{\mathrm{LR}}}, \quad \Delta p_{rv} = \frac{b_{\mathrm{R}}\alpha_{\mathrm{LL}} + b_{\mathrm{L}}\alpha_{\mathrm{RL}}}{\alpha_{\mathrm{LL}}\alpha_{\mathrm{RR}} - \alpha_{\mathrm{RL}}\alpha_{\mathrm{LR}}}. \tag{3.45}$$

Notice that we have to the solve three linear systems (3.43) in order to obtain the solution (3.45).

3.2.4 Segregated-Intergrid-Staggered scheme

In summary, for the numerical approximation of the 3D-0D coupled model (3.24) we follow the approach proposed in [199], which is extended here to the biventricular case. The core models $(\mathscr{E}) - (\mathscr{A}) - (\mathscr{M}) - (\mathscr{C})$ are solved sequentially in a segregated manner by using different resolutions in space and time, to properly handle the different space and time scales of the core models contributing to both cardiac EM and blood circulation [159, 188, 187]. For this reason we call this numerical approach Segregated-Intergrid-Staggered (SIS).

For the space discretization, we use FEM with continuous FE and hexahedral meshes. We consider two nested meshes Ω_{h_1} and Ω_{h_2} of the computational domain Ω^0_{biv} (with $h_1 < h_2$), where Ω_{h_1} is built by uniformly refining Ω_{h_2} [1, 40]. We adopt the finer mesh Ω_{h_1} for $(\mathscr{E})$, while the coarser one Ω_{h_2} is used for both $(\mathscr{A})$ and $(\mathscr{M})$.

We employ an efficient intergrid transfer operator between the nested grids Ω_{h_1} and Ω_{h_2}, which allows to evaluate the feedback between $(\mathscr{E})$ and $(\mathscr{A}) - (\mathscr{M})$ [199]. In [199], the displacement field $\mathbf{d}$ is interpolated on Ω_{h_1} and $\nabla\mathbf{d}$ is assembled on the fine mesh directly. Here, we follow the more effective strategy proposed in [209], where $\nabla\mathbf{d}$ is recovered on Ω_{h_2} thanks to an L^2 projection [1]. Then, $\nabla\mathbf{d}$ is interpolated on Ω_{h_1}.

For the time discretization, we use FD schemes [189]. The cardiac EP model is solved by employing BDFσ (with $\sigma \geq 2$). We adopt an IMEX scheme, denoted by $(\mathscr{E}_{\mathrm{IMEX}})$ with the ICI approach, where the diffusion term is treated implicitly, whereas the ionic and reaction terms explicitly [199, 152]. For MA, TM and fluid problems we employ the BDF1 scheme, where $(\mathscr{A}_{\mathrm{E}})$ and $(\mathscr{C}_{\mathrm{E}})$ advanced in time with an explicit method, whereas a fully implicit scheme is used for $(\mathscr{M}_{\mathrm{I}}) - (\mathscr{V}_{\mathrm{I}})$ [199].

We use two different time steps, Δt for $(\mathscr{A}_{\mathrm{E}}) - (\mathscr{M}_{\mathrm{I}}) - (\mathscr{V}_{\mathrm{I}}) - (\mathscr{C}_{\mathrm{E}})$ and $\tau = \Delta t / N_{sub}$ for $(\mathscr{E}_{\mathrm{IMEX}})$, with $N_{sub} \in \mathbb{N}$. We first update the variables of $(\mathscr{E}_{\mathrm{IMEX}})$, then those of $(\mathscr{A}_{\mathrm{E}})$ and finally, after updating the unknowns of $(\mathscr{M}_{\mathrm{I}}) - (\mathscr{V}_{\mathrm{I}})$, we update the ones of $(\mathscr{C}_{\mathrm{E}})$, see Figure 3.9.

The whole algorithm for the SIS numerical scheme is reported in Figure 3.9.

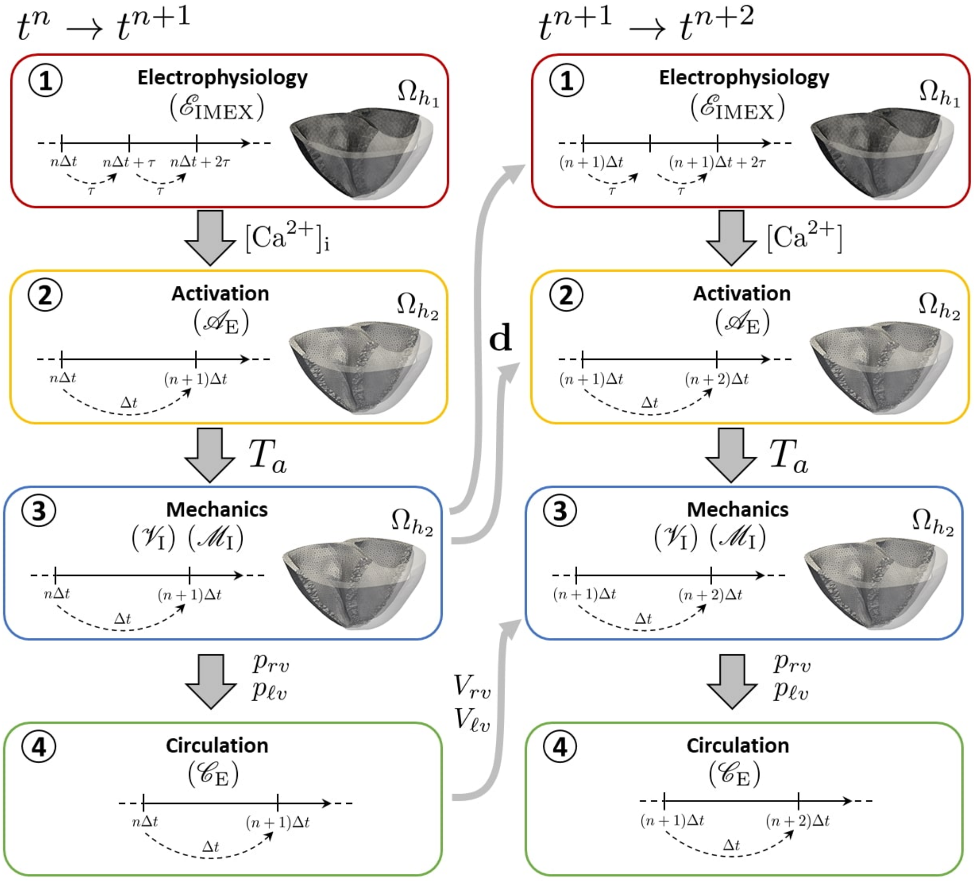

Figure 3.9: Graphical representation of the SIS numerical scheme employed to numerically solve the 3D-0D problem (3.24).

3.2.5 Setting initial conditions for the multiphysics problem

The numerical results of the 3D-0D biventricular model typically feature a temporal transient, which lasts for several heartbeats and converges to a periodic solution, known as *limit cycle*. The outputs of clinical interest should be computed from the numerical solution that is associated with the limit cycle. To reduce the computational overhead of reaching a periodic solution, we follow the strategy proposed in [197], aimed at accelerating the convergence towards the limit cycle. This strategy – named 3D-0D-3D V-cycle – comprises three stages (see Figure 3.10). In a first step, three heartbeats are simulated with the 3D-0D model. Then, based on the PV-loops obtained from the previous 3D-0D model, a 0D emulator of each ventricle is built with the aim of surrogating the pressure-volume relationships, and substituted to the 3D model. These emulators, coupled with the 0D model of blood circulation for the remaining compartments, allow to simulate the transient phase toward a periodic solution in less than one minute of computational time on a standard laptop. Finally, the state obtained by means of this fully 0D model is used to initialize the 3D-0D model, and three additional heartbeats are simulated. Overall, the computational cost of reaching the limit cycle amounts to that of simulating six heartbeats, regardless of

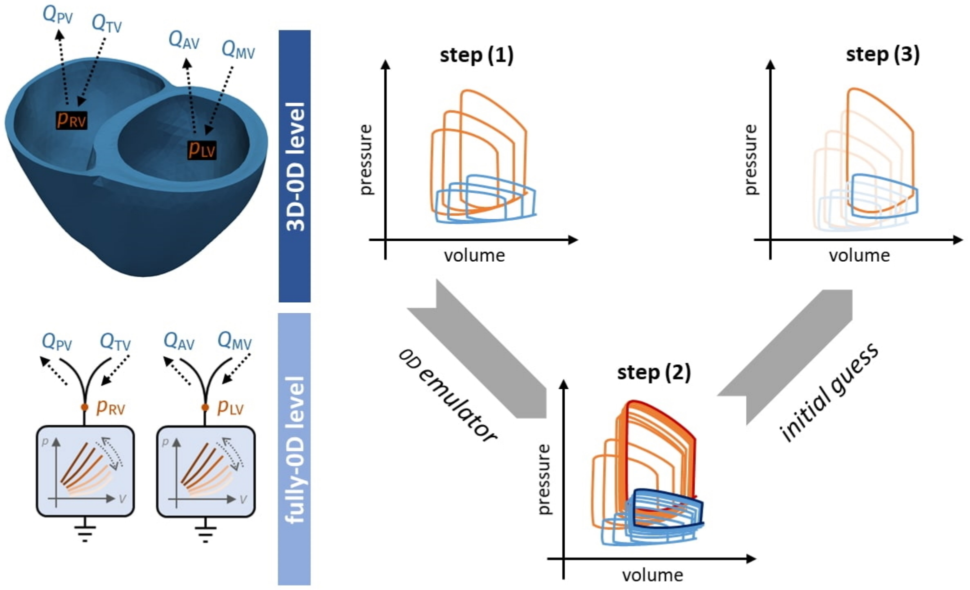

Figure 3.10: Graphical display of the 3D-0D-3D V-cycle for the initialization of a numerical simulation employing the 3D-0D biventricular model. See [197] for further details.

the number of cycles required to converge to a periodic solution. As a matter of fact, the computational time required by the 0D surrogate model is negligible compared to that of the full-order 3D-0D model. More details on this procedure are available in [197].

To find an initial guess for the remaining variables, we initialize the ionic model by running a 1000-cycle long single-cell simulation. Similarly, we initialize the force generation model by means of a single-cell simulation with a constant calcium input (corresponding to the final calcium concentration of the single-cell ionic simulation) and a reference sarcomere length $SL = 2.2\,\mu\text{m}$.

3.3 Numerical results for biventricular electromechanics

In this section, we presents some biventricular EM simulations that employ the 3D-0D model discussed in Sections 3.1 and 3.2.

We organize this section as follows. After a brief description regarding the setting of the numerical simulations (Section 3.3.1), we compare the results of a physiological EM simulation with a comprehensive set of experimental data available in literature (Section 3.3.2). Then, in Section 3.3.3 we investigate how different cross-fibers active contraction arrangements affect the electromechanical simulations, by setting different combinations of n_f, n_s and n_n, i.e. of the prescribed proportion of active tension along the myofibers, see Equation (3.5). Finally, in Section 3.3.4 we evaluate the impact of different myofiber architectures, obtained by three types of LDRBMs, on the biventricular pumping function.

Variable	Value	Unit	Description
Electrophysiology			
T_{HB}	0.8	s	Heartbeat duration
χ_m	1	μF/cm^2	Surface-to-volume ratio
C_m	1400	cm^{-1}	Transmembrane capacitance
ϵ	0.01	–	Threshold of the fast conduction layer
$(\sigma_{\ell,\mathrm{fast}}, \sigma_{\mathrm{t,fast}}, \sigma_{\mathrm{n,fast}})$	(4.28, 1.96, 0.64)	mS/cm	Fast layer conductivities
$(\sigma_{\ell,\mathrm{myo}}, \sigma_{\mathrm{t,myo}}, \sigma_{\mathrm{n,myo}})$	(1.07, 0.49, 0.16)	mS/cm	Myocardial conductivities
$\mathcal{I}^{max}$	$50 \cdot 10^3$	μA/cm^3	Applied current value
t_{app}	3.0	ms	Applied current duration
$t^0_{\mathrm{LV,app}}$	(0.0,0.0,0.0)	ms	Applied current LV initial times
$t^0_{\mathrm{RV,app}}$	(5.0,5.0)	ms	Applied current RV initial times
δ_{app}	2.5	mm	Applied current radius
Mechanics			
ρ_s	10^3	kg m^{-3}	Tissue density
$K^{vepi}_{\parallel}$	$2 \cdot 10^4$	Pa m^{-1}	Normal stiffness of epicardium
$K^{vepi}_{\perp}$	$2 \cdot 10^5$	Pa m^{-1}	Tangential stiffness of epicardial tissue
$C^{vepi}_{\perp}$	$2 \cdot 10^4$	Pa s m^{-1}	Normal viscosity of epicardial tissue
$C^{vepi}_{\parallel}$	$2 \cdot 10^3$	Pa s m^{-1}	Tangential viscosity of epicardial tissue
a	$0.88 \cdot 10^3$	Pa	Material stiffness
$\kappa^{(\mathrm{G})}$	$50 \cdot 10^3$	Pa	Bulk modulus
b_{ff}	8	–	Fiber strain scaling
b_{ss}	6	–	Radial strain scaling
b_{nn}	3	–	Cross-fiber in-plain strain scaling
b_{fs}	12	–	Shear strain in fiber-sheet plane scaling
b_{fn}	3	–	Shear strain in fiber-normal plane scaling
b_{sn}	3	–	Shear strain in sheet-normal plane scaling
Reference Configuration			
$\widehat{p}_{\ell v}$	600	Pa	Residual left ventricular pressure
$\widehat{p}_{rv}$	400	Pa	Residual right ventricular pressure
$\widehat{T}_a$	$350 \cdot 10^3$	Pa	Residual active tension
$C_{\ell rv}$	1	–	Residual contractility ratio
Activation			
SL_0	2	µm	Reference sarcomere length
T_a^{max}	$840 \cdot 10^3$	Pa	Maximum tension
$C_{\ell rv}$	0.60	–	Contractility ratio

Table 3.1: Input parameters of the 3D EM model.

3.3.1 Settings of numerical simulations

All the simulations are performed on a realistic biventricular geometry processed from the Zygote 3D heart [107], a CAD-model representing an average healthy human heart reconstructed from high-resolution CT-scan. To build the computational mesh associated with the biventricular Zygote model, we use the vmtk software [10] (`http://www.vmtk.org`) by exploiting the semi-automatic meshing tool recently proposed in [66].

For the space discretization, we used continuous bilinear FE ($\mathbb{Q}_1$) and we employ two nested meshes where for the mechanical and activation problems we adopt a mesh size of 3 mm, while for the electrophysiology problem we employ a mesh size four time smaller [199]. For the time discretization, we use BDF2 with $\tau = 50\,\mu$s for EP problem and BDF1 with $\Delta t = 500\,\mu$s for TM, MA and fluid problems [199, 176].

The parameters of the 3D-0D model used for all the simulations presented in

Variable	Value	Unit	Description
Circulation			
R_{ar}^{sys}	0.416	$\mathrm{mmHg\,s\,mL^{-1}}$	Resistance of systemic arterial system
R_{ven}^{sys}	0.260	$\mathrm{mmHg\,s\,mL^{-1}}$	Resistance of systemic venous system
R_{ar}^{pul}	0.048	$\mathrm{mmHg\,s\,mL^{-1}}$	Resistance of pulmonary arterial system
R_{ven}^{pul}	0.036	$\mathrm{mmHg\,s\,mL^{-1}}$	Resistance of pulmonary venous system
C_{ar}^{sys}	1.62	$\mathrm{mL\,mmHg^{-1}}$	Capacitance of systemic arterial system
C_{ven}^{sys}	60.00	$\mathrm{mL\,mmHg^{-1}}$	Capacitance of systemic venous system
C_{ar}^{pul}	5.00	$\mathrm{mL\,mmHg^{-1}}$	Capacitance pulmonary arterial system
C_{ven}^{pul}	16.00	$\mathrm{mL\,mmHg^{-1}}$	Capacitance of pulmonary venous system
L_{ar}^{sys}	$5 \cdot 10^{-3}$	$\mathrm{mmHg\,s^2\,mL^{-1}}$	Impedance of systemic arterial system
L_{ven}^{sys}	$5 \cdot 10^{-4}$	$\mathrm{mmHg\,s^2\,mL^{-1}}$	Impedance of systemic venous system
L_{ar}^{pul}	$5 \cdot 10^{-4}$	$\mathrm{mmHg\,s^2\,mL^{-1}}$	Impedance pulmonary arterial system
L_{ven}^{pul}	$5 \cdot 10^{-4}$	$\mathrm{mmHg\,s^2\,mL^{-1}}$	Impedance of pulmonary venous system
$E_{\ell a}^{A}$	0.09	$\mathrm{mmHg\,mL^{-1}}$	Left atrium elastance amplitude
E_{ra}^{A}	0.06	$\mathrm{mmHg\,mL^{-1}}$	Right atrium elastance amplitude
$E_{\ell a}^{B}$	0.07	$\mathrm{mmHg\,mL^{-1}}$	Left atrium elastance baseline
E_{ra}^{B}	0.07	$\mathrm{mmHg\,mL^{-1}}$	Right atrium elastance baseline
$T_{\ell a}^{ac}$	0.17	–	Duration of left atrium contraction (w.r.t. T_{hb})
T_{ra}^{ac}	0.17	–	Duration of right atrium contraction (w.r.t. T_{hb})
$t_{\ell a}^{ac}$	0.80	–	Initial time of left atrium contraction (w.r.t. T_{hb})
t_{ra}^{ac}	0.80	–	Initial time of right atrium contraction (w.r.t. T_{hb})
$T_{\ell a}^{ar}$	0.17	–	Duration of left atrium relaxation (w.r.t. T_{hb})
T_{ra}^{ar}	0.17	–	Duration of right atrium relaxation (w.r.t. T_{hb})
$V_{0,la}$	4.0	mL	Left atrium resting volume
$V_{0,ra}$	4.0	mL	Right atrium resting volume
R_{min}	$75 \cdot 10^{-4}$	$\mathrm{mmHg\,s\,mL^{-1}}$	Valves minimal resistance
R_{max}	$75 \cdot 10^{3}$	$\mathrm{mmHg\,s\,mL^{-1}}$	Valves maximum resistance

Table 3.2: Input parameters of the 0D closed-loop hemodynamical model.

Physics/Fields	Linear solver (preconditioner)	Abs. tol.
Fiber Laplace problems	GMRES(AMG)	10^{-10}
Monodomain model	CG (AMG)	10^{-10}
Activation	GMRES (AMG)	10^{-10}
Mechanics	GMRES (AMG)	10^{-10}
Reference configuration	GMRES (AMG)	10^{-6}

Table 3.3: Tolerances of the linear solver for the different core models.

Physics/Fields	non-linear solver	Rel. tol.	Abs. tol.
Mechanics	Newton	10^{-10}	10^{-8}
Reference configuration	Newton	10^{-6}	10^{-4}

Table 3.4: Tolerances of the non-linear solver for the mechanical problem.

Section 3.3 are listed in Tables 3.1 and 3.2. In particular, Table 3.1 contains the parameters of the 3D EM model (referred to $\mathscr{E}$, $\mathscr{A}$, $\mathscr{M}$) and Table 3.2 those of the 0D closed-loop hemodynamical model ($\mathscr{C}$). Moreover, for the TTP06 ionic model, we use the parameters (for epicardium cells) reported in [247], while for the RDQ18-ANN model, we employ those in [196]. Tables 3.3 and 3.4 report the setting used for the linear and non-linear solvers, respectively. The settings related to LDRBMs, adopted for prescribing the fiber architectures, will be specified for each case reported in Sections 3.3.2 – 3.3.3.

To approach the limit cycle, we initialize all the numerical simulations following the procedure illustrated in Section 3.2.5 (see also [197]). Then, we perform three further heartbeats using the fully framework of the 3D-0D model presented in Sections 3.1 and 3.2. We neglected the first two, so that all the reported results refer to the last heartbeat.

In all the simulations we adopted the same pacing protocol in which five ventricular endocardial areas are activated by spherical impulses (see Table 3.1): in the anterior para-septal wall, in the left surface of inter-ventricular septum and in the bottom of postero-basal area, for LV; in the septum and in the free endocardial wall, for RV [176, 59], see also Figure 3.2. This, combined with the fast endocardial conduction layer (see Section 3.1.2), surrogates the action of the Purkinje network [127, 252].

3.3.2 Baseline physiological simulation

We present a human EM simulation in physiological conditions related to the Zygote biventricular geometry.

For the fibers generation we adopted D-RBM [176, 58] (see Section 3.1.1). The input angle values were chosen according to observations based on histological studies in the human heart [134, 9]:

$$\begin{aligned} &\alpha_{epi,\mathrm{LV}} = -60^\circ, \quad \alpha_{endo,\mathrm{LV}} = +60^\circ, \quad \alpha_{epi,\mathrm{RV}} = -25^\circ, \quad \alpha_{endo,\mathrm{RV}} = +90^\circ; \\ &\beta_{epi,\mathrm{LV}} = +20^\circ, \quad \beta_{endo,\mathrm{LV}} = -20^\circ, \quad \beta_{epi,\mathrm{RV}} = +20^\circ, \quad \beta_{endo,\mathrm{RV}} = 0^\circ. \end{aligned} \tag{3.46}$$

Moreover, to surrogate the effect of dispersed myofibers, we set in (3.5) $n_f = 0.7$, $n_s = 0$ and $n_n = 0.3$ for the proportion of active tension along the fiber, sheet and normal directions, respectively [87, 3].

Figure 3.11 illustrates the time evolution of calcium ions concentration (a), the mechanical deformation (b, e), the activation times (c), the PV-loop curves for both ventricles and the time evolution of pressures and volumes of the four chambers (d). Specifically, in Figure 3.11(a) we display the time evolution of the TTP06 ionic model calcium transient showing the physiological wave propagation up to the complete depolarization of both ventricles ($t = 0.12\,\mathrm{s}$). In Figure 3.11(b) we report different snapshots of the biventricular geometry warped by the displacement vector. As expected, at the beginning of the contraction the volumes of both ventricles remain nearly constant while the pressure increases ($t = 0.0 - 0.10\,\mathrm{s}$); during the ejection phase, the ventricular contraction is clearly visible, with the basal plane that moves towards the bottom while the apex remains almost fixed. Moreover, a significant thickening of the myocardium wall takes place ($t = 0.35\,\mathrm{s}$). Then, the ventricles start to relax. This leads to a slow recovery of the initial volumes ($t = 0.45 \div 0.60\,\mathrm{s}$). Finally, in Figure 3.11(c) we display the simulated activation map in which both the total activation time (120 ms) and the activation pattern are in accordance with the literature [176, 59]. PV-loops morphologies, showed in Figure 3.11(c), for both LV and RV, are in

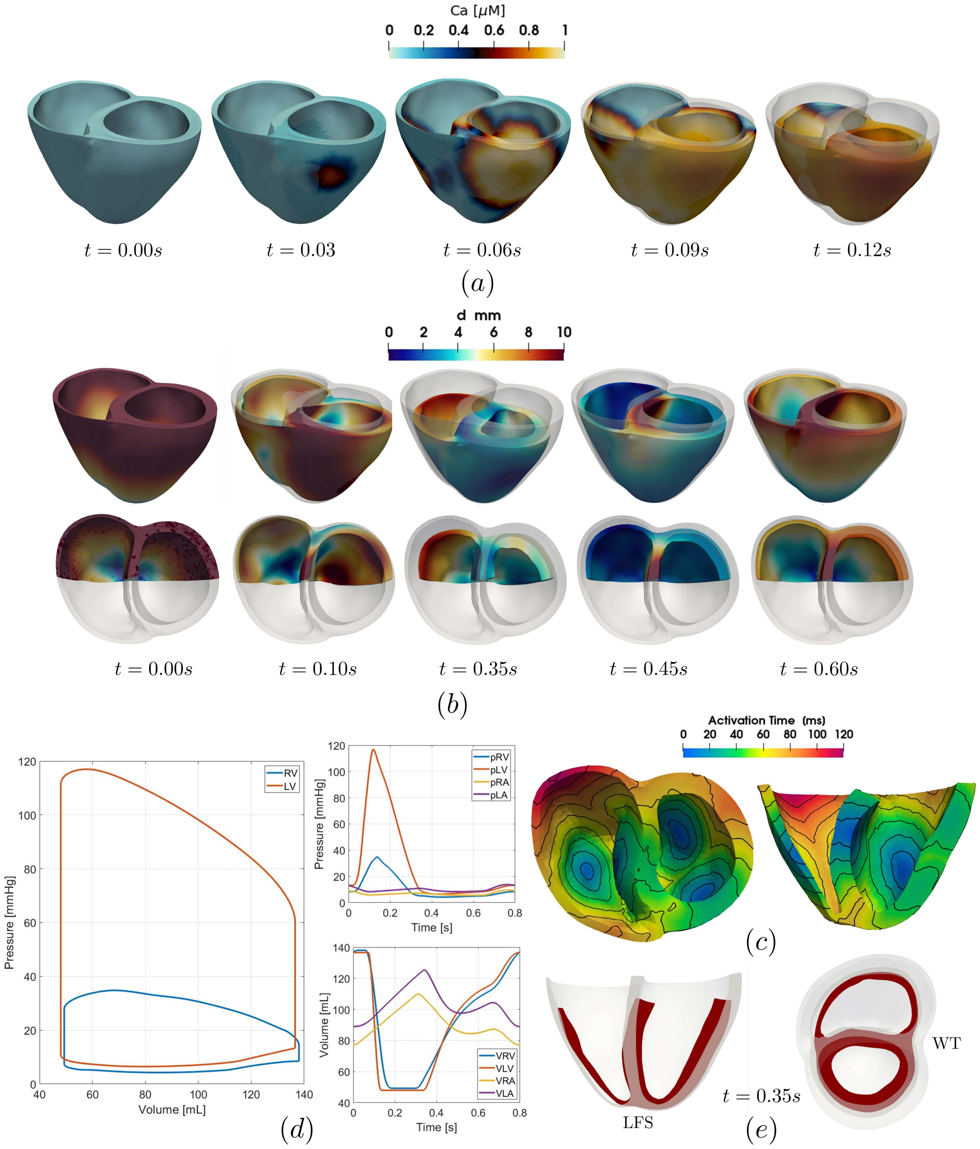

Figure 3.11: Baseline electromechanical simulation; (a) calcium transient at five time instants in the cardiac cycle; (b) mechanical displacement magnitude (with respect to the reference configuration) at five time instants of the heartbeat where $0.35\,s$ is the end of systole. (c) activation map; (d, left) PV-loop LV (orange) and RV (blue); (d, right) pressures (top) and volumes (bottom) transient during the cardiac cycle for the four chambers; (e) mid ventricular slices at the end of systole, showing LFS on the left and WT on the right.

Mechanical biomarkers	Literature values	Simulation results	Description
$\mathrm{EDV_{LV}}$ (mL)	142 ± 21 [137]	137	Left end diastolic volume
$\mathrm{EDV_{RV}}$ (mL)	144 ± 23 [138]	138	Right end diastolic volume
$\mathrm{ESV_{LV}}$ (mL)	47 ± 10 [137]	48	Left end systolic volume
$\mathrm{ESV_{RV}}$ (mL)	50 ± 14 [138]	49	Right end systolic volume
$\mathrm{EF_{LV}}$ (%)	67 ± 5 [137]	66	Left ventricular ejection fraction
$\mathrm{EF_{RV}}$ (%)	67± 8 [238]	65	Right ventricular ejection fraction
$\mathrm{P_{LV}}$ (mmHg)	119 ± 13 [236]	117	Left systolic pressure peak
$\mathrm{P_{RV}}$ (mmHg)	35 ± 11 [31]	35	Right systolic pressure peak
LFS (%)	13-21 [61]	21	Longitudinal fractional shortening
WT (%)	18-100 [219]	41	Fractional wall thickening

Table 3.5: Comparison between the simulation results, employing the 3D-0D biventricular model, and literature values of mechanical biomarkers in physiological conditions (references are reported in the Table, see also [130, 260]).

accordance with other physiological PV-loop curves found in literature[137]. In Table 3.5 we compare some relevant mechanical biomarkers obtained by our numerical simulation with those provided by the data reported in the literature [137, 238, 138, 236, 31, 61, 219]. Notice that all the values in Table 3.5, related to the ventricular volumes, are expressed with absolute values, in mL, estimated for an adult subject, as reported in the quoted references. However, we are aware that in the clinical practice the ventricular volumes are always indicated as “indexed ventricular volumes”, by dividing the ventricular volume for the Body Surface Area of the related patient.

The chosen mechanical biomarkers were: i) left and right end diastolic/systolic volumes ($\mathrm{EDV_{LV}}$, $\mathrm{EDV_{RV}}$, $\mathrm{ESV_{LV}}$, $\mathrm{ESV_{RV}}$), representing the maximal and minimal left and right ventricular volumes achieved during the heartbeat, computed as the maximal ($\mathrm{EDV_{LV}}$, $\mathrm{EDV_{RV}}$) and minimal ($\mathrm{ESV_{LV}}$, $\mathrm{ESV_{RV}}$) volumes in the PV-loop curves, see Figure 3.11(d); ii) left and right ventricular ejection fractions ($\mathrm{EF_{LV}}$, $\mathrm{EF_{RV}}$), which represent the amount of blood that is pumped by LV and RV during a cardiac cycle, computed as

$$\mathrm{EF}_i(\%) = \frac{\mathrm{EDV}_i - \mathrm{ESV}_i}{\mathrm{EDV}_i} 100 \qquad i = \mathrm{LV,RV};$$

iii) left and right ventricular systolic pressure peaks ($\mathrm{P_{LV}}$, $\mathrm{P_{RV}}$), the maximal pressures reached in LV and RV, computed as the maximal pressures in the PV-loop curves, see Figure 3.11(d); iv) the systolic longitudinal fractional shortening (LFS), standing for the fractional displacement between the epicardial apex and the base [130], evaluated as

$$\mathrm{LFS}(\%) = \frac{\mathrm{L}_0 - \mathrm{L}}{\mathrm{L}_0} 100,$$

where L_0 and L are the apico-basal distance measured at the beginning ($t = 0.0\,\mathrm{s}$) and at the end of systole ($t = 0.35\,\mathrm{s}$), see Figure 3.11(e); v) the systolic wall thickening (WT), representing the fractional cardiac wall thickening [130], measured as

$$\mathrm{WT}(\%) = \frac{\mathrm{T} - \mathrm{T}_0}{\mathrm{T}} 100,$$

where T_0 and T are the cardiac wall thickening at the beginning ($t = 0.0\,\mathrm{s}$) and at the end of systole ($t = 0.35\,\mathrm{s}$), see Figure 3.11(e).

All the above mechanical biomarkers, obtained by our numerical simulation, fall within the physiological range (references in Table 3.5).

Cross-fiber configuration	$\mathrm{EF}_{\mathrm{LV}}$	$\mathrm{EF}_{\mathrm{RV}}$	$\mathrm{SV}_{\mathrm{LV}}$	$\mathrm{SV}_{\mathrm{RV}}$
i) $n_f = 0.7$, $n_s = 0.3$, $n_n = 0$	45 %	44 %	70.69 mL	71.04 mL
ii) $n_f = 1$, $n_s = 0.3$, $n_n = 0$	54 %	53 %	79.40 mL	79.50 mL
iii) $n_f = 1$, $n_s = 0$, $n_n = 0$	65 %	64 %	89.14 mL	89.08 mL
iv) $n_f = 0.7$, $n_s = 0$, $n_n = 0.3$	66 %	65 %	89.27 mL	89.23 mL
v) $n_f = 1$, $n_s = 0$, $n_n = 0.3$	69 %	67 %	91.14 mL	91.09 mL

Table 3.6: Ejection fraction (EF_i) of the left ($i = \mathrm{LV}$) and right ($i = \mathrm{RV}$) ventricles for the different cross-fibers active contraction cases i−v. The stroke volume (SV_i) of the two ventricles is also shown.

3.3.3 Cross-fibers active contraction in cardiac electromechanics

To surrogate the dispersion effect in the cardiac fibers, we analyse several cross-fibers active contraction arrangements, by setting in (3.5) different combinations of n_f, n_s and n_n, i.e. the prescribed proportion of active tension along the myofibers. Five different sets were chosen: i) $n_f = 0.7$, $n_s = 0.3$, $n_n = 0$; ii) $n_f = 1$, $n_s = 0.3$, $n_n = 0$; iii) $n_f = 1$, $n_s = 0$, $n_n = 0$; iv) $n_f = 0.7$, $n_s = 0$, $n_n = 0.3$; v) $n_f = 1$, $n_s = 0$, $n_n = 0.3$. Apart from the prescribed proportion of active tension, the settings are the same as the baseline simulation[6] presented in Section 3.3.2.

Figure 3.12(a) shows the PV-loops from the five cases. An active tension along the sheet direction ($n_s > 0$, cases i and ii) produces a PV-loop with a reduced area compared to case iii with no cross-fibers active contraction. Conversely, an active tension along the normal direction ($n_n > 0$, cases iv and v) yields a PV-loop with an increased area. Table 3.6 displays, for all the cases, the ejection fraction (EF_i) and the stroke volume ($\mathrm{SV}_i = \mathrm{EDV}_i - \mathrm{ESV}_i$) of the left ($i = \mathrm{LV}$) and right ($i = \mathrm{RV}$) ventricles. The maximal cardiac work is achieved for case v while the minimal for case i. The above analysis shows that the active tension along the sheet direction ($n_s > 0$) counteracts the myofiber contraction, while the one along the normal direction ($n_n > 0$) enhances the cardiac work, in accordance to [87, 88, 79].

In order to better appreciate the differences among the arrangements of cross-fibers active contraction , we further compared cases i and iv with case iii. In these particular cases, the proportion of active tension sums up to 1 ($n_\mathrm{f} + n_\mathrm{s} + n_\mathrm{n} = 1$), meaning that the myofibers contraction is redistributed along the three directions: case iii ($n_f = 1$, $n_s = 0$, $n_n = 0$) is a pure fiber contraction, in the following denoted by $\boldsymbol{f}$ configuration; case i ($n_f = 0.7$, $n_s = 0$, $n_n = 0.3$) is a contraction in the fiber and normal directions, hereafter indicated by $\boldsymbol{f}$-$\boldsymbol{n}$ configuration; case iv ($n_f = 0.7$, $n_s = 0.3$, $n_n = 0$) is a contraction along the fiber and sheet directions, named $\boldsymbol{f}$-$\boldsymbol{s}$ configuration.

Figure 3.12(b) illustrates the mechanical displacements at the end of systole ($0.35\,s$) for the three considered configurations ($\boldsymbol{f}$, $\boldsymbol{f}$-$\boldsymbol{n}$ and $\boldsymbol{f}$-$\boldsymbol{s}$). Both the apico-basal shortening and the wall thickening is dramatically reduced for $\boldsymbol{f}$-$\boldsymbol{s}$ configuration. Almost the same mechanical contraction is achieved for $\boldsymbol{f}$ and $\boldsymbol{f}$-$\boldsymbol{n}$ configurations with a slightly more pronounced longitudinal shortening and wall thickening for $\boldsymbol{f}$-$\boldsymbol{n}$ configuration. The LFS and WT are reported in Table 3.7. We also evaluate the components

---

[6] Notice that case iv is the baseline simulation.

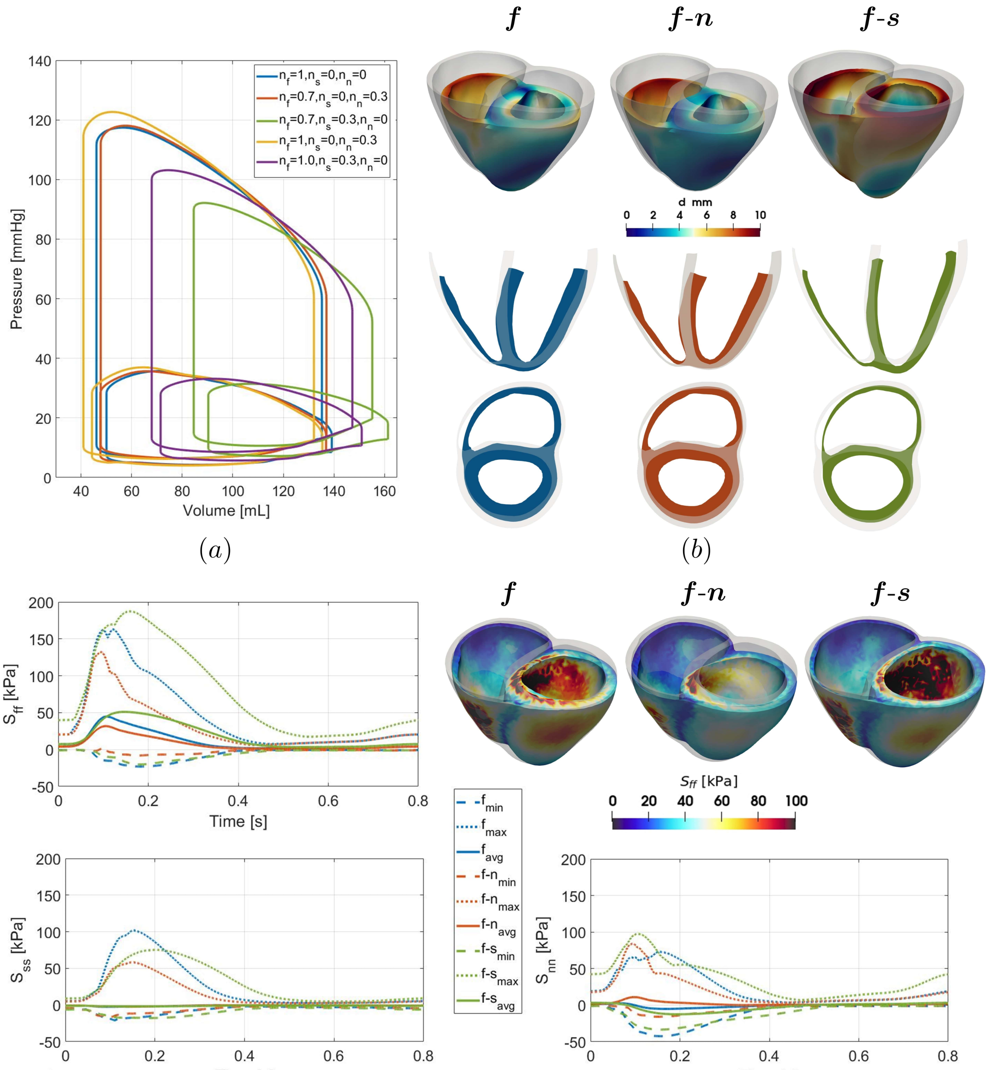

(a) (b) (c)

Figure 3.12: Cross-fibers active contraction simulations; (a) PV-loops from several cross-fibers active contraction arrangements built by setting in (3.5) different combinations of n_f, n_s and n_n; (b) mechanical displacements (top) and mid ventricular slices at the end of systole (0.35 s), showing LFS (middle) and WT (bottom) for redistributed cross-fibers active contraction configurations: a pure fiber $\boldsymbol{f}$ (blue), a fiber-normal $\boldsymbol{f}$-$\boldsymbol{n}$ (orange) and a fiber-sheet $\boldsymbol{f}$-$\boldsymbol{s}$ (green) contractions; (c) circumferential stress S_{ff} (top-right) at the peak pressure time instant (0.1 s) and the time trace of the average, minimum and maximum axial stresses S_{ff} (top-left), S_{ss} (bottom-left) and S_{nn} (bottom-right) for $\boldsymbol{f}$, $\boldsymbol{f}$-$\boldsymbol{n}$ and $\boldsymbol{f}$-$\boldsymbol{s}$ configurations.

Cross-fiber configuration	LFS	WT
iii) $\boldsymbol{f}$	17 %	30 %
iv) $\boldsymbol{f}$-$\boldsymbol{n}$	21 %	41 %
i) $\boldsymbol{f}$-$\boldsymbol{s}$	7 %	8 %

Table 3.7: LFS and WT for the three configurations of redistributed myofibers active contraction ($\boldsymbol{f}$, $\boldsymbol{f}$-$\boldsymbol{n}$ and $\boldsymbol{f}$-$\boldsymbol{s}$).

of the mechanical stress by means of the following indicators [199]:

$$S_{ff} = (\mathbf{P}\mathbf{f}_0) \cdot \frac{\mathbf{F}\mathbf{f}_0}{|\mathbf{F}\mathbf{f}_0|}, \quad S_{ss} = (\mathbf{P}\mathbf{s}_0) \cdot \frac{\mathbf{F}\mathbf{s}_0}{|\mathbf{F}\mathbf{s}_0|}, \quad S_{nn} = (\mathbf{P}\mathbf{n}_0) \cdot \frac{\mathbf{F}\mathbf{n}_0}{|\mathbf{F}\mathbf{n}_0|},$$

where $\mathbf{f}_0$, $\mathbf{s}_0$ and $\mathbf{n}_0$ are the myofiber directions, $\mathbf{P}$ is the first Piola-Kirchhoff stress tensor and $\mathbf{F}$ is the deformation gradient tensor. The metric S_{aa} (with $a = f, s, n$) measures the axial stresses along the circumferential ($a = f$), radial ($a = s$) and longitudinal ($a = n$) directions.

Figure 3.12(c) displays, for the three configurations $\boldsymbol{f}$, $\boldsymbol{f}$-$\boldsymbol{n}$ and $\boldsymbol{f}$-$\boldsymbol{s}$, the circumferential stress (S_{ff}) at the peak pressure time instant ($0.1\,s$) and the time trace of the average, minimum and maximum axial stresses S_{ff}, S_{ss} and S_{nn}. The circumferential stress at the peak pressure instant is much higher, especially on LV side, for $\boldsymbol{f}$-$\boldsymbol{s}$ configuration with respect to the other two. Conversely, $\boldsymbol{f}$-$\boldsymbol{n}$ configuration produces the lowest circumferential stress. Almost the same considerations hold for the time trace of the three axial stresses during the complete cardiac cycle, see Figure 3.12(c).

The previous results reveal that the configuration $\boldsymbol{f}$-$\boldsymbol{n}$ allows to obtain a more efficient cardiac contraction with a much lower axial stress with respect to $\boldsymbol{f}$ configuration. On the contrary, $\boldsymbol{f}$-$\boldsymbol{s}$ configuration yields an unphysiological cardiac contraction with EF, LFS and WT below the physiological range reported in literature (see Tables 3.5-3.7).

3.3.4 Impact of myofiber architecture on the electromechanical function

We investigate the effect of different myofibers architecture on the biventricular EM model, by considering three types of LDRBMs: D-RBM, B-RBM and R-RBM (see Section 3.1.1). Apart from the employed LDRBM, used to prescribe the myofibers architecture, all the other settings, including the fiber input angles (3.46), are the same as the baseline simulation[7] presented in Section 3.3.2.

Fiber orientations obtained for the three LDRBMs (D-RBM, B-RBM and R-RBM) in the Zygote biventricular model are shown in Figure 3.13(a). For a detailed comparison among the three LDRBMs we refer the reader to Section 2.5 (see also [176]), where pure EP simulations were considered. Here, we are instead interested in the effect of fibers architecture on mechanical quantities obtained by means of EM simulations. We recall that B-RBM produces a smooth change in the fiber field in the transition across the two ventricles, while R-RBM and D-RBM a strong discontinuity [176]. Moreover, R-RBM and D-RBM feature a linear transition passing from the endocardium to the epicardium, while B-RBM employs a bidirectional spherical interpolation `bislerp` (see [176, 26, 58, 188]). In Figure 3.13(b) the PV-loop curves (for both ventricles)

---

[7] Notice that the case with D-RBM is the baseline simulation.

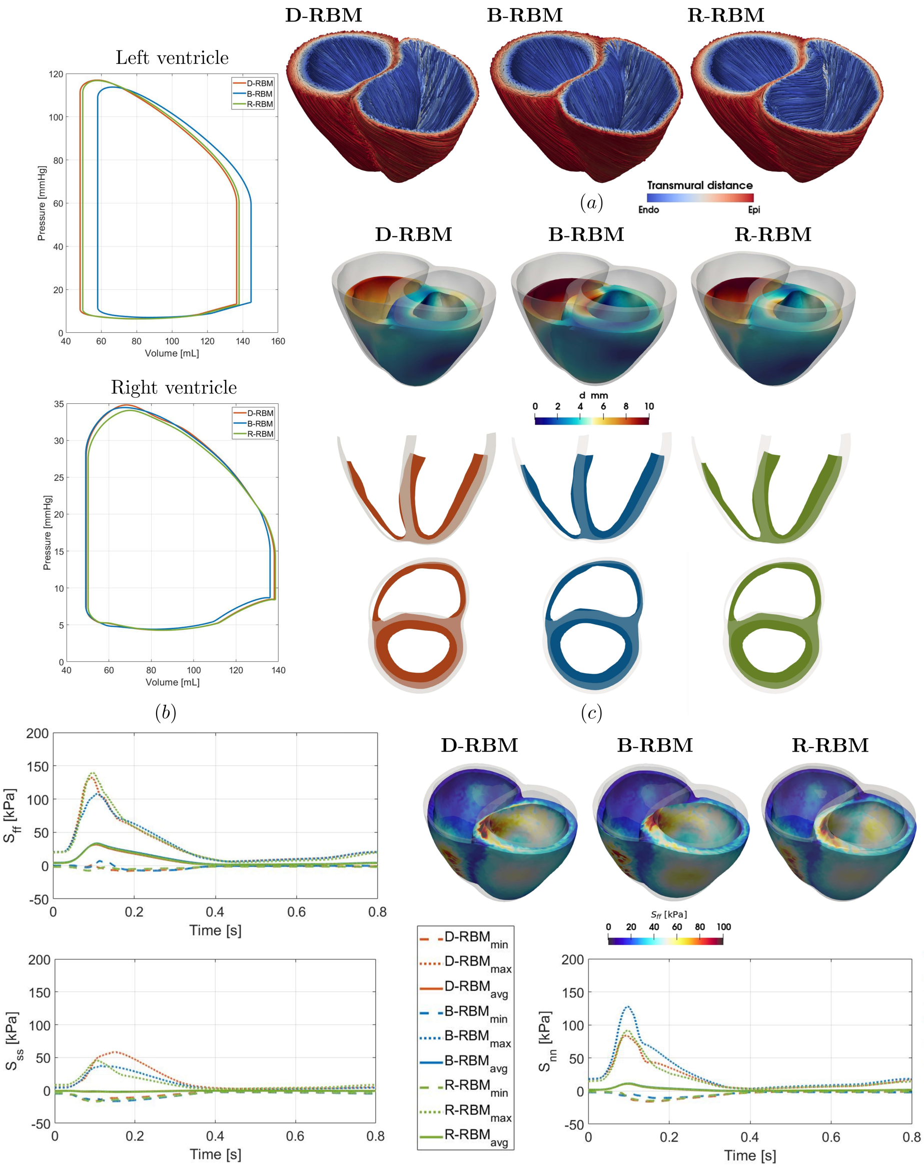

(a)

(b)

(c)

(d)

Figure 3.13: Results of EM simulations employing different LDRBMs (R-RBM, B-RBM and D-RBM) to generate the fiber architecture; (a) fiber orientations obtained for the three LDRBMs in the Zygote biventricular model; (b) PV-loop curves, for LV (top) and RV (bottom), obtained with the three LDRBMs: D-RBM (orange), B-RBM (blue) and R-RBM (green); (c) mechanical displacements (top) and mid ventricular slices at the end of systole (0.35 s), showing LFS (middle) and WT (bottom) obtained by D-RBM (orange), B-RBM (blue) and R-RBM (green); (d) circumferential stress S_{ff} (top-right) at the peak pressure instant (0.1 s) and the time trace of the average, minimum and maximum axial stresses S_{ff} (top-left), S_{ss} (bottom-left) and S_{nn} (bottom-right) for the three LDRBMs.

Mechanical biomarkers	D-RBM	B-RBM	R-RBM
EDV_{LV} (mL)	137	145	138
EDV_{RV} (mL)	138	136	139
ESV_{LV} (mL)	48	58	50
ESV_{RV} (mL)	49	49	50
EF_{LV} (%)	66	60	64
EF_{RV} (%)	65	64	64
P_{LV} (mmHg)	117	114	117
P_{RV} (mmHg)	35	34	33
LFS (%)	21	25	20
WT (%)	41	36	38

Table 3.8: Comparison of relevant mechanical biomarkers among EM simulations using D-RBM,B-RBM and R-RBM for the myofiber architecture.

are displayed, while in Table 3.8 some relevant mechanical biomarkers are compared among the simulation results. The left ventricular PV-loop area of B-RBM is shifted towards larger volumes with respect to the ones of D-RBM and R-RBM that show almost a compatible PV-loop for LV, see Figure 3.13(b, top). Moreover, the left systolic pressure peak decreases for B-RBM with respect to D-RBM and R-RBM, see Figures 3.13(b, top) and Table 3.8. As a consequence, the left ventricular ejection fraction obtained with B-RBM (60%) is smaller than those obtained with D-RBM and R-RBM (66% and 65%, respectively), see Table 3.8. On the contrary, small differences are observed for the right ventricular PV-loops with only a slightly larger ejection fraction for D-RBM, see Figure 3.13(b, bottom) and Table 3.8.

Figure 3.13(d) shows the circumferential stress (S_{ff}) at the peak pressure instant ($0.1\,s$) and the time trace of the average, minimum and maximum axial stresses S_{ff}, S_{ss} and S_{nn}. The patterns of S_{ff} are very similar for the three methods, see Figure 3.13(d, top-right). Instead, the time traces of the axial stresses present several discrepancies. Specifically, S_{ff} reveals lower values obtained by B-RBM with respect to D-RBM and R-RBM, see Figure 3.13(d, top-left). This is associated to a lower cardiac work produced by B-RBM ($\text{EF}_{\text{LV}} = 60\%$) compared to D-RBM and R-RBM ($\text{EF}_{\text{LV}} = 66\%$, 64%, respectively). On the contrary, the longitudinal stress S_{nn} presents an opposite trend, see Figure 3.13(d, bottom-right). This is ascribed to a larger apico-basal shortening for B-RBM (LFS = 25%) with respect to D-RBM and R-RBM (LFS = 21%, 20%, respectively). Meanwhile, larger values of the radial stress S_{ss} are observed for D-RBM with respect to B-RBM and R-RBM, see Figure 3.13(d,bottom-right), associated to a larger wall thickening of D-RBM (WT = 41%) against the ones of R-RBM and B-RBM (WT = 38%, 36%, respectively).

The previous results highlight that there is a strong interaction on the cardiac pump function between the LV and RV [163, 259]. A different fibers architecture in the transmural wall (from epicardium to endocardium) and a different septal fibers interconnection between the two ventricles affect the ventricular cardiac pump work, in particular the LV one. Indeed, a biventricular myofibers architecture has much more information (e.g. in the inter-ventricular septum) compared to a stand-alone LV model.

Chapter 4

Towards the electromechanical modeling of the whole heart

In this chapter, we extend the biventricular 3D-0D model presented in Chapter 3, to the whole heart. More precisely, we consider a 3D description of cardiac electromechanics (EM) in all the four chambers and a 0D representation of the circulatory system, which includes the cardiac blood haemodynamics. Our whole heart 3D-0D model includes a detailed myocardial fiber architecture and embeds state of the art human models for the atrial and ventricular electrophysiology (EP). Moreover, the model simulates mechanical activation (MA) and tissue mechanics (TM) of the atria and the ventricles, which are strongly coupled with a closed-loop lumped-parameters model of the whole cardiovascular system. We begin by presenting a Laplace-Dirichlet Rule-Based Method (LDRBM) for generating myocardial fibers directly on the whole heart (Section 4.1). The methodology, based on the combination of the atrial and ventricular LDRBMs presented in Chapter 2, can be easily applied to any four chambers heart geometry. Then, we describe the 3D-0D whole heart model, detailing the modeling differences with respect to the 3D-0D biventricular model (Section 4.2). Furthermore, we discuss the strategy employed to couple the 3D EM and the 0D fluid models. Finally, after presenting a procedure for the generation of a whole heart mesh, we illustrate numerical results of EP and EM simulations with physiological activation sites in a four chamber realistic computational domain of the heart (Section 4.3). The results presented in this chapter, for the whole heart EP simulation, have been published in [176].

Contents

4.1 Whole heart Rule-Based Method

In this section we present a LDRBM for the generation of full heart myofibers architecture, that is able to reproduce all the important characteristic features of the four chambers, needed to provide a realistic cardiac musculature. Our newly developed method is built upon the combination of the ventricular and atrial LDRBMs presented in Chapter 2 and on the novel definition of several inter-heart harmonic functions, which couple together the different LDRBMs for the atria and the ventricles. With this aim, the heart LDRBM combines the gradient of the inter-heart and intra-heart harmonic functions to properly represent the whole cardiac fiber architecture.

Following the backbone structure of LDRBMs presented in Sections 2.1 and 2.2, we detail hereafter the steps of the new heart LDRBM. We refer to Figure 4.1 for a schematic representation of the method in a realistic heart geometry.

1. Labelled mesh: label the mesh of the heart computational domain Ω_{heart} to define the boundary partitions $\partial\Omega_{heart} = \partial\Omega_{biv} \cup \partial\Omega_{bia}$ (see step 1 in Figure 4.1) where

$$\begin{aligned}\partial\Omega_{bia} =&\Gamma_{aepi} \cup \Gamma_{top,\ell} \cup \Gamma_{top,r} \cup \Gamma_{\ell a} \cup \Gamma_{\ell a,caps} \cup \Gamma_{ra} \cup \Gamma_{ra,caps} \cup \Gamma_{\ell ap} \cup \\ &\Gamma_{rap} \cup \Gamma_{lpv} \cup \Gamma_{rpv} \cup \Gamma_{icv} \cup \Gamma_{scv} \cup \Gamma_{mv} \cup \Gamma_{mv,caps} \cup \Gamma_{tv} \cup \Gamma_{tv,caps},\\ \partial\Omega_{biv} =&\Gamma_{vepi} \cup \Gamma_{lv} \cup \Gamma_{rv} \cup \Gamma_{av} \cup \Gamma_{pv} \cup \Gamma_{pv,cap} \cup \Gamma_{a\ell v} \cup \Gamma_{arv},\end{aligned}$$

with Γ_{aepi}, Γ_{vepi} the atrial and ventricular epicardia; $\Gamma_{\ell a}$, Γ_{ra}, $\Gamma_{\ell v}$ and Γ_{rv} the left and right atrial and ventricular endocardia; $\Gamma_{\ell a,caps}$ and $\Gamma_{ra,caps}$ the cut vein caps of LA and RA; $\Gamma_{a\ell v}$, Γ_{arv} the left and right ventricular apices; $\Gamma_{\ell ap}$, Γ_{rap} the left and right atrial appendage; Γ_{lpv}, Γ_{rpv} left and right pulmonary vein (LPV, RPV) rings; Γ_{icv}, Γ_{scv} inferior and superior caval vein (ICV, SCV) rings; Γ_{mv}, Γ_{tv} mitral (MV) and tricuspid (TV) valve rings, further subdivided in a part facing the atrial septum Γ_{mv-s}, Γ_{tv-s} and the other related to the free wall Γ_{mv-f}, Γ_{tv-f}, such that $\Gamma_{mv} = \Gamma_{mv-s} \cup\ \Gamma_{mv-f}$ and $\Gamma_{tv} = \Gamma_{tv-s} \cup\ \Gamma_{tv-f}$; $\Gamma_{mv,caps}$ and $\Gamma_{tv,caps}$ the atrioventricular caps of MV and TV; $\Gamma_{top,\ell}$ and $\Gamma_{top,r}$ the top upper region connecting the anterior LPV to RPV rings and ICV to SCV rings; Γ_{av}, Γ_{pv} aortic (AV) and pulmonary (PV) valve rings; $\Gamma_{pv,cap}$ PV cap; see step 1 in Figure 4.1.

2. Laplace problems: definition of several inter-heart and intra-heart distances, obtained by solving Laplace problems in the form of

$$\begin{cases}-\Delta\chi = 0 & \text{in } \Omega_{heart},\\ \chi = \chi_a & \text{on } \Gamma_a,\\ \chi = \chi_b & \text{on } \Gamma_b,\\ \nabla\chi \cdot \mathbf{n} = 0 & \text{on } \Gamma_n,\end{cases} \tag{4.1}$$

with proper Dirichlet boundary conditions on the heart boundaries, see step 2 in Figure 2.8. Specifically, the transmural ϕ and two inter-heart ξ and ω distances are introduced. In particular, ξ and ω are used to discriminate the left from the right heart and the atria from the ventricles, respectively (see step 2a in Figure 4.1). Then, several intra-heart distances ψ_i are computed, see step 2b in Figure 4.1. In particular, ψ_{ab}, ψ_r, ψ_v, ψ_w and ψ_{sw} stand for the same inter-atrial distances introduced in the atrial LDRBM, described in Section 2.2. Meanwhile, $\psi_{ab,\ell}$, $\psi_{ab,r}$, $\psi_{ot,\ell}$, $\psi_{ot,r}$, $\psi_{w,\ell}$

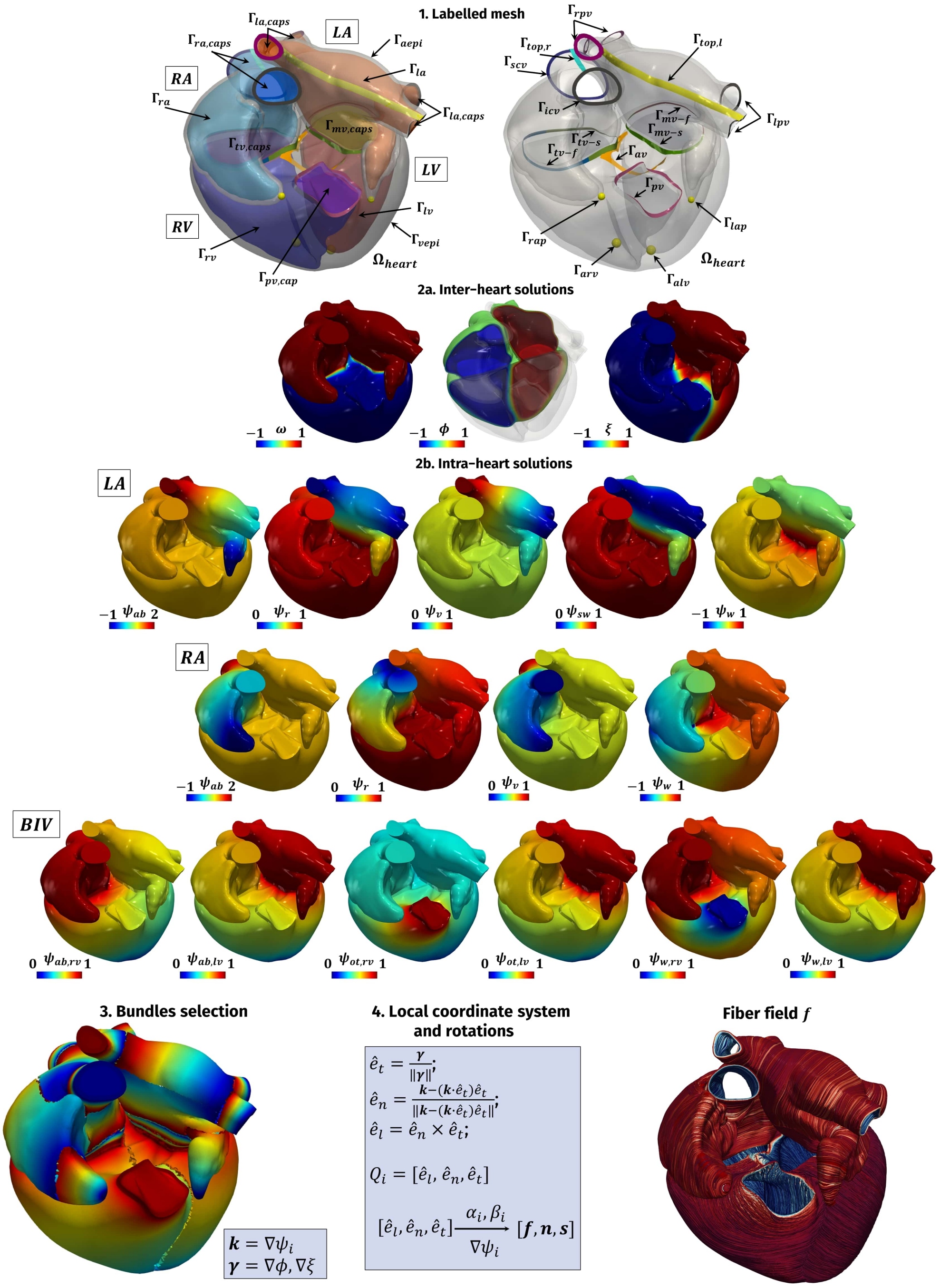

Figure 4.1: Schematic procedure of the heart LDRBM in a realistic whole heart geometry.

Type	χ	χ_a	Γ_a	χ_b	Γ_b
HEART	ϕ	1 -1	$\Gamma_{\ell a} \cup \Gamma_{\ell v}$ $\Gamma_{ra} \cup \Gamma_{rv}$	0	$\Gamma_{aepi} \cup \Gamma_{vepi} \cup \Gamma_{mv} \cup \Gamma_{tv} \cup \Gamma_{top,\ell} \cup \Gamma_{top,r}$
	ξ	1	$\Gamma_{\ell a} \cup \Gamma_{\ell v}$	-1	$\Gamma_{ra} \cup \Gamma_{rv}$
	ω	1	$\Gamma_{\ell a} \cup \Gamma_{ra}$	-1	$\Gamma_{\ell v} \cup \Gamma_{rv}$
LA	ψ_{ab}	2 0	Γ_{rpv} Γ_{lpv}	1 -1	Γ_{mv} Γ_{lap}
	ψ_r	1	Γ_{mv}	0	$\Gamma_{lpv} \cup \Gamma_{rpv}$
	ψ_v	1	Γ_{rpv}	0	Γ_{lpv}
	ψ_{sw}	1	Γ_{mv}	0	$\Gamma_{lpv} \cup \Gamma_{top,\ell} \cup \Gamma_{lap}$
	ψ_w	1 -1	Γ_{mv-s} Γ_{mv-f}	0	$\Gamma_{top,\ell}$
RA	ψ_{ab}	2 0	Γ_{icv} Γ_{scv}	1 -1 -2	Γ_{tv} Γ_{rap} Γ_{cs}
	ψ_r	1	Γ_{tv}	0	$\Gamma_{top,r}$
	ψ_v	1 0	Γ_{icv} Γ_{scv}	-1	Γ_{rap}
	ψ_w	1 -1	Γ_{tv-s} Γ_{tv-f}	0	$\Gamma_{top,r}$
BIV	$\psi_{ab,\ell}$	1	Γ_{mv}	0	$\Gamma_{a\ell v}$
	$\psi_{ab,r}$	1	Γ_{tv}	0	Γ_{arv}
	$\psi_{ot,\ell}$	1	Γ_{av}	0	$\Gamma_{a\ell v}$
	$\psi_{ot,r}$	1	Γ_{pv}	0	Γ_{arv}
	$\psi_{w,\ell}$	1	$\Gamma_{mv} \cup \Gamma_{a\ell v}$	0	Γ_{av}
	$\psi_{w,r}$	1	$\Gamma_{tv} \cup \Gamma_{arv}$	0	Γ_{pv}

Table 4.1: Boundary data chosen in the Laplace problem (4.1) for the inter-heart distances (HEART) ϕ, ξ and ω, and the intra-heart distances (LA, RA, BIV) ψ_i, where $i = ab; r; v; sw; w$ in LA and RA, while $i = ab,\ell; ab,r; ot,\ell; ot,r; w,\ell; w,r$ for LV and RV (BIV). It is understood that $\Gamma_n = \partial\Omega_{heart}/(\Gamma_a \cup \Gamma_b)$ for each Laplace problem (4.1).

and $\psi_{w,r}$ refer to the same inter-ventricular distances introduced in the ventricular D-RBM, described in Section 2.1; see step 2b in Figure 4.1. We refer to Table 4.1 for the specific choices in problem (4.1) made by the heart LDRBM.

3. Heart bundles selection: definition of the heart bundles and their dimensions throughout the domain Ω_{heart}, in order to match histology and DTI observations. With this aim, the heart LDRBM first sorts the atria from the ventricles by exploiting the inter-heart distance ω: positive value ($\omega \geq 0$) are assigned to the atria and negative ones ($\omega < 0$) to the ventricles. Afterwords, the heart LDRBM defines a unique transmural $\boldsymbol{\gamma}$ and normal $\boldsymbol{k}$ directions, for each point in Ω_{heart}, by taking the gradient of a specified inter-heart distance, $\boldsymbol{\gamma} = \nabla\phi, \nabla\xi$, and of a specific intra-heart distance, $\boldsymbol{k} = \nabla\psi_i$, respectively. For the atria, it follows the rules reported in Algorithm 1 ($\mathbf{compute_{BIA}}$), to compute inter-atrial connection (IC), LA and RA bundles (see step 3 of Section 2.2). For the ventricles, on the other hand, it exploits the steps 3-4 of the ventricular LDRBMs, detailed in Section 2.1. The complete bundles selection procedure for the heart LDRBM is fully detailed in Algorithm 5 ($\mathbf{compute_{HEART}}$), see step 3 in Figure 4.1 and also Figure 4.2).

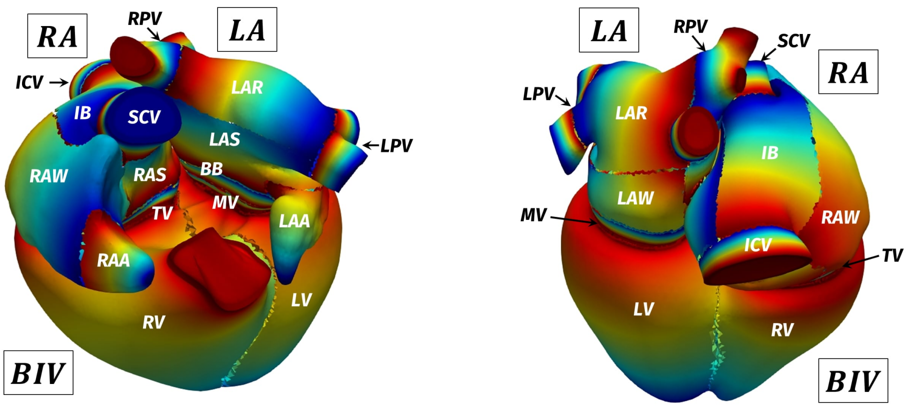

Figure 4.2: Complete bundles selection in the whole heart domain following the rules reported in Algorithms 1, 2, 3, 4 and 5; Left: frontal view; Right: posterior view.

Algorithm 5 compute$_{\mathbf{HEART}}$: *bundles selection for whole heart geometry*

```
if $\omega \geq 0$
    compute$_{\mathbf{BIA}}$
else
    if $\xi \geq 0$
        $\boldsymbol{\gamma} = \nabla\phi \ , \ \boldsymbol{k} = \psi_{w,\ell}\nabla\psi_{ab,\ell} + (1-\psi_{w,\ell})\nabla\psi_{ot,\ell} \longrightarrow$ LV
    else
        $\boldsymbol{\gamma} = \nabla\phi \ , \ \boldsymbol{k} = \psi_{w,r}\nabla\psi_{ab,r} + (1-\psi_{w,r})\nabla\psi_{ot,r} \longrightarrow$ RV
```

4. Local coordinate system and rotations: definition of the myofiber orientations $[\boldsymbol{f}, \boldsymbol{n}, \boldsymbol{s}]$ by rotating an orthonormal local coordinate system, $[\widehat{\boldsymbol{e}}_l, \widehat{\boldsymbol{e}}_n, \widehat{\boldsymbol{e}}_t]$ built at each point of the heart domain, using the transmural $\boldsymbol{\gamma}$ and normal $\boldsymbol{k}$ directions computed in the previous step. This is performed in the same way as for the other LDRBMs, by applying first the function `axis`, which takes as inputs the transmural direction $\boldsymbol{\gamma}$ together with the normal direction $\boldsymbol{k}$, and then exploiting the function `orient` (see Section 2.1):

$$Q = [\widehat{\boldsymbol{e}}_l, \widehat{\boldsymbol{e}}_n, \widehat{\boldsymbol{e}}_t] = \texttt{axis}(\boldsymbol{k}, \boldsymbol{\gamma}), \qquad [\boldsymbol{f}, \boldsymbol{n}, \boldsymbol{s}] = \texttt{orient}(Q, \alpha, \beta). \tag{4.2}$$

As done for the atrial LDRBM (see step 4 of Section 2.2), a transmural fibers variation can be prescribed in each heart bundle, in two combined ways: by defining the unique normal direction $\boldsymbol{k} = (1-|\phi|)\nabla\psi_j + |\phi|\nabla\psi_k$ $(j \neq k)$ as a linear combination of the gradients of two intra-heart distances, within the function `axis`; and/or by setting a linear relationships for the angles $\alpha_i = \alpha_{epi_i}(1-|\phi|)+\alpha_{endo_i}|\phi|$ and $\beta_i = \beta_{epi_i}(1-|\phi|)+\beta_{endo_i}|\phi|$, inside the function `orient`, where α_{epi_i}, α_{endo_i}, β_{epi_i} and β_{endo_i} are fixed rotation angles on the epicardium and endocardium of the i-th bundle, respectively.

The three unit directions correspond to the final fiber, sheet and sheet-normal directions $\boldsymbol{f}$, $\boldsymbol{n}$ and $\boldsymbol{s}$ (see step 4 in Figure 4.1).

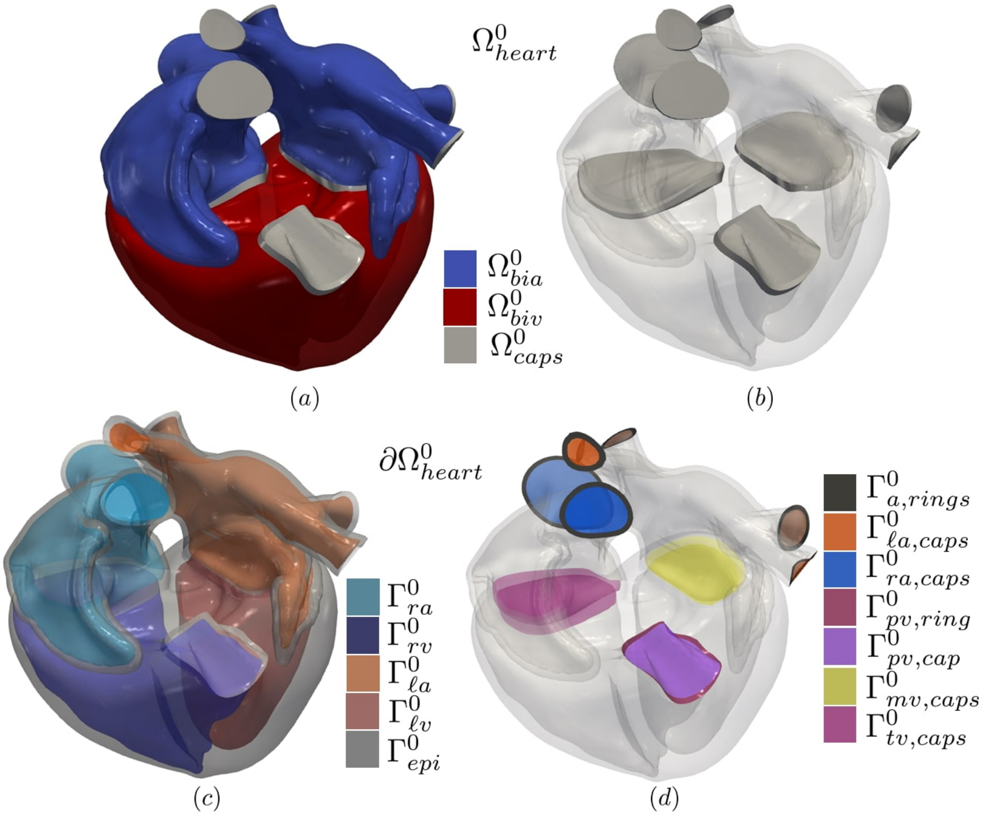

Figure 4.3: Representation of a labelled Heart reference domain Ω^0_{heart}; Top (a-b): Volume Ω^0_{heart} partitioned in $\Omega^0_{heart} = \Omega^0_{biv} \cup \Omega^0_{bia} \cup \Omega^0_{caps}$, where Ω^0_{biv} and Ω^0_{bia} are LV, RV and LA, RA regions, respectively, while Ω^0_{caps} represents the planes for the valves and for the cut veins. Bottom (c-d): Border $\partial\Omega^0_{heart}$ partitioned in $\partial\Omega^0_{heart} = \Gamma^0_{epi} \cup \Gamma^0_{\ell v} \cup \Gamma^0_{\ell a} \cup \Gamma^0_{rv} \cup \Gamma^0_{ra} \cup \Gamma^0_{a,rings} \cup \Gamma^0_{\ell a,caps} \cup \Gamma^0_{ra,caps} \cup \Gamma^0_{pv,ring} \cup \Gamma^0_{pv,cap} \cup \Gamma^0_{mv,caps} \cup \Gamma^0_{tv,caps}$.

4.2 3D-0D closed-loop model for the whole heart

In this section, we extend the biventricular 3D-0D model, presented in Chapter 3 to the whole heart. With this aim, we consider a 3D description of cardiac EM for the whole heart and a 0D representation of the circulatory system, which includes the haemodynamics of the cardiac chambers.

The 3D-0D heart model includes a detailed myofiber architecture obtained thanks to the heart LDRBM (presented in Section 4.1), which is able to account for the different fiber orientations of LA, RA, LV and RV. Moreover, the 3D-0D heart model comprises the core models for the cardiac EP, the sarcomere MA, the myocardial TM and blood haemodynamics, plus four coupling conditions, between the 3D EM and the 0D fluid models, established by volume conservation constraints.

We denote by Ω^0_{heart} the computational heart domain in the reference configuration, see Figure 4.3(a), representing the region occupied by LV, RV, LA and RA at rest. We split the domain Ω^0_{heart} in $\Omega^0_{heart} = \Omega^0_{biv} \cup \Omega^0_{bia} \cup \Omega^0_{caps}$, where Ω^0_{biv} and Ω^0_{bia} are the regions occupied by the LV, RV and LA, RA, respectively, while Ω^0_{caps} represents the planes for the valves and for the cut veins, see Figure 4.3(b). The boundary

$\partial\Omega^0_{heart}$ is partitioned into

$$\begin{aligned}\partial\Omega^0_{heart} =& \Gamma^0_{epi} \cup \Gamma^0_{\ell v} \cup \Gamma^0_{\ell a} \cup \Gamma^0_{rv} \cup \Gamma^0_{ra} \cup \Gamma^0_{mv,caps} \cup \Gamma^0_{tv,caps} \cup \\ & \Gamma^0_{a,rings} \cup \Gamma^0_{\ell a,caps} \cup \Gamma^0_{ra,caps} \cup \Gamma^0_{pv,ring} \cup \Gamma^0_{pv,cap},\end{aligned}$$

where Γ^0_{epi} is the heart epicardium, $\Gamma^0_{\ell v}$, $\Gamma^0_{\ell a}$, Γ^0_{rv} and Γ^0_{ra} are the left, right ventricular and atrial endocardia; $\Gamma^0_{mv,caps}$ and $\Gamma^0_{tv,caps}$ are the atrioventricular caps of MV and TV; $\Gamma^0_{a,rings}$ are the atrial SCV, ICV, LPV and RPV rings; $\Gamma^0_{\ell a,caps}$ and $\Gamma^0_{ra,caps}$ are LA and RA epicardial caps; $\Gamma^0_{pv,ring}$ and $\Gamma^0_{pv,cap}$ are the PV ring and epicardial cap of RV, respectively.

4.2.1 The coupled 3D-0D whole heart problem

Given the computational domain Ω^0_{heart} and the time interval $t \in (0, T]$, our complete 3D-0D Heart model reads as follows:

3D-0D Whole Heart model

$$\begin{cases}
J\chi_m \left[C_m \dfrac{\partial u}{\partial t} + \widetilde{\mathcal{I}_{ion}}(u, \boldsymbol{w}) \right] - \nabla \cdot (J\mathbf{F}^{-1}\widetilde{\mathbf{D}}\,\mathbf{F}^{-T}\nabla u) = J\chi_m \mathcal{I}_{app} & \\
\qquad\qquad\qquad\qquad\qquad\qquad\qquad\qquad \text{in } \Omega^0_{heart} \times (0, T], & (4.3a) \\
\dfrac{\partial \boldsymbol{w}}{\partial t} - \widetilde{\boldsymbol{H}}(u, \boldsymbol{w}) = \mathbf{0} & \text{in } \Omega^0_{heart} \times (0, T], \quad (4.3b) \\
\left(J\mathbf{F}^{-1}\widetilde{\mathbf{D}}\,\mathbf{F}^{-T}\nabla u \right) \cdot \mathbf{N} = 0 & \text{on } \partial\Omega^0_{heart} \times (0, T], \quad (4.3c) \\
\dfrac{\partial \mathbf{s}}{\partial t} = \boldsymbol{K}(\mathbf{s}, [\mathrm{Ca}^{2+}]_{\mathrm{i}}, SL) & \text{in } (\Omega^0_{biv} \cup \Omega^0_{bia}) \times (0, T], \quad (4.3d) \\
\rho_s \dfrac{\partial^2 \mathbf{d}}{\partial t^2} - \nabla \cdot \widetilde{\mathbf{P}}(\mathbf{d}, \widetilde{T}_a(\mathbf{s}, \boldsymbol{x})) = \mathbf{0} & \text{in } \Omega^0_{heart} \times (0, T], \quad (4.3e) \\
\widetilde{\mathbf{P}}(\mathbf{d}, \widetilde{T}_a(\mathbf{s}, \boldsymbol{x}))\mathbf{N} = \mathbf{K}^{epi}\mathbf{d} + \mathbf{C}^{epi}\dfrac{\partial \mathbf{d}}{\partial t} & \text{on } \Gamma^0_{epi} \times (0, T], \quad (4.3f) \\
\widetilde{\mathbf{P}}(\mathbf{d}, \widetilde{T}_a(\mathbf{s}, \boldsymbol{x}))\mathbf{N} = \mathbf{K}^{pv}\mathbf{d} + \mathbf{C}^{pv}\dfrac{\partial \mathbf{d}}{\partial t} & \text{on } (\Gamma^0_{pv,cap} \cup \Gamma^0_{pv,ring}) \times (0, T], \quad (4.3g) \\
\widetilde{\mathbf{P}}(\mathbf{d}, \widetilde{T}_a(\mathbf{s}, \boldsymbol{x}))\mathbf{N} = -p_{\ell v}(t)\, J\mathbf{F}^{-T}\mathbf{N} & \text{on } \Gamma^0_{\ell v} \times (0, T], \quad (4.3h) \\
\widetilde{\mathbf{P}}(\mathbf{d}, T_a(\mathbf{s}, \boldsymbol{x}))\mathbf{N} = -p_{rv}(t)\, J\mathbf{F}^{-T}\mathbf{N} & \text{on } \Gamma^0_{rv} \times (0, T], \quad (4.3i) \\
\widetilde{\mathbf{P}}(\mathbf{d}, \widetilde{T}_a(\mathbf{s}, \boldsymbol{x}))\mathbf{N} = -p_{\ell a}(t)\, J\mathbf{F}^{-T}\mathbf{N} & \text{on } (\Gamma^0_{\ell a} \cup \Gamma^0_{\ell a,caps}) \times (0, T], \quad (4.3j) \\
\widetilde{\mathbf{P}}(\mathbf{d}, \widetilde{T}_a(\mathbf{s}, \boldsymbol{x}))\mathbf{N} = -p_{ra}(t)\, J\mathbf{F}^{-T}\mathbf{N} & \text{on } (\Gamma^0_{ra} \cup \Gamma^0_{ra,caps}) \times (0, T], \quad (4.3k) \\
\widetilde{\mathbf{P}}(\mathbf{d}, \widetilde{T}_a(\mathbf{s}, \boldsymbol{x}))\mathbf{N} = \mathbf{0} & \text{on } (\Gamma^0_{mv,caps} \cup \Gamma^0_{tv,caps}) \times (0, T], \quad (4.3l) \\
\mathbf{d} = \mathbf{0} & \text{on } \Gamma^0_{a,rings} \times (0, T], \quad (4.3m) \\
\dfrac{d\boldsymbol{c}(t)}{dt} = \boldsymbol{G}_{\mathrm{H}}(t, \boldsymbol{c}(t), p_{\ell v}(t), p_{rv}(t), p_{\ell a}(t), p_{ra}(t)) & \text{for } t \in (0, T], \quad (4.3n) \\
\widetilde{V}^{3\mathrm{D}}_{\ell v}(\mathbf{d}(t)) = V_{\ell v}(\boldsymbol{c}(t)) & \text{for } t \in (0, T], \quad (4.3o) \\
\widetilde{V}^{3\mathrm{D}}_{rv}(\mathbf{d}(t)) = V_{rv}(\boldsymbol{c}(t)) & \text{for } t \in (0, T], \quad (4.3p) \\
\widetilde{V}^{3\mathrm{D}}_{\ell a}(\mathbf{d}(t)) = V_{\ell a}(\boldsymbol{c}(t)) & \text{for } t \in (0, T], \quad (4.3q) \\
\widetilde{V}^{3\mathrm{D}}_{ra}(\mathbf{d}(t)) = V_{ra}(\boldsymbol{c}(t)) & \text{for } t \in (0, T]. \quad (4.3r)
\end{cases}$$

where the generalized variables with the tilde symbol ($\sim$) are detailed hereafter.

The model unknowns are the transmembrane action potential u, the ionic variables vector $\boldsymbol{w}$, the state variables of the active force generation model $\mathbf{s}$, the tissue mechanical displacement $\mathbf{d}$, the state vector of the circulation model $\boldsymbol{c}$ (including pressures, volumes and fluxes of the different compartments composing the vascular network, see Equation (3.18)) and the pressures of the four heart chambers $p_{\ell v}$, p_{rv}, $p_{\ell a}$ and p_{ra}. Finally, the model is closed by the initial conditions in $\Omega^0_{heart} \times \{0\}$:

$$\begin{gathered} u = u_0, \quad \boldsymbol{w} = \boldsymbol{w}_0, \quad \mathbf{s} = \mathbf{s}_0, \quad \mathbf{d} = \mathbf{d}_0, \quad \frac{\partial \mathbf{d}}{\partial t} = \dot{\mathbf{d}}_0, \\ \boldsymbol{c} = \boldsymbol{c}_0, \quad p_{\ell v} = p_{\ell v,0}, \quad p_{rv} = p_{rv,0}, \quad p_{\ell a} = p_{\ell a,0}, \quad p_{ra} = p_{ra,0}. \end{gathered}$$

Equations (4.3a)-(4.3c) represent the EP core model. With respect to the 3D-0D biventricular case (3.24), the 3D-0D heart model employs two different ionic models to properly describe the cardiac EP: TTP06 [247] for the ventricles and CRN98 [47] for the atria. To account for this ionic heterogeneity, we introduced the following generalized diffusion tensor $\widetilde{\mathbf{D}}$ as

$$\begin{gathered} \widetilde{\mathbf{D}} = \sigma_f \frac{\mathbf{F}\boldsymbol{f}_0 \otimes \mathbf{F}\boldsymbol{f}_0}{|\mathbf{F}\boldsymbol{f}_0|^2} + \sigma_s \frac{\mathbf{F}\boldsymbol{s}_0 \otimes \mathbf{F}\boldsymbol{s}_0}{|\mathbf{F}\boldsymbol{s}_0|^2} + \sigma_n \frac{\mathbf{F}\boldsymbol{n}_0 \otimes \mathbf{F}\boldsymbol{n}_0}{|\mathbf{F}\boldsymbol{n}_0|^2}, \\ \text{with } \sigma_k = \begin{cases} \sigma_k(\phi_{fast}) & \text{in } \Omega^0_{biv} \\ \sigma_k^{(a)} & \text{in } \Omega^0_{bia} \\ 0 & \text{in } \Omega^0_{caps} \end{cases} \quad \text{for } k = f, s, n, \end{gathered}$$

and the generalized reaction terms $\widetilde{\mathcal{I}_{ion}}$ and $\widetilde{\boldsymbol{H}}$ as

$$\widetilde{\mathcal{I}_{ion}} = \begin{cases} \mathcal{I}_{ion} & \text{in } \Omega^0_{biv} \\ \mathcal{I}_{ion}^{(a)} & \text{in } \Omega^0_{bia} \\ 0 & \text{in } \Omega^0_{caps} \end{cases}, \qquad \widetilde{\boldsymbol{H}} = \begin{cases} \boldsymbol{H} & \text{in } \Omega^0_{biv} \\ \boldsymbol{H}^{(a)} & \text{in } \Omega^0_{bia} \\ 0 & \text{in } \Omega^0_{caps} \end{cases},$$

where $\sigma_k^{(a)}$, $\mathcal{I}_{ion}^{(a)}$ and $\boldsymbol{H}^{(a)}$ refer to CRN98 ionic model for the atria (see [47] for details on the definition of $\mathcal{I}_{ion}^{(a)}$ and $\boldsymbol{H}^{(a)}$), while $\sigma_k(\phi_{fast})$, $\mathcal{I}_{ion}$ and $\boldsymbol{H}$ are the terms related to the TTP06 ionic model for the ventricles, see Section 3.1.2. Moreover, thanks to the generalized terms ($\widetilde{\mathbf{D}}$, $\widetilde{\mathcal{I}_{ion}}$ and $\widetilde{\boldsymbol{H}}$) the volume domain Ω^0_{caps} is a non conductive region, which electrically isolates the atria from the ventricles.

Equation (4.3d) stands for the MA core model. Both in the ventricular (Ω^0_{biv}) and in the atrial domain (Ω^0_{bia}), the RDQ18-ANN model, described in Section 3.1.3, has been considered [196]. However, to account for the different intracellular calcium ionic concentration $[\mathrm{Ca}^{2+}]_\mathrm{i}$, provided by the TTP06 and CRN98 ionic models, the function $\boldsymbol{K}$ takes as input the calcium variable of TTP06 (w_{Ca}) in Ω^0_{biv} and the one of CRN98 ($w^{(a)}_{\mathrm{Ca}}$) in Ω^0_{bia}

$$\begin{aligned} &\boldsymbol{K}(\mathbf{s}, w_{\mathrm{Ca}}, SL) && \text{in } \Omega^0_{biv}, \\ &\boldsymbol{K}(\mathbf{s}, w^{(a)}_{\mathrm{Ca}}, SL) && \text{in } \Omega^0_{bia}. \end{aligned}$$

Moreover, to account for different active tensions between the ventricles and the atria, we defined a generalized active tension $\widetilde{T_a}$ as

$$\widetilde{T_a} = \begin{cases} T_a(\mathbf{s}, \boldsymbol{x}) = T_a^{max} G(\mathbf{s}) \; [\xi(\boldsymbol{x}) + C_{\ell rv}(1 - \xi(\boldsymbol{x}))] & \text{in } \Omega^0_{biv}, \\ T_a^{(a)}(\mathbf{s}, \boldsymbol{x}) = T_a^{max,(a)} G(\mathbf{s}) \; [\xi(\boldsymbol{x}) + C_{\ell ra}(1 - \xi(\boldsymbol{x}))] & \text{in } \Omega^0_{bia}, \end{cases}$$

where T_a^{max} and $T_a^{max,(a)}$ denote the maximal tension prescribed for the ventricles and the atria, respectively; $C_{\ell rv}, C_{\ell ra} \in (0,1]$ represent the left-right ventricular and atrial contractility ratio, respectively; $\xi \in [0,1]$ is the inter-heart distance, defined in Section 4.1, see also Figure 4.1.

Equations (4.3e)−(4.3m) act as the TM core model. The 3D-0D heart model exploits the same active stress formalism presented in Section 3.1.4 for the biventricular case. For the active part of the heart Ω^0_{biv} and Ω^0_{bia}, we use the Guccione orthotropic model [90], presented in Section 3.1.4, while purely passive tissues Ω^0_{caps} (veins and valve planes) are characterized by a Neo–Hookean model [160]. In addition to the passive material behaviour, we describe the active response to electrical activation with an orthotropic active stress formulation for the ventricles in Ω^0_{biv}. Instead, one-dimensional active tension, along the fiber, is imposed in the stress tensor for the atria in Ω^0_{bia}. Finally, incompressibility of all tissues is enforced with a penalty method. Therefore, we introduced in Equation (4.3e), the generalized first Piola-Kirchhoff stress tensor $\widetilde{\mathbf{P}} = \widetilde{\mathbf{P}}(\mathbf{d}, \widetilde{T}_a)$, defined as

$$\widetilde{\mathbf{P}} = \begin{cases} \dfrac{\partial \mathcal{W}^{(\mathrm{G})}(\mathbf{F})}{\partial \mathbf{F}} + T_a(\boldsymbol{x}, \mathbf{s}) \left[n_f \frac{\mathbf{F}\boldsymbol{f}_0 \otimes \boldsymbol{f}_0}{\sqrt{\mathcal{I}_{4f}}} + n_s \frac{\mathbf{F}\boldsymbol{s}_0 \otimes \boldsymbol{s}_0}{\sqrt{\mathcal{I}_{4s}}} + n_n \frac{\mathbf{F}\boldsymbol{n}_0 \otimes \boldsymbol{n}_0}{\sqrt{\mathcal{I}_{4n}}} \right] & \text{in } \Omega^0_{biv}, \\ \dfrac{\partial \mathcal{W}^{(\mathrm{G})}(\mathbf{F})}{\partial \mathbf{F}} + T_a^{(a)}(\boldsymbol{x}, \mathbf{s}) \frac{\mathbf{F}\boldsymbol{f}_0 \otimes \boldsymbol{f}_0}{\sqrt{\mathcal{I}_{4f}}} & \text{in } \Omega^0_{bia}, \\ \dfrac{\partial \mathcal{W}^{(\mathrm{N})}(\mathbf{F})}{\partial \mathbf{F}} & \text{in } \Omega^0_{caps}, \end{cases} \tag{4.4}$$

where $\mathcal{W}^{(\mathrm{G})}$ is the Guccione constitutive law, defined in Section 3.1.4, and $\mathcal{W}^{(\mathrm{N})}$ is the Neo–Hookean strain energy density function, defined as

$$\mathcal{W}^{(\mathrm{N})} = \frac{\mu}{2} \left(J^{-\frac{2}{3}} \mathbf{F} : \mathbf{F} - 3 \right) + \frac{\kappa^{(\mathrm{N})}}{4} \left[(J-1)^2 + \log^2(J) \right],$$

with the shear modulus μ and the bulk modulus $\kappa^{(\mathrm{N})}$.

For the mechanical boundary conditions, we impose:

- generalized Robin boundary conditions (4.3f)−(4.3g) on the epicardial boundary Γ^0_{epi} and on PV cap and ring $\Gamma^0_{pv,cap} \cup \Gamma^0_{pv,ring}$, to model the mechanical constrains provided by the pericardium and the pulmonary valve, respectively. In accordance to Equations (3.6), we define the following tensors

  $$\begin{aligned} \mathbf{K}^k &= K^k_{\parallel}(\mathbf{N} \otimes \mathbf{N} - \mathbf{I}) - K^k_{\perp}(\mathbf{N} \otimes \mathbf{N}) & \qquad i &= epi, pv, \\ \mathbf{C}^k &= C^k_{\parallel}(\mathbf{N} \otimes \mathbf{N} - \mathbf{I}) - C^k_{\perp}(\mathbf{N} \otimes \mathbf{N}) & \qquad i &= epi, pv, \end{aligned}$$

  where $K^k_{\parallel}$, $K^k_{\perp}$, $C^k_{\parallel}$, $C^k_{\perp} \in \mathbb{R}^+$ are the stiffness and viscosity parameters of the tissue in the normal and tangential directions to the surface $\Gamma^0_{pv,cap} \cup \Gamma^0_{pv,ring}$ ($k = pv$) and Γ^0_{epi} ($k = epi$), respectively;

- normal stress boundary conditions (4.3h)−(4.3k) on LV, RV, LA and RA endocardia $\Gamma^0_{\ell v}$, Γ^0_{rv}, $\Gamma^0_{\ell a}$ and Γ^0_{ra}, where $p_{\ell v}(t)$, $p_{rv}(t)$, $p_{\ell a}(t)$ and $p_{ra}(t)$ are the pressures exerted by the blood in LV, RV, LA and RA, respectively. Moreover, to model the continuity of pressure from LA to the pulmonary veins and from RA to the caval veins, normal stress boundary conditions are applied also on LA and RA caps, $\Gamma^0_{\ell a,caps}$ and $\Gamma^0_{ra,caps}$, with $p_{\ell a}(t)$ and $p_{ra}(t)$, respectively;

- homogeneous Neumann boundary conditions (4.3l) on the atrioventricular valves caps $\Gamma^0_{mv,caps} \cup \Gamma^0_{tv,caps}$;
- homogeneous Dirichlet boundary conditions (4.3m) on the atrial rings $\Gamma^0_{a,rings}$ to account for the constrain imposed by the pulmonary and caval veins.

Coupling conditions in the 3D-0D heart model

To couple the 3D EM heart model, given by Equations (4.3a)−(4.3m), with the 0D fluid model (3.19) (see Section 3.1.5), we follow the same strategy, presented in Section 3.1.6, for the 3D-0D biventricular model and here extended to the whole heart. Specifically, we replace the time-varying elastance elements, representing LV, RV, LA and RA in the circulation model, with their corresponding 3D description, obtaining the coupled 3D-0D heart model sketched in Figure 4.4. The 3D heart model replaces Equations (3.17a)−(3.17d) for all the pressure variables of the 0D circulation model and, in place, it introduces the four volume-consistency coupling conditions (4.3o)−(4.3r), where $V_{\ell v}$, V_{rv}, $V_{\ell a}$ and V_{ra} are LV, RV, LA and RA volumes within the 0D circulation model and $V_i^{3\text{D}}$ (with $i = \ell v, rv, \ell a, ra$) represents the 3D ventricular volume for the four heart chambers, computed by exploiting the divergence (Gauss) theorem

$$\widetilde{V}_i^{3\text{D}}(\mathbf{d}(t)) = \frac{1}{3}\int_{\Gamma^0_{pool,i}} J(t)\,(\mathbf{x} + \mathbf{d}(t) - \mathbf{b}_i)\cdot \mathbf{F}^{-T}(t)\,\mathbf{N}\,d\Gamma_0 \qquad i = \ell v, rv, \ell a, ra,$$

where $\Gamma^0_{pool,i}$ are the blood pools of LV, RV, LA and RA[1], defined as

$$\begin{aligned}\Gamma^0_{pool,i} &= \Gamma^0_i \cup \Gamma^0_{mv,caps} &&\text{for } i = \ell v, \ell a,\\ \Gamma^0_{pool,i} &= \Gamma^0_i \cup \Gamma^0_{tv,caps} &&\text{for } i = rv, ra.\end{aligned}$$

Moreover, $\mathbf{b}_i$ is a vector that lays inside LV, RV, LA or RA. Notice that in the 3D-0D heart model the volume integral are exactly computed because $\Gamma^0_{pool,i}$ are closed surfaces.

The 3D-0D coupled model must satisfy at each time $t \in (0, T]$ the volume-consistency coupling conditions (4.3o)−(4.3r). Moreover, having introduced four additional equations (i.e (4.3o)−(4.3r)), four additional unknowns are associated to the 3D-0D model: the pressure of all the four chambers, $p_{\ell v}(t)$, $p_{rv}(t)$, $p_{\ell a}(t)$ and $p_{ra}(t)$, are no longer determined by the 0D circulation model, but rather act as Lagrange multipliers associated to the constraints (4.3o)−(4.3r). Hence, the 0D "reduced" circulation model is expressed by Equation (4.3n) where $\boldsymbol{G}_{\text{H}}$ is a proper function that collects the right hand sides of Equations (3.16) and (3.17), apart from those corresponding to (3.17a)−(3.17d).

We remark that with the above coupling approach, both the continuity of volumes and pressures, between the 3D EM and the 0D circulation models, are ensured (see Section 3.1.6 for further details).

4.2.2 Heart reference configuration and initial displacement

To recover the reference configuration Ω^0_{heart}, to which the 3D-0D heart model (4.3) refers, we adopt the same procedure presented for the biventricular model in Section 3.1.8 and here extend to the whole heart case.

---

[1] Concerning the caps surfaces $\Gamma^0_{mv,caps}$ and $\Gamma^0_{tv,caps}$, the volume integral are indeed computed only on the cap surface facing to the corresponding heart chamber.

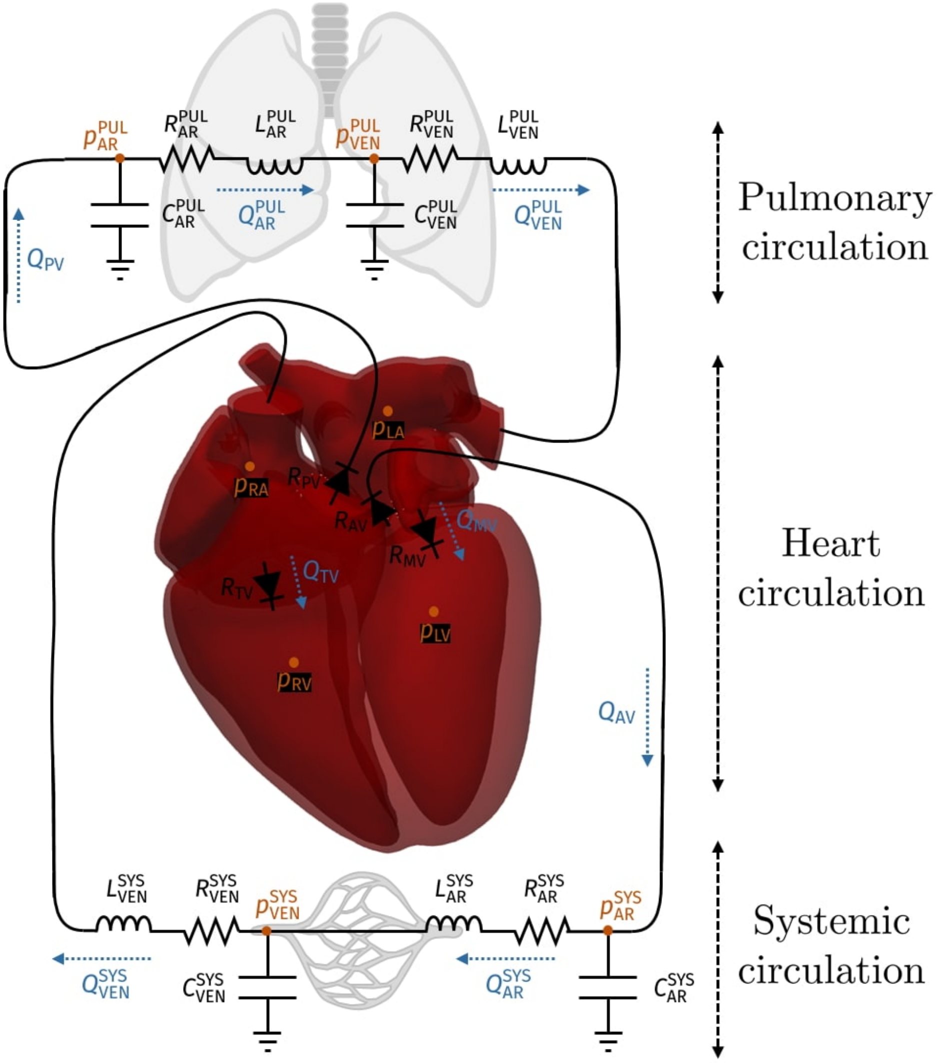

Figure 4.4: 3D-0D coupling between the 3D EM heart model and the 0D fluid model. The state variables corresponding to pressures and fluxes are depicted in orange and blue, respectively.

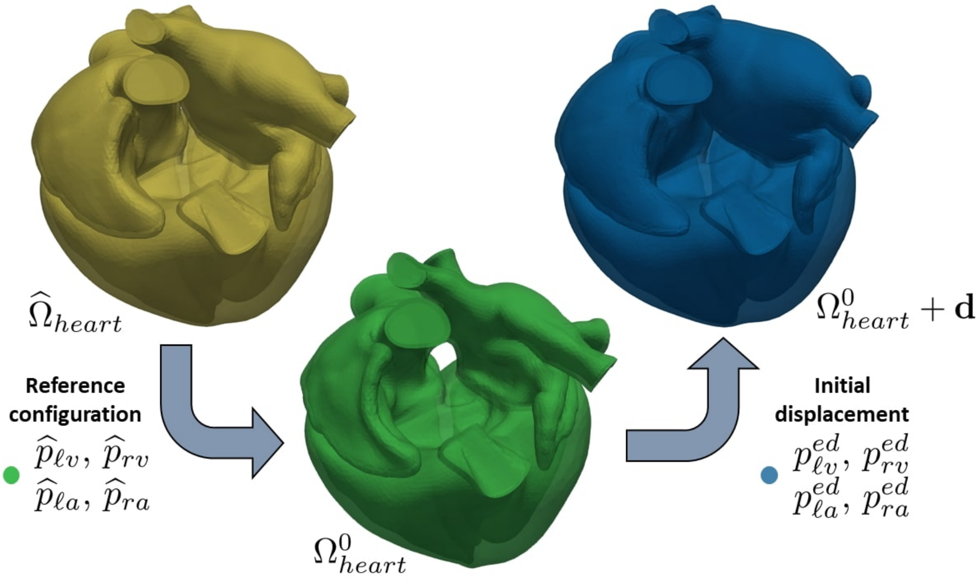

Figure 4.5: Schematic representation of the strategy used to recover the reference configuration Ω^0_{heart} and to set the mechanics initial condition in the 3D-0D heart model (4.3).

To recover the reference configuration Ω^0_{heart}, starting from a geometry $\widehat{\Omega}_{heart}$ acquired from medical images during the diastolic phase, when the heart is loaded with the pressures $\pi_{\ell v} = \widehat{p}_{\ell v}$, $\pi_{rv} = \widehat{p}_{rv}$, $\pi_{\ell a} = \widehat{p}_{\ell a}$, $\pi_{ra} = \widehat{p}_{ra}$ and with a residual active tension $\widetilde{T}_a = \widehat{T}_a$, we solve the following inverse problem:
Find the domain Ω^0_{heart} such that, if we inflate Ω^0_{heart} by $\mathbf{d}$, solution of the mechanical problem

$$\begin{cases}
\nabla \cdot \widetilde{\mathbf{P}}(\mathbf{d}, \widetilde{T}_a(\mathbf{s}, \boldsymbol{x})) = \mathbf{0} & \text{in } \Omega^0_{heart}, \\
\widetilde{\mathbf{P}}(\mathbf{d}, \widetilde{T}_a(\mathbf{s}, \boldsymbol{x}))\mathbf{N} + \mathbf{K}^{epi}\mathbf{d} = \mathbf{0} & \text{on } \Gamma^0_{epi}, \\
\widetilde{\mathbf{P}}(\mathbf{d}, \widetilde{T}_a(\mathbf{s}, \boldsymbol{x}))\mathbf{N} + \mathbf{K}^{pv}\mathbf{d} = \mathbf{0} & \text{on } \Gamma^0_{pv,cap} \cup \Gamma^0_{pv,ring}, \\
\widetilde{\mathbf{P}}(\mathbf{d}, \widetilde{T}_a(\mathbf{s}, \boldsymbol{x}))\mathbf{N} = -\pi_{\ell v}\, J\mathbf{F}^{-T}\mathbf{N} & \text{on } \Gamma^0_{\ell v}, \\
\widetilde{\mathbf{P}}(\mathbf{d}, \widetilde{T}_a(\mathbf{s}, \boldsymbol{x}))\mathbf{N} = -\pi_{rv}\, J\mathbf{F}^{-T}\mathbf{N} & \text{on } \Gamma^0_{rv}, \\
\widetilde{\mathbf{P}}(\mathbf{d}, \widetilde{T}_a(\mathbf{s}, \boldsymbol{x}))\mathbf{N} = -\pi_{\ell a}\, J\mathbf{F}^{-T}\mathbf{N} & \text{on } \Gamma^0_{\ell a} \cup \Gamma^0_{\ell a,caps}, \\
\widetilde{\mathbf{P}}(\mathbf{d}, \widetilde{T}_a(\mathbf{s}, \boldsymbol{x}))\mathbf{N} = -\pi_{ra}\, J\mathbf{F}^{-T}\mathbf{N} & \text{on } \Gamma^0_{ra} \cup \Gamma^0_{ra,caps}, \\
\widetilde{\mathbf{P}}(\mathbf{d}, \widetilde{T}_a(\mathbf{s}, \boldsymbol{x}))\mathbf{N} = \mathbf{0} & \text{on } \Gamma^0_{mv,caps} \cup \Gamma^0_{tv,caps}, \\
\mathbf{d} = \mathbf{0} & \text{on } \Gamma^0_{a,rings},
\end{cases} \tag{4.5}$$

obtained for $\pi_{\ell v} = \widehat{p}_{\ell v}$, $\pi_{rv} = \widehat{p}_{rv}$, $\pi_{\ell a} = \widehat{p}_{\ell a}$, $\pi_{ra} = \widehat{p}_{ra}$ and $\widetilde{T}_a = \widehat{T}_a$, we get the domain $\widehat{\Omega}_{heart}$.

After recovering Ω^0_{heart}, we inflate the heart reference configuration Ω^0_{heart} by solving again (4.5) (but now as a forward problem), where we set the pressures $\pi_{\ell v} = p^{ed}_{\ell v}$, $\pi_{rv} = p^{ed}_{rv}$, $\pi_{\ell a} = p^{ed}_{\ell a}$ and $\pi_{ra} = p^{ed}_{ra}$, with the superscript *ed* stands for the end-diastolic phase. Thus, the solution $\mathbf{d}$ of the problem (4.5) and the pressures $p^{ed}_{\ell v}$, p^{ed}_{rv}, $p^{ed}_{\ell a}$, p^{ed}_{ra} are set as initial conditions $\mathbf{d}_0$ (for $\mathbf{d}$), $p_{\ell v,0}$ (for $p_{\ell v}$), $p_{rv,0}$ (for p_{rv}), $p_{\ell a,0}$ (for $p_{\ell a}$) and $p_{ra,0}$ (for p_{ra}) in the 3D-0D heart problem (4.3). For the numerical resolution of the above inverse problem we refer to [199], where several algorithms, based on fixed-point iteration schemes, are proposed.

4.2.3 Numerical approximation of the 3D-0D whole heart problem

For the numerical approximation of the 3D-0D heart model (4.3) we adopt the same Segregated-Intergrid-Staggered (SIS) numerical scheme, presented in detail for the biventricular 3D-0D model in Section 3.2. The core models, contributing to both cardiac EM and blood circulation, are solved sequentially once per time step in a segregated manner, by using different resolutions in space and time: we consider two nested meshes Ω_{h_1} and Ω_{h_2} of the computational domain Ω^0_{heart} (with $h_1 < h_2$). We adopt the finer mesh Ω_{h_1} for EP, while the coarser one Ω_{h_2} for both MA and TM, and we employ an efficient intergrid transfer operator between the nested grids Ω_{h_1} and Ω_{h_2}, which allows to evaluate the feedback between the different core models. Moreover, the cardiac EP model is solved with a finer time step τ with respect to the other core models, which are solved with a time resolution $\Delta t = N_{sub}\tau$, with $N_{sub} \in \mathbb{N}$. In the SIS numerical scheme, we first update the variables of EP, then those of MA and finally, after updating the unknowns of TM, constrained by volume-consistency coupling conditions (4.3o)−(4.3r), we update the circulation variables. The whole algorithm for the SIS numerical scheme is reported in Figure 3.9. We refer the reader to Section 3.2 for further details about the space-time discretization of the different core models in the SIS numerical scheme.

In what follows, we illustrate the extension, to the whole heart, of the numerical solution of the 3D-0D coupled problem, presented in Section 3.2.3 for the biventricular model.

In the 3D-0D heart model (4.3), we couple the 3D TM model (4.3e)−(4.3m) with the 0D closed-loop model (4.3n) by means of the volume conservation constraints (4.3o)-(4.3r), where the pressures $p_{\ell v}$, p_{rv}, $p_{\ell a}$ and p_{ra} act as Lagrange multipliers.

Introducing the discrete times $t^n = n\Delta t$ (with $n \geq 0$) and denoting by $\underline{\boldsymbol{a}}^n_{h_2} \simeq \underline{\boldsymbol{a}}_{h_2}(t^n)$ the fully discretized FEM approximation of the generic (scalar a, vectorial $\boldsymbol{a}$ or tensorial $\mathbf{A}$) variable $\boldsymbol{a}(t)$, the fully discretized version of the 3D TM model coupled with 0D fluid model, at each time step t^{n+1}, reads:

Given $\underline{\widetilde{T_a}}_{h_2}^{(n+1)}$, find $\underline{\mathbf{d}}^{n+1}_{h_2}$, $p^{n+1}_{\ell v}$, p^{n+1}_{rv}, $p^{n+1}_{\ell a}$ and p^{n+1}_{ra} by solving:

$$\begin{cases} \left(\rho_s \dfrac{1}{\Delta t^2}\mathcal{M}^{(2)} + \dfrac{1}{\Delta t}(\mathcal{F}_{epi} + \mathcal{F}_{pv}) + \mathcal{G}_{epi} + \mathcal{G}_{pv}\right)\underline{\mathbf{d}}^{n+1}_{h_2} + \widetilde{\boldsymbol{S}}(\underline{\mathbf{d}}^{n+1}_{h_2}, \underline{\widetilde{T_a}}_{h_2}^{(n+1)}) + \\ \qquad + p^{n+1}_{\ell v}\boldsymbol{P}_{\ell v}(\underline{\mathbf{d}}^{n+1}_{h_2}) + p^{n+1}_{rv}\boldsymbol{P}_{rv}(\underline{\mathbf{d}}^{n+1}_{h_2}) + \\ \qquad + p^{n+1}_{\ell a}\boldsymbol{P}_{\ell a}(\underline{\mathbf{d}}^{n+1}_{h_2}) + p^{n+1}_{ra}\boldsymbol{P}_{ra}(\underline{\mathbf{d}}^{n+1}_{h_2}) = \\ \qquad = \rho_s \dfrac{2}{\Delta t^2}\mathcal{M}^{(2)}\underline{\mathbf{d}}^{n}_{h_2} - \rho_s \dfrac{1}{\Delta t^2}\mathcal{M}^{(2)}\underline{\mathbf{d}}^{n-1}_{h_2} + \dfrac{1}{\Delta t}(\mathcal{F}_{epi} + \mathcal{F}_{pv})\underline{\mathbf{d}}^{n}_{h_2}, \\ V_{\ell v}(\boldsymbol{c}^n) = \widetilde{V}^{3\mathrm{D}}_{\ell v}(\underline{\mathbf{d}}^{n+1}_{h_2}), \\ V_{rv}(\boldsymbol{c}^n) = \widetilde{V}^{3\mathrm{D}}_{rv}(\underline{\mathbf{d}}^{n+1}_{h_2}), \\ V_{\ell a}(\boldsymbol{c}^n) = \widetilde{V}^{3\mathrm{D}}_{\ell a}(\underline{\mathbf{d}}^{n+1}_{h_2}), \\ V_{ra}(\boldsymbol{c}^n) = \widetilde{V}^{3\mathrm{D}}_{ra}(\underline{\mathbf{d}}^{n+1}_{h_2}). \end{cases} \tag{4.6}$$

where

$$\begin{aligned}
\mathcal{M}^{(2)}_{ij} &= \int_{\Omega_{h_2}} \boldsymbol{\varphi_j} \cdot \boldsymbol{\varphi_i}\, d\Omega, \qquad \widetilde{\boldsymbol{S}}_i = \int_{\Omega_{h_2}} \widetilde{\mathbf{P}}(\underline{\mathbf{d}}^{n+1}_{h_2}, \widetilde{\underline{T_a}_{h_2}}^{(n+1)}) : \nabla\boldsymbol{\varphi}_i\, d\Omega,\\
(\mathcal{F}_k)_{ij} &= \int_{\Gamma^k_{h_2}} \left[C^k_{\parallel}(\mathbf{N}_{h_2} \otimes \mathbf{N}_{h_2} - \mathbf{I}_{h_2}) - C^k_{\perp}(\mathbf{N}_{h_2} \otimes \mathbf{N}_{h_2})\right] \boldsymbol{\varphi}_j \cdot \boldsymbol{\varphi}_i\, d\Gamma, \quad k = epi, pv,\\
(\mathcal{G}_k)_{ij} &= \int_{\Gamma^k_{h_2}} \left[K^k_{\parallel}(\mathbf{N}_{h_2} \otimes \mathbf{N}_{h_2} - \mathbf{I}_{h_2}) - K^k_{\perp}(\mathbf{N}_{h_2} \otimes \mathbf{N}_{h_2})\right] \boldsymbol{\varphi}_j \cdot \boldsymbol{\varphi}_i\, d\Gamma, \quad k = epi, pv,\\
(\boldsymbol{P}_k)_i &= \int_{\Gamma^k_{h_2}} J^{n+1}_{h_2} (\mathbf{F}^{n+1}_{h_2})^{-T} \mathbf{N}_{h_2} \cdot \boldsymbol{\varphi}_i\, d\Gamma, \quad k = \ell v, rv, \ell a, ra,
\end{aligned}$$

with

$$\begin{aligned}
&\Omega_{h_2} = (\Omega^0_{heart})_{h_2},\\
\Gamma^{epi}_{h_2} &= (\Gamma^0_{epi})_{h_2}, \quad \Gamma^{pv}_{h_2} = (\Gamma^0_{pv,cap})_{h_2} \cup (\Gamma^0_{pv,ring})_{h_2},\\
\Gamma^{\ell v}_{h_2} &= (\Gamma^0_{\ell v})_{h_2}, \quad \Gamma^{\ell a}_{h_2} = (\Gamma^0_{\ell a})_{h_2} \cup (\Gamma^0_{\ell a,caps})_{h_2},\\
\Gamma^{rv}_{h_2} &= (\Gamma^0_{rv})_{h_2}, \quad \Gamma^{ra}_{h_2} = (\Gamma^0_{ra})_{h_2} \cup (\Gamma^0_{ra,caps})_{h_2}.
\end{aligned}$$

The fully discretized version of the system (4.6), can be compactly written as:

$$\begin{cases}
\mathbf{r_d}(\underline{\mathbf{d}}^{n+1}_h, p^{n+1}_{\ell v}, p^{n+1}_{rv}, p^{n+1}_{\ell a}, p^{n+1}_{ra}) & = \mathbf{0}\\
r_{p_{\ell v}}(\underline{\mathbf{d}}^{n+1}_h) & = 0\\
r_{p_{rv}}(\underline{\mathbf{d}}^{n+1}_h) & = 0\\
r_{p_{\ell a}}(\underline{\mathbf{d}}^{n+1}_h) & = 0\\
r_{p_{ra}}(\underline{\mathbf{d}}^{n+1}_h) & = 0
\end{cases}, \tag{4.7}$$

where we moved all the terms to the right hand side and $r_{p_{\ell v}}$, $r_{p_{rv}}$,$r_{p_{\ell a}}$, $r_{p_{ra}}$ and $\mathbf{r_d}$ are suitable functions; $h = h_2$ is understood. We solve the non-linear saddle-point problem (4.7) by means of the Newton algorithm:

- We initialize, for $j = 0$, $\underline{\mathbf{d}}^{(0)}_h = \underline{\mathbf{d}}^n_h$, $p^{(0)}_{\ell v} = p^n_{\ell v}$, $p^{(0)}_{rv} = p^n_{rv}$, $p^{(0)}_{\ell a} = p^n_{\ell a}$ and $p^{(0)}_{ra} = p^n_{ra}$;
- For $j = 1, 2, \dots$, we solve the linear system

  $$\begin{pmatrix}
  J^{(j-1)}_{\mathbf{d},\mathbf{d}} & J^{(j-1)}_{\mathbf{d},p_{\ell v}} & J^{(j-1)}_{\mathbf{d},p_{rv}} & J^{(j-1)}_{\mathbf{d},p_{\ell a}} & J^{(j-1)}_{\mathbf{d},p_{ra}}\\
  J^{(j-1)}_{p_{\ell v},\mathbf{d}} & 0 & 0 & 0 & 0\\
  J^{(j-1)}_{p_{rv},\mathbf{d}} & 0 & 0 & 0 & 0\\
  J^{(j-1)}_{p_{\ell a},\mathbf{d}} & 0 & 0 & 0 & 0\\
  J^{(j-1)}_{p_{ra},\mathbf{d}} & 0 & 0 & 0 & 0
  \end{pmatrix}
  \begin{pmatrix}
  \Delta\underline{\mathbf{d}}^{(j)}_h\\
  \Delta p^{(j)}_{\ell v}\\
  \Delta p^{(j)}_{rv}\\
  \Delta p^{(j)}_{\ell a}\\
  \Delta p^{(j)}_{ra}
  \end{pmatrix}
  =
  \begin{pmatrix}
  \mathbf{r}^{(j-1)}_{\mathbf{d}}\\
  r^{(j-1)}_{p_{\ell v}}\\
  r^{(j-1)}_{p_{rv}}\\
  r^{(j-1)}_{p_{\ell a}}\\
  r^{(j-1)}_{p_{ra}}
  \end{pmatrix}, \tag{4.8}$$

  where

  $$\begin{aligned}
  J^{(j-1)}_{\mathbf{d},\mathbf{d}} &= \tfrac{\partial}{\partial \underline{\mathbf{d}}} \mathbf{r_d}(\underline{\mathbf{d}}^{(j-1)}_h, p^{(j-1)}_{\ell v}, p^{(j-1)}_{rv}, p^{(j-1)}_{\ell a}, p^{(j-1)}_{ra}),\\
  J^{(j-1)}_{\mathbf{d},p_i} &= \tfrac{\partial}{\partial p_i} \mathbf{r_d}(\underline{\mathbf{d}}^{(j-1)}_h, p^{(j-1)}_{\ell v}, p^{(j-1)}_{rv}, p^{(j-1)}_{\ell a}, p^{(j-1)}_{ra}), \quad i = \ell v, rv, \ell a, ra,\\
  J^{(j-1)}_{p_i,\mathbf{d}} &= \tfrac{\partial}{\partial \underline{\mathbf{d}}} r_{p_i}(\underline{\mathbf{d}}^{(j-1)}_h), \qquad\qquad i = \ell v, rv, \ell a, ra;
  \end{aligned}$$

- We update $\underline{\mathbf{d}}_h^{(j)} = \underline{\mathbf{d}}_h^{(j-1)} - \Delta\underline{\mathbf{d}}_h^{(j)}$, $p_{\ell v}^{(j)} = p_{\ell v}^{(j-1)} - \Delta p_{\ell v}^{(j)}$, $p_{rv}^{(j)} = p_{rv}^{(j-1)} - \Delta p_{rv}^{(j)}$, $p_{\ell a}^{(j)} = p_{\ell a}^{(j-1)} - \Delta p_{\ell a}^{(j)}$ and $p_{ra}^{(j)} = p_{ra}^{(j-1)} - \Delta p_{ra}^{(j)}$;
- When the convergence criterion (based on the increment) is satisfied, we set $\underline{\mathbf{d}}_h^{n+1} = \underline{\mathbf{d}}_h^{(j)}$, $p_{\ell v}^{n+1} = p_{\ell v}^{(j)}$, $p_{rv}^{n+1} = p_{rv}^{(j)}$, $p_{\ell a}^{n+1} = p_{\ell a}^{(j)}$ and $p_{ra}^{n+1} = p_{ra}^{(j)}$.

We solve the saddle-point problem (4.8) via Schur complement reduction [28]. Specifically, the linear System (4.8) can be compactly written as

$$\begin{pmatrix} J_{\mathbf{d},\mathbf{d}} & \boldsymbol{J}_{\mathbf{d},\boldsymbol{p}} \\ \boldsymbol{J}_{\boldsymbol{p},\mathbf{d}} & \mathbf{0} \end{pmatrix} \begin{pmatrix} \Delta\underline{\mathbf{d}}_h \\ \Delta\boldsymbol{p} \end{pmatrix} = \begin{pmatrix} \mathbf{r}_{\mathbf{d}} \\ \boldsymbol{r}_{\boldsymbol{p}} \end{pmatrix}, \tag{4.9}$$

where for simplicity we omitted the superscript (j) and we introduced the following vectors

$$\boldsymbol{J}_{\mathbf{d},\boldsymbol{p}} = \begin{pmatrix} J_{\mathbf{d},p_{\ell v}} & J_{\mathbf{d},p_{rv}} & J_{\mathbf{d},p_{\ell a}} & J_{\mathbf{d},p_{ra}} \end{pmatrix}, \quad \boldsymbol{J}_{\boldsymbol{p},\mathbf{d}} = \begin{pmatrix} J_{p_{\ell v},\mathbf{d}} & J_{p_{rv},\mathbf{d}} & J_{p_{\ell a},\mathbf{d}} & J_{p_{ra},\mathbf{d}} \end{pmatrix}^T,$$

$$\Delta\boldsymbol{p} = \begin{pmatrix} \Delta p_{\ell v} & \Delta p_{rv} & \Delta p_{\ell a} & \Delta p_{ra} \end{pmatrix}^T, \quad \boldsymbol{r}_{\boldsymbol{p}} = \begin{pmatrix} r_{p_{\ell v}} & r_{p_{rv}} & r_{p_{\ell a}} & r_{p_{ra}} \end{pmatrix}^T.$$

System (4.9) reads:

$$\begin{cases} J_{\mathbf{d},\mathbf{d}}\Delta\underline{\mathbf{d}}_h + \boldsymbol{J}_{\mathbf{d},\boldsymbol{p}} \cdot \Delta\boldsymbol{p} = \mathbf{r}_{\mathbf{d}} \\ \boldsymbol{J}_{\boldsymbol{p},\mathbf{d}}\Delta\underline{\mathbf{d}}_h = \boldsymbol{r}_{\boldsymbol{p}} \end{cases}. \tag{4.10}$$

Deriving $\Delta\underline{\mathbf{d}}_h$ form the first equation of (4.10) we have

$$\begin{cases} \Delta\underline{\mathbf{d}}_h = J_{\mathbf{d},\mathbf{d}}^{-1}\mathbf{r}_{\mathbf{d}} - J_{\mathbf{d},\mathbf{d}}^{-1}\boldsymbol{J}_{\mathbf{d},\boldsymbol{p}} \cdot \Delta\boldsymbol{p} \\ \boldsymbol{J}_{\boldsymbol{p},\mathbf{d}}J_{\mathbf{d},\mathbf{d}}^{-1}\mathbf{r}_{\mathbf{d}} - \boldsymbol{J}_{\boldsymbol{p},\mathbf{d}}J_{\mathbf{d},\mathbf{d}}^{-1}\boldsymbol{J}_{\mathbf{d},\boldsymbol{p}} \cdot \Delta\boldsymbol{p} = \boldsymbol{r}_{\boldsymbol{p}} \end{cases}. \tag{4.11}$$

Introducing

$$\mathbf{v} = J_{\mathbf{d},\mathbf{d}}^{-1}\mathbf{r}_{\mathbf{d}}, \qquad \mathbf{w} = J_{\mathbf{d},\mathbf{d}}^{-1}\boldsymbol{J}_{\mathbf{d},\boldsymbol{p}}, \tag{4.12}$$

Equation (4.11) can be written as

$$\begin{cases} \Delta\underline{\mathbf{d}}_h = \mathbf{v} - \mathbf{w} \cdot \Delta\boldsymbol{p} \\ \boldsymbol{J}_{\boldsymbol{p},\mathbf{d}}\mathbf{w} \cdot \Delta\boldsymbol{p} = \boldsymbol{J}_{\boldsymbol{p},\mathbf{d}}\mathbf{v} - \boldsymbol{r}_{\boldsymbol{p}} \end{cases}, \tag{4.13}$$

Solving (4.13), we obtain the solution of the saddle-point problem (4.8) in the form of

$$\begin{gathered} \Delta\underline{\mathbf{d}}_h = \mathbf{v} - \mathbf{w}_{\ell v}\Delta p_{\ell v} - \mathbf{w}_{rv}\Delta p_{rv} - \mathbf{w}_{\ell a}\Delta p_{\ell a} - \mathbf{w}_{ra}\Delta p_{ra}, \\ \begin{pmatrix} J_{p_{\ell v},\mathbf{d}}\mathbf{w}_{\ell v} & J_{p_{\ell v},\mathbf{d}}\mathbf{w}_{rv} & J_{p_{\ell v},\mathbf{d}}\mathbf{w}_{\ell a} & J_{p_{\ell v},\mathbf{d}}\mathbf{w}_{ra} \\ J_{p_{rv},\mathbf{d}}\mathbf{w}_{\ell v} & J_{p_{rv},\mathbf{d}}\mathbf{w}_{rv} & J_{p_{rv},\mathbf{d}}\mathbf{w}_{\ell a} & J_{p_{rv},\mathbf{d}}\mathbf{w}_{ra} \\ J_{p_{\ell a},\mathbf{d}}\mathbf{w}_{\ell v} & J_{p_{\ell a},\mathbf{d}}\mathbf{w}_{rv} & J_{p_{\ell a},\mathbf{d}}\mathbf{w}_{\ell a} & J_{p_{\ell a},\mathbf{d}}\mathbf{w}_{ra} \\ J_{p_{ra},\mathbf{d}}\mathbf{w}_{\ell v} & J_{p_{ra},\mathbf{d}}\mathbf{w}_{rv} & J_{p_{ra},\mathbf{d}}\mathbf{w}_{\ell a} & J_{p_{ra},\mathbf{d}}\mathbf{w}_{ra} \end{pmatrix} \begin{pmatrix} \Delta p_{\ell v} \\ \Delta p_{rv} \\ \Delta p_{\ell a} \\ \Delta p_{ra} \end{pmatrix} = \begin{pmatrix} J_{p_{\ell v},\mathbf{d}}\mathbf{v} - r_{p_{\ell v}} \\ J_{p_{rv},\mathbf{d}}\mathbf{v} - r_{p_{rv}} \\ J_{p_{\ell a},\mathbf{d}}\mathbf{v} - r_{p_{\ell a}} \\ J_{p_{ra},\mathbf{d}}\mathbf{v} - r_{p_{ra}} \end{pmatrix}. \end{gathered} \tag{4.14}$$

Notice that we have to the solve five linear systems (4.12), which are

$$J_{\mathbf{d},\mathbf{d}}\mathbf{v} = \mathbf{r}_{\mathbf{d}}, \; J_{\mathbf{d},\mathbf{d}}\mathbf{w}_{\ell v} = J_{\mathbf{d},p_{\ell v}}, \; J_{\mathbf{d},\mathbf{d}}\mathbf{w}_{rv} = J_{\mathbf{d},p_{rv}}, \; J_{\mathbf{d},\mathbf{d}}\mathbf{w}_{\ell a} = J_{\mathbf{d},p_{\ell a}}, \; J_{\mathbf{d},\mathbf{d}}\mathbf{w}_{ra} = J_{\mathbf{d},p_{ra}},$$

in order to obtain the solution for $\Delta\underline{\mathbf{d}}_h$, $\Delta p_{\ell v}$, Δp_{rv}, $\Delta p_{\ell a}$ and Δp_{ra} of Equation (4.14).

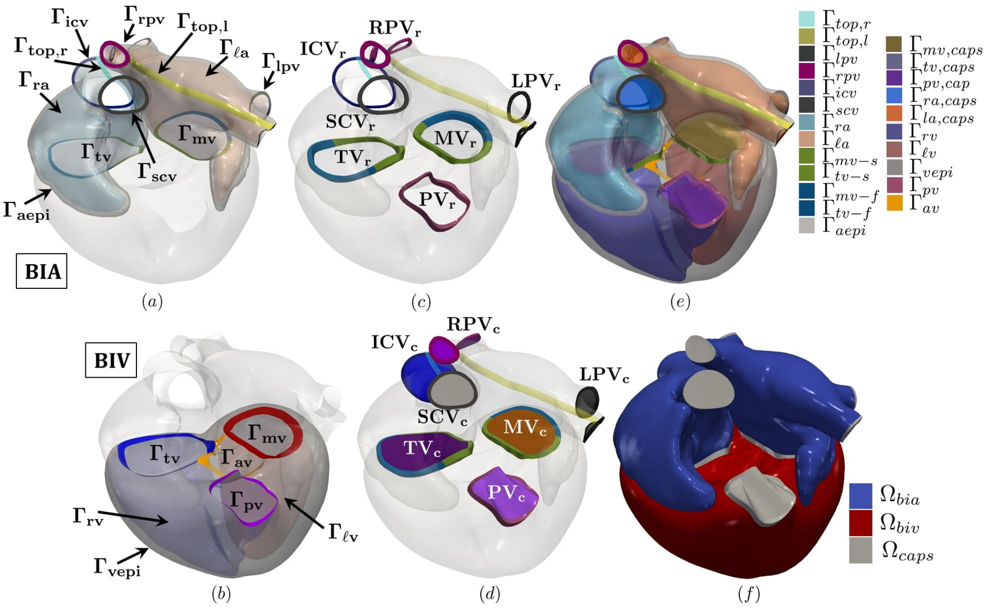

Figure 4.6: Procedure for the generation of the Zygote whole heart mesh. Left (a-b): Generating accurate boundary tags for biatrial and biventricular geometries; Centre (c-d): Connecting different heart chambers by means of closed annular rings and cap planes; Right (e-f): Labelled whole heart volumetric mesh.

4.3 Numerical results: whole heart simulations

In this section, we present numerical results related to both the fiber generation and EP/EM simulations, employing the full heart LDRBM and the 3D-0D whole heart model, discussed in Sections 4.1 and 4.2, respectively. These have been performed on the realistic 3D Zygote heart, a CAD-model representing an average healthy human heart reconstructed from high-resolution CT-scan [107]. As it is a very detailed geometry of the human heart, it demonstrates the applicability of the proposed models to arbitrary patient-specific scenarios.

We organize this section as follows. We begin illustrating a procedure for the generation of a whole heart mesh, starting from an acquired cardiac geometry (Section 4.3.1). Then, in Section 4.3.2, we present the whole heart fiber generation applied to the Zygote heart. Finally, we show numerical results of EP and EM simulations, using the 3D-0D whole heart model, with physiological activation sites and including the myofibers generated by the full heart LDRBM, in the realistic computational domain of the Zygote heart (Sections 4.3.3 and 4.3.4).

4.3.1 Whole heart mesh generation

The generation of a computational whole heart mesh is of crucial importance in order to properly simulate the cardiac function. Practically, the starting point is a set of unprocessed polygonal surfaces coming either from segmented images, acquired from medical imaging techniques such as MRI or CT-scan, or from template CAD models. These surfaces need ad-hoc processing to move from surfaces to a volumetric whole heart labelled mesh, in order to suitable impose specific electrical or mechanical tissue

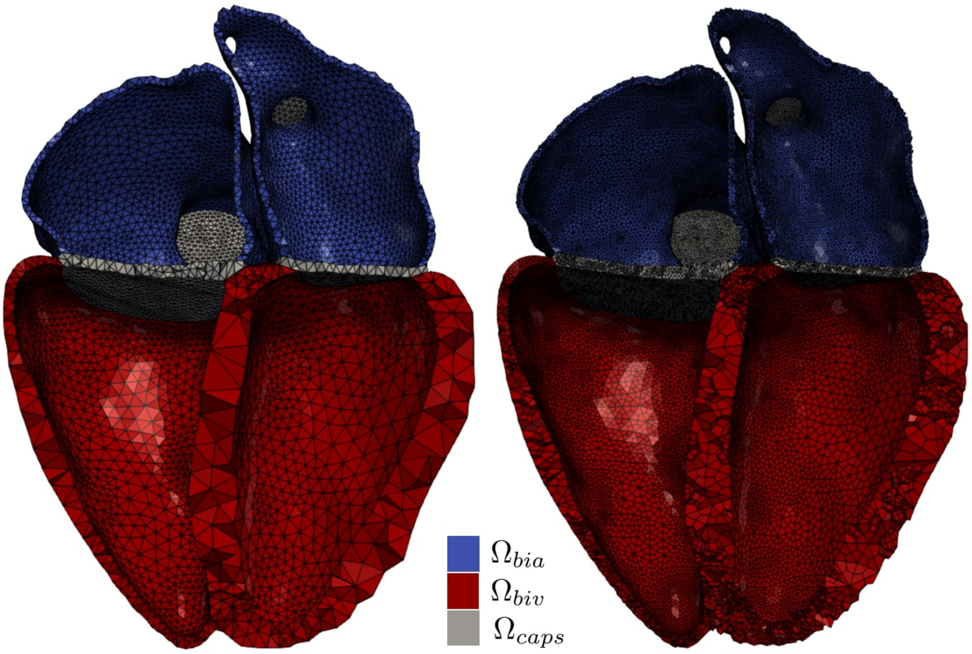

(a) (b)

Figure 4.7: Whole heart Zygote labelled FE meshes. (a): FE mesh of tetrahedral elements; (b): FE mesh of hexahedral elements, exploiting the *tet-hex* algorithm [66].

properties and boundary conditions.

To build the whole heart Zygote mesh, we rely on the Vascular Modelling Toolkit `vmtk` software [11] (`http://www.vmtk.org`), together with the new semi-automatic meshing tools proposed in [66]. In particular, our cardiac mesh generation consists of multiple steps, which includes:

1. Generating accurate boundary tags;
2. Connecting different heart chambers;
3. Connecting together several volumetric meshes.

1. Generating accurate boundary tags: we start the Zygote whole heart mesh generation by using the biatrial and biventricular triangular labelled surfaces, created from the labelling procedures detailed in Section 2.4.1 (see also Figure 2.11). Figures 4.6(a-b) show the biatrial (BIA) and the biventricular (BIV) labelled surface triangular meshes, respectively composed by:

BIA : atrial epicardium (including the top LA and RA bands), LA and RA endocardia, MV and TV rings (both subdivided in one part facing the atrial septum and another one related to the free wall), LPV and RPV rings, SCV and ICV rings, see Figure 4.6(a);

BIV : ventricular epicardium, LV and RV endocardia, MV and TV rings, AV and PV rings, see Figure 4.6(b).

2. Connecting different heart chambers: to physically join together the atria to the ventricles, we first extract from both BIA and BIV the MV and TV rings, and then we connect MV and TV rings of the atria to the corresponding ones of the ventricles, by means of the *surface-connector* algorithm (see [66] for further details about this procedure). In this way, we obtain a closed surface for both MV and TV annulus, see Figure 4.6(c). Finally, we create closed TV and MV caps by capping the internal upper and lower rings of MV and TV annuli, see Figure 4.6(d).

To provide closed surfaces for cut-veins of the caval veins in RA, the pulmonary veins in LA and the outflow track in RV, we first extrude each ring (of SCV, ICV, LPV, RPV and PV) along its mean outward normal. Then, we connect the extruded rings to the corresponding original ones, by means of the *surface-connector* algorithm [66], see Figure 4.6(c). Finally, as done for the atrioventricular valve planes, we create closed caps for each cut-vein by capping the inner and the outer rings, see Figure 4.6(d).

The above procedures ensure the construction of a set of conforming triangular closed tagged surfaces of the whole heart, composed by atria, ventricles and the planes for the valves and for the cut veins, see Figure 4.6(e).

3. Connecting together several volumetric meshes: the final step of the Zygote whole heart mesh generation consists in creating tetrahedral volumes separately for the atria, the ventricles, the valves and the cut vein planes, obtaining in this way a set of conforming tetrahedral volumes, which are finally appended together to build the whole heart tagged volumetric mesh, see Figure 2.11(d). The whole heart tetrahedral mesh is then converted to an hexahedral one, obtained by subdividing each tetrahedron into four hexahedra, exploiting the *tet-hex* algorithm [66], see Figure 4.7.

4.3.2 Whole heart myocardial fibers generation

For the fibers generation in the whole heart Zygote mesh, we adopt the full heart LDRBM, presented in Section 4.1.

The input angles values for the ventricles $\alpha_{endo,\ell}$, $\alpha_{epi,\ell}$, $\alpha_{endo,r}$, $\alpha_{epi,r}$, $\beta_{endo,\ell}$, $\beta_{epi,\ell}$, $\beta_{endo,r}$ and $\beta_{epi,r}$ were chosen based on the observations of histological studies in the human heart [134, 86, 9, 99, 210, 136, 229]:

$$\begin{aligned} &\alpha_{epi,\ell} = -60^o, \quad \alpha_{endo,\ell} = +60^o, \quad \alpha_{epi,r} = -25^o, \quad \alpha_{endo,r} = +90^o; \\ &\beta_{epi,\ell} = +20^o, \quad \beta_{endo,\ell} = -20^o, \quad \beta_{epi,r} = +20^o, \quad \beta_{endo,r} = 0^o. \end{aligned} \tag{4.15}$$

Furthermore, we specified also the angles in the outflow track (OT) regions of PV and AV, as follows [58]:

$$\alpha_{epi,OT} = 0^o, \quad \alpha_{endo,OT} = +90^o, \quad \beta_{epi,OT} = 0^o, \quad \beta_{endo,OT} = 0^o. \tag{4.16}$$

Finally, we set the position of LV apex $\Gamma_{a\ell v}$ equal to that of RV apex $\Gamma_{a\ell v}$, selected as the LV epicardial point furthest from MV caps $\Gamma_{mv,caps}$, see step 1 in Section 4.1.

Regarding the atria, the input values of the parameters τ_i, which define the dimensions of biatrial bundles, are reported in Tables 4.2 and 4.3 for RA and LA, respectively. In addition, we fix $N_{raa} = N_{raw} = 0$, implying that we do not prescribe any PM in RA endocardium. Finally, although possible in the heart LDRBM, no IC bundles are prescribed. Hence, LA and RA fibers are computed using the function $\mathbf{compute_{LA}}$ and $\mathbf{compute_{RA}}$, for positive and negative values of ξ, respectively (see Algorithms 1, 2, 4 of Section 2.2 and Algorithm 5 of Section 4.1).

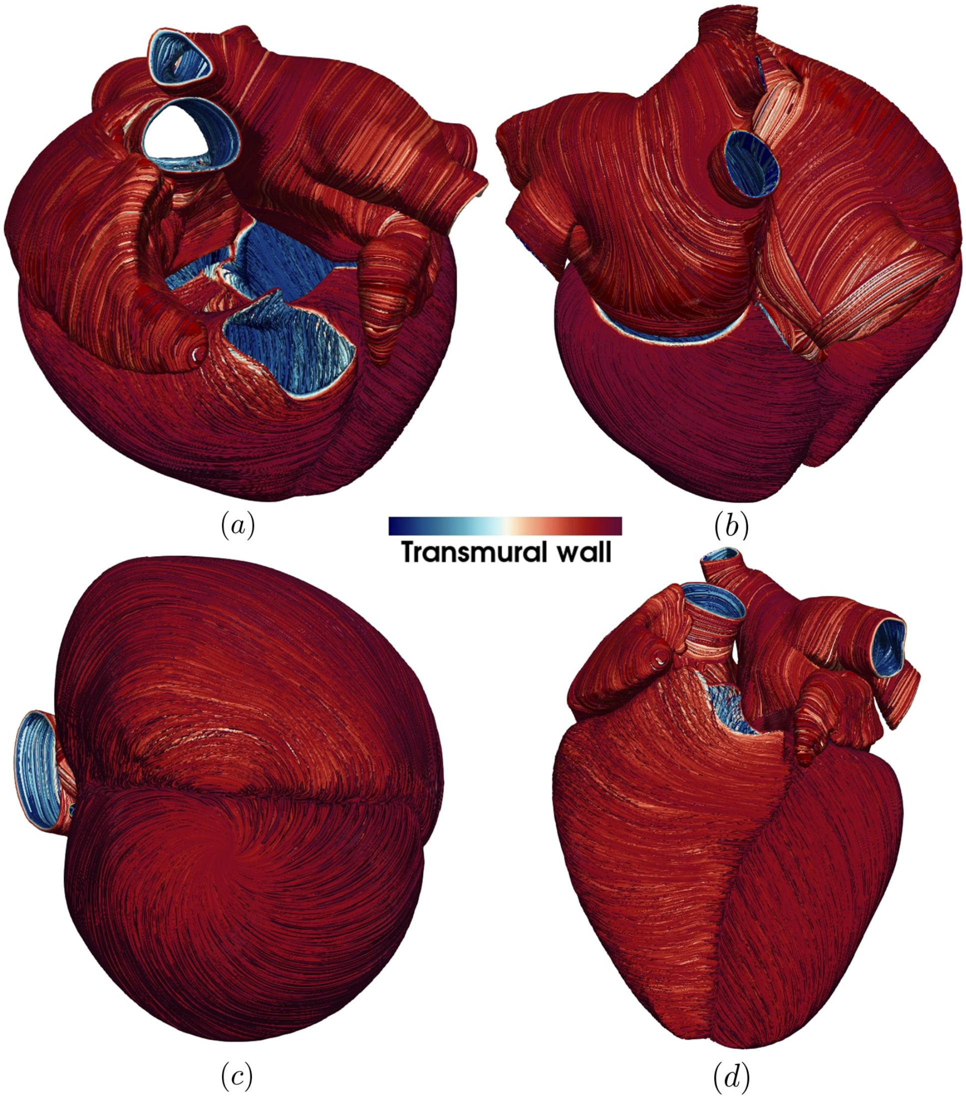

Figure 4.8: Fiber generation, employing the full heart LDRBM, applied to the realistic Zygote Heart model. (a): Anterior view; (b): Posterior view; (c): Apex view; (d): Frontal view. For visualization purpose we removed the valve and cut vein planes.

Figure 4.8 displays the Zygote heart geometry equipped with the prescribed LDRBM fibers. We observe that the full heart LDRBM well reproduce the characteristic helical structure of the ventricles up to MV and TV regions, presenting circular fiber arrangements around PV-OT and AV-OT, see Figure 4.8(a,c,d). Moreover, circumferential and longitudinal fiber orientations are predominant in RV with respect to LV, with a strong discontinuity in the transition across the two ventricles around the inter-ventricular junctions, see Figure 4.8(c,d).

The complex arrangement of fiber directions in almost every anatomical atrial regions are well captured by the full heart LDRBM. In particular, following the atrial LDRBM rules, reported in Section 2.2.1, circular fiber arrangements are exhibited

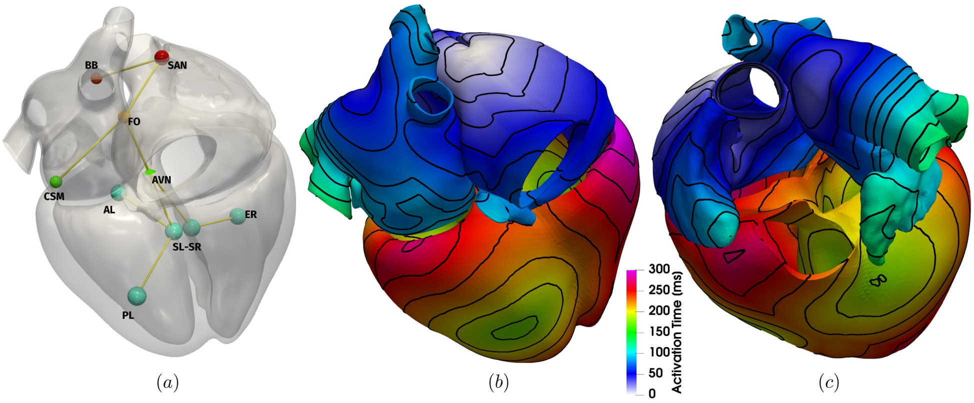

(a) (b) (c)

Figure 4.9: (a): Stimuli applied in the four chamber model to mimic the Cardiac Conduction System (CCS); SAN: Sino-Atrial Node; BB: Bachmann's Bundle; FO: Fossa Ovalis; CSM: Coronary Sinus Musculature; AVN: Atrio-Ventricular Node; AL: Left Anterior; PL: Left Posterior; SL, SR: Left and Right Septum; ER: Right Endocardium. (b-c): Activation maps computed from EP simulation; posterior (b) and frontal (c) views.

RA	τ_{tv}	τ_{icv}	τ_{scv}	τ_{raa}	τ_{csm}	$\tau_{sw,r}$
Zygote heart	0.90	0.90	0.215	0.55	0.00	-0.15
RA	τ_{raw}	τ_{ct_-}	τ_{ct_+}	τ_{ib}	τ_{ras}	
Zygote heart	0.75 (0^o-30^o)	-0.22	-0.22	0.44 (20^o-20^o)	0.28	

Table 4.2: Bundle parameters used for RA fibers generation in the Zygote heart geometry. We use the convention $\tau_i(\alpha_{endo}$-$\alpha_{epi})$ to set a linear transmural angle variation for α inside the i-th bundle, while τ_i alone to imply $\alpha_{endo} = \alpha_{epi} = 0^o$.

LA	τ_{mv}	τ_{rpv}	τ_{lpv}	$\tau_{sw,l}$	$\tau_{laa,in}$	$\tau_{laa,up}$	τ_{bb}	τ_{law}
Zygote heart	0.90	0.15	0.835	0.04	0.43	0.60	0.75	0.65 (20^o-0^o)

Table 4.3: Bundle parameters used for LA fibers generation in the Zygote heart geometry. We use the convention $\tau_i(\alpha_{endo}$-$\alpha_{epi})$ to set a linear transmural angle variation for α inside the i-th bundle, while τ_i alone to imply $\alpha_{endo} = \alpha_{epi} = 0^o$.

around LPV, RPV, SCV, ICV, TV, MV and both appendages (RAA and LAA), see Figure 4.8(a,b). RA fiber structures like IB and RAW are vertically oriented, whereas those of RAS are almost parallel to TV, Figure 4.8(b). LAS fibers present a smooth transition going to LAA and the adjacent region of RAS. Directions of LAR and LAW fibers descend perpendicularly to MV, see Figure 4.8(a).

4.3.3 Whole heart electrophysiology

We employ the whole heart LDRBM fiber architecture to perform an EP simulation of the Zygote heart. To model the EP activity in the cardiac tissue we used the monodomain equation endowed with TTP06 and CRN98 ionic models for the ventricles and for the atria, respectively (see Sections 2.3 and 4.2.1), with the settings described in Section 2.4.2. The interactions among atria and ventricles are based on the following assumptions on the cardiac conductions system (CCS), showed in Figure 4.9(a).

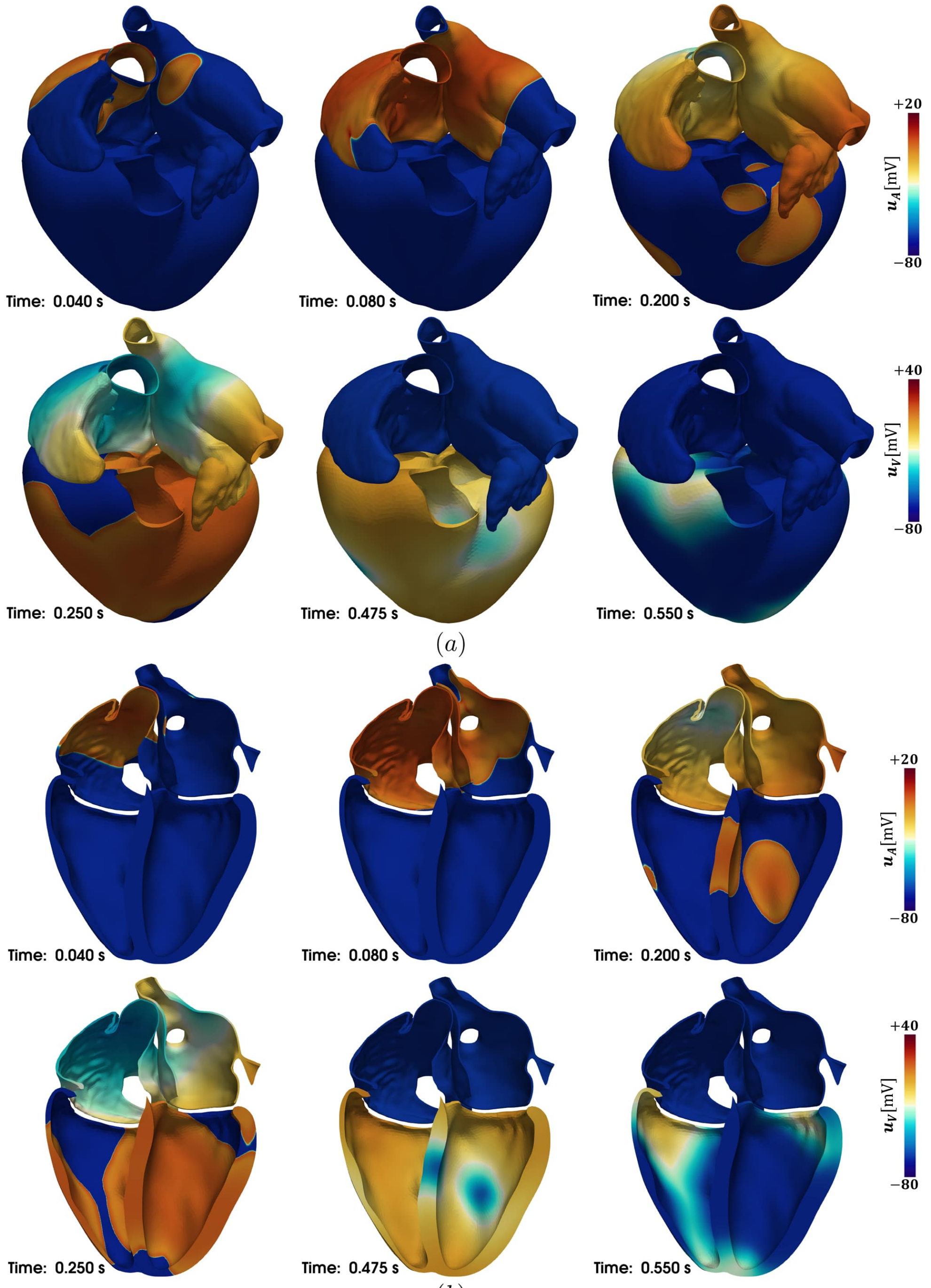

(a)

(b)

Figure 4.10: Evolution of the transmembrane potential for the ventricles u_V and for the atria u_A in the Zygote EP simulation, during a cardiac cycle. (a) full heart frontal view; (b) clipped internal view. For visualization purpose we removed the valve and cut vein planes.

The ventricles are electrically isolated from the atria by the atrioventricular grooves [8]; the atria are electrically separated by the insulating nature of the atrial septum (dividing RA from LA) apart from muscular continuity at the rim of Fossa Ovalis [100]. The CCS pathway is modelled as a series of spherical delayed stimuli along the heart geometry that mimic the electrical atrial connections, the Atrio-Ventricular Node (AVN) delay and the main area of ventricular electrical activation: specifically, when the transmembrane potential front reaches these points a stimulus current is triggered, see Figure 4.9(a). Notice that, although the Purkinje network system should be used to account for a detailed ventricular activation (see e.g. [252, 166]), for the sake of simplicity several spherical endocardial stimuli were applied to each ventricle [59].

The CCS electric signal originates at the Sino-Atrial Node (SAN, $t = 0$ ms) and travels from RA to LA through three electrical atrial connections, the Bachmann's Bundle (BB, $t = 28$ ms), the rim of Fossa Ovalis (FO, $t = 42$ ms) and the Coronary Sinus Musculature (CSM, $t = 80$ ms) [100, 208]. When the electric signal reaches the AVN, located at the lower back section of the inter-atrial septum near the coronary sinus opening, it is subject to a delay (90 ms), that allows the complete activation of the atria before ventricles electric propagation starts [100]. Finally, ventricular endocardial areas are activated: in the anterior para-septal wall (AL), in the left surface of inter-ventricular septum (SL) and in the bottom of postero-basal area (PL), for LV; in the septum (SR) and in the free endocardial wall (ER), for RV, 5 ms after the onset of LV stimuli [59]; see Figure 4.9(a).

Figure 4.9(b-c) depicts the activation maps computed by the Zygote heart EP simulation. We obtained a physiologically compatible timing for the heart activation [188, 72, 187]: the complete atrial depolarization occurs after about 120 ms, while that of ventricles after about $t = 270$ ms. The last region to be activated is LAA for the atria, while the postero-basal area of RV for the ventricles, both in accordance with [208, 59].

The transmembrane potentials evolution for the ventricles u_V and for the atria u_A are shown in Figures 4.10. As expected, the electric signal initiates at SAN and spreads from RA to LA. Then, after the delay of AVN, the ventricles start to activate. The atrial repolarization arises during ventricular depolarization. Finally, after the isoelectric ventricular activity, the whole heart return to the depolarized initial configuration, see Figure 4.10.

4.3.4 Whole heart electromechanics

We present an human heart EM simulation in physiological conditions in the Zygote heart, employing the 3D-0D whole heart model, presented in Section 4.2. For the fiber generation of the cardiac muscular architecture we adopted the heart LDRBM described in Section 4.1.

Regarding the space discretization of the 3D-0D whole heart model, we used continuous bilinear FE ($\mathbb{Q}_1$) and we employed two nested meshes, where for TM and MA problems we adopted an average mesh size of 1.5 mm, while for EP problem a mesh size two time smaller. Meanwhile, for the time discretization, we used BDF1 with $\tau = 50\,\mu$s for EP problem and with $\Delta t = 20\,\tau$ for TM, MA and fluid problems [199, 176].

The parameters of the 3D-0D heart model are listed in Tables 4.4 and 4.5, see also Section 4.2. Specifically, Table 4.4 contains the parameters of the 3D EM model and Table 4.5 those of the 0D closed-loop hemodynamical model. Moreover, for the

Variable	Value	Unit	Description
Electrophysiology			
T_{HB}	0.8	s	Heartbeat duration
χ_m	1	μF/cm^2	Surface-to-volume ratio
C_m	1400	cm^{-1}	Transmembrane capacitance
ϵ	0.05	–	Threshold of the fast conduction layer
$(\sigma_{\ell,\text{fast}}, \sigma_{\text{t,fast}}, \sigma_{\text{n,fast}})$	(5.00, 2.50, 0.75)	mS/cm	Fast ventricular layer conductivities
$(\sigma_{\ell,\text{myo}}, \sigma_{\text{t,myo}}, \sigma_{\text{n,myo}})$	(1.00, 0.50, 0.15)	mS/cm	ventricular conductivities
$(\sigma_{\ell}^{(a)}, \sigma_{\text{t}}^{(a)}, \sigma_{\text{n}}^{(a)})$	(7.00, 0.70, 0.70)	mS/cm	atrial conductivities
$\mathcal{I}^{max}$	$50 \cdot 10^3$	μA/cm^3	Applied current value
t_{app}	3.0	ms	Applied current duration
δ_{app}	2.5	mm	Applied current radius
Mechanics			
ρ_s	10^3	$\text{kg}\,\text{m}^{-3}$	Tissue density
$K_{\parallel}^{epi}$	$2 \cdot 10^4$	$\text{Pa}\,\text{m}^{-1}$	Normal stiffness of epicardium
$K_{\perp}^{epi}$	$2 \cdot 10^5$	$\text{Pa}\,\text{m}^{-1}$	Tangential stiffness of epicardial tissue
$C_{\perp}^{epi}$	$2 \cdot 10^4$	$\text{Pa}\,\text{s}\,\text{m}^{-1}$	Normal viscosity of epicardial tissue
$C_{\parallel}^{epi}$	$2 \cdot 10^3$	$\text{Pa}\,\text{s}\,\text{m}^{-1}$	Tangential viscosity of epicardial tissue
$K_{\parallel}^{pv}$	$2 \cdot 10^4$	$\text{Pa}\,\text{m}^{-1}$	Normal stiffness of pulmonary caps
$K_{\perp}^{pv}$	$2 \cdot 10^5$	$\text{Pa}\,\text{m}^{-1}$	Tangential stiffness of pulmonary caps
$C_{\perp}^{pv}$	$2 \cdot 10^4$	$\text{Pa}\,\text{s}\,\text{m}^{-1}$	Normal viscosity of pulmonary caps
$C_{\parallel}^{pv}$	$2 \cdot 10^3$	$\text{Pa}\,\text{s}\,\text{m}^{-1}$	Tangential viscosity of pulmonary caps
Guccione law:			
a	$0.88 \cdot 10^3$	Pa	Material stiffness
$\kappa^{(\text{G})}$	$50 \cdot 10^3$	Pa	Bulk modulus
b_{ff}	8	–	Fiber strain scaling
b_{ss}	6	–	Radial strain scaling
b_{nn}	3	–	Cross-fiber in-plane strain scaling
b_{fs}	12	–	Shear strain in fiber-sheet plane scaling
b_{fn}	3	–	Shear strain in fiber-normal plane scaling
b_{sn}	3	–	Shear strain in sheet-normal plane scaling
Neo-Hookean law:			
μ	10^5	Pa	Shear modulus
$\kappa^{(\text{N})}$	$5 \cdot 10^5$	Pa	Bulk modulus
Reference Configuration			
$\widehat{p}_{\ell v}$	650	Pa	Residual left ventricular pressure
$\widehat{p}_{rv}$	450	Pa	Residual right ventricular pressure
$\widehat{p}_{\ell a}$	800	Pa	Residual left atrial pressure
$\widehat{p}_{ra}$	600	Pa	Residual right atrial pressure
$\widehat{T}_a$	$350 \cdot 10^3$	Pa	Residual ventricular active tension
$\widehat{T}_a^{(a)}$	$350 \cdot 10^3$	Pa	Residual atrial active tension
$C_{\ell rv}$	1	–	Residual ventricular contractility ratio
$C_{\ell ra}$	1	–	Residual atrial contractility ratio
Activation			
SL_0	2	µm	Reference sarcomere length
T_a^{max}	$800 \cdot 10^3$	Pa	Ventricular maximum tension
$T_a^{max,(a)}$	$400 \cdot 10^3$	Pa	Atrial maximum tension
$C_{\ell rv}$	1	–	Ventricular contractility ratio
$C_{\ell ra}$	1	–	Atrial contractility ratio

Table 4.4: Input parameters of the 3D EM heart model.

Variable	Value	Unit	Description
Circulation			
R_{ar}^{sys}	0.640	$\mathrm{mmHg\,s\,mL^{-1}}$	Resistance of systemic arterial system
R_{ven}^{sys}	0.260	$\mathrm{mmHg\,s\,mL^{-1}}$	Resistance of systemic venous system
R_{ar}^{pul}	0.032	$\mathrm{mmHg\,s\,mL^{-1}}$	Resistance of pulmonary arterial system
R_{ven}^{pul}	0.036	$\mathrm{mmHg\,s\,mL^{-1}}$	Resistance of pulmonary venous system
C_{ar}^{sys}	1.200	$\mathrm{mL\,mmHg^{-1}}$	Capacitance of systemic arterial system
C_{ven}^{sys}	60.00	$\mathrm{mL\,mmHg^{-1}}$	Capacitance of systemic venous system
C_{ar}^{pul}	10.00	$\mathrm{mL\,mmHg^{-1}}$	Capacitance pulmonary arterial system
C_{ven}^{pul}	16.00	$\mathrm{mL\,mmHg^{-1}}$	Capacitance of pulmonary venous system
L_{ar}^{sys}	$5 \cdot 10^{-3}$	$\mathrm{mmHg\,s^2\,mL^{-1}}$	Impedance of systemic arterial system
L_{ven}^{sys}	$5 \cdot 10^{-4}$	$\mathrm{mmHg\,s^2\,mL^{-1}}$	Impedance of systemic venous system
L_{ar}^{pul}	$5 \cdot 10^{-4}$	$\mathrm{mmHg\,s^2\,mL^{-1}}$	Impedance pulmonary arterial system
L_{ven}^{pul}	$5 \cdot 10^{-4}$	$\mathrm{mmHg\,s^2\,mL^{-1}}$	Impedance of pulmonary venous system
R_{min}	$75 \cdot 10^{-4}$	$\mathrm{mmHg\,s\,mL^{-1}}$	Valves minimal resistance
R_{max}	$75 \cdot 10^{3}$	$\mathrm{mmHg\,s\,mL^{-1}}$	Valves maximum resistance

Table 4.5: Parameters of the 0D closed-loop model in the 3D-0D heart model.

Physics/Fields	Linear solver (preconditioner)	Abs. tol.
Fiber Laplace problems	GMRES(AMG)	10^{-10}
Monodomain model	CG (AMG)	10^{-8}
Activation	GMRES (AMG)	10^{-10}
Mechanics	GMRES (AMG)	10^{-8}
Reference configuration	GMRES (AMG)	10^{-6}

Table 4.6: Tolerances of the linear solver for the different 3D-0D heart core models.

Physics/Fields	non-linear solver	Rel. tol.	Abs. tol.
Mechanics	Newton	10^{-8}	10^{-6}
Reference configuration	Newton	10^{-6}	10^{-4}

Table 4.7: Tolerances of the non-linear solver for the 3D-0D heart mechanical problem.

TTP06 and CRN98 ionic models, we use the parameters[2] reported in [247] and [47], respectively, while for the RDQ18-ANN model, we employed those in [196]. Tables 4.6 and 4.7 report the setting used for the linear and non-linear solvers, respectively. The setting related to the heart LDRBM, adopted for prescribing the fiber architectures, is detailed in Section 4.3.2. Moreover, to surrogate the effect of ventricular dispersed myofibers, we fixed in (4.4) $n_f = 1$, $n_s = 0$ and $n_n = 0.4$ for the proportion of active tension along the fiber, sheet and normal directions, respectively [87, 3, 177].

To approach the limit cycle, we performed five heartbeats using the fully framework of the 3D-0D model presented in Section 4.2. All the reported results refer to the last heartbeat. Moreover, we initialized both the ionic models (TTP06 and CRN98) by running a 1000-cycle long single-cell 0D simulation. Similarly, we initialized the force generation model by means of a single-cell 0D simulation with a constant calcium inputs (corresponding to the final calcium concentrations of the single-cell ionic simulations of TTP06 and CRN98) and a reference sarcomere length $SL = 2.2\,\mu\mathrm{m}$.

---

[2] For the TTP06 ionic model we used the endocardium cells parameters [247].

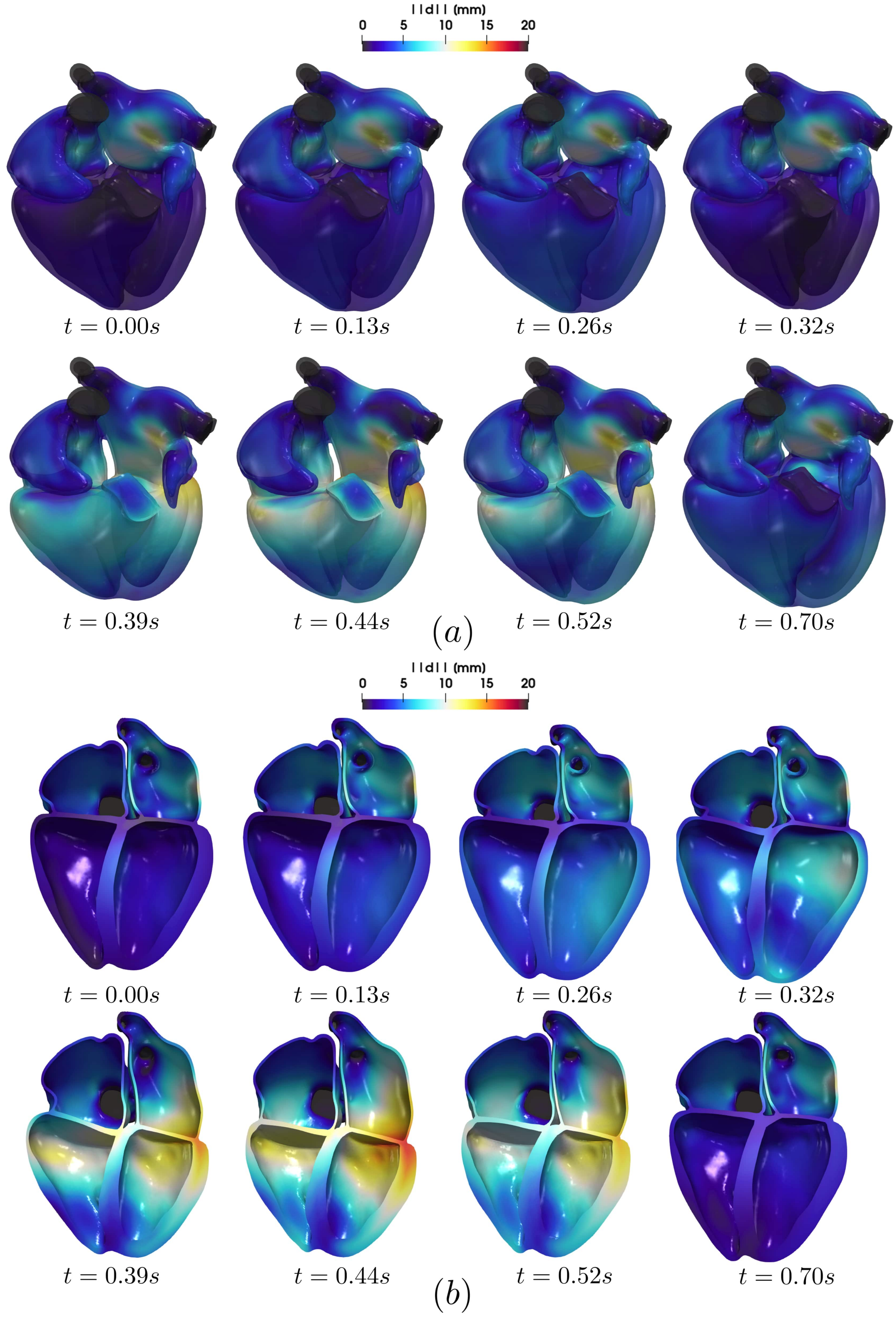

Figure 4.11: Evolution of the mechanical displacement magnitude (with respect to the reference configuration) in the Zygote heart EM simulation during a cardiac cycle. (a) full heart frontal view; (b) clipped internal view.

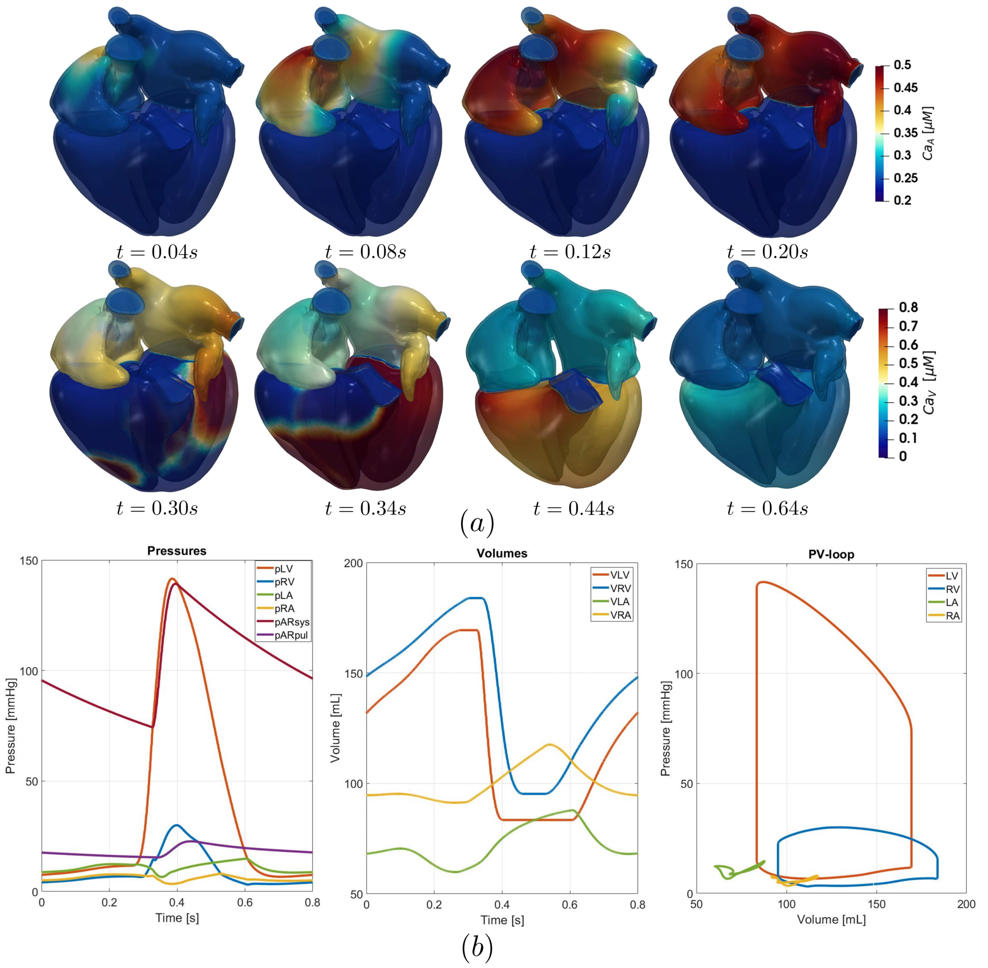

Figure 4.12: (a) Evolution of the calcium transient for the ventricles Ca_V (of TTP06) and for the atria Ca_A (of CRN98) in the Zygote heart EM simulation during a cardiac cycle; (b) pressures (left), volumes (centre) and PV-loop (right) for LV (orange), RV (blue), LA (green) and RA (yellow). Moreover, also the pressures p_{ar}^{sys} (red) and p_{ar}^{pul} (violet) are plotted.

The pacing protocol, composed by atrial and ventricular endocardial spherical stimuli, is the same as the whole heart EP simulation showed in Section 4.3.3. Moreover, in the ventricles we combined the impulses with the fast endocardial conduction layer (see Section 3.1.2) in order to surrogates the action of the Purkinje network [127, 252].

Figure 4.11 illustrates the time evolution of the mechanical displacement magnitude, in the Zygote heart EM simulation, during a cardiac cycle. Specifically, we report different snapshots of the atrial (in the first line) and of the ventricular (in the second line) contraction of the heart geometry, warped by the displacement vector (taken with respect to the reference configuration). At the beginning, we observe a passive filling phase (from the atria to the ventricles) with a slow increase of ventricular volumes ($t = 0.0 \div 0.13\,\mathrm{s}$). Then, the atrial systole, also named “atrial kick”,

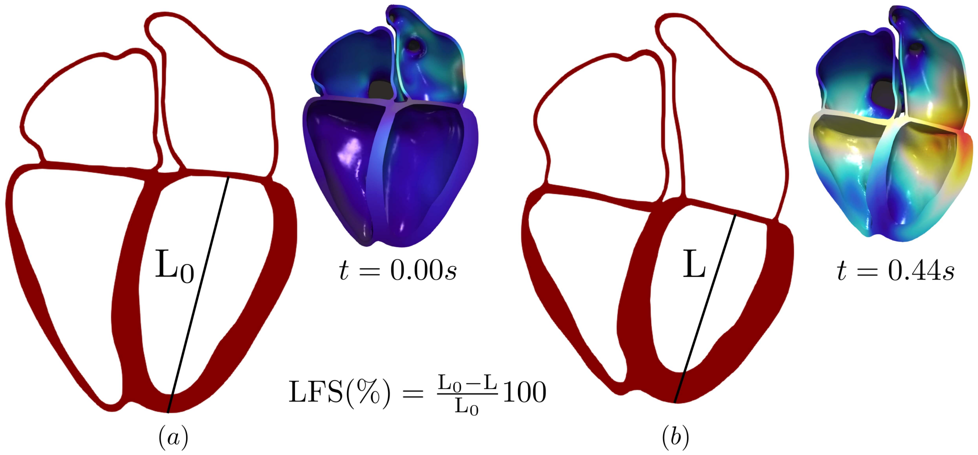

Figure 4.13: Schematic representation of the measured Longitudinal Fractional Shortening (LFS) in the Zygote heart EM simulation: (a) mid heart slice at the beginning of the heartbeat ($t = 0.00$ s), showing the apico-basal distance L_0; (b) mid heart slice at the end of systole ($t = 0.44$ s), showing the apico-basal distance L.

occurs, with the consequent decrease of atrial volumes and increase of the ventricular ones ($t = 0.26 \div 0.32\,\text{s}$). During the ventricular contraction, the ejection phase is clearly visible, with the atrioventricular plane that moves towards the bottom of the heart, while the apex remains almost fixed. Moreover, a significant thickening of the ventricular wall takes place ($t = 0.39 \div 0.44\,\text{s}$). Then, the ventricles start to relax. This leads to a slow recovery of the heart initial volumes ($t = 0.52 \div 0.60\,\text{s}$).

Figure 4.12(a) shows the physiological wave propagation of calcium ions concentrations (coming from TTP06 and CRN98) Ca_V and Ca_A, during a cardiac cycle, for the ventricles and the atria, respectively. Following the electrical activity of the heart, the release of calcium originates at the SAN, ($t = 0.04\,\text{s}$) and travels from RA to LA ($t = 0.08 \div 0.12\text{s}$) up to the complete activation of atria ($t = 0.20\,\text{s}$). The AVN delay ($\sim 0.09\,\text{s}$) ensures that the atria contract before ventricular endocardial areas are activated ($t = 0.30\,\text{s}$). The calcium wave spreads from LV to RV ($t = 0.30 \div 0.34\,\text{s}$) up to the complete activation of both ventricles ($t = 0.44\,\text{s}$). Finally, after the ventricular contraction, the calcium concentration goes back to its resting value ($t = 0.64\,\text{s}$).

Figure 4.12(b) displays the PV-loop curves and the time evolution of pressures and volumes of the four chambers. During the atrial contraction the volume of both ventricles increases while the pressure remains almost constant ($t = 0.00 \div 0.30\,\text{s}$). At this stage, MV and TV are opened, while AV and PV are closed. Then, the ventricular systole starts: at the beginning the volume of the ventricles is almost constant while the pressure increases. This produces the ventricular contraction and the closing of MV and TV. The ventricular pressures raise until they overcame the aorta and pulmonary artery pressures (p_{ar}^{sys} and p_{ar}^{pul}), triggering AV and PV to open with a rapid volume decrease in both ventricles, due to the blood ejection ($t = 0.30 \div 0.60\,\text{s}$). Finally, the ventricles relax, AV and PV close and when the ventricular pressures reach those of the atria, MV and TV open again and a slow filling phase (from the atria to the ventricles) begins ($t = 0.60 \div 0.80\,\text{s}$).

In Table 4.8 we compare some relevant mechanical biomarkers obtained by our numerical simulation with those provided by the data reported in the literature [122,

Mechanical biomarkers	Literature values	Simulation results	Description
$\mathrm{EF}_{\mathrm{LV}}$ (%)	50-75 [122]	51	Left ventricular ejection fraction
$\mathrm{EF}_{\mathrm{RV}}$ (%)	48 ± 5 [147]	48	Right ventricular ejection fraction
P_{LV} (mmHg)	119 ± 13 [236]	140	Left ventricle pressure peak
P_{RV} (mmHg)	35 ± 11 [31]	30	Right ventricle pressure peak
P_{LA} (mmHg)	12-14 [178]	14	Left atrium pressure peak
P_{RA} (mmHg)	1-8 [52]	8	Right atrium pressure peak
LFS (%)	13-21 [61]	21	Longitudinal fractional shortening

Table 4.8: Comparison between the simulation results, employing the 3D-0D whole heart model, and literature values of mechanical biomarkers in physiological conditions (references are reported in the Table).

147, 236, 31, 178, 52, 61]. The chosen mechanical biomarkers were: i) left and right ventricular ejection fractions ($\mathrm{EF}_{\mathrm{LV}}$, $\mathrm{EF}_{\mathrm{RV}}$), which represent the amount of blood that is pumped by LV and RV during a cardiac cycle, computed as

$$\mathrm{EF}_i(\%) = \frac{\mathrm{EDV}_i - \mathrm{ESV}_i}{\mathrm{EDV}_i} 100 \qquad i = \mathrm{LV,RV},$$

where EDV_i and ESV_i (with $i = \mathrm{LV}, \mathrm{RV}$) represent the maximal and minimal (left $i = \mathrm{LV}$ and right $i = \mathrm{RV}$) ventricular volumes achieved during the heartbeat, computed as the maximal and minimal volumes in the PV-loop curves, see Figure 4.12(b); ii) left and right atrial and ventricular systolic pressure peaks (P_{LV}, P_{RV}, P_{LA}, P_{RA}), the maximal pressures reached in LV, RV, LA and RA, computed as the maximal pressures in the PV-loop curves, see Figure 4.12(b); iii) the systolic longitudinal fractional shortening (LFS), standing for the fractional displacement between the apex and the atrioventricular plane [130], evaluated as

$$\mathrm{LFS}(\%) = \frac{\mathrm{L}_0 - \mathrm{L}}{\mathrm{L}_0} 100,$$

where L_0 and L are the apico-basal distance measured at the beginning ($t = 0.0\,\mathrm{s}$) and at the end of systole ($t = 0.44\,\mathrm{s}$), see Figure 4.13.

Apart from the left ventricular systolic pressure peak (P_{LV}), with a slightly higher value, all the other mechanical biomarkers, obtained by our numerical simulation, fall within the physiological range (references in Table 3.5).

Conclusions

This thesis presented a fully-coupled multiscale mathematical and numerical model of the electrical and mechanical activity of the whole human heart, wherein the main contribution is given by the generation of the full heart myofibers, described by means of a newly developed Rule-Based Method (RBM).

The whole heart fiber architecture is built upon a new Laplace-Dirichlet Rule-Based Method (LDRBM), a particular class of RBM strictly related to the solution of Laplace boundary-value problems [176]. The latter is based on the novel definition of several inter-heart and intra-heart harmonic functions, which couple together the different LDRBMs for the atria and the ventricles [176, 58]. To properly reproduce the characteristic features of the cardiac fiber bundles in all the four chambers, the heart LDRBM uses the gradient of inter-heart and intra-heart harmonic functions combined with a precise definition of the boundary sections, where boundary conditions are prescribed for the harmonic problems (see Section 4.1). This strategy makes the fibers less open to subjective variability. On the other hand, the heart fiber bundles dimension could be adapted case by case changing the parameters involved in the RBM. The proposed methodology was demonstrated to quantitatively replicate the complex arrangement of the fiber directions in almost every anatomical atrial and ventricular regions: the helical structure of LV, the characteristic fibers of RV, the outflow tracks (OT) regions and the fiber bundles of LA and RA, including the inter-atrial connections (see Section 4.3.2). The heart LDRBM is computationally inexpensive, efficient and easy to implement, and it allows to include realistic cardiac muscle fibers architecture on whole heart geometries of arbitrary shape. As a consequence, it is possible to generate patient specific heart fibers, fed by input parameters inferred from histology or DT-MRI studies, through an automated and computationally efficient procedure.

Apart from a very detailed myocardial fiber architecture, the whole heart model of this thesis considers a 3D description of cardiac electromechanics (EM) in all the four chambers and a 0D representation of the circulatory system, which includes the cardiac blood haemodynamics (see Section 4.2). The 3D EM part comprises:

i) the cardiac electrophysiology (EP), described by means of the monodomain equation endowed with state of the art human ionic models for the ventricle (TTP06 [247]) and the atria (CRN98 [47]), which are able to accurately describe ions dynamics across the cell membrane in physiological conditions;

ii) the sarcomere mechanical activation (MA), based on an Artificial Neural Network (ANN) model, known as the RDQ18-ANN model (recently proposed in [196]), which is able to represent in detail the sophisticated microscopic active force generation mechanisms, taking place at the scale of sarcomeres, with the great advantage of strikingly reducing the computational burden associated to the numerical solution of the RDQ18 full order model [195];

iii) the myocardial tissue mechanics (TM), for both the atria and the ventricles, represented adopting, for the passive behaviour, the Guccione constitutive law [90] and, for the active part, an orthotropic active stress formulation [89], which surrogates the contraction caused by dispersed myofibers [87].

The whole heart EM model, comprising EP-MA-TM, is strongly coupled with a 0D closed-loop lamped parameters model (recently proposed in [198]) for the blood haemodynamics through the entire cardiovascular network, where systemic and pulmonary circulations (both arterial and venous) are modeled with RLC circuits. The heart chambers are described by time-varying elastance elements and non-ideal diodes stand for the heart valves (see Section 3.1.5). The coupling between the 0D-fluid and 3D-EM models is achieved by means of the volume-consistency coupling conditions, where the pressures of all the four chambers act as Lagrange multipliers associated to the volume constraints (see Sections 3.1.6 and 4.2.1). The above coupling approach, between the 3D EM and the 0D circulation models, ensures both the continuity of volumes and pressures and is complaint with the principles of conservation of mechanical energy [198, 199].

The numerical approximation of the 3D-0D heart model included: finite Element Method (FEM) with continuous FE and hexahedral meshes, for the space discretization, and Finite difference (FD) schemes with Backward Difference Formulae of order $\sigma \geq 1$ (BDFσ), for the time discretization. The Segregated-Intergrid-Staggered (SIS) numerical scheme was adopted. The core models, contributing to both cardiac EM and blood circulation, are solved sequentially once per time step in a segregated manner, by using different resolutions in space and time, to properly handle the different space-time scales of the core models (see Sections 4.2.3 and 3.2).

The validity of the whole heart 3D-0D model was demonstrated through EM and EP simulations (see Sections 4.3.3 and 4.3.4), with physiological activation sites in a four chamber realistic computational domain of the Zygote heart, a CAD-model representing an average healthy human heart reconstructed from high-resolution CT-scan [107]. As it is a very detailed geometry of the human heart, it demonstrates the applicability of the proposed whole-heart model to arbitrary patient-specific scenarios. EP simulation of the whole heart produced a physiologically compatible timing for the cardiac activation [188, 187, 72] in accordance with previous reports [59, 208]; see Section 4.3.3. In EM simulation of the whole heart, some relevant mechanical biomarkers, obtained by our simulation, are compared with those provided by the data reported in the literature [122, 147, 236, 31, 178, 52, 61]. Almost all the mechanical biomarkers fall within the physiological range; see Section 4.3.4.

The proposed 3D-0D whole heart model, presented in this thesis, provides an important contribution to the whole heart modeling and to perform full heart EM simulations, allowing both the study of four chambers heart clinical cases as well as investigating medical questions.

Besides the above mentioned achievements of the 3D-0D whole heart model, this thesis obtained the following results:

- it provided a novel unified framework, based on LDRBMs, for generating cardiac muscle fibers in biventricular and biatrial computational domain (see Chapter 2);

- it reviewed existing ventricular LDRBMs, proposed by Rossi et al. [204] (R-RBM), by Bayer et al. [26] (B-RBM) and by Doste et al. [58] (D-RBM), by means of a communal mathematical description. Some extensions were also introduced allowing the inclusion of different fiber orientations in LV and RV for R-RBM and B-RBM, the rotation of all the myofiber vectors for R-RBM, and the fibers generation up to cardiac valve rings for B-RBM (see Section 2.1);

- it proposed a novel LDRBM for the generation of atrial myofibers, which is able to reproduce all the important features, such as the fiber bundles, needed to provide a realistic atrial musculature architecture. The newly developed method has been proposed in [176], and in this thesis has been presented the extension to the biatrial geometries. The novel methodology makes the fibers less open to subjective variability. On the other hand, the bundles dimension could be adapted case by case changing the parameters involved in the method. Therefore, unlike most of the existing atrial RBM requiring manual or semi-automatic interventions, the new method can be easily adapted to any arbitrary geometry (see Section 2.2);

- it carried out systematic comparisons of ventricular LDRBMs, performed on either idealized and realistic human biventricular geometries. R-RBM and B-RBM were able to recover almost the same fiber orientations of D-RBM thanks to the proposed extensions. However, some local differences persist in the methods utilized (see Section 2.5). Furthermore, the influence of the different ventricular fibers architecture on EP signal propagation in terms of activation times, computed as output of numerical simulations, was investigated, highlighting the importance of including a proper fiber orientation for RV (see Section 2.5);

- it presented the fiber generation results of the new atrial LDRBM to reconstruct LA, RA and biatrial myofiber architectures, both in idealized and realistic geometries. The new LDRBM quantitatively captures the complex arrangement of fiber directions in almost all the anatomical atrial regions, including the inter-atrial connections (see Sections 2.6 and 2.7). This was demonstrated through comparisons with another RBM, with anatomical atrial dissections and with DT-MRI fiber data.

- it analysed the influence of atrial fiber bundles by means of EP simulations in realistic and real geometries (coming from DT-MRI data). Specifically, the comparison between the fiber activation map and an isotropic electrical propagation or a change in size of a single bundle strongly affect the total activation sequence in the atria. These results putted in evidence the strong effect of the atrial bundles in the electric signal propagation and the importance of including a detailed fiber architecture in EP atrial models (see Sections 2.6 and 2.7);

- it presented a 3D biventricular EM model coupled with a 0D closed-loop model of the whole cardiovascular system, providing a rigorous mathematical and numerical formulation of the 3D-0D model, and detailing the approach to couple the 3D and the 0D models (see Chapter 3). The biventricular 3D-0D model was the building block for the 3D-0D whole heart model (see Chapter 4);

- it introduced a boundary condition for the mechanical problem that accounts for the neglected part of the domain located on top of the biventricular basal plane and that is consistent with the principles of momentum and energy conservation. In particular, the energy-consistent boundary condition (proposed for LV in [196]) was extended to the weighted-stress distribution form, applicable to biventricular geometries (see Section 3.1.4);

- it carried out several numerical biventricular EM simulations aimed at reproducing physiological quantities like the PV-loops. The results quantitatively matched the experimental data of all the relevant mechanical biomarkers available in literature [137, 238, 138, 236, 31, 61, 219], such as the end systolic and diastolic volumes, the ejection fractions, the systolic pressure peaks, the longitudinal fractional shortening and the fractional wall thickening (see Section 3.3.2);

- it studied different configurations in cross-fibers active contraction, which surrogate the dispersion effect in the cardiac fibers. These results proved that an active tension along the sheet-normal direction enhances the cardiac work, whereas along the sheet direction it has the opposite effect. Moreover, an active contraction in the sheet-normal direction allows to obtain a more efficient cardiac pumping function with a much lower axial stress with respect to a pure fiber configuration. Conversely, a sheet active contraction yields unphysiological ejection fraction, longitudinal shortening and wall thickening. These results putted in evidence that the proportion of active tension along the sheet direction should be avoided in the framework of an orthotropic active stress (see Section 3.3.3);

- it evaluated the impact of different myofibers architecture on the biventricular EM, showing the importance of considering a biventricular model with respect to a standalone LV model. A different fibers architecture in the transmural wall and in the inter-ventricular septum influence the ventricular cardiac pump work, in particular the LV one. This highlighted the strong interaction on the cardiac pump function between LV and RV, and consequently the importance of considering the two chambers together during ventricular EM simulations. The continuous interrelationships between right and left ventricular functions are well known not only in physiological conditions, but particularly in pathological situations, for which any pressure and/or volume overload of a ventricle is instantaneously reflected in impairment of the function of the contralateral ventricle (see Section 3.3.4);

- it provided a detailed description of the process behind the generation of whole heart mesh, starting from an acquired cardiac geometry. The following procedure was applied to generate labelled volumetric mesh of a realistic whole heart geometry, employed for EP and EM simulations (see Section 4.3.1).

Future directions and improvements

Several possible improvements and prospectives arise from th work carried out in this thesis:

- further investigations should be performed to establish which ventricular LDRBM better reproduces the anatomical ground truth. In particular, concerning the septal fibers, standard anatomical observations claim that the fibers are almost continuous through the septum [99, 210], though recent studies support the thesis of septal fibers discontinuity [115, 34];

- the validation of the atrial LDRBM, presented in Section 2.7.3, based on the comparison between the LDRBM fibers and the DT-MRI fiber data, should be extended to more than one biatrial geometries, in order to verify the adaptability of the proposed methodology to inter-patient variations;

- the EP at cellular and tissue levels was modelled as homogeneous through the whole heart. Although in principle this assumption is a well accepted approximation for the ventricular tissues of healthy individuals, several atrial regions exhibit distinct EP properties. These should be taken into consideration to achieve a more realistic activation/repolarization pattern [67, 129], particularly when reproducing pathological conditions affecting the atrial chambers [57];

- the Purkinje network was not explicitly modelled (as for instance done in [252, 46, 126]). Instead, to surrogates the effect of the Purkinje network (as done in [127]), a series of spherical impulses, taken along LV and RV endocardia where an electrical stimulus is applied, was combined with the fast endocardial conduction layer. Although this approximation is reasonable in physiological condition, the Purkinje network should be explicitly modelled in order to achieve a more realistic activation sequence in the ventricles, in particular when attempting to reproduce pathological conditions, like for instance the Left Bundle Branch Block [156, 252];

- the RDQ18 activation model does not take into account the feedback of the shortening velocity along the muscle fibers on the subcellular force generation mechanism. This effect (known as the force-velocity relationship) entails that when the tissue rapidly contracts, the force generated decreases, thus making the pressure transient smoother. Hence, the sharp pressure peaks shown in Figures 3.11(d) and 4.12(b) would be smoothed by using a model that takes into account the force-velocity relationship, such as the RDQ20 model, as shown in [194]. The integration of a the recently developed RDQ20 force generation model [195] into the multiscale 3D-0D cardiac model will be the subject of a future work.

- the proposed whole heart fibers generation methodology is computationally inexpensive, efficient and easy to implement, and it allows to include realistic cardiac muscle fibers architecture on whole heart geometries of arbitrary shape. As a consequence, it is possible to generate patient cohorts heart fibers. Recently, a publicly available virtual cohort of about twenty linear tetrahedral four chamber meshes was reported in [234]. However, these heart meshes embed only the ventricular fibers. The application of the heart LDRBM will easily extend this cohort to include full heart muscular architecture;

- the whole heart EM simulation, presented in Section 4.3.4, needs further calibrations in order to better reproduce realistic atrial PV-loops.

Bibliography

[1] P.C. Africa. "Scalable adaptive simulation of organic thin-film transistors". PhD thesis. Politecnico di Milano, 2019.

[2] P.C. Africa, R. Piersanti, M. Fedele, L. Dede', and A. Quarteroni. "life^x - heart module: a high-performance simulator for the cardiac function. Package 1: Fiber generation". In: *arXiv preprint arXiv:2201.03303* (2022).

[3] F. Ahmad, S. Soe, N. White, R. Johnston, I. Khan, J. Liao, M. Jones, R. Prabhu, I. Maconochie, and P. Theobald. "Region-specific microstructure in the neonatal ventricles of a porcine model". In: *Annals of Biomedical Engineering* 46.12 (2018), pp. 2162–2176.

[4] A. Ahmad Bakir, A. Al Abed, M.C. Stevens, N.H. Lovell, and S. Dokos. "A Multiphysics Biventricular Cardiac Model: Simulations With a Left-Ventricular Assist Device". In: *Frontiers in Physiology* 9 (2018), p. 1259.

[5] A.L. Alexander, K.M. Hasan, M. Lazar, J.S. Tsuruda, and D.L. Parker. "Analysis of partial volume effects in diffusion-tensor MRI". In: *Magnetic Resonance in Medicine: An Official Journal of the International Society for Magnetic Resonance in Medicine* 45.5 (2001), pp. 770–780.

[6] R.R. Aliev and A.V. Panfilov. "A simple two-variable model of cardiac excitation". In: *Chaos, Solitons & Fractals* 7.3 (1996), pp. 293–301.

[7] D. Ambrosi, G. Arioli, F. Nobile, and A. Quarteroni. "Electromechanical coupling in cardiac dynamics: the active strain approach". In: *SIAM Journal on Applied Mathematics* 71.2 (2011), pp. 605–621.

[8] R.H. Anderson, S.Y. Ho, and A.E. Becker. "Anatomy of the human atrioventricular junctions revisited". In: *The Anatomical Record: An Official Publication of the American Association of Anatomists* 260.1 (2000), pp. 81–91.

[9] R.H. Anderson, M. Smerup, D. Sanchez-Quintana, M. Loukas, and P.P. Lunkenheimer. "The three-dimensional arrangement of the myocytes in the ventricular walls". In: *Clinical Anatomy: The Official Journal of the American Association of Clinical Anatomists and the British Association of Clinical Anatomists* 22.1 (2009), pp. 64–76.

[10] L. Antiga, M. Piccinelli, L. Botti, B. Ene-Iordache, A. Remuzzi, and D.A. Steinman. "An image-based modeling framework for patient-specific computational hemodynamics". In: *Medical & Biological Engineering & Computing* 46.11 (2008), pp. 1097–1112.

[11] L. Antiga and D.A. Steinman. “The vascular modeling toolkit”. In: *URL: http://www. vmtk. org* (2008).

[12] S.S. Antman. *Nonlinear Problems of Elasticity.* Springer, 1995.

[13] H.J. Arevalo, F. Vadakkumpadan, E. Guallar, A. Jebb, P. Malamas, K.C. Wu, and N.A. Trayanova. “Arrhythmia risk stratification of patients after myocardial infarction using personalized heart models”. In: *Nature Communications* 7 (2016), pp. 1–8.

[14] D. Arndt, W. Bangerth, T.C. Clevenger, D. Davydov, M. Fehling, D. Garcia-Sanchez, G. Harper, T. Heister, L. Heltai, M. Kronbichler, R.M. Kynch, M. Maier, J.-P. Pelteret, B. Turcksin, and D. Wells. “The `deal.II` Library, Version 9.1”. In: *Journal of Numerical Mathematics* (2019).

[15] T. Arts, T. Delhaas, P. Bovendeerd, X. Verbeek, and F.W. Prinzen. “Adaptation to mechanical load determines shape and properties of heart and circulation: the CircAdapt model”. In: *American Journal of Physiology-Heart and Circulatory Physiology* 288 (2005), H1943–H1954.

[16] O.V. Aslanidi, T. Nikolaidou, J. Zhao, B.H. Smaill, S. Gilbert, A.V. Holden, T. Lowe, P.J. Withers, R.S. Stephenson, J.C. Jarvis, et al. “Application of micro-computed tomography with iodine staining to cardiac imaging, segmentation, and computational model development”. In: *IEEE Transactions on Medical Imaging* 32 (2012), pp. 8–17.

[17] C.M. Augustin, T.E. Fastl, A. Neic, C. Bellini, J. Whitaker, R. Rajani, M.D. O’Neill, M.J. Bishop, G. Plank, and S.A. Niederer. “The impact of wall thickness and curvature on wall stress in patient-specific electromechanical models of the left atrium”. In: *Biomechanics and Modeling in Mechanobiology* (2019), pp. 1–20.

[18] C.M. Augustin, T.E. Fastl, A. Neic, C. Bellini, J. Whitaker, R. Rajani, M.D. O’Neill, M.J. Bishop, G. Plank, and S.A. Niederer. “The impact of wall thickness and curvature on wall stress in patient-specific electromechanical models of the left atrium”. In: *Biomechanics and Modeling in Mechanobiology* 19.3 (2020), pp. 1015–1034.

[19] C.M. Augustin, M.A.F. Gsell, E. Karabelas, and G. Plank. “Physiologically valid 3D-0D closed loop model of the heart and circulation–Modeling the acute response to altered loading and contractility”. In: *arXiv preprint arXiv:2009.08802* (2020).

[20] C.M. Augustin, A. Neic, M. Liebmann, A.J. Prassl, S.A. Niederer, G. Haase, and G. Plank. “Anatomically accurate high resolution modeling of human whole heart electromechanics: a strongly scalable algebraic multigrid solver method for nonlinear deformation”. In: *Journal of Computational Physics* 305 (2016), pp. 622–646.

[21] L. Azzolin, L. Dedè, A. Gerbi, and A. Quarteroni. “Effect of fibre orientation and bulk modulus on the electromechanical modelling of human ventricles”. In: *Mathematics in Engineering* 2.4 (2020), pp. 614–638.

[22] B. Baillargeon, N. Rebelo, D.D. Fox, R.L. Taylor, and E. Kuhl. “The living heart project: a robust and integrative simulator for human heart function”. In: *European Journal of Mechanics-A/Solids* 48 (2014), pp. 38–47.

[23] L. Barbarotta, S. Rossi, L. Dedè, and A. Quarteroni. "A transmurally heterogeneous orthotropic activation model for ventricular contraction and its numerical validation". In: *International Journal for Numerical Methods in Biomedical Engineering* 34.12 (2018), e3137.

[24] J. Bayer, A.J. Prassl, A. Pashaei, J.F. Gomez, A. Frontera, A. Neic, G. Plank, and E.J. Vigmond. "Universal ventricular coordinates: A generic framework for describing position within the heart and transferring data". In: *Medical Image Analysis* 45 (2018), pp. 83–93.

[25] J.D. Bayer, J. Beaumont, and A. Krol. "Laplace–Dirichlet energy field specification for deformable models. An FEM approach to active contour fitting". In: *Annals of Biomedical Engineering* 33.9 (2005), pp. 1175–1186.

[26] J.D. Bayer, R.C. Blake, G. Plank, and N. Trayanova. "A novel rule-based algorithm for assigning myocardial fiber orientation to computational heart models". In: *Annals of Biomedical Engineering* 40.10 (2012), pp. 2243–2254.

[27] R. Beinart, S. Abbara, A. Blum, M. Ferencik, K. Heist, J. Ruskin, and M. Mansour. "Left atrial wall thickness variability measured by CT scans in patients undergoing pulmonary vein isolation". In: *Journal of Cardiovascular Electrophysiology* 22.11 (2011), pp. 1232–1236.

[28] M. Benzi, G.H. Golub, J. Liesen, et al. "Numerical solution of saddle point problems". In: *Acta Numerica* 14 (2005), pp. 1–137.

[29] D. Bers. *Excitation-contraction coupling and cardiac contractile force.* Vol. 237. Springer Science & Business Media, 2001.

[30] R. Beyar and S. Sideman. "A computer study of the left ventricular performance based on fiber structure, sarcomere dynamics, and transmural electrical propagation velocity." In: *Circulation Research* 55.3 (1984), pp. 358–375.

[31] A. Bishop, P. White, P. Oldershaw, R. Chaturvedi, C. Brookes, and A. Redington. "Clinical application of the conductance catheter technique in the adult human right ventricle". In: *International Journal of Cardiology* 58.3 (1997), pp. 211–221.

[32] M. J. Bishop, G. Plank, R.A.B. Burton, J.E. Schneider, D.J. Gavaghan, V. Grau, and P. Kohl. "Development of an anatomically detailed MRI-derived rabbit ventricular model and assessment of its impact on simulations of electrophysiological function". In: *American Journal of Physiology-Heart and Circulatory Physiology* 298.2 (2009), H699–H718.

[33] P.J. Blanco, R.A. Feijóo, et al. "A 3D-1D-0D computational model for the entire cardiovascular system". In: *Computational Mechanics* 29 (2010), pp. 5887–5911.

[34] P. Boettler, P. Claus, L. Herbots, M. McLaughlin, J. D'hooge, B. Bijnens, S.Y. Ho, D. Kececioglu, and G.R. Sutherland. "New aspects of the ventricular septum and its function: an echocardiographic study". In: *Heart* 91.10 (2005), pp. 1343–1348.

[35] J. Bols, J. Degroote, B. Trachet, B. Verhegghe, P. Segers, and J. Vierendeels. "A computational method to assess the in vivo stresses and unloaded configuration of patient-specific blood vessels". In: *Journal of computational and Applied mathematics* 246 (2013), pp. 10–17.

[36] C. Brooks, H.H. Lu, and X. Lu. *The sinoatrial pacemaker of the heart.* Charles C. Thomas Publisher, 1972.

[37] M. Bucelli, M. Salvador, and A. Quarteroni. "Multipatch Isogeometric Analysis for electrophysiology: Simulation in a human heart". In: *Computer Methods in Applied Mechanics and Engineering* 376 (2021), p. 113666.

[38] M. Carlsson, M. Ugander, H. Mosén, T. Buhre, and H. Arheden. "Atrioventricular plane displacement is the major contributor to left ventricular pumping in healthy adults, athletes, and patients with dilated cardiomyopathy". In: *American Journal of Physiology-Heart and Circulatory Physiology* 292.3 (2007), H1452–H1459.

[39] F. Carreras, J. Garcia-Barnes, D. Gil, S. Pujadas, C.H. Li, R. Suarez-Arias, R. Leta, X. Alomar, M. Ballester, and G. Pons-Llado. "Left ventricular torsion and longitudinal shortening: two fundamental components of myocardial mechanics assessed by tagged cine-MRI in normal subjects". In: *The International Journal of Cardiovascular Imaging* 28.2 (2012), pp. 273–284.

[40] B. Carsten, C.W. Lucas, and G. Omar. "`p4est`: Scalable Algorithms for Parallel Adaptive Mesh Refinement on Forests of Octrees". In: *SIAM Journal on Scientific Computing* 33 (2011), pp. 1103–1133.

[41] R. Chabiniok, V.Y. Wang, M. Hadjicharalambous, L. Asner, J. Lee, M. Sermesant, E. Kuhl, A.A. Young, P. Moireau, M.P. Nash, et al. "Multiphysics and multiscale modelling, data–model fusion and integration of organ physiology in the clinic: ventricular cardiac mechanics". In: *Interface Focus* 6.2 (2016), p. 20150083.

[42] D. Chapelle, M.A. Fernández, J. Gerbeau, P. Moireau, J. Sainte-Marie, and N. Zemzemi. "Numerical simulation of the electromechanical activity of the heart". In: *International Conference on Functional Imaging and Modeling of the Heart.* Springer. 2009, pp. 357–365.

[43] P. Chinchapatnam, K.S. Rhode, M. Ginks, T. Mansi, J.M. Peyrat, P. Lambiase, C.A. Rinaldi, R. Razavi, S. Arridge, and M. Sermesant. "Estimation of volumetric myocardial apparent conductivity from endocardial electro-anatomical mapping". In: *2009 Annual International Conference of the IEEE Engineering in Medicine and Biology Society.* IEEE. 2009, pp. 2907–2910.

[44] A. Collin, J. Gerbeau, M. Hocini, M. Haïssaguerre, and D. Chapelle. "Surface-based electrophysiology modeling and assessment of physiological simulations in atria". In: *International Conference on Functional Imaging and Modeling of the Heart.* 2013, pp. 352–359.

[45] C.M. Costa, E. Hoetzl, B.M. Rocha, A.J. Prassl, and G. Plank. "Automatic parameterization strategy for cardiac electrophysiology simulations". In: *Computing in Cardiology.* 2013, pp. 373–376.

[46] F.S. Costabal, D.E. Hurtado, and E. Kuhl. "Generating Purkinje networks in the human heart". In: *Journal of Biomechanics* 49 (2016), pp. 2455–2465.

[47] M. Courtemanche, R.J. Ramirez, and S. Nattel. "Ionic mechanisms underlying human atrial action potential properties: insights from a mathematical model". In: *American Journal of Physiology-Heart and Circulatory Physiology* 275 (1998), H301–H321.

[48] E.J. Crampin, M. Halstead, P. Hunter, P. Nielsen, D. Noble, N. Smith, and M. Tawhai. “Computational physiology and the physiome project”. In: *Experimental Physiology* 89.1 (2004), pp. 1–26.

[49] A. Crozier, C.M. Augustin, A. Neic, A.J. Prassl, M. Holler, T.E. Fastl, A. Hennemuth, K. Bredies, T. Kuehne, M.J. Bishop, et al. “Image-based personalization of cardiac anatomy for coupled electromechanical modeling”. In: *Annals of Biomedical Engineering* 44.1 (2016), pp. 58–70.

[50] A. Crozier, B. Blazevic, P. Lamata, G. Plank, M. Ginks, S. Duckett, M. Sohal, A. Shetty, C.A. Rinaldi, R. Razavi, et al. “The relative role of patient physiology and device optimisation in cardiac resynchronisation therapy: a computational modelling study”. In: *Journal of molecular and cellular cardiology* 96 (2016), pp. 93–100.

[51] D. D. Sánchez-Quintana, G. Pizarro, J.R. López-Mínguez, S.Y. Ho, and J.A. Cabrera. “Standardized review of atrial anatomy for cardiac electrophysiologists”. In: *Journal of Cardiovascular Translational Research* 6 (2013), pp. 124–144.

[52] R. De Vecchis, C. Baldi, G. Giandomenico, M. Di Maio, A. Giasi, and C. Cioppa. “Estimating right atrial pressure using ultrasounds: an old issue revisited with new methods”. In: *Journal of clinical medicine research* 8.8 (2016), p. 569.

[53] L. Dedè, A. Gerbi, and A. Quarteroni. “Segregated algorithms for the numerical simulation of cardiac electromechanics in the left human ventricle”. In: *The Mathematics of Mechanobiology*. Springer, 2020, pp. 81–116.

[54] L. Dedè, F. Regazzoni, C. Vergara, P. Zunino, M. Guglielmo, R. Scrofani, L. Fusini, C. Cogliati, G. Pontone, and A. Quarteroni. “Modeling the cardiac response to hemodynamic changes associated with COVID-19: a computational study”. In: *Mathematical Biosciences and Engineering* 18.4 (2021), pp. 3364–3383.

[55] H. Dimitri, M. Ng, A.G. Brooks, P. Kuklik, M.K. Stiles, D.H. Lau, N. Antic, A. Thornton, D.A. Saint, D. McEvoy, et al. “Atrial remodeling in obstructive sleep apnea: implications for atrial fibrillation”. In: *Heart Rhythm* 9 (2012), pp. 321–327.

[56] S. Doll and K. Schweizerhof. “On the development of volumetric strain energy functions”. In: *Journal of Applied Mechanics* 67 (2000), pp. 17–21.

[57] O. Dössel, M.W. Krueger, F.M. Weber, M. Wilhelms, and G. Seemann. “Computational modeling of the human atrial anatomy and electrophysiology”. In: *Medical & Biological Engineering & Computing* 50 (2012), pp. 773–799.

[58] R. Doste, D. Soto-Iglesias, G. Bernardino, A. Alcaine, R. Sebastian, S. Giffard-Roisin, M. Sermesant, A. Berruezo, D. Sanchez-Quintana, and O. Camara. “A rule-based method to model myocardial fiber orientation in cardiac biventricular geometries with outflow tracts”. In: *International Journal for Numerical Methods in Biomedical Engineering* 35.4 (2019), e3185.

[59] D. Durrer, R.Th. Van Dam, G.E. Freud, M.J. Janse, F.L. Meijler, and R.C. Arzbaecher. “Total excitation of the isolated human heart”. In: *Circulation* 41.6 (1970), pp. 899–912.

[60] G. Elzinga and N. Westerhof. “Pressure and flow generated by the left ventricle against different impedances”. In: *Circulation Research* 32.2 (1973), pp. 178–186.

[61] K. Emilsson, R. Egerlid, B. Nygren, and B. Wandt. “Mitral annulus motion versus long-axis fractional shortening”. In: *Experimental & Clinical Cardiology* 11.4 (2006), p. 302.

[62] T.S.E. Eriksson, A.J. Prassl, G. Plank, and G.A. Holzapfel. “Influence of myocardial fiber/sheet orientations on left ventricular mechanical contraction”. In: *Mathematics and Mechanics of Solids* 18.6 (2013), pp. 592–606.

[63] T.S.E. Eriksson, A.J. Prassl, G. Plank, and G.A. Holzapfel. “Modeling the dispersion in electromechanically coupled myocardium”. In: *International Journal for Numerical Methods in Biomedical Engineering* 29.11 (2013), pp. 1267–1284.

[64] T.E. Fastl, C. Tobon-Gomez, A. Crozier, J. Whitaker, R. Rajani, K.P. McCarthy, D. Sanchez-Quintana, S.Y. Ho, M.D. O’Neill, G. Plank, et al. “Personalized computational modeling of left atrial geometry and transmural myofiber architecture”. In: *Medical Image Analysis* (2018).

[65] T.E. Fastl, C. Tobon-Gomez, W.A. Crozier, J. Whitaker, R. Rajani, K.P. McCarthy, D. Sanchez-Quintana, S.Y. Ho, M.D. O’Neill, G. Plank, et al. “Personalized modeling pipeline for left atrial electromechanics”. In: *2016 Computing in Cardiology Conference (CinC)*. 2016, pp. 225–228.

[66] M. Fedele and A. Quarteroni. “Polygonal surface processing and mesh generation tools for the numerical simulation of the cardiac function”. In: *International Journal for Numerical Methods in Biomedical Engineering* 37.4 (2021), e3435.

[67] A. Ferrer, R. Sebastián, D. Sánchez-Quintana, J.F. Rodríguez, E.J. Godoy, L. Martínez, and J. Saiz. “Detailed anatomical and electrophysiological models of human atria and torso for the simulation of atrial activation”. In: *PloS One* 10.11 (2015), e0141573.

[68] H. Finsberg, C. Xi, J. Le Tan, L. Zhong, M. Genet, J. Sundnes, L.C. Lee, and S.T. Wall. “Efficient estimation of personalized biventricular mechanical function employing gradient-based optimization”. In: *International journal for numerical methods in biomedical engineering* 34.7 (2018), e2982.

[69] D. Forti, M. Bukac, A. Quaini, S. Canic, and S. Deparis. “A monolithic approach to fluid–composite structure interaction”. In: *Journal of Scientific Computing* 72.1 (2017), pp. 396–421.

[70] D. Forti and L. Dedè. “Semi-implicit BDF time discretization of the Navier–Stokes equations with VMS-LES modeling in a high performance computing framework”. In: *Computers & Fluids* 117 (2015), pp. 168–182.

[71] P.C. Franzone, L.F. Pavarino, and G. Savaré. “Computational electrocardiology: mathematical and numerical modeling”. In: *Complex systems in Biomedicine*. Springer, 2006, pp. 187–241.

[72] P.C. Franzone, L.F. Pavarino, and S. Scacchi. *Mathematical Cardiac Electrophysiology*. Vol. 13. Springer, 2014.

[73] P.C. Franzone, L.F. Pavarino, and S. Scacchi. “A numerical study of scalable cardiac electro-mechanical solvers on HPC architectures”. In: *Frontiers in Physiology* 9 (2018), p. 268.

[74] T. Fritz, C. Wieners, G. Seemann, H. Steen, and Olaf Dössel. “Simulation of the contraction of the ventricles in a human heart model including atria and pericardium”. In: *Biomechanics and Modeling in Mechanobiology* 13.3 (2014), pp. 627–641.

[75] E. Garcia-Blanco, R. Ortigosa, A.J. Gil, and J. Bonet. “Towards an efficient computational strategy for electro-activation in cardiac mechanics”. In: *Computer Methods in Applied Mechanics and Engineering* 356 (2019), pp. 220–260.

[76] M.W. Gee, C. Förster, and W.A. Wall. “A computational strategy for prestressing patient-specific biomechanical problems under finite deformation”. In: *International Journal for Numerical Methods in Biomedical Engineering* 26.1 (2010), pp. 52–72.

[77] M. Genet, L.C. Lee, R. Nguyen, H. Haraldsson, G. Acevedo-Bolton, Z. Zhang, L. Ge, K. Ordovas, S. Kozerke, and J.M. Guccione. “Distribution of normal human left ventricular myofiber stress at end diastole and end systole: a target for in silico design of heart failure treatments”. In: *Journal of Applied Physiology* 117.2 (2014), pp. 142–152.

[78] T. Gerach, S. Schuler, J. Fröhlich, L. Lindner, E. Kovacheva, R. Moss, E. M. Wülfers, G. Seemann, C. Wieners, and A. Loewe. “Electro-Mechanical Whole-Heart Digital Twins: A Fully Coupled Multi-Physics Approach”. In: *Mathematics* 9.11 (2021), p. 1247.

[79] T. Gerach, S. Schuler, E. Kovacheva, O. Dössel, and A. Loewe. “Consequences of Using an Orthotropic Stress Tensor for Left Ventricular Systole”. In: *2020 Computing in Cardiology*. IEEE. 2020, pp. 1–4.

[80] A. Gerbi, L. Dedè, and A. Quarteroni. “A monolithic algorithm for the simulation of cardiac electromechanics in the human left ventricle”. In: *Mathematics in Engineering* 1 (2018), pp. 1–37.

[81] D. Gil, R. Aris, A. Borras, E. Ramírez, R. Sebastian, and M. Vázquez. “Influence of fiber connectivity in simulations of cardiac biomechanics”. In: *International Journal of Computer Assisted Radiology and Surgery* 14.1 (2019), pp. 63–72.

[82] K. Gillette, M. Gsell, J. Bouyssier, A.J. Prassl, A. Neic, E.J. Vigmond, and G. Plank. “Automated Framework for the Inclusion of a His–Purkinje System in Cardiac Digital Twins of Ventricular Electrophysiology”. In: *Annals of Biomedical Engineering* (2021), pp. 1–11.

[83] S. Göktepe and E. Kuhl. “Electromechanics of the heart: a unified approach to the strongly coupled excitation–contraction problem”. In: *Computational Mechanics* 45.2-3 (2010), pp. 227–243.

[84] S. Göktepe, J. Wong, and E. Kuhl. “Atrial and ventricular fibrillation: computational simulation of spiral waves in cardiac tissue”. In: *Archive of Applied Mechanics* 80.5 (2010), pp. 569–580.

[85] S. Govindjee and P.A. Mihalic. “Computational methods for inverse finite elastostatics”. In: *Computer Methods in Applied Mechanics and Engineering* 136.1-2 (1996), pp. 47–57.

[86] R.A. Greenbaum, S.Y. Ho, D.G. Gibson, A.E. Becker, and R.H. Anderson. “Left ventricular fibre architecture in man”. In: *Heart* 45.3 (1981), pp. 248–263.

[87] D. Guan, J. Yao, X. Luo, and H. Gao. “Effect of myofibre architecture on ventricular pump function by using a neonatal porcine heart model: from DT-MRI to rule-based methods”. In: *Royal Society Open Science* 7.4 (2020), p. 191655.

[88] D. Guan, X. Zhuan, W. Holmes, X. Luo, and H. Gao. “Modelling of fibre dispersion and its effects on cardiac mechanics from diastole to systole”. In: *Journal of Engineering Mathematics* 128.1 (2021), pp. 1–24.

[89] J.M. Guccione and A.D. McCulloch. “Finite element modeling of ventricular mechanics”. In: *Theory of Heart*. Springer, 1991, pp. 121–144.

[90] J.M. Guccione, A.D. McCulloch, and L.K. Waldman. “Passive material properties of intact ventricular myocardium determined from a cylindrical model”. In: *Journal of Biomechanical Engineering* 113 (1991), pp. 42–55.

[91] O. Gültekin, G. Sommer, and G.A. Holzapfel. “An orthotropic viscoelastic model for the passive myocardium: continuum basis and numerical treatment”. In: *Computer methods in biomechanics and biomedical engineering* 19.15 (2016), pp. 1647–1664.

[92] V. Gurev, T. Lee, J. Constantino, H. Arevalo, and N.A. Trayanova. “Models of cardiac electromechanics based on individual hearts imaging data”. In: *Biomechanics and Modeling in Mechanobiology* 10.3 (2011), pp. 295–306.

[93] B.J. Hansen, J. Zhao, and V.V. Fedorov. “Fibrosis and atrial fibrillation: computerized and optical mapping: a view into the human atria at submillimeter resolution”. In: *JACC: Clinical Electrophysiology* 3 (2017), pp. 531–546.

[94] D.M. Harrild and C.S Henriquez. “A computer model of normal conduction in the human atria”. In: *Circulation Research* 87 (2000), e25–e36.

[95] P.A. Helm, H.J. Tseng, L. Younes, E.R. McVeigh, and R.L. Winslow. “Ex vivo 3D diffusion tensor imaging and quantification of cardiac laminar structure”. In: *Magnetic Resonance in Medicine: An Official Journal of the International Society for Magnetic Resonance in Medicine* 54.4 (2005), pp. 850–859.

[96] M. Hirschvogel, M. Bassilious, L. Jagschies, S.M. Wildhirt, and M.W. Gee. “A monolithic 3D-0D coupled closed-loop model of the heart and the vascular system: experiment-based parameter estimation for patient-specific cardiac mechanics”. In: *International Journal for Numerical Methods in Biomedical Engineering* 33 (2017), e2842.

[97] S.Y. Ho, R.H. Anderson, and D. Sánchez-Quintana. “Atrial structure and fibres: morphologic bases of atrial conduction”. In: *Cardiovascular Research* 54 (2002), pp. 325–336.

[98] S.Y. Ho, J.A. Cabrera, and D. Sanchez-Quintana. “Left atrial anatomy revisited”. In: *Circulation: Arrhythmia and Electrophysiology* 5 (2012), pp. 220–228.

[99] S.Y. Ho and P. Nihoyannopoulos. “Anatomy, echocardiography, and normal right ventricular dimensions”. In: *Heart* 92 (2006), pp. i2–i13.

[100] S.Y. Ho and D. Sánchez-Quintana. “The importance of atrial structure and fibers”. In: *Clinical Anatomy: The Official Journal of the American Association of Clinical Anatomists and the British Association of Clinical Anatomists* 22 (2009), pp. 52–63.

[101] J.M. Hoermann, M.R. Pfaller, L. Avena, C. Bertoglio, and W.A. Wall. “Automatic mapping of atrial fiber orientations for patient-specific modeling of cardiac electromechanics using image registration”. In: *International Journal for Numerical Methods in Biomedical Engineering* 35.6 (2019), e3190.

[102] G.A. Holzapfel, J.A. Niestrawska, R.W. Ogden, A.J. Reinisch, and A.J. Schriefl. “Modelling non-symmetric collagen fibre dispersion in arterial walls”. In: *Journal of the Royal Society Interface* 12.106 (2015), p. 20150188.

[103] G.A. Holzapfel and R.W. Ogden. “Constitutive modelling of passive myocardium: a structurally based framework for material characterization”. In: *Philosophical Transactions of the Royal Society A: Mathematical, Physical and Engineering Sciences* 367 (2009), pp. 3445–3475.

[104] E.W. Hsu, A.L. Muzikant, S.A. Matulevicius, R.C. Penland, and C.S. Henriquez. “Magnetic resonance myocardial fiber-orientation mapping with direct histological correlation”. In: *American Journal of Physiology-Heart and Circulatory Physiology* 274.5 (1998), H1627–H1634.

[105] D.E. Hurtado and G. Rojas. “Non-conforming finite-element formulation for cardiac electrophysiology: an effective approach to reduce the computation time of heart simulations without compromising accuracy”. In: *Computational Mechanics* 61.4 (2018), pp. 485–497.

[106] J. Hussan, P.P. de Tombe, and J.J. Rice. “A spatially detailed myofilament model as a basis for large-scale biological simulations”. In: *IBM journal of research and development* 50.6 (2006), pp. 583–600.

[107] Zygote Media Group Inc. “Zygote solid 3d heart generation II developement report.” In: *Technical report* (2014).

[108] V. Jacquemet, N. Virag, Z. Ihara, L. Dang, O. Blanc, S. Zozor, J. Vesin, L. Kappenberger, and C. Henriquez. “Study of unipolar electrogram morphology in a computer model of atrial fibrillation”. In: *Journal of Cardiovascular Electrophysiology* 14 (2003), S172–S179.

[109] J. Jilberto and D.E. Hurtado. “Semi-implicit non-conforming finite-element schemes for cardiac electrophysiology: a framework for mesh-coarsening heart simulations”. In: *Frontiers in Physiology* 9 (2018), p. 1513.

[110] A. Kanai and G. Salama. “Optical mapping reveals that repolarization spreads anisotropically and is guided by fiber orientation in guinea pig hearts”. In: *Circulation Research* 77.4 (1995), pp. 784–802.

[111] E. Karabelas, G. Haase, G. Plank, and C.M. Augustin. “Versatile stabilized finite element formulations for nearly and fully incompressible solid mechanics”. In: *Computational mechanics* 65.1 (2020), pp. 193–215.

[112] J.P. Keener and J. Sneyd. *Mathematical physiology.* Vol. 1. Springer, 1998.

[113] R.C.P. Kerckhoffs, M.L. Neal, Q. Gu, J.B. Bassingthwaighte, J.H. Omens, and A.D. McCulloch. “Coupling of a 3D finite element model of cardiac ventricular mechanics to lumped systems models of the systemic and pulmonic circulation”. In: *Annals of Biomedical Engineering* 35 (2007), pp. 1–18.

[114] S. Klotz, I. Hay, M.L. Dickstein, G. Yi, J. Wang, M.S. Maurer, D.A. Kass, and D. Burkhoff. “Single-beat estimation of end-diastolic pressure-volume relationship: a novel method with potential for noninvasive application”. In: *American Journal of Physiology-Heart and Circulatory Physiology* 291 (2006), H403–H412.

[115] M.J. Kocica, A.F. Corno, F. Carreras-Costa, M. Ballester-Rodes, M.C. Moghbel, C.N.C. Cueva, V. Lackovic, V.I. Kanjuh, and F. Torrent-Guasp. “The helical ventricular myocardial band: global, three-dimensional, functional architecture of the ventricular myocardium”. In: *European Journal of Cardio-thoracic Surgery* 29 (2006), S21–S40.

[116] S. Krishnamoorthi, M. Sarkar, and W.S. Klug. “Numerical quadrature and operator splitting in finite element methods for cardiac electrophysiology”. In: *International Journal for Numerical Methods in Biomedical Engineering* 29 (2013), pp. 1243–1266.

[117] A. Krishnamurthy, M.J. Gonzales, G. Sturgeon, W.P. Segars, and A.D. McCulloch. “Biomechanics simulations using cubic Hermite meshes with extraordinary nodes for isogeometric cardiac modeling”. In: *Computer aided geometric design* 43 (2016), pp. 27–38.

[118] A. Krishnamurthy, C.T. Villongco, J. Chuang, L.R. Frank, V. Nigam, E. Belezzuoli, P. Stark, D.E. Krummen, S. Narayan, J.H. Omens, et al. “Patient-specific models of cardiac biomechanics”. In: *Journal of computational physics* 244 (2013), pp. 4–21.

[119] M.W. Krueger, K. Rhode, F.M. Weber, D. Keller, D. Caulfield, G. Seemann, B. Knowles, R. Razavi, and O. Dössel. “Patient-specific volumetric atrial models with electrophysiological components: a comparison of simulations and measurements”. In: *Biomedizinische Technik/Biomedical Engineering* 55 (2010).

[120] M.W. Krueger, V. Schmidt, C. Tobón, F.M. Weber, C. Lorenz, D.U.J. Keller, H. Barschdorf, M. Burdumy, P. Neher, G. Plank, et al. “Modeling atrial fiber orientation in patient-specific geometries: a semi-automatic rule-based approach”. In: *International Conference on Functional Imaging and Modeling of the Heart.* 2011, pp. 223–232.

[121] J.B. Kuipers et al. *Quaternions and Rotation Sequences.* Vol. 66. Princeton University Press, 1999.

[122] V. Kumar, A.K. Abbas, N. Fausto, and J.C. Aster. *Robbins and Cotran pathologic basis of disease.* Elsevier Health Sciences, 2014.

[123] S. Labarthe, Y. Coudiere, J. Henry, and H. Cochet. “A semi-automatic method to construct atrial fibre structures: A tool for atrial simulations”. In: *Computing in Cardiology.* 2012, pp. 881–884.

[124] S. Land and S.A. Niederer. “Influence of atrial contraction dynamics on cardiac function”. In: *International Journal for Numerical Methods in Biomedical Engineering* 34.3 (2018), e2931.

[125] S. Land, S. Park-Holohan, N.P. Smith, C.G. Dos Remedios, J.C. Kentish, and S.A. Niederer. “A model of cardiac contraction based on novel measurements of tension development in human cardiomyocytes”. In: *Journal of Molecular and Cellular Cardiology* 106 (2017), pp. 68–83.

[126] M. Landajuela, C. Vergara, A. Gerbi, L. Dedè, L. Formaggia, and A. Quarteroni. “Numerical approximation of the electromechanical coupling in the left ventricle with inclusion of the Purkinje network”. In: *International Journal for Numerical Methods in Biomedical Engineering* 34 (2018), e2984.

[127] A.W.C. Lee, U.C. Nguyen, O. Razeghi, J. Gould, B.S. Sidhu, B. Sieniewicz, J. Behar, M. Mafi-Rad, G. Plank, F.W. Prinzen, et al. "A rule-based method for predicting the electrical activation of the heart with cardiac resynchronization therapy from non-invasive clinical data". In: *Medical Image Analysis* 57 (2019), pp. 197–213.

[128] I.J. LeGrice, B.H. Smaill, L.Z. Chai, S.G. Edgar, J.B. Gavin, and P.J. Hunter. "Laminar structure of the heart: ventricular myocyte arrangement and connective tissue architecture in the dog". In: *American Journal of Physiology-Heart and Circulatory Physiology* 269.2 (1995), H571–H582.

[129] R. Lemery, D. Birnie, A.S.L. Tang, M. Green, M. Gollob, M. Hendry, and E. Lau. "Normal atrial activation and voltage during sinus rhythm in the human heart: an endocardial and epicardial mapping study in patients with a history of atrial fibrillation". In: *Journal of cardiovascular electrophysiology* 18.4 (2007), pp. 402–408.

[130] F. Levrero-Florencio, F. Margara, E. Zacur, A. Bueno-Orovio, Z.J. Wang, A. Santiago, J. Aguado-Sierra, G. Houzeaux, V. Grau, D. Kay, et al. "Sensitivity analysis of a strongly-coupled human-based electromechanical cardiac model: Effect of mechanical parameters on physiologically relevant biomarkers". In: *Computer Methods in Applied Mechanics and Engineering* 361 (2020), p. 112762.

[131] L.S. Lilly. *Pathophysiology of heart disease: a collaborative project of medical students and faculty.* Lippincott Williams & Wilkins, 2012.

[132] D.H.S. Lin and F.C.P. Yin. "A multiaxial constitutive law for mammalian left ventricular myocardium in steady-state barium contracture or tetanus". In: *Journal of Biomechanical Engineering* 120.4 (1998), pp. 504–517.

[133] H. Liu, F. Liang, J. Wong, T. Fujiwara, W. Ye, K. Tsubota, and M. Sugawara. "Multi-scale modeling of hemodynamics in the cardiovascular system". In: *Acta Mechanica Sinica* 31.4 (2015), pp. 446–464.

[134] H. Lombaert, J. Peyrat, P. Croisille, S. Rapacchi, L. Fanton, F. Cheriet, P. Clarysse, I. Magnin, H. Delingette, and N. Ayache. "Human atlas of the cardiac fiber architecture: study on a healthy population". In: *IEEE Transactions on Medical Imaging* 31.7 (2012), pp. 1436–1447.

[135] A. Lopez-Perez, R. Sebastian, and J.M. Ferrero. "Three-dimensional cardiac computational modelling: methods, features and applications". In: *Biomedical Engineering Online* 14 (2015), p. 35.

[136] P.P. Lunkenheimer, P. Niederer, D. Sanchez-Quintana, M. Murillo, and M. Smerup. "Models of ventricular structure and function reviewed for clinical cardiologists". In: *Journal of Cardiovascular Translational Research* 6 (2013), pp. 176–186.

[137] A.M. Maceira, S.K. Prasad, M. Khan, and D.J. Pennell. "Normalized left ventricular systolic and diastolic function by steady state free precession cardiovascular magnetic resonance". In: *Journal of Cardiovascular Magnetic Resonance* 8.3 (2006), pp. 417–426.

[138] A.M. Maceira, S.K. Prasad, M. Khan, and D.J. Pennell. "Reference right ventricular systolic and diastolic function normalized to age, gender and body surface area from steady-state free precession cardiovascular magnetic resonance". In: *European Heart Journal* 27.23 (2006), pp. 2879–2888.

[139] L. Marx, M.A.F. Gsell, A. Rund, F. Caforio, A.J. Prassl, G. Toth-Gayor, T. Kuehne, C.M. Augustin, and G. Plank. “Personalization of electro-mechanical models of the pressure-overloaded left ventricle: fitting of Windkessel-type afterload models”. In: *Philosophical Transactions of the Royal Society A* 378.2173 (2020), p. 20190342.

[140] L. Marx, J.A. Niestrawska, M. Gsell, F. Caforio, G. Plank, and C.M. Augustin. “Efficient identification of myocardial material parameters and the stress-free reference configuration for patient-specific human heart models”. In: *arXiv preprint arXiv:2101.04411* (2021).

[141] K.S. McDowell, S. Zahid, F. Vadakkumpadan, J. Blauer, R.S. MacLeod, and N. Trayanova. “Virtual electrophysiological study of atrial fibrillation in fibrotic remodeling”. In: *PloS One* 10 (2015).

[142] J.C. Mercier, T.G. DiSessa, J.M. Jarmakani, T. Nakanishi, S. Hiraishi, J. Isabel-Jones, and W.F. Friedman. “Two-dimensional echocardiographic assessment of left ventricular volumes and ejection fraction in children”. In: *Circulation* 65 (1982), pp. 962–969.

[143] A. Nagler, C. Bertoglio, M. Gee, and W. Wall. “Personalization of cardiac fiber orientations from image data using the unscented Kalman filter”. In: *International Conference on Functional Imaging and Modeling of the Heart.* 2013, pp. 132–140.

[144] M.L. Neal and J.B. Bassingthwaighte. “Subject-specific model estimation of cardiac output and blood volume during hemorrhage”. In: *Cardiovascular Engineering* 7.3 (2007), pp. 97–120.

[145] A. Neic, F.O. Campos, A.J. Prassl, S.A. Niederer, M.J. Bishop, E.J. Vigmond, and G. Plank. “Efficient computation of electrograms and ECGs in human whole heart simulations using a reaction-eikonal model”. In: *Journal of computational physics* 346 (2017), pp. 191–211.

[146] A. Neic, M. Gsell, E. Karabelas, A. Prassl, and G. Plank. “Automating image-based mesh generation and manipulation tasks in cardiac modeling workflows using meshtool”. In: *SoftwareX* 11 (2020), p. 100454.

[147] M. Nemerovski, P.K. Shah, M. Pichler, D.S. Berman, F. Shellock, and H.J.C. Swan. “Radionuclide assessment of sequential changes in left and right ventricular function following first acute transmural myocardial infarction”. In: *American heart journal* 104.4 (1982), pp. 709–717.

[148] T.D. Nguyen, O.E. Kadri, and R.S. Voronov. “An Introductory Overview of Image-Based Computational Modeling in Personalized Cardiovascular Medicine”. In: *Frontiers in Bioengineering and Biotechnology* 8 (2020).

[149] S.A. Niederer, P.J. Hunter, and N.P. Smith. “A quantitative analysis of cardiac myocyte relaxation: a simulation study”. In: *Biophysical journal* 90.5 (2006), pp. 1697–1722.

[150] S.A. Niederer, E. Kerfoot, A.P. Benson, M.O. Bernabeu, O. Bernus, C. Bradley, E.M. Cherry, R. Clayton, F.H. Fenton, A. Garny, et al. “Verification of cardiac tissue electrophysiology simulators using an N-version benchmark”. In: *Philosophical Transactions of the Royal Society A: Mathematical, Physical and Engineering Sciences* 369 (2011), pp. 4331–4351.

[151] S.A. Niederer, J. Lumens, and N.A. Trayanova. “Computational models in cardiology”. In: *Nature Reviews Cardiology* 16 (2019), pp. 100–111.

[152] S.A. Niederer, L. Mitchell, N. Smith, and G. Plank. “Simulating human cardiac electrophysiology on clinical time-scales”. In: *Frontiers in Physiology* 2 (2011), p. 14.

[153] S.A. Niederer, G. Plank, P. Chinchapatnam, M. Ginks, P. Lamata, K.S. Rhode, C.A. Rinaldi, R. Razavi, and N.P. Smith. “Length-dependent tension in the failing heart and the efficacy of cardiac resynchronization therapy”. In: *Cardiovascular Research* 89 (2011), pp. 336–343.

[154] P. Nielsen, I.J. Le Grice, B.H. Smaill, and P.J. Hunter. “Mathematical model of geometry and fibrous structure of the heart”. In: *American Journal of Physiology-Heart and Circulatory Physiology* 260.4 (1991), H1365–H1378.

[155] F. Nobile, A. Quarteroni, and R. Ruiz-Baier. “An active strain electromechanical model for cardiac tissue”. In: *International Journal for Numerical Methods in Biomedical Engineering* 28 (2012), pp. 52–71.

[156] A. Nogami. “Purkinje-related arrhythmias part I: monomorphic ventricular tachycardias”. In: *Pacing and Clinical Electrophysiology* 34.5 (2011), pp. 624–650.

[157] D. Nordsletten, A. Capilnasiu, W. Zhang, A. Wittgenstein, M. Hadjicharalambous, G. Sommer, R. Sinkus, and G.A. Holzapfel. “A Viscoelastic Model for Human Myocardium”. In: *arXiv preprint arXiv:2105.06671* (2021).

[158] D. Nordsletten, M. McCormick, P.J. Kilner, P. Hunter, D. Kay, and N.P. Smith. “Fluid–solid coupling for the investigation of diastolic and systolic human left ventricular function”. In: *International Journal for Numerical Methods in Biomedical Engineering* 27.7 (2011), pp. 1017–1039.

[159] D.A. Nordsletten, S.A. Niederer, M.P. Nash, P.J. Hunter, and N.P. Smith. “Coupling multi-physics models to cardiac mechanics”. In: *Progress in Biophysics and Molecular Biology* 104 (2011), pp. 77–88.

[160] R.W. Ogden. *Non-linear elastic deformations.* Courier Corporation, 1997.

[161] S. Ordas, E. Oubel, R. Sebastian, and A.F. Frangi. “Computational anatomy atlas of the heart”. In: *2007 5th International Symposium on Image and Signal Processing and Analysis.* 2007, pp. 338–342.

[162] S. Paeme, K.T. Moorhead, J.G. Chase, B. Lambermont, P. Kolh, V. D’orio, L. Pierard, M. Moonen, P. Lancellotti, P.C. Dauby, et al. “Mathematical multi-scale model of the cardiovascular system including mitral valve dynamics. Application to ischemic mitral insufficiency”. In: *Biomedical Engineering Online* 10.1 (2011), pp. 1–20.

[163] A. Palit, S.K. Bhudia, T.N. Arvanitis, G.A. Turley, and M.A. Williams. “Computational modelling of left-ventricular diastolic mechanics: Effect of fibre orientation and right-ventricle topology”. In: *Journal of Biomechanics* 48.4 (2015), pp. 604–612.

[164] C. Papadacci, V. Finel, J. Provost, O. Villemain, P. Bruneval, J. Gennisson, M. Tanter, M. Fink, and M. Pernot. “Imaging the dynamics of cardiac fiber orientation in vivo using 3D Ultrasound Backscatter Tensor Imaging”. In: *Scientific reports* 7.1 (2017), pp. 1–9.

[165] J.W. Papez. “Heart musculature of the atria”. In: *American Journal of Anatomy* 27 (1920), pp. 255–285.

[166] A. Pashaei, D. Romero, R. Sebastian, O. Camara, and A.F. Frangi. "Fast Multiscale Modeling of Cardiac Electrophysiology Including Purkinje System". In: *IEEE Transactions on Biomedical Engineering* 58.10 (2011), pp. 2956–2960.

[167] F. Pashakhanloo, D.A. Herzka, H. Ashikaga, S. Mori, N. Gai, D.A. Bluemke, N. Trayanova, and E.R. McVeigh. "Myofiber architecture of the human atria as revealed by submillimeter diffusion tensor imaging". In: *Circulation: Arrhythmia and Electrophysiology* 9 (2016), e004133.

[168] A.S. Patelli, L. Dedè, T. Lassila, A. Bartezzaghi, and A. Quarteroni. "Isogeometric approximation of cardiac electrophysiology models on surfaces: An accuracy study with application to the human left atrium". In: *Computer Methods in Applied Mechanics and Engineering* 317 (2017), pp. 248–273.

[169] P. Pathmanathan, M.O. Bernabeu, S.A. Niederer, D.J. Gavaghan, and D. Kay. "Computational modelling of cardiac electrophysiology: explanation of the variability of results from different numerical solvers". In: *International journal for numerical methods in biomedical engineering* 28.8 (2012), pp. 890–903.

[170] P. Pathmanathan, G.R. Mirams, J. Southern, and J.P. Whiteley. "The significant effect of the choice of ionic current integration method in cardiac electrophysiological simulations". In: *International Journal for Numerical Methods in Biomedical Engineering* 27.11 (2011), pp. 1751–1770.

[171] L. Pegolotti, L. Dedè, and A. Quarteroni. "Isogeometric Analysis of the electrophysiology in the human heart: Numerical simulation of the bidomain equations on the atria". In: *Computer Methods in Applied Mechanics and Engineering* 343 (2019), pp. 52–73.

[172] M. Peirlinck, F.S. Costabal, J. Yao, J.M. Guccione, S. Tripathy, Y. Wang, D. Ozturk, P. Segars, T.M. Morrison, S. Levine, et al. "Precision medicine in human heart modeling". In: *Biomechanics and Modeling in Mechanobiology* (2021), pp. 1–29.

[173] S.H. Peng and W.V. Chang. "A compressible approach in finite element analysis of rubber-elastic materials". In: *Computers & Structures* 62 (1997), pp. 573–593.

[174] J.M. Peyrat, M. Sermesant, X. Pennec, H. Delingette, C. Xu, E.R. McVeigh, and N. Ayache. "A computational framework for the statistical analysis of cardiac diffusion tensors: application to a small database of canine hearts". In: *IEEE Transactions on Medical Imaging* 26.11 (2007), pp. 1500–1514.

[175] M.R. Pfaller, J.M. Hörmann, M. Weigl, A. Nagler, R. Chabiniok, C. Bertoglio, and W.A. Wall. "The importance of the pericardium for cardiac biomechanics: from physiology to computational modeling". In: *Biomechanics and Modeling in Mechanobiology* 18.2 (2019), pp. 503–529.

[176] R. Piersanti, P.C. Africa, M. Fedele, C. Vergara, L. Dedè, A.F. Corno, and A. Quarteroni. "Modeling cardiac muscle fibers in ventricular and atrial electrophysiology simulations". In: *Computer Methods in Applied Mechanics and Engineering* 373 (2021), p. 113468.

[177] R. Piersanti, F. Regazzoni, M. Salvador, A.F. Corno, L. Dede', C. Vergara, and A. Quarteroni. "3D-0D closed-loop model for the simulation of cardiac biventricular electromechanics". In: *preprint arXiv:2108.01907, and accepted for pubblication in Computer Methods in Applied Mechanics and Engineering* (2022).

[178] A. Pironet, P.C. Dauby, S. Paeme, S. Kosta, J.G. Chase, and T. Desaive. "Simulation of left atrial function using a multi-scale model of the cardiovascular system". In: *PloS one* 8.6 (2013), e65146.

[179] G. Plank, R. Burton, P. Hales, M. Bishop, T. Mansoori, M. Bernabeu, A. Garny, A.J. Prassl, C. Bollensdorff, F. Mason, et al. "Generation of histo-anatomically representative models of the individual heart: tools and application". In: *Philosophical Transactions of the Royal Society A: Mathematical, Physical and Engineering Sciences* 367.1896 (2009), pp. 2257–2292.

[180] G. Plank, A. Prassl, E. Hofer, and N. Trayanova. "Evaluating intramural virtual electrodes in the myocardial wedge preparation: simulations of experimental conditions". In: *Biophysical Journal* 94 (2008), pp. 1904–1915.

[181] G. Plank, L. Zhou, J.L. Greenstein, S. Cortassa, R. L Winslow, B. O'Rourke, and N.A. Trayanova. "From mitochondrial ion channels to arrhythmias in the heart: computational techniques to bridge the spatio-temporal scales". In: *Philosophical Transactions of the Royal Society A: Mathematical, Physical and Engineering Sciences* 366 (2008), pp. 3381–3409.

[182] M. Pluijmert, T. Delhaas, A.F. De la Parra, W. Kroon, F.W. Prinzen, and P.H.M. Bovendeerd. "Determinants of biventricular cardiac function: a mathematical model study on geometry and myofiber orientation". In: *Biomechanics and Modeling in Mechanobiology* 16.2 (2017), pp. 721–729.

[183] M. Potse, B. Dubé, J. Richer, A. Vinet, and R. M. Gulrajani. "A comparison of monodomain and bidomain reaction-diffusion models for action potential propagation in the human heart". In: *IEEE Transactions on Biomedical Engineering* 53.12 (2006), pp. 2425–2435.

[184] A. Propp, A. Gizzi, F. Levrero-Florencio, and R. Ruiz-Baier. "An orthotropic electro-viscoelastic model for the heart with stress-assisted diffusion". In: *Biomechanics and Modeling in Mechanobiology* 19.2 (2020), pp. 633–659.

[185] B.B. Punske, B. Taccardi, B. Steadman, P.R. Ershler, A. England, M.L. Valencik, J.A. McDonald, and S.E. Litwin. "Effect of fiber orientation on propagation: electrical mapping of genetically altered mouse hearts". In: *Journal of Electrocardiology* 38.4 (2005), pp. 40–44.

[186] A. Quarteroni. *Numerical models for differential problems.* Vol. 2. Springer, 2009.

[187] A. Quarteroni, L. Dedè, A. Manzoni, and C. Vergara. *Mathematical modelling of the human cardiovascular system: data, numerical approximation, clinical applications.* Cambridge Monographs on Applied and Computational Mathematics. Cambridge University Press, 2019.

[188] A. Quarteroni, T. Lassila, S. Rossi, and R. Ruiz-Baier. "Integrated Heart-Coupling multiscale and multiphysics models for the simulation of the cardiac function". In: *Computer Methods in Applied Mechanics and Engineering* 314 (2017), pp. 345–407.

[189] A. Quarteroni, R. Sacco, and F. Saleri. *Numerical mathematics.* Vol. 37. Springer Science & Business Media, 2010.

[190] A. Quarteroni, A. Veneziani, and C. Vergara. "Geometric multiscale modeling of the cardiovascular system, between theory and practice". In: *Computer Methods in Applied Mechanics and Engineering* 302 (2016), pp. 193–252.

[191] M.K. Rausch, M. Genet, and J.D. Humphrey. “An augmented iterative method for identifying a stress-free reference configuration in image-based biomechanical modeling”. In: *Journal of biomechanics* 58 (2017), pp. 227–231.

[192] A.A. Razumov, K.S. Ushenin, K.A. Butova, and O.E. Solovyova. “The study of the influence of heart ventricular wall thickness on pseudo-ECG”. In: *Russian Journal of Numerical Analysis and Mathematical Modelling* 33 (2018), pp. 301–313.

[193] F. Regazzoni. “Mathematical modeling and Machine Learning for the numerical simulation of cardiac electromechanics”. PhD thesis. Politecnico di Milano, 2020.

[194] F. Regazzoni, L. Dedè, and A. Quarteroni. “Active contraction of cardiac cells: a reduced model for sarcomere dynamics with cooperative interactions”. In: *Biomechanics and modeling in mechanobiology* 17.6 (2018), pp. 1663–1686.

[195] F. Regazzoni, L. Dedè, and A. Quarteroni. “Biophysically detailed mathematical models of multiscale cardiac active mechanics”. In: *PLoS Computational Biology* 16 (2020), e1008294.

[196] F. Regazzoni, L. Dedè, and A. Quarteroni. “Machine learning of multiscale active force generation models for the efficient simulation of cardiac electromechanics”. In: *Computer Methods in Applied Mechanics and Engineering* 370 (2020), p. 113268.

[197] F. Regazzoni and A. Quarteroni. “Accelerating the convergence to a limit cycle in 3D cardiac electromechanical simulations through a data-driven 0D emulator”. In: *Computers in Biology and Medicine* (2021), p. 104641.

[198] F. Regazzoni, M. Salvador, P.A. Africa, M. Fedele, L. Dede’, and A. Quarteroni. “A cardiac electromechanics model coupled with a lumped parameters model for closed-loop blood circulation. Part I: model derivation”. In: *preprint arXiv:2011.15040* (2020).

[199] F. Regazzoni, M. Salvador, P.A. Africa, M. Fedele, L. Dede’, and A. Quarteroni. “A cardiac electromechanics model coupled with a lumped parameters model for closed-loop blood circulation. Part II: numerical approximation”. In: *preprint arXiv:2011.15051* (2020).

[200] D. E. Roberts, L. T. Hersh, and A. M. Scher. “Influence of cardiac fiber orientation on wavefront voltage, conduction velocity, and tissue resistivity in the dog.” In: *Circulation Research* 44.5 (1979), pp. 701–712.

[201] S. Rocher, A. López, A. Ferrer, L. Martínez, D. Sánchez, and J. Saiz. “A Highly-Detailed 3D Model of the Human Atria”. In: *World Congress on Medical Physics and Biomedical Engineering 2018*. Springer. 2019, pp. 649–653.

[202] C.H. Roney, R. Bendikas, F. Pashakhanloo, C. Corrado, E.J. Vigmond, E.R. McVeigh, N.A. Trayanova, and S.A. Niederer. “Constructing a Human Atrial Fibre Atlas”. In: *Annals of Biomedical Engineering* (2020).

[203] C.H. Roney, A. Pashaei, M. Meo, R. Dubois, P.M. Boyle, N. Trayanova, H. Cochet, S.A. Niederer, and E.J. Vigmond. “Universal atrial coordinates applied to visualisation, registration and construction of patient specific meshes”. In: *Medical Image Analysis* 55 (2019), pp. 65–75.

[204] S. Rossi, T. Lassila, R. Ruiz-Baier, A. Sequeira, and A. Quarteroni. “Thermodynamically consistent orthotropic activation model capturing ventricular systolic wall thickening in cardiac electromechanics”. In: *European Journal of Mechanics-A/Solids* 48 (2014), pp. 129–142.

[205] B.J. Roth. “Action potential propagation in a thick strand of cardiac muscle”. In: *Circulation Research* 68 (1991), pp. 162–173.

[206] R. Ruiz-Baier, A. Gizzi, S. Rossi, C. Cherubini, A. Laadhari, S. Filippi, and A. Quarteroni. “Mathematical modelling of active contraction in isolated cardiomyocytes”. In: *Mathematical Medicine and Biology: a Journal of the IMA* 31 (2014), pp. 259–283.

[207] K.L. Sack, E. Aliotta, D.B. Ennis, J.S. Choy, G.S. Kassab, J.M. Guccione, and T. Franz. “Construction and validation of subject-specific biventricular finite-element models of healthy and failing swine hearts from high-resolution DT-MRI”. In: *Frontiers in Physiology* 9 (2018), p. 539.

[208] S.I. Sakamoto, T. Nitta, Y. Ishii, Y. Miyagi, H. Ohmori, and K. Shimizu. “Interatrial electrical connections: the precise location and preferential conduction”. In: *Journal of Cardiovascular Electrophysiology* 16.10 (2005), pp. 1077–1086.

[209] M. Salvador, L. Dedè, and A. Quarteroni. “An intergrid transfer operator using radial basis functions with application to cardiac electromechanics”. In: *Computational Mechanics* 66 (2020), pp. 491–511.

[210] D. Sánchez-Quintana, M. Doblado-Calatrava, J.A. Cabrera, Y. Macías, and F. Saremi. “Anatomical basis for the cardiac interventional electrophysiologist”. In: *BioMed Research International* (2015).

[211] D. Sanchez-Quintana, V. Garcia-Martinez, and J.M. Hurle. “Myocardial fiber architecture in the human heart”. In: *Cells Tissues Organs* 138.4 (1990), pp. 352–358.

[212] D. Sánchez-Quintana, J.R. López-Mínguez, Y. Macías, J.A. Cabrera, and F. Saremi. “Left atrial anatomy relevant to catheter ablation”. In: *Cardiology Research and Practice* 2014 (2014).

[213] A. Santiago, J. Aguado-Sierra, M. Zavala-Aké, R. Doste-Beltran, S. Gómez, R. Arís, J.C. Cajas, E. Casoni, and M. Vázquez. “Fully coupled fluid-electro-mechanical model of the human heart for supercomputers”. In: *International Journal for Numerical Methods in Biomedical Engineering* 34.12 (2018), e3140.

[214] F. Saremi, S.Y. Ho, J.A. Cabrera, and D. Sanchez-Quintana. “Right ventricular outflow tract imaging with CT and MRI: part 2, function”. In: *American Journal of Roentgenology* 200.1 (2013), W51–W61.

[215] A. Satriano, C. Bellini, E.J. Vigmond, and E.S. Di Martino. “A feature-based morphing methodology for computationally modeled biological structures applied to left atrial fiber directions”. In: *Journal of Biomechanical Engineering* 135 (2013).

[216] S. Schuler, N. Pilia, D. Potyagaylo, and A. Loewe. “Cobiveco: Consistent biventricular coordinates for precise and intuitive description of position in the heart–with MATLAB implementation”. In: *arXiv preprint arXiv:2102.02898* (2021).

[217] D.F. Scollan, A. Holmes, J. Zhang, and R.L. Winslow. “Reconstruction of cardiac ventricular geometry and fiber orientation using magnetic resonance imaging”. In: *Annals of Biomedical Engineering* 28.8 (2000), pp. 934–944.

[218] R. Sebastian, V. Zimmerman, D. Romero, and A.F. Frangi. “Construction of a computational anatomical model of the peripheral cardiac conduction system”. In: *IEEE Transactions on Biomedical Engineering* 58.12 (2011), pp. 3479–3482.

[219] U. Sechtem, B.A. Sommerhoff, W. Markiewicz, R.D. White, M.D. Cheitlin, and C.B. Higgins. “Regional left ventricular wall thickening by magnetic resonance imaging: evaluation in normal persons and patients with global and regional dysfunction”. In: *The American Journal of Cardiology* 59.1 (1987), pp. 145–151.

[220] G. Seemann, C. Höper, F.B. Sachse, O. Dössel, A.V. Holden, and H. Zhang. “Heterogeneous three-dimensional anatomical and electrophysiological model of human atria”. In: *Philosophical Transactions of the Royal Society A: Mathematical, Physical and Engineering Sciences* 364 (2006), pp. 1465–1481.

[221] P. Segers, E.R. Rietzschel, M.L. De Buyzere, N. Stergiopulos, N. Westerhof, L.M. Van Bortel, T. Gillebert, and P.R. Verdonck. “Three-and four-element Windkessel models: assessment of their fitting performance in a large cohort of healthy middle-aged individuals”. In: *Proceedings of the Institution of Mechanical Engineers, Part H: Journal of Engineering in Medicine* 222.4 (2008), pp. 417–428.

[222] M. Sellier. “An iterative method for the inverse elasto-static problem”. In: *Journal of Fluids and Structures* 27.8 (2011), pp. 1461–1470.

[223] M. Sermesant, R. Chabiniok, P. Chinchapatnam, T. Mansi, F. Billet, P. Moireau, J.M. Peyrat, K. Wong, J. Relan, K. Rhode, et al. “Patient-specific electromechanical models of the heart for the prediction of pacing acute effects in CRT: a preliminary clinical validation”. In: *Medical Image Analysis* 16.1 (2012), pp. 201–215.

[224] M. Sermesant, K. Rhode, G.I. Sanchez-Ortiz, O. Camara, R. Andriantsimiavona, S. Hegde, D. Rueckert, P. Lambiase, C. Bucknall, E. Rosenthal, et al. “Simulation of cardiac pathologies using an electromechanical biventricular model and XMR interventional imaging”. In: *Medical Image Analysis* 9.5 (2005), pp. 467–480.

[225] F. Shaffer, R. McCraty, and C.L. Zerr. “A healthy heart is not a metronome: an integrative review of the heart’s anatomy and heart rate variability”. In: *Frontiers in psychology* 5 (2014), p. 1040.

[226] K. Shoemake. “Animating rotation with quaternion curves”. In: *ACM SIGGRAPH Computer Graphics*. Vol. 19. 1985, pp. 245–254.

[227] N.P. Smith, D.P. Nickerson, E.J. Crampin, and P.J. Hunter. “Multiscale computational modelling of the heart”. In: *Acta Numerica* 13 (2004), p. 371.

[228] G. Sommer, A.J. Schriefl, M. Andrä, M. Sacherer, C. Viertler, H. Wolinski, and G.A. Holzapfel. “Biomechanical properties and microstructure of human ventricular myocardium”. In: *Acta Biomaterialia* 24 (2015), pp. 172–192.

[229] R.S. Stephenson, P. Agger, P.P. Lunkenheimer, J. Zhao, M. Smerup, P. Niederer, R.H. Anderson, and J.C. Jarvis. “The functional architecture of skeletal compared to cardiac musculature: Myocyte orientation, lamellar unit morphology, and the helical ventricular myocardial band”. In: *Clinical Anatomy* 29 (2016), pp. 316–332.

[230] R.S. Stephenson, P. Agger, C. Omann, D. Sanchez-Quintana, J.C. Jarvis, and R.H. Anderson. “Resolving the true ventricular mural architecture”. In: *Journal of cardiovascular development and disease* 5.2 (2018), p. 34.

[231] N. Stergiopulos, B.E. Westerhof, and N. Westerhof. “Total arterial inertance as the fourth element of the Windkessel model”. In: *American Journal of Physiology-Heart and Circulatory Physiology* 276.1 (1999), H81–H88.

[232] D. D. Streeter Jr, H. M. Spotnitz, D. P. Patel, J. Ross Jr, and E. H. Sonnenblick. “Fiber orientation in the canine left ventricle during diastole and systole”. In: *Circulation Research* 24.3 (1969), pp. 339–347.

[233] M. Strocchi, C.M. Augustin, M. Gsell, E. Karabelas, A. Neic, K. Gillette, C.H. Roney, O. Razeghi, J.M. Behar, C.A. Rinaldi, et al. “The Effect of Ventricular Myofibre Orientation on Atrial Dynamics”. In: *International Conference on Functional Imaging and Modeling of the Heart.* 2021, pp. 659–670.

[234] M. Strocchi, C.M. Augustin, M.A.F. Gsell, E. Karabelas, A. Neic, K. Gillette, O. Razeghi, A.J. Prassl, E.J. Vigmond, J.M. Behar, et al. “A publicly available virtual cohort of four-chamber heart meshes for cardiac electro-mechanics simulations”. In: *PloS One* 15 (2020), e0235145.

[235] M. Strocchi, M. Gsell, C.M. Augustin, O. Razeghi, C.H. Roney, A.J. Prassl, E.J. Vigmond, J.M. Behar, J.S. Gould, C.A. Rinaldi, et al. “Simulating ventricular systolic motion in a four-chamber heart model with spatially varying robin boundary conditions to model the effect of the pericardium”. In: *Journal of Biomechanics* 101 (2020), p. 109645.

[236] T. Sugimoto, R. Dulgheru, A. Bernard, F. Ilardi, L. Contu, K. Addetia, L. Caballero, N. Akhaladze, G.D. Athanassopoulos, D. Barone, et al. “Echocardiographic reference ranges for normal left ventricular 2D strain: results from the EACVI NORRE study”. In: *European Heart Journal-Cardiovascular Imaging* 18.8 (2017), pp. 833–840.

[237] S. Sugiura, T. Washio, A. Hatano, J. Okada, H. Watanabe, and T. Hisada. “Multi-scale simulations of cardiac electrophysiology and mechanics using the University of Tokyo heart simulator”. In: *Progress in Biophysics and Molecular Biology* 110.2-3 (2012), pp. 380–389.

[238] G. Tamborini, N.A. Marsan, P. Gripari, F. Maffessanti, D. Brusoni, M. Muratori, E.G. Caiani, C. Fiorentini, and M. Pepi. “Reference values for right ventricular volumes and ejection fraction with real-time three-dimensional echocardiography: evaluation in a large series of normal subjects”. In: *Journal of the American Society of Echocardiography* 23.2 (2010), pp. 109–115.

[239] S. Tawara. *The Conduction System Of The Mammalian Heart: An Anatomico-histological Study Of The Atrioventricular Bundle And The Purkinje Fibers.* World Scientific, 2000.

[240] C.E. Thomas. “The muscular architecture of the atria of hog and dog hearts”. In: *American Journal of Anatomy* 104 (1959), pp. 207–236.

[241] A. Timmis, N. Townsend, C.P. Gale, A. Torbica, M. Lettino, S.E. Petersen, E.A. Mossialos, A.P. Maggioni, D. Kazakiewicz, H.T. May, et al. “European Society of Cardiology: cardiovascular disease statistics 2019”. In: *European Heart Journal* 41 (2020), pp. 12–85.

[242] C. Tobón, C.A. Ruiz-Villa, E. Heidenreich, L. Romero, F. Hornero, and J. Saiz. "A three-dimensional human atrial model with fiber orientation. Electrograms and arrhythmic activation patterns relationship". In: *PloS One* 8 (2013).

[243] N. Toussaint, C.T. Stoeck, T. Schaeffter, S. Kozerke, M. Sermesant, and P.G. Batchelor. "In vivo human cardiac fibre architecture estimation using shape-based diffusion tensor processing". In: *Medical Image Analysis* 17.8 (2013), pp. 1243–1255.

[244] N.A. Trayanova. "Whole-heart modeling: applications to cardiac electrophysiology and electromechanics". In: *Circulation Research* 108 (2011), pp. 113–128.

[245] N.A. Trayanova, P.M. Boyle, H.J. Arevalo, and S. Zahid. "Exploring susceptibility to atrial and ventricular arrhythmias resulting from remodeling of the passive electrical properties in the heart: a simulation approach". In: *Frontiers in Physiology* 5 (2014), p. 435.

[246] K.H.W.J. ten Tusscher, D. Noble, P.J. Noble, and A.V. Panfilov. "A model for human ventricular tissue". In: *American Journal of Physiology-Heart and Circulatory Physiology* 286 (2004), H1573–H1589.

[247] K.H.W.J. ten Tusscher and A.V. Panfilov. "Alternans and spiral breakup in a human ventricular tissue model". In: *American Journal of Physiology-Heart and Circulatory Physiology* 291 (2006), H1088–H1100.

[248] T.P. Usyk, I.J. LeGrice, and A.D. McCulloch. "Computational model of three-dimensional cardiac electromechanics". In: *Computing and Visualization in Science* 4.4 (2002), pp. 249–257.

[249] T.P. Usyk, R. Mazhari, and A.D. McCulloch. "Effect of laminar orthotropic myofiber architecture on regional stress and strain in the canine left ventricle". In: *Journal of Elasticity and the Physical Science of Solids* 61.1 (2000), pp. 143–164.

[250] F. Vadakkumpadan, H. Arevalo, A.J. Prassl, J. Chen, F. Kickinger, P. Kohl, G. Plank, and N. Trayanova. "Image-based models of cardiac structure in health and disease". In: *Wiley Interdisciplinary Reviews: Systems Biology and Medicine* 2.4 (2010), pp. 489–506.

[251] C. Vergara, M. Lange, S. Palamara, T. Lassila, A.F. Frangi, and A. Quarteroni. "A coupled 3D–1D numerical monodomain solver for cardiac electrical activation in the myocardium with detailed Purkinje network". In: *Journal of Computational Physics* 308 (2016), pp. 218–238.

[252] C. Vergara, S. Palamara, D. Catanzariti, F. Nobile, E. Faggiano, C. Pangrazzi, M. Centonze, M. Maines, A. Quarteroni, and G. Vergara. "Patient-specific generation of the Purkinje network driven by clinical measurements of a normal propagation". In: *Medical & Biological Engineering & Computing* 52 (2014), pp. 813–826.

[253] F.J. Vetter and A.D. McCulloch. "Three-dimensional analysis of regional cardiac function: a model of rabbit ventricular anatomy". In: *Progress in biophysics and molecular biology* 69.2-3 (1998), pp. 157–183.

[254] E.J. Vigmond, R.W. Dos Santos, A.J. Prassl, M. Deo, and G. Plank. "Solvers for the cardiac bidomain equations". In: *Progress in Biophysics and Molecular Biology* 96 (2008), pp. 3–18.

[255] E.J. Vigmond, M. Hughes, G. Plank, and L.J. Leon. "Computational tools for modeling electrical activity in cardiac tissue". In: *Journal of Electrocardiology* 36 (2003), pp. 69–74.

[256] E.J. Vigmond, R. Ruckdeschel, and N. Trayanova. "Reentry in a morphologically realistic atrial model". In: *Journal of Cardiovascular Electrophysiology* 12 (2001), pp. 1046–1054.

[257] S.S. Virani, A. Alonso, E.J. Benjamin, M.S. Bittencourt, C.W. Callaway, A.P. Carson, A.M. Chamberlain, A.R. Chang, S. Cheng, F.N. Delling, et al. "Heart disease and stroke statistics—2020 update: a report from the American Heart Association". In: *Circulation* 141 (2020), e139–e596.

[258] J.J. Wang, A.B. O'Brien, N.G. Shrive, K.H. Parker, and J.V. Tyberg. "Time-domain representation of ventricular-arterial coupling as a windkessel and wave system". In: *American Journal of Physiology-Heart and Circulatory Physiology* 284.4 (2003), H1358–H1368.

[259] L. Wang, Z.J. Wang, R. Doste, A. Santiago, X. Zhou, A. Quintanas, M. Vazquez, and B. Rodriguez. "Effects of Fibre Orientation on Electrocardiographic and Mechanical Functions in a Computational Human Biventricular Model". In: *International Conference on Functional Imaging and Modeling of the Heart.* Springer. 2021, pp. 351–361.

[260] Z.J. Wang, A. Santiago, X. Zhou, L. Wang, F. Margara, F. Levrero-Florencio, A. Das, C. Kelly, E. Dall'Armellina, M. Vazquez, et al. "Human biventricular electromechanical simulations on the progression of electrocardiographic and mechanical abnormalities in post-myocardial infarction". In: *EP Europace* 23.Supplement_1 (2021), pp. i143–i152.

[261] T. Washio, J. Okada, A. Takahashi, K. Yoneda, Y. Kadooka, S. Sugiura, and T. Hisada. "Multiscale heart simulation with cooperative stochastic cross-bridge dynamics and cellular structures". In: *Multiscale Modeling & Simulation* 11.4 (2013), pp. 965–999.

[262] H. Watanabe, S. Sugiura, H. Kafuku, and T. Hisada. "Multiphysics simulation of left ventricular filling dynamics using fluid-structure interaction finite element method". In: *Biophysical journal* 87.3 (2004), pp. 2074–2085.

[263] M.W. Watkins and M.M. LeWinter. "Physiologic role of the normal pericardium". In: *Annual review of medicine* 44.1 (1993), pp. 171–180.

[264] J.F. Wenk, D. Klepach, L.C. Lee, Z. Zhang, L. Ge, E.E. Tseng, A. Martin, S. Kozerke, J.H. Gorman III, R.C. Gorman, et al. "First evidence of depressed contractility in the border zone of a human myocardial infarction". In: *The Annals of Thoracic Surgery* 93.4 (2012), pp. 1188–1193.

[265] N. Westerhof and G. Elzinga. "Normalized input impedance and arterial decay time over heart period are independent of animal size". In: *American Journal of Physiology-Regulatory, Integrative and Comparative Physiology* 261.1 (1991), R126–R133.

[266] J. Wong and E. Kuhl. "Generating fibre orientation maps in human heart models using Poisson interpolation". In: *Computer Methods in Biomechanics and Biomedical Engineering* 17.11 (2014), pp. 1217–1226.

[267] E.X. Wu, Y. Wu, H. Tang, J. Wang, J. Yang, M.C. Ng, E.S. Yang, C.W. Chan, S. Zhu, C. Lau, et al. "Study of myocardial fiber pathway using magnetic resonance diffusion tensor imaging". In: *Magnetic Resonance Imaging* 25.7 (2007), pp. 1048–1057.

[268] J. Zhao, B.J. Hansen, T.A. Csepe, P. Lim, Y. Wang, M. Williams, P.J. Mohler, P.M.L. Janssen, R. Weiss, J.D. Hummel, et al. "Integration of high-resolution optical mapping and 3-dimensional micro-computed tomographic imaging to resolve the structural basis of atrial conduction in the human heart". In: *Circulation: Arrhythmia and Electrophysiology* 8 (2015), pp. 1514–1517.

[269] J. Zhao, B.J. Hansen, Y. Wang, T.A. Csepe, L.V. Sul, A. Tang, Y. Yuan, N. Li, A. Bratasz, K.A. Powell, et al. "Three-dimensional integrated functional, structural, and computational mapping to define the structural "fingerprints" of heart-specific atrial fibrillation drivers in human heart ex vivo". In: *Journal of the American Heart Association* 6 (2017), e005922.

Roberto Piersanti

Born in Teramo (Italy) 01-04-1984
+39 3806358116
viale sette fratelli cervi n.7, 43123 Parma (PR), Italy
roberto.piersanti@polimi.it

EDUCATION

Bachelor of Science | ***Physics*** 2015
Universitá degli studi dell'Aquila L'Aquila, Italy

- Thesis: Numerical processing of geomagnetic signal: the Hilbert-Huang transform compared with Fourier's spectral analysis
  Final mark 100/110

Master of Science | ***Physics::Biophysics*** 2018
Universitá degli studi di Parma Parma, Italy

- Master Thesis: Turbulence Large Eddy simulations in Adominal Aortic Aneurysm
  Final mark 110/110 cum laude
  in collaboration with MOX-Modelling and Scientific Computing, Politecnico di Milano

PhD candidate | ***Mathematical models and methods in engineering*** Nov. 2018 – Oct. 2021
Politecnico di Milano Milano, Italy

- Research Field: Mathematical and numerical modeling for the simulation of cardiac function
- Project title: Mathematical modeling of cardiac fibers in electro-mechanics: towards the simulation of the whole heart
- Advisor: Prof. Alfio Maria Quarteroni
  Co-Advisors: Prof. Luca Dede', Prof. Christian Vergara
  The PhD project is a part of the ERC iHEART project whose aim is to create a complete mathematical model of the human heart

WORK EXPERIENCE

Fondazione IRCCS Ca' Granda Ospedale Maggiore Policlinico di Milano Aug.-Nov. 2018
Data analyst Milano, IT

- Project: "Computational fluid dynamics (CFD) analysis of the behavior of the aneurysm sac and its goemtries after placement of endoprostheses"

Istituto Nazionale di Alta Matematica "Francesco Severi" | ***Affiliated*** Nov. 2018 - today
Gruppo Nazionale per il Calcolo Scientifico Roma, IT

Post-Doc Research fellowships: Politecnico di Milano Nov. 2021 - today
Research Fellow Milano, IT

- iHeart ERC project: "An Integrated Heart Model for the Simulation of the Cardiac Function"
  P.I.: Prof. Alfio Quarteroni

RESEARCH ACTIVITY

2019 RISM Congress iHEART - Modelling the Cardiac Function | ***Workshop attended*** July 2019
Varese, IT

2019 RISM Congress iHEART - Modelling the Cardiac Function | ***Poster presentation*** July 2019
"Influence of cardiac muscle fibers on the heart electrophysiology" Varese, IT

ISCRA Class C project application on Cineca HPC system | ***Application approved*** Feb. 2020
"Mathematical and numerical modelling of cardiac electromechanics:
towards the simulation of whole heart"

2020 MCF Congress iHEART - Modelling the Cardiac Function | ***Workshop attended*** Aug.-Sept. 2020
Milano, IT

2020 MCF Congress iHEART - Modelling the Cardiac Function | ***Oral presentation*** Aug.-Sept. 2020
"Modeling cardiac muscle fibers in ventricular and atrial electrophysiology simulations" Milano, IT

2021 MCF Congress iHEART - Modelling the Cardiac Function | ***Workshop attended*** July 2021
Milano, IT

2021 MCF Congress iHEART - Modelling the Cardiac Function | ***Oral presentation*** July 2021
"3D-0D closed-loop numerical modeling of cardiac biventricular electromechanics" Milano, IT

XV SIMAI 2020+21 Congress | ***Workshop attended*** Aug.-Sept. 2021
Parma, IT

XV SIMAI 2020+21 Congress | ***Contributed talk*** Aug.-Sept. 2021
"Modelling cardiac muscle fibers in electro-mechanical simulations" Parma, IT

Young MNCM: Mathematical and Numerical Cardiac Modeling | ***Workshop attended*** December 2021
Pavia, IT

Young MNCM: Mathematical and Numerical Cardiac Modeling | ***Opening talk*** December 2021
"Modelling whole heart muscle fibers in electro-mechanical simulations" Pavia, IT

PUBLICATIONS

Modeling cardiac muscle fibers in ventricular and atrial electrophysiology simulations Published
R.Piersanti, P.C. Africa, M.Fedele, C.Vergara, L.Dede', A.F.Corno, A.Quarteroni
Journal: Computer Methods in Applied Mechanics and Engineering,
vol. 373, p. 113468-113500, ISSN: 0045-7825
doi./10.1016/j.cma.2020.113468, arXiv:2101.10960 January 2021

3D-0D closed-loop model for the simulation of cardiac biventricular electromechanics Accepted
R.Piersanti, M.Salvador, F.Regazzoni, C.Vergara, A.F.Corno, L.Dede', A.Quarteroni
Journal: Computer Methods in Applied Mechanics and Engineering
arXiv:2108.01907
Jan 2022: accepted for publication in Computer Methods in Applied Mechanics
and Engineering January 2022

life^x - heart module: a high-performance simulator for the cardiac function. Package 1: Fiber generation Submitted
P.C. Africa, R.Piersanti, M.Fedele, L.Dede', A.Quarteroni
arXiv:2201.03303 January 2022

TEACHING EXPERIENCE

Applied numerical Analysis **(10 CFU, 48 hours)** February 2019 - June 2019
Teaching assistant to Prof. Micheletti
Bachelor of Science degree, Aerospace Engineering Politecnico di Milano, Milano, IT

Applied numerical Analysis **(10 CFU, 40 hours)** February 2020 - June 2020
Teaching assistant to Prof. Micheletti
Bachelor of Science degree, Aerospace Engineering Politecnico di Milano, Milano, IT

Applied numerical Analysis **(10 CFU, 40 hours)** February 2021 - June 2021
Teaching assistant to Prof. Micheletti
Bachelor of Science degree, Aerospace Engineering Politecnico di Milano, Milano, IT

TUTORING ACTIVITY

Master of Science Thesis | ***Co-Advisor*** Academic year 2017/2018
Biomedical Engineering Politecnico di Milano, Milano, IT

- Title: ”Intraluminal thrombus growth rate in Abdominal Aortic Aneurysms: image-based analysis from computational fluid-dynamics”
- Student: Elena Pretalli
- Advisor: Prof. Christian Vergara

Master of Science Thesis | ***Co-Advisor*** Academic year 2017/2018
Biomedical Engineering Politecnico di Milano, Milano, IT

- Title: ”Computational study of the influence of fluid dynamics on the growth of abdominal aneurysms”
- Student: Francesca Stagni
- Advisor: Prof. Christian Vergara

Numerical Analysis for Partial Differential Equation | ***Tutoring Project*** April - September 2020
Master of Science degree, Mathematical Engineering Politecnico di Milano, Milano, IT

- Title: ”Atrial electrophysiology simulations including myofibers in the coronary sinus muscle and transmurality”
- Students: Michela Ceoloni, Edoardo Conchetto

Numerical Analysis for Partial Differential Equation | ***Tutoring Project*** April - August 2020
Master of Science degree course, Mathematical Engineering Politecnico di Milano, Milano, IT

- Title: ”Active and Passive mechanics of the atria”
- Students: Margherita Pirrone, Ziarelli Giovanni

Advanced Programming for Scientific Computing | ***Tutoring Project*** April 2021 - August 2021
Master of Science degree course, Mathematical Engineering Politecnico di Milano, Milano, IT

- Title: ”Cardiac electrophysiology in the Purkinje network and myocardial tissue”
- Student: Michele Barucca

Numerical Analysis for Partial Differential Equation | ***Tutoring Project*** April 2021 - Today
Master of Science degree course, Mathematical Engineering Politecnico di Milano, Milano, IT

- Title: ”Time and space convergence analysis in cardiac electrophysiology”
- Students: Luca Edoardo Mosconi, Alessandro Guelfi

Numerical Analysis for Partial Differential Equation | ***Tutoring Project*** April 2021 - Today
Master of Science degree course, Mathematical Engineering Politecnico di Milano, Milano, IT

- Title: ”Predict the conduction velocity in cardiac electromechanics”
- Student: Gian Marco Pellicciotta

SPORT INVOLVEMENT

Volleyball player 2003 - 2020
FIPAV Federvolley — Federazione Italiana Pallavolo Parma, Italy

Beach-Volleyball player 2020 - today
AIVBC — Associazione Italiana Beach Volley Club Parma, Italy

SKILLS

Languages: Italian (Native), English (TOEFL iBT test score 78)
Programming: MATLAB, Python, FreeFem++, C++, lifev, lifex
Software: Paraview, Meshmixer, Gmsh, VMTK
OS: Microsoft Windows, Linux-like (e.g. Ubuntu), SSH server
Document Creation: Microsoft Office Suite, LaTex